

**University of Strathclyde**  
**Department of Physics**

Experimental Studies of Laser Plasma  
Wakefield Acceleration

Constantin Aniculaesei

A thesis presented for the partial fulfilment of the  
requirements for the degree of Doctor of Philosophy

2015

*“Chaos is merely order waiting to be deciphered”*

**José Saramago**

# Copyright Declaration

This thesis is the result of the author's original research. It has been composed by the author and has not been previously submitted for examination which has led the award of a degree.

The copyright of the thesis belongs to the author under the terms of the United Kingdom Copyright Act as qualified by University of Strathclyde Regulation 3.50. Due acknowledgement must always be made of the use of any material contained in, or derived from, this thesis.

Signed:

Date:

# Abstract

This thesis describes experiments that explore the possibility of improving the quality of an electron beam obtained from a laser wakefield accelerator (LWFA) by shaping the longitudinal plasma density profile. Different density profiles have been obtained by employing a range of Laval nozzles with different geometries. These are modelled and numerically simulated under different conditions using Fluent 6.3. Density lineouts from simulations for different heights above the nozzle give the plasma density profile for each experimental condition.

The plasma density profile is modified by changing the geometry of the nozzle, the interaction point, the laser beam angle relative to the exit plane of the nozzle and pressure of the gas. In this way the leading up-ramp length of the density profile (that interacts first with the laser) has been varied between 0.47 mm to 1.39 mm and the maximum plasma density varied between  $1.29 \times 10^{19} \text{ cm}^{-3}$  to  $2.03 \times 10^{19} \text{ cm}^{-3}$ .

The influence of the density profile parameters on the LWFA process is quantified by monitoring the properties of the generated electron beam. It is shown that the leading ramp of the plasma density profile *i.e.* the ramp that interacts first with the laser, has a strong influence on the quality of the electron beam. Density profiles with the same peak plasma density but different ramp lengths generate electron beams with a factor of 1.4 difference in charge, 1.1 in electron energy, 2 in pointing and 1.45 in energy spread. Longer ramp lengths enhance the quality of electron beams, which suggest that LWFA injection occurs at the entrance density ramp.

Complex density profiles are produced by tilting the nozzle relative to the direction of propagation of the laser. This allows continuous tuning of the peak energy of the electron beam from  $135 \pm 2 \text{ MeV}$  up to  $171 \pm 2 \text{ MeV}$ . The electron beam energy spread show improvements from  $20.7 \pm 1.2\%$  to  $8.9 \pm 0.9\%$ . The charge closely follows the evolution of the energy spread and has a mean value of  $0.61 \pm 0.16 \text{ pC}$ .

Experimental results also show that the angular distribution of the electron beam becomes elliptical when the laser focal plane is moved from the edge of the gas jet towards the centre of the density profile. This result is linked to the existence of a distorted LWFA bubble that propagates off-axis therefore affecting the pointing and transverse shape of the electron beam.

# Acknowledgements

This thesis could not have been done without the help of the ALPHA-X team, former and present members, and especially without financial support from the Engineering and Physical Sciences Research Council (EPSRC).

I would like to thank my supervisor, Prof. Dino A. Jaroszynski, who gave me the chance to conduct experiments in this fast evolving field of laser-matter interaction physics. Many thanks to my thesis examiners, Prof. Thomas Kuehl and Dr. Kevin Ronald, for their help in improving my manuscript. I also thank Prof. Bernhard Hidding for his unconditional support and for giving me all the time required to write my thesis. I want to thank Prof. Daniele Faccio for supporting me at difficult times in the project and encouraging me to press on in face of difficulties.

## **Role of the Author**

The experiments have been performed in ALPHA-X laboratory by the author with the help of Dr Enrico Brunetti, Dr Silvia Cipiccia, Dr Grace Manahan, Dr Anna Subiel, Dr Gregory Vieux, Dr Gregor Welsh, Dr Mark Wiggins, Mr Cristian Ciocarlan, Mr David Reboredo Gil and Mr Peter Grant. All experimental data have been processed and analysed by the author.

The supersonic nozzles have been designed (with the exception of nozzle A) by the author and manufactured by David Clark in the University of Strathclyde Mechanical Workshop.

All the computational fluid dynamics simulations of supersonic nozzles and numerical data analysis have been carried out by the author.

# List of Publications

The following key publications resulted from the work in this thesis:

1. Wiggins S. M., Issac R. C., Welsh G. H., Brunetti E., Shanks R. P., Anania M. P., Cipiccia S., Manahan G. G., **Aniculaesei C.**, Ersfeld B., Islam M. R., Burgess R. T. L., Vieux G., Gillespie, W. A., MacLeod A. M., van der Geer S. B., de Loos M. J., and Jaroszynski D. A., “High quality electron beams from a laser wakefield accelerator”, *Plasma Phys. Control. Fusion* 52, 124032 (2010).
2. Welsh, G. H., Anania, M. P., **Aniculaesei, C.**, Brunetti, E., Burgess, R. T. L., Cipiccia, S., Clark, D., Ersfeld, B., Islam, M., Issac, R., Manahan, G., McCanny, T., Raj, G., Reitsma, A., Shanks, R., Vieux, G., Wiggins, S. M., Jaroszynski, D. & 22 others “Electron beam quality measurements on the ALPHA-X Laser-plasma wakefield accelerator”, 18-Jun-2010 IPAC 2010 contributions to the proceedings . p. 1146-1148. (2010).
3. Gillespie, W. A., MacLeod, A. M., Jamison, S. P., Wiggins, S. M., Welsh, G. H., Aniculaesei, C., Issac, R., Brunetti, E., Shanks, R., Cipiccia, S., Anania, M. P., Manahan, G., **Aniculaesei, C.**, Ersfeld, B., Islam, M., and Jaroszynski, D. A. “High quality electron beams generated in a laser wakefield accelerator” PAC2011, Contributions to proceedings, p. 307-309. (2011).
4. Wiggins, S. M., Gallacher, J. G., Schlenvoigt, H-P., Schwoerer, H., Welsh, G. H., Issac, R., Brunetti, E., Vieux, G., Shanks, R., Cipiccia, S., Anania, M. P., Manahan, G., **Aniculaesei, C.**, Subiel, A., Grant, D. W., Reitsma, A., Ersfeld, B., Islam, M., and Jaroszynski, D. 2011 Harnessing relativistic plasma waves as novel radiation sources from terahertz to x-rays and beyond II. Jaroszynski, D. (ed.). Bellingham, (Proceedings of SPIE ; vol. 8075)
5. Manahan, G., Anania, M. P., **Aniculaesei, C.**, Brunetti, E., Cipiccia, S., Ersfeld, B., Islam, M. R., Issac, R. C., Shanks, R. P., Welsh, G. H., Wiggins, S. M., and Jaroszynski, D. A., “Emittance and energy spread measurements of relativistic electrons from laser-driven accelerator”, DIPAC2011 Contributions to the proceedings, p. 9-11, (2011).
6. Welsh, G. H., Wiggins, S. M., Issac, R. C., Brunetti, E., Manahan, G. G., Islam, M. R., Cipiccia, S., **Aniculaesei, C.**, Ersfeld, B., and Jaroszynski, D. A., “High resolution electron beam measurements on the ALPHA-X laser–plasma wakefield accelerator”, *J. Plasma Phys.* 78, 393 (2012).
7. Moskvina, V., Subiel, A., Desrosiers, C., Wiggins, M., Maryanski, M., Mendonca, M., Boyd, M., Sorensen, A., Cipiccia, S., Issac, R., Welsh, G., Brunetti, E., **Aniculaesei, C.**, and Jaroszynski, D. A., “Characterization of the Very High Energy Electrons, 150-250 MeV (VHEE) Beam Generated by ALPHA-X Laser Wakefield Accelerator Beam Line for Utilization in Monte Carlo Simulation for Biomedical Experiment Planning”, *Medical Phys.* 39, 3813 (2012).

8. Ciocarlan, C., Wiggins, S. M., Islam M. R., Ersfeld, B., Abuazoum, S., Wilson, R., **Aniculaesei, C.**, Welsh G. H., Vieux, G., and Jaroszynski D. A., “The role of the gas/plasma plume and self-focusing in a gas-filled capillary discharge waveguide for high-power laser-plasma applications”, *Phys. Plasmas* 20, 093108 (2013).
9. Anania, M. P., Brunetti, E., Wiggins, S. M., Grant, D. W., Welsh, G. H., Issac, R. C., Cipiccia, S., Shanks, R. P., Manahan, G. G., **Aniculaesei, C.**, van der Geer, S. B., de Loos, M. J., Poole, M. W., Shepherd, B. J. A., Clarke, J. A., Gillespie, W. A., MacLeod, A. M., and Jaroszynski, D. A., “An ultrashort pulse ultra-violet radiation undulator source driven by a laser plasma wakefield accelerator”, *Appl. Phys. Lett.* 104, 264102 (2014).
10. Manahan, G. G., Brunetti, E., **Aniculaesei, C.**, Anania, M. P., Cipiccia, S., Islam, M. R., Grant, D. W., Subiel, A., Shanks, R. P., Issac, R. C., Welsh, G. H., Wiggins, S. M., and Jaroszynski, “Characterisation of laser-driven single and double electron bunches with a permanent magnet quadrupole triplet and pepper-pot mask”, *New J. Phys.* 16, 103006 (2014)

# Contents

<b>COPYRIGHT DECLARATION</b> .....	<b>I</b>
<b>ABSTRACT</b> .....	<b>II</b>
<b>ACKNOWLEDGEMENTS</b> .....	<b>III</b>
<b>ROLE OF THE AUTHOR</b> .....	<b>IV</b>
<b>LIST OF PUBLICATIONS</b> .....	<b>V</b>
<b>LIST OF FIGURES</b> .....	<b>X</b>
<b>LIST OF TABLES</b> .....	<b>XXV</b>
<b>1 INTRODUCTION</b> .....	<b>1</b>
1.1 FROM RADIO-FREQUENCY ACCELERATORS TO PLASMA BASED ACCELERATORS .....	1
1.2 PLASMA BASED ACCELERATORS: HISTORICAL OVERVIEW AND PERSPECTIVES.....	3
1.3 MOTIVATION FOR AN EXPERIMENTAL INVESTIGATION OF THE INFLUENCE OF LONGITUDINAL PLASMA PROFILE ON THE QUALITY OF THE LWFA .....	8
1.4 STRUCTURE OF THE THESIS .....	9
<b>2 THEORY OF LASER WAKEFIELD ACCELERATION</b> .....	<b>11</b>
2.1 PLASMA THEORY .....	11
2.2 PROPAGATION OF ELECTROMAGNETIC WAVES IN PLASMA.....	13
2.2.1 <i>Electromagnetic waves propagation in a plasma in the linear regime</i> .....	14
2.2.2 <i>Nonlinear regime</i> .....	16
2.3 LASER WAKEFIELD ACCELERATION. WAVE-BREAKING AND SELF-INJECTION IN THE HIGHLY NON-LINEAR REGIME .....	21
2.3.1 <i>Trajectory of electrons inside the LWFA channel. Betatron oscillation and electron                 beam divergence control</i> .....	24
2.3.2 <i>General limitations of laser wakefield acceleration</i> .....	27
2.3.3 <i>Scaling laws for the laser wakefield acceleration</i> .....	34
<b>3 GAS TARGET CHARACTERISATION AND OPTIMISATION</b> .....	<b>36</b>
3.1 THEORY OF DE LAVAL SUPERSONIC GAS NOZZLES.....	36
3.1.1 <i>A general description of thermodynamic systems</i> .....	36
3.1.2 <i>Compressible gas flows</i> .....	39
3.2 NUMERICAL SIMULATION OF SUPERSONIC GAS JETS .....	50
3.2.1 <i>Flow model and approximations</i> .....	50
3.2.2 <i>Simulation results</i> .....	53
3.3 EXPERIMENTAL CHARACTERISATION AND OPTIMISATION OF VALVE-LAVAL NOZZLES ASSEMBLY .....	58

3.3.1	<i>Characterisation of supersonic gas jets using interferometry</i> .....	58
3.3.2	<i>Optimisation of the solenoid valve – supersonic nozzle assembly for LWFA experiments</i> 63	
3.4	SUMMARY OF THE CHAPTER AND CONCLUSIONS.....	73
<b>4</b>	<b>EXPERIMENTAL SETUP OF LWFA FOR ELECTRON ACCELERATION AND DIAGNOSIS</b> .....	<b>75</b>
4.1	LASER AND LASER BEAM TRANSPORT SYSTEM.....	75
4.2	GAS NOZZLE SYSTEMS .....	78
4.3	ELECTRON BEAM DIAGNOSTIC SYSTEMS .....	79
4.4	EXPERIMENTAL METHOD .....	85
<b>5</b>	<b>LWFA EXPERIMENTAL RESULTS WITH DIFFERENT PLASMA DENSITY PROFILES</b> .....	<b>88</b>
5.1	INFLUENCE OF DENSITY RAMP ON ELECTRON BEAM PROPERTIES .....	88
5.1.1	<i>Quality of the electron beam for plasma medium with density ramps</i> .....	88
5.1.2	<i>Electron beam charge control</i> .....	97
5.1.3	<i>Angular distribution of the electrons and influence of the laser focal plane position inside the gas jet</i> .....	100
5.2	DISCUSSION .....	118
5.2.1	<i>Possible mechanism that controls, for a limited range, the energy of the electron beam</i> 118	
5.3	CONCLUSIONS OF THE CHAPTER .....	122
<b>6</b>	<b>LWFA EXPERIMENTS WITH TILTED SUPERSONIC GAS NOZZLES</b> .....	<b>125</b>
6.1	ELECTRON BEAM ENERGY AND ENERGY SPREAD CONTROL FROM A WAKEFIELD ACCELERATOR USING TILTED NOZZLES .....	125
6.1.1	<i>Influence of tilted gas jet with relatively short density ramps and in presence of gas density shocks</i> .....	129
6.1.2	<i>Influence of tilted gas jet with relatively long density ramps and smooth profile</i> .....	134
6.2	VERY LARGE GAS NOZZLE TILTING ANGLE. LWFA EXPERIMENTS WITH DOWN-RAMP PLASMA DENSITY .....	144
<b>7</b>	<b>CONCLUSIONS</b> .....	<b>149</b>
7.1	SUMMARY OF RESULTS .....	149
7.1.1	<i>Supersonic gas jet simulations and optimisation</i> .....	149
7.1.2	<i>LWFA experiments with vertical nozzles</i> .....	149
7.1.3	<i>LWFA experiments with tilted nozzles</i> .....	151
7.2	FUTURE DEVELOPMENTS OF THE PRESENT WORK AND SUGGESTIONS FOR IMPROVEMENT ....	152

7.2.1	<i>Supersonic gas jet generation and characterisation</i> .....	152
7.2.2	<i>Electron beam transport and characterisation</i> .....	152
7.2.3	<i>Energy and energy spread control by tilted nozzle</i> .....	153
7.2.4	<i>LWFA experiments with upward and downward plasma density ramps</i> .....	153
7.2.5	<i>Plasma lens effect investigation. Symmetric and asymmetric case</i> .....	155
<b>8</b>	<b>APPENDICES</b> .....	<b>156</b>
8.1	PLASMA LENS EFFECT: ASYMMETRIC CASE .....	156
8.2	LASER WAVEFRONT ABERRATIONS .....	158
8.3	SUPERSONIC NOZZLES DRAWINGS.....	160
<b>9</b>	<b>BIBLIOGRAPHY</b> .....	<b>164</b>

# List of figures

Figure 1-1: Ernest Lawrence, the first pioneer in particle acceleration physics, holding one of the first circular electron accelerators, a cyclotron (inset) (newscenter.lbl.gov, 2015). ..... 1

Figure 1-2: Aerial view of the location of the Large Hadron Collider, at CERN in Geneva. The circle marks the underground placement of 27 km of tunnel where the LHC is installed (CERN, 2000). ..... 2

Figure 1-3: The ion bubble generated as a result of nonlinear laser-plasma interaction (Lu, Huang, Mori, & Katsouleas, 2006) ..... 5

Figure 2-1: Figure-of-eight motion of an electron in a plane wave. The reference frame moves with the average drift velocity ..... 16

Figure 2-2: Diffraction angle  $\Theta$  vs. relativistic defocussing angle  $\theta$  ..... 17

Figure 2-3: Plasma density perturbation  $\delta n / n_0$  (red curve) and plasma wave electric field  $E_z / E_0$  (black curve) excited by a Gaussian laser pulse with  $a_0 = 2$  and pulse length  $\tau = 6$  fs. .... 21

Figure 2-4: Trajectory of the trapped (solid line) and untrapped electrons (dashed line) according to Kostyukov (Kostyukov, Nerush, Pukhov, & Seredov, 2009) ..... 22

Figure 2-5: Experimental results from the current study showing the electron energy spread vs. charge. A proof of the presence of beam loading is the increase in the energy spread with charge..... 23

Figure 2-6: Variation of the electron beam profile with the polarisation of the laser. The polarisation of the laser is a)  $-20^\circ$ , b)  $10^\circ$ , c)  $30^\circ$  and d)  $50^\circ$  (Mangles, et al., 2006) ..... 25

Figure 2-7: The evolution of the electron output angle as a function of the electron energy and plasma frequency.....	26
Figure 2-8: A false colour image of the electron distribution 64 cm from the accelerator exit (inset) The profile has a central spot surrounded by a halo. A line out of the profile fitted with double Gaussian is also shown. Caption taken from Issac et al. (Issac, et al., 2009) .....	26
Figure 2-9: The diffraction and the Rayleigh length of a laser beam. ....	28
Figure 2-10: The structure of the “bubble”. $v_{back}$ is the velocity of the back of the bubble with respect to the front velocity $v_{front}$ and $v_e$ is the velocity of the electron bunch.....	31
Figure 2-11: Plasma wave phase representation. The charge will experience a focusing field and an accelerating field. Only the first quadrant is suitable for simultaneous focusing and acceleration.....	33
Figure 3-1: In a) a low amplitude pressure wave propagates through a fluid at rest while in b) the pressure wave is stationary and the fluid moves through the control volume.....	40
Figure 3-2: A typical convergent-divergent nozzle. ....	42
Figure 3-3: Critical area ratio versus pressure ratio. For $k = 1.4$ the maximum $A^*/A = 1$ is obtained for $p/p_0 = 0.528$ . The two branches of the graph represent two possible flow regimes: subsonic and supersonic regime (Krause, 2005).....	47
Figure 3-4: Critical area versus Mach number. For $k = 1.4$ the critical area $A^* / A \approx 0$ for Mach numbers $M \approx 0$ or $M \rightarrow \infty$ .....	48

Figure 3-5: Contours of density in a logarithmic scale of the zoomed interior of a supersonic flow close to the nozzle wall. Due to friction at the wall, boundary layers are produced which results in the generation of density gradients close to the nozzle wall..... 51

Figure 3-6: The evolution of  $Y^+$  along the nozzle walls beginning with the throat position. The condition  $Y^+ < 1$  is satisfied for any wall nozzle position. .... 52

Figure 3-7: The supersonic nozzle model used in simulations. Due to cylindrical symmetry only one side of the nozzle is simulated..... 52

Figure 3-8: Example of simulation results showing logarithmic density contour plots for (a) Nozzle 510 and (b) Nozzle 511. The backing pressure is 2.5 MPa. The legend shows the gas density distribution from low density (blue) to high density (red) ..... 54

Figure 3-9: The evolution of gas density along the centre line of the gas nozzle. The nozzle outlet is placed at 10 mm. Note the quasi-exponential decrease in density. The simulated nozzle is 510 with a backing pressure of 3 MPa and argon gas. .... 55

Figure 3-10: Lineouts of density at the axis of the nozzle taken at the nozzle outlet. The lineouts are shown for different backing pressures. The density profiles are obtained with Nozzle A..... 56

Figure 3-11: Density of the gas at a point situated at the middle of the gas nozzle outlet. The evolution of the density with backing pressure is linear..... 56

Figure 3-12: Evolution of density profiles with gas temperature. The lineouts of density are determined at the outlet of the nozzle..... 57

Figure 3-13: The evolution of mean density with the gas temperature. Lineouts of density are made at the outlet of the nozzle and the density is averaged over whole radial direction. Vertical bars represent the standard error. .... 57

Figure 3-14: Examples of plasma density profiles along the laser propagation direction crossing some distance $y$ above the gas nozzle exit. a) Density profiles when the gas nozzle is in straight position and b) density profiles obtained when the gas nozzle is tilted. ....	58
Figure 3-15: Basic setup of Mach-Zehnder interferometer used in ALPHA-X experiments for density profile retrieval. ....	59
Figure 3-16: Density profiles obtained from interferometry when different laser powers are employed. Courtesy of Anna Subiel (Subiel, 2012) .....	59
Figure 3-17: The density profile obtained from interferometry (red curve) and the density profile obtained from CFD simulations (blue curve). The inset shows a false colour image of the plasma channel created by the laser. Courtesy of Anna Subiel (Subiel, 2012).....	60
Figure 3-18: The lineouts of density (a) and radial velocity (b) at different heights from the nozzle outlet. CFD simulated gases: Ar and He with a backing pressure of 3 MPa for Nozzle 510. Note the difference in density profiles although both gases are monatomic.....	62
Figure 3-19: Experimental observation of Ar and He flow under the same conditions. The lineouts of density are taken 170 $\mu\text{m}$ above the nozzle outlet. The data are taken from Quan-Zhi et al. (Quan-Zhi, et al., 2004).....	63
Figure 3-20: Mechanical design of the fast solenoid valve (a) and valve-nozzle assembly (b) (www.smijapan.com, 2015).....	64
Figure 3-21: Typical valve driver pulse with the two components: high voltage pulse followed a low voltage plateau. ....	64

Figure 3-22: DIP switches for controlling the high voltage pulse length. ....	66
Figure 3-23: Setup used for measuring the stroke distance of the solenoid valves. On the left side of the picture is the power supply used to move the poppet inside the valve. At the right side there is a micrometre gauge with the measuring tip resting inside the valve, on the poppet. ....	66
Figure 3-24: Calibration of the pressure transducer.....	67
Figure 3-25: Evolution of the pressure drop with the trigger duration T for stroke distance 160 $\mu\text{m}$ , backing pressure 2.1 MPa and high voltage pulse duration of 220 $\mu\text{s}$ .....	68
Figure 3-26: Maximum pressure drop with increase of the trigger pulse duration T. The high voltage pulse duration is changed from 180 $\mu\text{s}$ to 300 $\mu\text{s}$ with a step of 40 $\mu\text{s}$ . .....	69
Figure 3-27: Evolution of the flow profile with the high voltage trigger window for stroke distance 160 $\mu\text{m}$ , backing pressure 2.1 MPa and trigger length 2 ms.....	69
Figure 3-28: Evolution of pressure drop with backing pressure for 160 $\mu\text{m}$ stroke distance for four high voltage pulse durations: 180 $\mu\text{s}$ , 220 $\mu\text{s}$ , 260 $\mu\text{s}$ and 300 $\mu\text{s}$ . The trigger duration is 2.0 ms for all curves. ....	70
Figure 3-29: Evolution of pressure drop with stroke distance (SD) under the same conditions of backing pressure $p = 5$ MPa and trigger duration $T = 2$ ms. For each stroke distance there are 4 curves for 4 different high voltage pulse durations: 180 $\mu\text{s}$ , 220 $\mu\text{s}$ , 260 $\mu\text{s}$ and 300 $\mu\text{s}$ . ....	71
Figure 3-30: a) Sketch of the poppet and its dimensions, b) image of the cut and original poppets.....	72

Figure 3-31: Comparison between the operation of the valve for the case where the poppet is cut by 350 $\mu\text{m}$ (dotted and dash-dotted curves) and the poppet is unmodified (straight and dashed curves).....	72
Figure 4-1: The Ti:sapphire laser system used in the LWFA experiments.....	75
Figure 4-2: An image of the laser spot (inset) after the compressor and the normalised intensity plots for X and Y axes. Correlation between spot shape/laser wavefront tilting and good quality electron beam requires symmetry in spot shape be as high as possible. ....	78
Figure 4-3: Basic schematics of the LWFA setup after the compressor. It contains components for electron beam characterisation and different setups for applications (for instance an undulator). ....	79
Figure 4-4: A false colour image showing a typical plasma channel formed during the LWFA process. The laser travels from left to the right. The white circle marks the outlet of the nozzle and has 2.8 mm diameter.....	80
Figure 4-5: False colour images recorded on Lanex 1 with a) halo + main electron beam and b) background subtracted in such a way that the halo visibility is decreased. ....	81
Figure 4-6: Accumulated false colour images of the electron beam recorded on the L1 screen. The image a) shows the electron beam pointing to the right of the centre of the beam line. The image b) shows the electron beam pointing through the centre of the beam line. Further discussion on the electron beam pointing direction control is given in Chapter 6. ....	82
Figure 4-7: Electron spectrometer layout with an example electron energy spectrum recorded (inset). Different colours correspond to different energies of the electrons forming the electron beam. ....	84

Figure 4-8: Simulated energy spread vs charge. Predicted energy spread measurements for simulated electron spectra embedded with noise for a 2 mrad electron beam divergence and peak energy (at maximum fluence) of 150 MeV. EMQ currents are (5,-4, 5) A respectively. The dotted lines indicate the theoretical/actual energy spread. Courtesy of Grace Manahan (Manahan, 2013)..... 85

Figure 4-9: An upper view of the nozzle axis configuration. The laser moves in the negative z axis direction and the distance between laser and the position of the outlet of the nozzle relative to the laser focal plane is varied by moving the nozzle in the negative y axis direction..... 86

Figure 4-10: An example electron energy spectrum obtained in the electron spectrometer. Only the marked part of the spectrum is used in data analysis. .... 86

Figure 4-11: Pictures of the gas nozzle on the tilt configuration setup. The angle between the direction of propagation of the laser and the normal to the nozzle outlet defines the tilting angle. .... 87

Figure 5-1: Typical density profile used in LWFA experiments with supersonic gas jets as generated by Nozzle 511. .... 89

Figure 5-2: Five example spectra of quasi- mono-energetic electron beams produced at various experimental conditions by McGuffey. (McGuffey, et al., Experimental laser wakefield acceleration scalings exceeding 100 TW, 2012)..... 89

Figure 5-3: Different density profiles used in experiments to test the influence of the density ramp on the quality of the electron beam. These density profiles correspond to conditions for stable electron beam formation by adjusting the backing pressure p, 90

Figure 5-4: The evolution of plasma density, assuming full ionisation vs a) entrance ramp length, and b) vs. plateau length for the Nozzle A (black squares), Nozzle 510

(green triangles) and Nozzle 511(red dots).The dashed line is drawn just to guide the eye. .... 92

Figure 5-5: The relative charge recorded on Lanex1 vs entrance ramp length (a) and density plateau length (b). The vertical bars represent the standard error. The data is recorded with the Nozzle A (black squares), Nozzle 510 (green triangles) and Nozzle 511(red dots).The dashed line is drawn just to guide the eye. .... 92

Figure 5-6: The relative charge vs. peak density. It can be seen that for the same peak density, the relative charge is different; this difference is determined by the density ramp. The vertical bars represent the standard error. The data is recorded with the Nozzle A (black squares), Nozzle 510 (green triangles) and Nozzle 511(red dots).. 93

Figure 5-7: Mean peak electron beam energy measured as a function of the maximum plasma density. This result seems to contradict the predicted trend (red points) if the density ramps are ignored in the data analysis. The vertical bars represent the standard error. .... 94

Figure 5-8: Electron beam energy as a function of the plasma density ramp slope. The two results corresponding to two different electron beam energies at the same plasma density make sense when taking into account the ramp slope (the 2 points marked by a blue circle). The vertical bars represent the standard error. .... 95

Figure 5-9: Electron beam energy (square data points) and absolute energy spread (round data points) as a function of the plasma density ramp slope. Black, green and red data points are obtained with the Nozzle A, B, and C, respectively. .... 96

Figure 5-10: The charge vs. plasma density according to McGuffey et al. (McGuffey, et al., Experimental laser wakefield acceleration scalings exceeding 100 TW, 2012) ..... 97

Figure 5-11: The entrance ramp length (a) and relative charge (b) versus plasma density in the experiment designed to replicate the trend observed in McGuffey's experiment. The vertical bars represent the standard error. The gas jet is generated by Nozzle 508. The dashed line is drawn just to guide the eye. .... 99

Figure 5-12: Numerical simulation results showing the laser pulse  $a_0$  evolution in the plasma ramp region as a function of the longitudinal distance normalized to the Rayleigh length (negative axis up to zero position). Maximum plasma density values are  $\rho_1 = 1.54 \times 10^{18} \text{ cm}^{-3}$  (black curve),  $\rho_2 = 2.75 \times 10^{18} \text{ cm}^{-3}$  (red curve) and  $\rho_3 = 3.49 \times 10^{18} \text{ cm}^{-3}$  (blue curve) and  $\rho_0 = 0$  (green curve) (Ciocarlan, et al., 2013)..... 99

Figure 5-13: Plasma density profile at  $y = 2.95 \text{ mm}$  above the Nozzle A. The backing pressure is 3.5 MPa. .... 101

Figure 5-14: a) The relative charge evolution, b) the electron beam pointing and c) the pointing stability as a function of the laser focal plane inside the gas jet. The vertical bars represent the standard error. .... 102

Figure 5-15: The Ejection Angle EA on both x and y axes as a function of the peak plasma density. The vertical bars represent the standard error. The gas jet is generated by nozzle A. .... 103

Figure 5-16: Two false colour pictures of the plasma channel taken during experiments. The left plasma channel produced an electron beam with  $EA_x = -0.03 \text{ mrad}$  (almost no deviation) and the right channel produced an electron beam with  $EA_x = 9.63 \text{ mrad}$  (strong deviation). In both cases no deviation of the plasma channel can be observed (bottom). The laser is propagating from left to right in the figures. .... 104

Figure 5-17: The side-view plasma imaging in the experiment described by Chen et al. (Chen, et al., 2007) when the laser energy is 2.5 J and plasma density  $5 \times 10^{18} \text{ cm}^{-3}$  for different shots (a,b,c). d) represents the Thomson scattering measurement

corresponding to image b). The laser deviation is clearly seen, a result that cannot be confirmed in experiments here..... 104

Figure 5-18: The plasma density profile for the Nozzle A tilted at positive 30° ..... 106

Figure 5-19: Change in the cumulative (400 shots) electron beam distribution on L1 (top right and left false colour images) as the laser focal plane is moves from the edge of the gas jet (left) towards a position inside the gas jet (right). This effect cannot be explained using a plasma lens effect..... 107

Figure 5-20: An accumulation of 400 shots showing the distribution of the electron beam on Lanex screen L1 as the laser focal plane moves from a position deep inside the gas jet towards the edge of the gas jet. The electron distribution changes from “polarised” to normal but only in the experiments run after the laser alignment (b and c group of images). Pictures recorded before laser realignment (image a) show normal angular distribution. The gas jets are produced by Nozzle A tilted at 30°..... 107

Figure 5-21: False colour images of individual electron bunches recorded on the fluorescent screen L1 when the laser focal plane is  $z = 0$ ..... 108

Figure 5-22: Evolution of the pulse intensity envelope with the focus parameters in the presence of wavefront aberration (upper row) and without aberration (lower row). Caption from Popp et al. (Popp, et al., 2010)..... 109

Figure 5-23: Cross-section through the central x-z plane (laser polarisation plane) of a 3D LWFA-simulation volume with (top) and without (bottom) a pulse-front-tilted driver laser. Caption from Popp et al. (Popp, et al., 2010)..... 110

Figure 5-24: The pointing of the electron beam as a function of the charge for two different values of  $z$ .  $z = 0$  corresponds to a position deep in the density ramp,  $\sim 1.2$  mm from the edge, and  $-1.2$  mm corresponds to a position close to edge of the gas jet. The legend shows the distribution of charge from lower values (black) to higher values (blue). ..... 111

Figure 5-25: False colour images showing the plasma channel movement as the laser focal position is changed inside the gas jet. The laser is propagating from up to down in the images and the white lines mark the initial position of the beginning of the channel and the final position of the end of the channel as the laser focal plane is scanned inside the gas jet. .... 111

Figure 5-26: A schematic view of a LWFA plasma channel created by the laser. It starts with the LWFA region, followed by an ion channel region and ends with a region where only plasma is found..... 113

Figure 5-27: The relative electron charge as a function of the Ejection Angle for different laser focal positions inside the gas jet. As the laser focal plane moves from  $z = 0.95$  mm (a) to  $z = 0.45$  mm (c), towards the edge of the gas jet, the electron beam ejection angle depends on the charge of the electron beam. .... 116

Figure 5-28: Angular distribution of electron bunches on the Lanex screen corresponding to laser focal plane placed at  $z = 0.45$  mm (top) and false colour images of accumulated electron shots on L1 when the laser focal plane is changed from 0.95 mm to 0.45 mm (bottom). .... 117

Figure 5-29: Dependence of the beam width parameter  $W$  on the distance of propagation  $\zeta$  in the under-dense plasma with the ramp density profile with the function of  $n(\zeta) = \tan(\zeta/d)$  with various conditions such as a laser intensity of  $I = 1.21 \times 10^{18}$  W cm<sup>-2</sup> and the laser wavelength is  $\lambda_0 = 1.06$   $\mu$ m and  $n_0 = 1.7 \times 10^{21}$  cm<sup>-3</sup>,  $d = 5.8$  (black curve),  $n_0 = 1.2 \times 10^{21}$  cm<sup>-3</sup>,  $d = 7.3$  (grey curve),  $n_0 = 0.6 \times 10^{21}$  cm<sup>-3</sup>,  $d = 5.8$  (dash-dotted curve), and the uniform density profile (dashed curve). (Sadighi-Bonabi, Habibi, & Yazdani, 2009)..... 119

Figure 5-30: Numerical simulations using the 2D axisymmetric code WAKE showing the evolution of the laser pulse normalised intensity  $a_0$  and spot waist  $w_0$  as it propagates in a different plasma density ramps. .... 121

Figure 5-31: A false colour camera image of the Thomson scattering from a LWFA plasma channel. A band-pass filter centred at 400 nm has been used. The plasma channel diameter is about 10  $\mu\text{m}$  and occupies around 5 pixels in the image therefore could not be used to monitor the small changes due to relativistic self-focussing in different plasma density ramps. The white circle marks the outlet of the nozzle.... 121

Figure 5-32: The relative charge (black), the peak energy (red) and the energy spread (green) as a function of the plasma plateau length. The data has been recorded with the Nozzle A (squares), Nozzle 510 (triangles) and Nozzle 511 (dots)..... 123

Figure 6-1: Evolution of charge (red solid line with squares), electron energy spread  $\Delta E$  at FWHM (blue dotted line with circles) as a function of the counter propagating laser normalised vector potential  $a_1$ . The error bars represent the r.m.s. fluctuation. Inset: variation of peak electron energy. Caption from Faure (Faure, et al., 2006). 126

Figure 6-2: The plasma density profiles used in simulations for the cases when the plasma density has been continuously adjusted (continuous line) and for the case when the plasma density has been kept constant (dashed line).  $z_0$  marks the beginning of the plasma density ramp of the SI profile. (Wen, et al., 2010) ..... 127

Figure 6-3: The evolution of the peak energy (squares) and energy spread (full dots) when an up-ramp density (SI) or a flat top profile (SII) is used. (Wen, et al., 2010) ..... 127

Figure 6-4: Energy spectra at different times for cases S-I and S-II. Solid lines show the energy spectra of electron bunches before exiting the plasma, and dashed lines show the energy spectra at  $t = 4.67$  ps. (Wen, et al., 2010) ..... 129

Figure 6-5: The plasma density profiles corresponding to different gas nozzle tilting angles  $\Phi$ . The laser is incident on the gas jet from the left side..... 130

Figure 6-6: False colour images of accumulated spectra corresponding to the three tilting angles: 0°, 15° and 30° .	131
Figure 6-7: Histograms of the electron peak energy (a) and energy spread (b) corresponding to different tilting angles. The energy tune is achieved but the energy spread is not controlled and remains quasi-constant.	131
Figure 6-8: Histograms of the charge of the electron bunch in the electron spectrometer a) and on L1 b).	132
Figure 6-9: Evolution of the electron beam energy (black squares), r.m.s energy spread (red dots) and charge in the main bunch (green triangles) as the laser focal point is scanned inside the tilted gas nozzle A. Tilting angles are a) 15° and b) 30°. The density profiles (magenta solid line) are given at 15° and 30° tilt, respectively. The vertical dotted line approximate the beginning of the down-ramp plasma density	133
Figure 6-10: The evolution of the dark current/Q1 ratio (circles) and of charge in the main bunch (full squares) as a function of the laser focal plane z inside the gas jet. Red data points correspond to 30° nozzle tilting and black data points correspond to 15° nozzle tilting.	134
Figure 6-11: The plasma density profiles generated by the Nozzle 511 tilted in different experimental conditions. Note the density profiles which are “smoother” compared with the density profile generated by the Nozzle A. Please see Table 11 for full conditions.	135
Figure 6-12: Histograms of the a) electron peak energy and b) r.m.s. energy spread corresponding to density profiles of Nozzle 511 with positive tilting.	136
Figure 6-13: Histograms of the a) electron peak energy and b) r.m.s. energy spread corresponding to density profiles of Nozzle 511 with negative tilting.	136

Figure 6-14: The mean values of electron beam parameters as a function of the entrance ramp slope. The electron beam shows a periodic strong enhancement as the slope varies. The vertical bars represent the standard error. The figure a) corresponds to data recorded with positive nozzle tilting and the figure b) corresponds to data recorded with negative nozzle tilting. .... 137

Figure 6-15: a) The divergence and b) electron beam energy as a function of the charge. .... 138

Figure 6-16: a) The electron peak energy (black), energy spread (red) and charge (green) and b) the r.m.s divergence of the electron beam as a function of the nozzle tilting angle. Data points with the same tilting angle correspond to different plasma density slopes. The curves are drawn just to guide the eye and do not necessarily have a physical meaning. .... 140

Figure 6-17: The charge recorded by the espec versus the charge recorded by the Lanex1 for a) the same dataset and b) for different datasets..... 141

Figure 6-18: Density profiles generated with the Nozzle 510. The nozzle is in straight or tilted geometry so that the density ramp slope can be varied. .... 142

Figure 6-19: Histograms of a) electron energy, b) energy spread and c) charge when Nozzle 510 is used in experiments with positive nozzle tilting. .... 143

Figure 6-20: Histograms of a) electron energy, b) energy spread and c) charge when Nozzle 510 is used in experiments with negative tilting..... 143

Figure 6-21: The plasma density profile for the experiments with a down-ramp density profile. This is split into three ramps, an up-ramp  $z_1$  and two down-ramps  $z_2$  and  $z_3$ . By focusing the laser inside the gas jet, the LWFA is constrained to the down-ramp density segment. .... 145

Figure 6-22: Charge measured by the ICT as a function of gas jet position with respect to the laser focus. The Gaussian fit to the plasma density indicates the relative laser focus position in the profile. (Geddes, et al., 2008) ..... 146

Figure 6-23: Evolution of the relative charge and absolute charge as the laser focal plane varies from -1.2 mm (edge of the gas nozzle) towards 0 mm (centre of the gas nozzle)..... 147

Figure 6-24: Evolution of the energy, absolute energy spread and relative energy spread as the laser focal position varies from -1.2 mm (edge of nozzle) to 0 mm (centre of nozzle). The vertical bars represent the standard error. .... 147

Figure 7-1: Electron bunch acceleration and energy spread reduction in plasma layers: (a) the plasma-density profile, (b) the mean energy of the electron bunch, (c) electron energy vs electron position in the bunch. Electrons are accelerated by the first laser pulse in the first two layers ( $0 < x < 43370\lambda_L$ ), whereas they are decelerated in the third and fourth layers ( $43370\lambda_L < x < 49820\lambda_L$ ). The solid and dotted lines correspond to the particle-in-cell (PIC) simulation results and theoretical estimates, respectively. To compare, the dashed line shows acceleration in homogeneous plasma with the constant density  $n_0 = 0.001n_c$ . The energy distributions in frame (c) are shown at the beginning of the deceleration at  $x = 43370\lambda_L$  (line 1), at  $x = 45370\lambda_L$  (line 2), at  $x = 47370\lambda_L$  (line 3), and the end of deceleration at  $x = 49820\lambda_L$  (line 4), respectively. The laser pulses are circularly polarised with Gaussian profile and wavelength  $1 \mu\text{m}$ . The laser pulse parameters are  $T = 10.6\lambda_L/c$ ,  $a_0 = 0.6$  for the pulse on the acceleration stage and  $T = 5.3\lambda_L/c$ ,  $a_0 = 0.5$  for the pulse on the deceleration stage. The image and caption is taken from Pukhov (Pukhov & Kostyukov, 2008). .... 154

Figure 8-1: Deviation of the electron beam due to refraction at a plasma boundary medium. The incidence and deviation angles are exaggerated for demonstration purposes. .... 156

## List of tables

Table 1: Sonic conditions for the monatomic ideal gas and diatomic ideal gas .....	46
Table 2: The geometrical parameters of the nozzles used in experiment and CFD simulations. For drawings see Section 8.3.....	54
Table 3: Properties of different gases.....	61
Table 4: Adjustable timings in the Iota One valve drive timing (www.smijapan.com, 2015) .....	65
Table 5: The parameters changed during solenoid valve testing .....	67
Table 6: The experimental conditions when the influence of the plasma density ramp is experimentally investigated. The position of the laser focal plane $z$ inside the gas jet is tuned by optimising the quality of the electron beam in terms of stability. In this experiment Nozzles A, 510, and 511 are used.....	91
Table 7: The parameters used in the experiment designed to replicate McGuffey's experiment. Nozzle 508 is used and the laser focal plane is fixed for the entire experiment at relative position $z = -5.25$ mm. ....	98
Table 8: Nozzle A's gas jet parameters in LWFA experiment where $z$ been varied inside the gas jet from 1.2 mm to 1.5 mm.....	101
Table 9: Gas jet parameters in LWFA experiment where $z$ varies inside the gas jet from 1.2 mm to 1.5 mm. The gas jet has been generated by Nozzle A.....	106
Table 10: Experimental conditions for tilted Nozzle A .....	129
Table 11: Experimental conditions for Nozzle 511 .....	135

Table 12: Experimental conditions for the Nozzle 510 tilted ..... 142

Table 13: The main parameters of the electron beam for Nozzles 510 and 511 at 0°  
tilting angle ..... 144

# 1 Introduction

## 1.1 From radio-frequency accelerators to plasma based accelerators

Particle accelerators were initially developed as a tool for fundamental research in atomic and nuclear physics. However, they soon became essential tools in many other fields such as biology, oncology, and the investigation of the structure of atomic, molecular and solid state matter, etc. The first circular particle accelerator, the cyclotron, was relatively modest in size and cost: built by Ernest Lawrence in 1931, it was 11.43 cm in diameter and cost \$25 (in 1932).



*Figure 1-1: Ernest Lawrence, the first pioneer in particle acceleration physics, holding one of the first circular electron accelerators, a cyclotron (inset) (newscenter.lbl.gov, 2015).*

Electric fields and special shaped radio frequency cavities are the basic constituents of a conventional particle accelerator. Alternating electric fields excited in the cavities accelerate negative particles when the field vector is opposed to the particle drift velocity, whereas they accelerate positive particles when the phase is such that the E field is aligned with the particle drift velocity. By synchronising the alternating fields with the passage of particles through the cavity the particles are periodically accelerated and gain kinetic energy. Adding a number of cavities in a row can lead to a continuous acceleration of the charged particles to speeds close to the speed of light in vacuum.

As the demand for higher particle energies grew, the dimension and the building costs of the particle accelerators increased: today's largest accelerator (the Large Hadron Collider at CERN) is located within a 27 km tunnel and had a

construction cost of \$9 billion. Its crowning accomplishment so far is the discovery of Higgs boson (CERN, 2013) in 2013, which has motivated scientists to support the construction of an even larger accelerator, e.g. the International Linear Collider, ILC ([www.linearcollider.com](http://www.linearcollider.com), 2015). The ILC will consist of two linear accelerators, in head-on configuration, one accelerating electrons and the other positrons up to 500 GeV (with a possible upgrade to 1 TeV). The total length of the planned accelerator is 31 km and the construction costs are estimated to be \$6.5 billion (in 2007). This project requires a substantial international effort.

In theory, any number of cavities can be added to increase the energy of an accelerated particle. In practice, there are two major constraints apart from the size. These are the construction and operating costs, which increase very rapidly with the size of the particle accelerator. One option is to increase the gradient of the accelerating electric field inside the cavities. However, this is constrained by electrical breakdown at the walls forming the cavities. Currently, the maximum achievable accelerating field is of the order of 100 MV/m.



*Figure 1-2: Aerial view of the location of the Large Hadron Collider, at CERN in Geneva. The circle marks the underground placement of 27 km of tunnel where the LHC is installed (CERN, 2000).*

A radical change in the design is required to reduce size and costs of particle accelerators and open up new frontiers to higher energies. In this context, plasma-based accelerators hold great promise to deliver the next generation of particle accelerator, which could be orders of magnitude lower in cost because they have orders of magnitude greater acceleration gradients, compared with conventional accelerators. Plasma, as an accelerating medium, is immune to electrical breakdown because it is already “broken down” into its basic components: electrons and ions.

A plasma-based accelerator can use either a laser or an electron/proton beam propagating in plasma to excite a charge separation wave with a phase velocity equal to the group velocity of the laser pulse or particle beam. This charge separation wave, known as a Langmuir wave, can produce acceleration fields up to 1 TV/m, depending on the electron temperature and plasma density. The use of plasma for next generation particle accelerators was initially proposed by Tajima and Dawson (Tajima & Dawson, 1979) and very quickly became the subject of intense experimental and theoretical investigation, as is shown in the next section.

## **1.2 Plasma based accelerators: historical overview and perspectives**

Laser Wakefield Acceleration (LWFA) and its use to generate a “Dream Beam”, as it was enthusiastically called in 2004 on the cover page of an issue of Nature ([www.nature.com](http://www.nature.com), 2004), has developed rapidly since it was proposed in 1979. Tajima and Dawson proposed the use of a high power laser to excite Langmuir waves in a plasma medium in an analogous way to a motorboat generating water waves as it moves across the surface of water. These plasma waves can be used to accelerate bunches of electrons that are either self-injected or externally injected with the correct phase and momentum into the accelerating phase of the wake.

When the theoretical foundations of LWFA were laid, technology had not yet provided intense enough lasers to explore the relativistic regime. Because of this technological limit, alternative solutions were proposed, such as the plasma wakefield acceleration (PWFA) (Rosenzweig, et al., 1988) (Rosenzweig, et al., 1989) (Nakanishi, et al., 1993) (Berezin, et al., 1994) (Hogan, et al., 2005) (Blumenfeld, et al., 2007) and plasma beat-wave acceleration (PBWA) (Kitagawa, et al., 1992), (Clayton, et al., 1994), (Everett, et al., 1994), (Ebrahim, 1994), (Amiraniff, et al., 1994).

The PWFA uses a relativistic charged particle beam to excite plasma waves, which can be used to accelerate a witness electron beam injected externally. Great progress has been made testing many different accelerator configurations and schemes, but in most cases relatively high energy spread electron beams were produced.

The plasma beat-wave accelerator (PBWA) utilises two co-propagating laser beams with different wavelength. The frequency difference is tuned to the plasma frequency, which provides the condition for resonant transfer of energy from the laser beam to the plasma waves. These plasma waves have been used to accelerate externally injected electrons. This scheme, as in the PWFA, had modest success, where energy gains of the order of 30 MeV were demonstrated (Clayton, et al., 1994), (Everett, et al., 1994).

The development of Ti:sapphire lasers and Chirped Pulse Amplification (CPA) (Strickland & Mourou, 1985), (Maine, Strickland, Bado, Pessot, & Mourou, 1988), (Mourou & Umstadter, 1992), (Perry & Mourou, 1994) was a tremendous innovation in laser technology, which almost immediately initiated further development of the LWFA. Chirped-pulse amplification was originally introduced as a technique to increase the available power in radar (Cook, 1960). The basis of CPA is initially temporally “stretching” a laser pulse using a pair of diffraction gratings or prisms to maintain the laser peak power of the laser beam below the damage threshold of the optical transport system and amplifiers. After amplification, the pulse is compressed using a similar pair of gratings, which permits terawatt (TW) to petawatt (PW) power levels to be accessed for sub-picosecond laser pulses. These powers allow the “bubble regime” or blowout regime to be accessed. The regime was first identified in simulations by A. Pukhov (Pukhov & Meyer-ter-Vehn, 2002) and further developed by W. Lu (Lu, Huang, Mori, & Katsouleas, 2006). The self-modulated LWFA (SM-LWFA) and the so-called at the time “forced LWFA” (F-LWFA) started to demonstrate experimentally the production of the first plasma accelerated electron beams with Maxwell energy distribution (Gorbunov & Kirsanov, 1987), (Bulanov, Kirsanov, & Sakharov, 1989), (Sprangle, Esarey, & Ting, 1990), (Hamster, Sullivan, Gordon, White, & Falcone, 1993), (Nakajima, et al., 1995), (Downer, et al., 1995), (Nakajima, et al., 1995), (Marquès, et al., 1996), (Sprangle, Esarey, & Ting, 1990), (Coverdale, et al., 1995), , (Modena, et al., 1995), (Wagner, Chen, Maksimchuk, & Umstadter, 1997), (Moore, et al., 1997), (Ting, et al., 1997), (Santala, et al., 2001) (Malka, et al., 2002) followed in 2004 by electron beams with monochromatic energy features (Mangles, et al., 2004), (Faure, et al., 2004), (Geddes, et al., 2004).

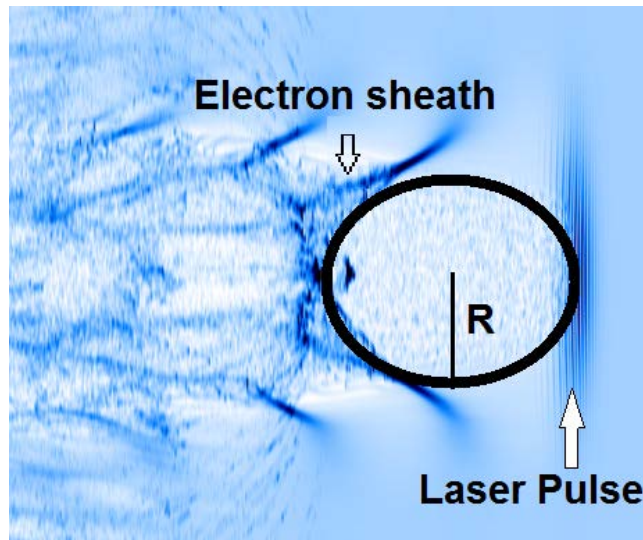


*Figure 1-3: The ion bubble generated as a result of nonlinear laser-plasma interaction (Lu, Huang, Mori, & Katsouleas, 2006)*

The bubble regime is a highly nonlinear interaction between the laser and plasma, which occurs when  $a_0 \geq 1$ , where  $a_0 \approx 0.855 \times 10^{-9} I^{1/2} [\text{W}/\text{cm}^2] \lambda_0 [\mu\text{m}]$  is the normalised laser vector potential,  $\lambda_0$  is the wavelength of the laser and  $I$  is the intensity of the laser. Under these conditions the quiver motion of electrons in the laser field becomes relativistic.

The laser pulse expels electrons radially to create an electron void structure that resembles a bubble with radius  $R$ . The radially expelled electrons execute a periodic oscillation around the axis of propagation of the laser at the plasma frequency. When their trajectories cross at the back of the bubble, some of these electrons are trapped inside the bubble and are accelerated. Even when the “bubble regime” is not directly accessible, due to limitations of laser pulse length and laser power, relativistic self-focussing, self-modulation (Max, Arons, & Langdon, 1974) and laser pulse self-steepening (DeMartini, Townes, Gustafson, & Kelley, 1967) cause the initial laser pulse to evolve to optimise the parameters required to drive the bubble. The technological advances in the past years have enabled the development of lasers with the required parameters to generate an electron beam through LWFA in direct bubble regime (Hafz, et al., 2008), (Schmid K. , et al., 2009).

Taking into account the latest advances in LWFA it can be said that, in many aspects, the “Dream Beam” is not a dream anymore. In the past few years, more and more encouraging results have been published (Mangles, et al., 2004), (Faure, et al.,

2004), (Geddes, et al., 2004), (Miura, et al., 2005), (Yamazaki, et al., 2005). Different plasma media for generating and accelerating electrons have been developed, from gas nozzles (Wiggins, et al., 2010) to discharge capillaries (Leemans, et al., 2006), gas cells (Osterhoff, et al., 2008), tapered plasma channels (Sprangle, et al., 2001), (Sprangle, et al., 2002). Counter propagating laser beams have been used for electron beam charge and energy control (Faure, et al., 2006). In the past years, the gap between the LWFA and traditional accelerators has been reduced. Plasma based accelerators show great improvements in emittance and achievable electron energy (Wiggins, et al., 2010), (Leemans, et al., 2006), (Brunetti, et al., 2010). Progress is now at a point where applications can be developed and the LWFA can be used to its full potential, e.g. in medical research (Kainz, Hogstrom, Antolak, Almond, & Bloch, Dose properties of x-ray beams produced by laser-wakefield-accelerated electrons, 2005), (Kainz, Hogstrom, Antolak, Almond, & Bloch, Dose properties of x-ray beams produced by laser-wakefield-accelerated electrons, 2005), matter investigation (Kim, et al., 2007) and development of new sources of radiation (Jaroszynski, et al., 2006), (Wiggins, et al., 20-21 April 2011), (Leemans, et al., 2004), (Catravas, Esarey, & Leemans, 2002) (Leemans, et al., 2003). The LWFA is so promising that, for example, an entire new centre has been built in Scotland (Scottish Centre for the Application of Plasma-based Accelerators, SCAPA) devoted to applications and the research and development of plasma-based accelerators ([www.scapa.co.uk](http://www.scapa.co.uk), 2015).

Important advances have been made in understanding the LWFA process. However, to effectively use LWFA technology in applications there are still many aspects that need to be clarified. For example, little is known about how to control the process of injection of electrons (Van der Wiel, et al., 2006) in the bubble or blowout regime (Bulanov, Pegoraro, Pukhov, & Sakharov, 1997), (Decker, Mori, Tzeng, & Katsouleas, 1996), (Pukhov & Meyer-ter-Vehn, 2002) and how to control the energy, energy spread, divergence and emittance of the electrons beams (Cheshkov, Tajima, Chiu, & Breitling, 2000) and, not least, how to improve the reproducibility of electron beams.

Methods of controlling injection of electrons in the plasma wave have recently been developed, which involve a “heater” laser (Geddes, et al., 2004) to create a guiding channel, while other methods utilise colliding lasers to create plasma density

transitions that are used to control injection (Chien, Chang, Jin, Wang, & Chen, 2005). These methods are proof-of-principle demonstrations but fail to give an electron beam with a high degree of quality or stability. Also, the setups required for these experiments are extremely difficult to align and control with a high degree of accuracy.

The main energy limitations of the LWFA are pump depletion and dephasing. The depletion length is the distance over which the energy of the laser is depleted due to transfer of energy to the plasma wake. Before the laser energy depletes the accelerated electrons travelling at a speed close to the speed of light,  $c$ , will outrun the accelerating wake and enter the decelerating region of the wake. The length over which this happens is known as the dephasing length. The depletion length  $L_{pd}$  and dephasing length  $L_{dp}$ , for the blowout or bubble regime, are given by (Lu, et al., 2007):

$$L_{dp} \cong \frac{4}{3} \frac{\omega_0^2}{\omega_p^2} \sqrt{a_0} k_p^{-1} \quad (1.1)$$

and

$$L_{pd} \cong \frac{\omega_0^2}{\omega_p^2} c \tau_{FWHM} , \quad (1.2)$$

where  $\omega_0$ ,  $\omega_p$ ,  $k_p = \omega_p/c$ ,  $\tau_{FWHM}$  are the laser frequency, plasma frequency, plasma wavenumber and laser pulse duration respectively. In LWFAs with constant density profiles the main limitation is the electron dephasing relative to the accelerating field. Its influence limits the energy gained by the accelerated electrons and increases the electron energy spread. A very basic explanation why this happens takes into account the structure of the longitudinal electric field inside the bubble. The accelerating field is not uniform inside the bubble but continuously decreases and its maximum value becomes smaller and smaller until the part of the bubble where it changes sign. This point defines the dephasing length. As the electron bunch propagates inside the bubble, for a uniform plasma profile, different parts of the bunch are subject to different acceleration gradients, which lead to an increase in energy spread and also to a limited energy gain. This is effect is more pronounced as the electron bunch charge increases, an effect known as beamloading.

During a LWFA experiment, with a given laser system, the maximum laser power is limited and, as can be seen in the formulae for pump depletion and dephasing length [(1.1), (1.2)], the only variable that can be manipulated is the plasma density

gradient so that  $L_{dp} \approx L_{pd}$ . Plasma manipulation includes, for example, tapering the plasma density profile to control the phase/group velocity of the electron bunch and plasma wave, as has been proposed by Katsouleas (Katsouleas, 1986), Sprangle et al. (Sprangle, et al., 2001), Rittershofer et al. (Rittershofer, Schroeder, Esaray, Gruner, & Leemans, 2010) and Wen et al. (Wen, et al., 2010). In these articles the authors theoretically explore the possibility of locking the velocity of the electron bunch relative to the accelerating wake by shaping the plasma density profile so that the electron bunch is kept in the accelerating phase of the wake for a longer time than would be possible with constant plasma density. In this way not only can the electron energy be increased but it is also possible to control other parameters, such as energy spread (Wen, et al., 2010). However, to validate the tapered density profile theory a systematic experimental study is required, which is the major topic of this thesis work, as described in the next section.

### **1.3 Motivation for an experimental investigation of the influence of longitudinal plasma profile on the quality of the LWFA**

The effect of different longitudinal density profiles (flat top density profiles, tapered density profiles) has not yet been comprehensively investigated experimentally and theoretically. There are few theoretical papers describing the influence of the plasma density profile on the quality of the electron beam and even fewer experimental papers. Contradictory information is found in the literature on the topic. Hemker (Hemker, Hafz, & Uesaka, 2002) claims that an up-ramp plasma density cannot be used in LWFA due to electron self-injection issues while Kim (Kim, Ju, & Yoo, 2011) prove experimentally that an up-ramp plasma density is useful for controlling the electron energy. Fast transition densities followed by down-ramp densities have been experimentally investigated by placing a blade (Schmid, et al., 2010) or a wire (Burza, et al., 2013) in a supersonic gas jet to produce density profiles that permit advanced control of different parameters of the electron beam such as energy, energy spread and charge.

It is common in LWFAs to change the gas jet interaction length by altering the interaction point relative to the exit of the nozzle or using nozzles with different outlet

diameters. Different nozzles have different gas jet density ramps, a parameter often ignored by experimentalists and theoreticians. It is shown in this thesis that this has a crucial effect on the stability of the electron beam, at least for relatively low power lasers (20 TW).

To the author's knowledge, this thesis presents the first detailed experimental attempt to systematically investigate the influence of the longitudinal plasma profile generated by a supersonic gas nozzle on the quality of the LWFA. The results presented here can be used, in correlation with other results, to design a staged plasma accelerator, where different density profiles are used to accelerate the electron beam over long distances by controlling the electron beam phase or maximising the amount of charge injected into the bubble.

## 1.4 Structure of the thesis

The thesis is structured in six main chapters:

**Chapter 2** briefly describes the theory of laser wakefield acceleration. Section 2.1 discusses the basic properties of plasma. The propagation of electromagnetic waves in different regimes, linear and non-linear, is presented in Section 2.2. Non-linear propagation of electromagnetic waves in plasma and the laser wakefield accelerator is presented in the Section 2.3 along with its limitations due to diffraction, electron dephasing and laser depletion.

**Chapter 3** presents the theory of supersonic gas jets followed by computational fluid dynamics simulations (CFD) applied to the supersonic gas nozzles. An experimental method for optimising Solenoid Parker Valves Series 99 for LWFA experiments is also described.

**Chapter 4** presents the experimental setup used in the LWFA experiments presented in this thesis. A schematic of the laser setup is presented in Section 4.1. Section 4.2 is dedicated to the description of the gas target. The chapter ends with Section 4.3 and Section 4.4, where the electron beam detection and characterisation setup is discussed in detail and the experimental methods are explained.

**Chapter 5:** The most important results of LWFA experiments with vertical nozzles are presented. In this chapter the influence of different parameters of the plasma longitudinal profile on the parameters of the electron beam is investigated.

In **Chapter 6** more complex profiles are explored by tilting the gas nozzle relative to the direction of laser propagation.

In **Chapter 7**, Section 7.1, the main results of the thesis are summarised and conclusions are drawn. In Section 7.2 the possible further developments of the results are outlined.

## 2 Theory of laser wakefield acceleration

In this chapter the theory of laser wakefield acceleration is briefly explained. The chapter begins with Section 2.1 where the basic properties of plasma are described. The propagation of an electromagnetic wave in the linear and non-linear regimes is presented in Section 2.2. An application of non-linear propagation of an electromagnetic wave in plasma, the laser wakefield accelerator, is presented in the Section 2.3 along with its limitations: laser diffraction, electron dephasing and laser depletion.

### 2.1 Plasma theory

Plasma (Chen F. F., 1984), in its most basic definition (Boyd & Sanderson, 2003), is a quasi-neutral ionised gas that behaves collectively. The property of quasi-neutrality allows the creation of strong accelerating gradients through separating positively and negatively charged particles forming the plasma. An estimate of the electric field inside such an accelerating structure created by an external force in cold and fully ionised plasma can be made using Gauss' Law (Halliday & Resnick, 1970):

$$\nabla \cdot \mathbf{E} = \frac{\rho}{\epsilon_0}, \quad (2.1)$$

where  $\epsilon_0 = 8.854 \times 10^{-12} \text{ F m}^{-1}$  is the vacuum permittivity,  $\rho$  is the space charge density distribution and  $\mathbf{E}$  is the electric field. "Cold plasma" is defined (Woods, 2008) as plasma where the thermal motion of electrons and ions can be ignored.

Assuming that the accelerating structure is created by a one dimensional density wave perturbation, it can be written that:

$$\rho = e\Delta n \exp(-ik_p z), \quad (2.2)$$

$$\nabla \equiv \hat{z} \frac{\partial}{\partial z}, \quad (2.3)$$

and

$$\mathbf{E} = \hat{z} E_0 \exp(-ik_p z), \quad (2.4)$$

where  $\Delta n$  plasma density perturbation,  $e$  is the electron charge and  $\hat{z}$  is the unit direction vector. The plasma frequency (Woods, 2008),  $\omega_p$ , one of the basic plasma

parameters, is the frequency at which the plasma oscillates when subject to an external impulse. For the timescales encountered in the LWFA, the plasma frequency is determined by its most mobile components, which are the electrons. Therefore the plasma frequency depends only on the electron fluid properties:

$$\omega_p = (n_e e^2 / m_e \epsilon_0)^{1/2}, \quad (2.5)$$

where  $m_e$  is the electron rest mass.

Assuming that the plasma wave has a velocity close to speed of light  $c$ , the relativistic plasma wavelength (Chen F. F., 1984) is given by

$$\lambda_p [\mu\text{m}] = 2\pi c / \omega_p \cong 3.3 \times 10^{10} / \sqrt{n_e [cm^{-3}]}. \quad (2.6)$$

Assuming 100% density perturbation  $\Delta n \cong n_e$  from Gauss' Law:

$$eE_0 \cong m_e c \omega_p. \quad (2.7)$$

For  $n_e = 1 \times 10^{18} \text{ cm}^{-3}$  one obtains accelerating gradient fields of  $eE_0 \approx 100 \text{ GV/m}$  for a plasma wavelength  $\lambda_p = 33 \mu\text{m}$ . Taking into account that the best state-of-the-art conventional accelerators have a maximum possible accelerating electric field, due to electrical breakdown of the accelerator walls, of the order of  $100 \text{ MV/m}$  it is obvious why plasma based accelerators are an attractive alternative: not only are the dimensions of the accelerator reduced by many orders of magnitude but the manufacture and exploitation costs are also greatly reduced. The impressive electric field gradients and promised short relativistic electron bunches are the indicators of the potential of future table-top high energy electron accelerators.

Another important property of plasma is the capacity to completely shield an electric field. The distance over which this takes place is known as the Debye length (Woods, 2008):

$$\lambda_D = \sqrt{\frac{\epsilon_0 k}{e^2} \left( \frac{n_e}{T_e} + \frac{n_0 Z}{T_{ion}} \right)^{-1}}, \quad (2.8)$$

where  $Z$  is the atomic number and  $k$  is the Boltzmann constant. The mobility of ions, due to their mass, is very small on the timescale of the interaction in LWFA experiments, therefore the ion temperature  $T_{ion}$  is also very small compared with electron temperature  $T_e$ ,  $T_{ion} < T_e$ . Under these conditions the formula (2.8) can be reduced to  $\lambda_D = \sqrt{\epsilon_0 k T_e / e^2 n_e}$ . Electrons are the most mobile component of plasma,

and therefore will dominate the interaction between plasma and external electromagnetic fields.

## 2.2 Propagation of electromagnetic waves in plasma

When an electromagnetic wave acts on plasma, the electrons forming the plasma quiver in the field of the electromagnetic wave and their quiver velocity determines the type of interaction. A quiver velocity comparable with the speed of light velocity is the threshold for transition between the sub-relativistic and relativistic regimes.

To study the propagation/interaction of an electromagnetic wave inside plasma (Ginzburg, 1964) one starts with Maxwell's equations (Maxwell, 1873):

$$\nabla \cdot \mathbf{E}(\mathbf{r}, t) = \frac{\rho}{\epsilon_0}, \quad (2.9)$$

$$\nabla \cdot \mathbf{B}(\mathbf{r}, t) = 0, \quad (2.10)$$

$$\nabla \times \mathbf{E}(\mathbf{r}, t) = -\frac{\partial \mathbf{B}(\mathbf{r}, t)}{\partial t}, \quad (2.11)$$

$$\nabla \times \mathbf{B}(\mathbf{r}, t) = \mu_0 \mathbf{J} + \mu_0 \epsilon_0 \frac{\partial \mathbf{E}(\mathbf{r}, t)}{\partial t}. \quad (2.12)$$

A plane wave is considered with a polarisation given by the polarisation vector  $\hat{\boldsymbol{\epsilon}}$  :

$$\begin{aligned} \mathbf{E} = \mathbf{E}(z, t) &= E_0 \hat{\boldsymbol{\epsilon}} e^{ikz - i\omega t} \\ \mathbf{B} = \mathbf{B}(z, t) &= \hat{z} \times \mathbf{E} \end{aligned} \quad (2.13)$$

$$\hat{\boldsymbol{\epsilon}} = \begin{cases} \hat{x}(\hat{y}) & \text{for linear polarisation} \\ \frac{(\hat{x} \pm i\hat{y})}{\sqrt{2}} & \text{for circular polarisation} \end{cases} \quad (2.14)$$

and, in this thesis, only linearly polarised plane waves are used in calculations.

From the Maxwell equations (2.11) and (2.12), together with the expression for a plane wave (2.13), the wave equation is:

$$\left( c^2 |\mathbf{k}|^2 - \omega^2 \right) \mathbf{E} = -\frac{n_e e^2}{\epsilon_0 m_e} \mathbf{E}. \quad (2.15)$$

From equation (2.15), the well-known expression for the dispersion relation of electromagnetic waves inside plasma (Swanson, 2003) is obtained:

$$\omega^2 = c^2 k^2 + \omega_p^2. \quad (2.16)$$

Relation (2.16) emphasises two regimes of laser-plasma interactions: over-dense and under-dense. The threshold between the two regimes is given by the critical density (Chen F. F., 1984), when  $\omega \approx \omega_p$ :

$$n_c = \frac{\epsilon_0 m_e \omega^2}{e^2}. \quad (2.17)$$

It can be observed from relation (2.17) that for lasers with a wavelength  $\lambda = 800$  nm the critical density is  $n_c = 1.71 \times 10^{21} \text{ cm}^{-3}$ .

For over-dense plasma, the frequency of the incident electromagnetic wave is less than the plasma frequency therefore it cannot propagate more than one Debye length (Woods, 2008) (2.8) before it is reflected.

The phase and group velocity of an electromagnetic wave propagating inside plasma can be calculated using the dispersion relation:

$$v_{ph} = \frac{\omega}{k} = \frac{c}{\eta}, \quad (2.18)$$

$$v_g = \frac{d\omega}{dk} = \eta c, \quad (2.19)$$

where

$$\eta = \sqrt{1 - \frac{\omega_p^2}{\omega^2}}, \quad (2.20)$$

is the refractive index of the plasma. For under-dense plasmas the refractive index is smaller than unity, therefore the group velocity of an electromagnetic wave in plasma is less than speed of light in vacuum  $c$ .

### 2.2.1 Electromagnetic waves propagation in a plasma in the linear regime

The Lorentz force is:

$$\mathbf{F} = m_e \frac{d\mathbf{v}}{dt} = q [\mathbf{E}(\mathbf{r}, t) + \mathbf{v} \times \mathbf{B}(\mathbf{r}, t)]. \quad (2.21)$$

In the Lorenz gauge:

$$\nabla \cdot \mathbf{A} + \frac{1}{c^2} \frac{\partial \varphi}{\partial t} = 0, \quad (2.22)$$

and the relations for electric and magnetic field vectors can be expressed as a function of vector and scalar potentials  $\mathbf{A}$  and  $\varphi$  by:

$$\mathbf{E} = -\nabla \varphi - \frac{\partial \mathbf{A}}{\partial t}, \quad \mathbf{B} = \nabla \times \mathbf{A}. \quad (2.23)$$

In the non-relativistic case, when  $v \ll c$ , in equation (2.21) the term  $\mathbf{v} \times \mathbf{B}(\mathbf{r}, t)$  can be ignored. It is therefore straightforward to integrate equation (2.21) and obtain the formulae for displacement and velocity of an electron in an electromagnetic field in the approximation  $v \ll c$ :

$$\mathbf{v} = -\frac{ie}{m_e \omega} \mathbf{E}, \quad \mathbf{r} = \frac{e}{m_e \omega^2} \mathbf{E}. \quad (2.24)$$

As can be seen here, the response of the electron follows closely the evolution of the electromagnetic field, therefore this regime is called the linear regime (Ginzburg, 1964). If it is assumed that the plane wave is linearly polarised then equations (2.24) become:

$$\begin{aligned} \mathbf{v}_{lin} &= \frac{eE_0}{m_e \omega} \hat{y} \sin \omega t = a_0 c \hat{y} \sin \omega t \\ y_{lin} &= -a_0 \frac{c}{\omega} \cos \omega t \end{aligned} \quad (2.25)$$

The peak amplitude of the velocity is  $v_0 = eE_0/m_e \omega$ , and when compared with the velocity of light in vacuum  $c$  it illustrates the regime that applies: sub-relativistic for  $a_0 < 1$  or relativistic for  $a_0 > 1$ .

In the case when  $a_0 \approx 1$  the  $\mathbf{v} \times \mathbf{B}(\mathbf{r}, t)$  term from equation (2.21) cannot be ignored. To solve the differential equation (2.21) it is assumed that the solution is the sum of two terms: one linear and the other nonlinear:

$$\mathbf{v} = \mathbf{v}_{lin} + \mathbf{v}_{nonlin}, \quad (2.26)$$

$$m_e \frac{d(\mathbf{v}_{lin} + \mathbf{v}_{nonlin})}{dt} = q \left[ \mathbf{E}(\mathbf{r}, t) + (\mathbf{v}_{lin} + \mathbf{v}_{nonlin}) \times \mathbf{B}(\mathbf{r}, t) \right]. \quad (2.27)$$

After arranging the terms, the following solution is obtained, which depends on the linear solution (2.25):

$$\frac{d \mathbf{v}_{nonlin}}{dt} = \hat{\mathbf{x}} \frac{e}{m_e c} (a_0 c \sin \omega t) (E_0 \cos \omega t) = -\hat{\mathbf{x}} \frac{a_0^2}{2} c \omega \sin 2\omega t. \quad (2.28)$$

After integration, taking  $x = 0$  as the initial position, an equation is obtained that describes the electron drifting, and oscillating at frequency  $2\omega$ , in the direction of propagation:

$$v_{nonlin}^x(t) = \frac{a_0^2 c}{4} \cos 2\omega t, \quad x_{nonlin} = -\frac{a_0^2 c}{8\omega} \sin 2\omega t. \quad (2.29)$$

Eliminating  $t$  from the solutions for  $y \approx y_{lin}$  and  $x \approx x_{nonlin}$  and using the notations  $X = \omega x / ca_0^2$  and  $Y = \omega y / ca_0$ , an equation that describes the well-known “figure of eight” motion (shown in Figure 2-1) is obtained (Gibbon, 2005), when represented in a frame that moves with average drift velocity:

$$16X^2 = Y^2(1 - Y^2) \quad (2.30)$$

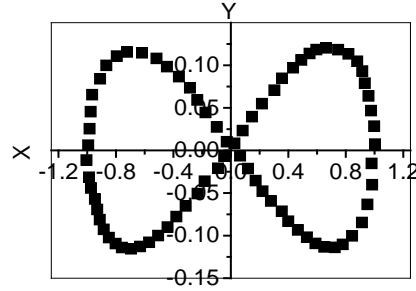


*Figure 2-1: Figure-of-eight motion of an electron in a plane wave. The reference frame moves with the average drift velocity*

## 2.2.2 Nonlinear regime

### 2.2.2.1 Ponderomotive force. Self-focussing, self-steepening, relativistic induced transparency and laser pulse compression

In the relativistic case, when  $a_0 \geq 1$ , a high intensity laser pulse propagating in under-dense plasma can experience self-focussing due to two different mechanisms that depend on the laser pulse length.

The formula (2.20) for the refractive index is valid only for the non-relativistic case. For the relativistic case, the change in electron mass must be included thus the plasma frequency becomes:

$$\omega_{p(rel)} = \omega_p / \sqrt{\bar{\gamma}}, \quad (2.31)$$

where  $\bar{\gamma}$  is the average value of the relativistic factor. The dispersion relation will also change, determining the phenomenon of relativistic induced transparency, which causes the electromagnetic wave to propagate inside plasma even when the original plasma density does not permit it.

Refractive index changes can also be induced by the ponderomotive force (Schluter, 1968) (Lindl & Kaw, 1971)  $\mathbf{F}_p = -\frac{e^2}{4m_e\omega^2} \nabla |\mathbf{E}|^2$ . Its effect is to push the electrons away from the path of the electromagnetic wave causing a local decrease in the electron density that depends on the radial position. Together with the relativistic mass change, these two phenomena modulate the refractive index: the refractive index becomes greater on-axis than off-axis, which is equivalent to a positive plasma lens. The refractive index can be written in this case as (Akhiezer & Polovin, 1956):

$$\eta(r, z) \approx 1 - \frac{1}{2} \left( \frac{\omega_p}{\omega} \right)^2 \left( 1 + \frac{\delta n_e}{n_e} - \frac{a^2(r, z)}{4} \right), \quad (2.32)$$

where  $\delta n_e$  is the change in plasma density due to relativistic interaction.

The change of refractive index in the relativistic regime alters the phase velocity of the laser, which produces *relativistic self-focussing* of the laser (due to the  $a^2(r, z)$  term), while ponderomotive self-focussing (the  $\delta n_e/n_e$  term) is important when the laser pulse length is longer than the plasma wavelength, which is usually not the case for the LWFA.

An estimate of the minimum laser power for relativistic self-focusing can be calculated using geometrical considerations that take into account the diffraction angle (for the definition see 2.3.2.1) and the focussing angle.

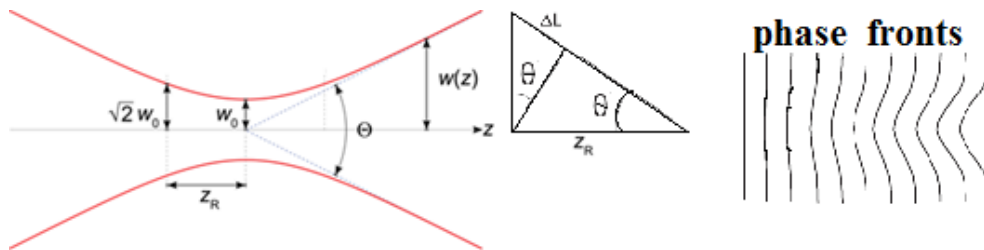


Figure 2-2: Diffraction angle  $\Theta$  vs. relativistic defocussing angle  $\theta$

The phase velocity of the wave fronts is written as:

$$\frac{v_{ph}(r, z)}{c} = \frac{1}{\eta} = 1 + \frac{\omega_p^2}{2\omega^2} \left[ 1 - \frac{a^2(r, z)}{4} \right], \quad (2.33)$$

therefore the wavefront velocity difference between on-axis and off-axis due to plasma refractive index modulation can be written as:

$$\frac{\Delta v_{ph}(r, z)}{c} = \frac{\omega_p^2}{8\omega^2} a^2(0, z) \exp\left[-\frac{r^2}{w_0^2}\right]. \quad (2.34)$$

The velocity difference bends the wavefront and leads to focussing and the rays along the wavefront are bent depending on their path difference. The maximum path difference between the centre and the edge of curvature (indicated by  $\Delta L$  in the above figure) is:

$$\Delta L = \left[ \Delta v_{ph} \right]_{\max} t = \left[ \frac{\Delta v_{ph}}{c} \right]_{\max} z_R = \frac{\omega_p^2 a^2(0, z)}{8\omega^2} z_R = \theta w(z) = \theta^2 z_R. \quad (2.35)$$

The maximum focusing angle of the beam is:

$$\theta^2 = \frac{\omega_p^2 a_0^2}{8\omega}. \quad (2.36)$$

Practically, relativistic self-focusing overcomes diffraction of the laser when the diffraction angle  $\Theta$  is equal to or less than the relativistic self-focusing angle  $\theta$ :

$$\frac{\lambda}{\pi w_0} \leq \sqrt{\frac{\omega_p^2 a_0^2}{4\omega^2}}. \quad (2.37)$$

One can now obtain a relation for the minimum power for relativistic self-focusing:

$$P_{cr} = \frac{m_e c^5 \omega^2}{e^2 \omega_p^2} \cong 17 \left( \frac{\omega}{\omega_p} \right)^2 \text{ GW}. \quad (2.38)$$

In the experiments described in this thesis the plasma density is varied in the range  $n_e = 1 - 4 \times 10^{19} \text{ cm}^{-3}$ , therefore the critical power for self-focusing varies between  $P_{cr} = 3 - 0.7 \text{ TW}$  for a laser wavelength of 800 nm. The power of the laser on target, during the experiments presented in this thesis, is  $P > 20 \text{ TW}$ , therefore the condition for relativistic self-focussing is always satisfied.

The variation of the refractive index occurs both transversely and longitudinally, which causes laser pulse compression (Mori, 1997). Practically, different spectral components of the laser pulse have different group velocities as they propagate. The

front of the laser pulse moves slower than the centre, therefore the laser pulse experiences self-compression and self-steepening.

### 2.2.2.2 Propagation of electromagnetic waves in plasma in the nonlinear regime

For the relativistic regime, when  $a_0 \geq 1$ , the relativistic variation of electron mass must be taken into account, therefore equation (2.21) is rewritten as:

$$\frac{d\mathbf{p}}{dt} = -e(\mathbf{E} + \mathbf{v} \times \mathbf{B}), \quad \mathbf{p} = m_e \gamma \mathbf{v}, \quad (2.39)$$

where  $\gamma = 1/\sqrt{1-\beta^2}$  is the Lorentz factor and  $\beta = v/c$ .

The Poynting vector,  $\mathbf{S} = \varepsilon_0 c^2 (\mathbf{E} \times \mathbf{B})$ , is defined as the energy flux of an electromagnetic wave. By averaging the Poynting vector  $\mathbf{S}$  one obtains the intensity as a function of the wave parameters:

$$I = \varepsilon_0 c^2 \langle |\mathbf{E} \times \mathbf{B}| \rangle = \frac{\varepsilon_0 c E_0^2}{2}. \quad (2.40)$$

From relation (2.40) it is easy to obtain the expression for  $a_0$ :

$$a_0 = 0.85 \left( \frac{I [\text{W cm}^{-2}] \lambda^2 [\mu\text{m}^2]}{10^{18}} \right)^{1/2}. \quad (2.41)$$

From relation (2.41) it can be seen that the relativistic regime  $a_0 \geq 1$  can be reached for a laser with wavelength  $\lambda = 0.8 \mu\text{m}$  and intensity  $I \geq 2 \times 10^{18} \text{ W cm}^{-2}$ , easily obtainable by today's laser technology.

In the following, a one dimensional equation describing nonlinear wakefield excited in a plasma by a linearly polarised electromagnetic plane wave is derived. The polarisation is considered to be along the  $y$  axis and the direction of propagation is along the  $x$  axis. From (2.39) the following relation is obtained:

$$\frac{dp_y}{dt} = e \frac{dA_y}{dt} = -eE_y + ev_x B_z. \quad (2.42)$$

In the previous equation  $p_y = eA_y$ , which is equivalent to  $\gamma\beta_y = a_0$ . Also the normalisation for the scalar potential  $\Phi$ :  $\Phi_0 = e\Phi/m_e c^2$  is used.

The equation of motion for the longitudinal waves has the form (Esarey, Schroeder, & Leemans, 2009):

$$\frac{d}{dt}(\gamma\beta_x) = c \left( \frac{\partial\Phi_0}{\partial x} - \frac{1}{2\gamma} \frac{\partial a_0^2}{\partial x} \right). \quad (2.43)$$

To have a closed set of equations for the coupled electromagnetic and plasma waves the continuity equation,  $\frac{\partial n_e}{\partial t} + c \frac{\partial}{\partial x}(n_e\beta_x) = 0$ , the Poisson equation,  $\nabla^2\Phi_0 = \frac{\omega_p^2}{c^2} \left( \frac{n_e}{n_0} - 1 \right)$ , and the relation for the relativistic factor,  $\gamma$ , of the electrons

forming the plasma wave,  $\gamma = \gamma_{\perp}\gamma_{\parallel} = \frac{\sqrt{1+a_0^2}}{\sqrt{1-\beta_x^2}}$  are used.

Using a reference frame co-moving with the laser group velocity  $v_g$ , one can define  $\tau = t$  and  $\xi = x - v_g t$ . To simplify, the quasi-static approximation is used, which means that the evolution of the laser envelope during the transit time of plasma electrons is neglected. Therefore,  $\partial/\partial\tau$  is much smaller than  $\partial/\partial\xi$  and can be neglected. The following relation can be obtained after some calculation (Gibbon, 2005) and using

the notation  $\beta_g = \frac{v_g}{c}$ ,  $\gamma_g = 1/\sqrt{1-\beta_g^2}$ ,  $\Psi = \sqrt{1 - \frac{1+a_0^2}{\gamma_g^2(1+\Phi_0)^2}}$ , then:

$$\begin{aligned} \gamma &= \gamma_g^2(1+\Theta_0)(1-\beta_g\Psi) \\ \beta_x &= \frac{\beta_g - \Psi}{1-\beta_g\Psi} \\ \frac{n_e}{n_0} &= \beta_g\gamma_g^2 \left( \frac{1}{\Psi} - \beta_g \right) \end{aligned} \quad (2.44)$$

The normalised scalar potential can be derived in the form of a second order, nonlinear ordinary differential equation:

$$\frac{\partial^2\Theta_0}{\partial\xi^2} = \frac{\omega_p^2\gamma_g^2}{c^2} \left| \frac{\beta_g}{\Psi} - 1 \right|. \quad (2.45)$$

The differential equation (2.45) can be solved only numerically. A possible solution is represented graphically in the Figure 2-3, where the excited plasma wave takes a non-sinusoidal shape compared with the linear case, where the plasma response is sinusoidal.

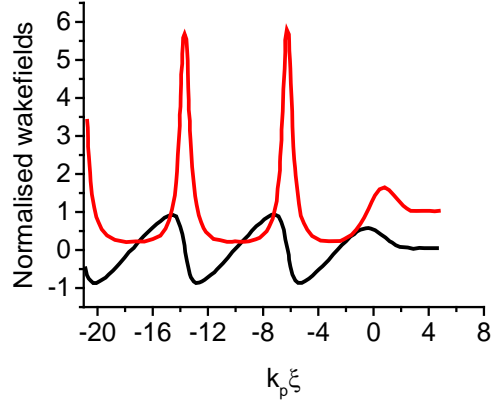


**Figure 2-3: Plasma density perturbation  $\delta n / n_0$  (red curve) and plasma wave electric field  $E_z / E_0$  (black curve) excited by a Gaussian laser pulse with  $a_0 = 2$  and pulse length  $\tau = 6$  fs.**

Using 1D nonlinear, relativistic, cold fluid equations, Esaray (Esarey, Schroeder, & Leemans, 2009) an expression for the maximum amplitude of the periodic plasma wave can be obtained:

$$E_{wb} = \sqrt{2} (\gamma_p - 1)^{1/2} E_0 \propto n_e^{-1/4}, \quad (2.46)$$

where  $\gamma_p = \omega_0 / \omega_p$  is the wake Lorentz factor (here it has been assumed that the group velocity of the wake equals the phase velocity of the laser wavefront). The solution for equations (2.44) at the maximum electric field becomes singular *i.e.* the cold plasma equations break down, which is why the process is called wave-breaking. This doesn't necessarily mean that the wave collapses. Its structure can keep its integrity and only a small portion of it collapses (Mangles, et al., 2004).

The wave-breaking limit for the 3D nonlinear case is currently under theoretical investigation (Kostyukov, Nerush, Pukhov, & Sereidov, 2009) (Kostyukov, Nerush, Pukhov, & Sereidov, 2010), and general expressions for this regime have not been obtained yet.

### **2.3 Laser wakefield acceleration. Wave-breaking and self-injection in the highly non-linear regime**

It has been shown in Section 2.2.1 that electromagnetic waves can excite linear Langmuir waves in plasma. In Section 2.2.2.2 it has been shown that when the laser power is sufficiently high then the electrons forming the plasma are pushed away by the ponderomotive force creating a structure void of electrons, which is called the

“bubble” (Pukhov & Meyer-ter-Vehn, 2002) or “blowout region” (Lu, Huang, Mori, & Katsouleas, 2006). At the same time, due to local modulation of the refractive index, relativistic self-focussing, laser pulse self-compression and self-steepening are present. This is a dynamic process occurring during one plasma period, therefore, while the laser pulse moves inside the plasma creating the bubble, the electrons expelled form a sheath that moves towards the back of the bubble. Some electrons have the correct momentum and phase to be injected into the bubble and are accelerated in the field of the nonlinear wake. The correct phase and momentum for electron trapping can be translated into the following conditions (Lu, et al., 2007):

- The radius of the ion bubble is large enough so that electrons can gain enough longitudinal momentum to move with the same group velocity as the laser pulse by the time they reach the back of the bubble
- At the back of the bubble, the region where the electrons are injected, *i.e.* the sheath crossing region, should be narrow enough to generate high accelerating (in the axial direction) and focusing (in the radial direction) fields.

These two conditions don't form the only possible scenario for electron injection into the bubble. For example, Kalmykov (Kalmykov, Yi, Khudik, & Shvets, 2009) or Tomassini (Tomassini, et al., 2003) explore theoretically the possibility of using an evolving bubble to obtain electron injection. This describes injection on density transitions in LWFA experiments (Schmid, et al., 2010), (Buck, et al., 2013). Electrons can also be injected into a preformed bubble, according to Chen (Chen, Sheng, Ma, & Zhang, 2006) and Hidding (Hidding, et al., 2012), by creating them (through ionisation) in different regions of the accelerating field of the bubble.

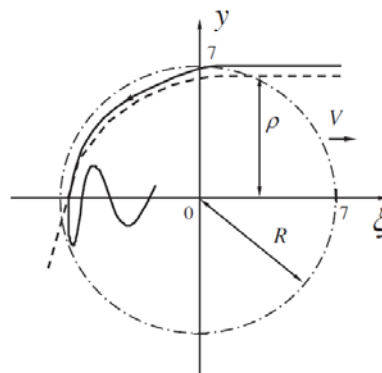


**Figure 2-4: Trajectory of the trapped (solid line) and untrapped electrons (dashed line) according to Kostyukov (Kostyukov, Nerush, Pukhov, & Serefov, 2009)**

It is worth mentioning here that the injected electron bunch creates its own wake whose electric field will shut down (at some point) the electron injection. This is known as beam loading (Reitsma, Cairns, Bingham, & Jaroszynski, 2005). The first undesirable effect of beam loading that can be observed experimentally is that the energy spread of the electron bunches increases as the charge increases. In Figure 2-5, experimental results are shown, and their full meaning and implications are explained in Chapter 5. The electron bunch charge is plotted versus energy spread and a quasi-linear relationship between them is obtained. This means that as the electric charge of the bunch increases, so does the energy spread.

Practically, the electric field of the electron bunches, which depends on their charge, counteracts the bubble electric field, which results in an accelerating field dependent on the electron bunch parameters. Of course, another effect of beam loading is the limitation of the maximum attainable electron energy due to decrease of the intensity of the accelerating field (Katsouleas, 1987),(Tzoufras, et al., 2008a) (Rechatin, et al., 2009), which means that higher charge comes at the expense of lower energy gain.

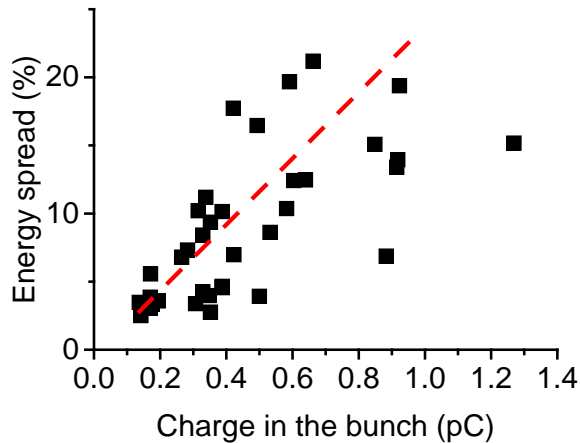


*Figure 2-5: Experimental results from the current study showing the electron energy spread vs. charge. A proof of the presence of beam loading is the increase in the energy spread with charge.*

Although different authors use different initial conditions for the laser in their numerical simulations, there is general agreement that the laser pulse length should fit into half of the plasma period and the laser spot size should be smaller than the plasma wavelength. Until recently (Schmid K. , et al., 2009), the experimental conditions were unmatched (mainly the laser pulse length) but due to laser pulse temporal and spatial

self-compression the laser pulse parameters evolve towards that required for accessing the bubble regime. This is why the unmatched regime of LWFA is called by some authors Forced Laser Wakefield Acceleration (F-LWFA) (Malka, et al., 2002).

### 2.3.1 Trajectory of electrons inside the LWFA channel. Betatron oscillation and electron beam divergence control

In this section some aspects of the trajectory of electrons inside the LWFA channel are briefly discussed, a subject that is closely connected with the emittance, pointing and divergence of the electron beam.

Electrons injected into the bubble experience a focussing force due to the ion column (Bosch & Gilgenbach, 1988) and start to execute betatron oscillations (Phuoc, et al., 2008), (Phuoc, et al., 2006) around the axis of propagation. Under certain conditions, as the electron bunch accelerates, it also experiences the influence of the laser pulse (Nemeth, et al., 2008), (Cipiccia, et al., 2011) producing harmonic betatron radiation. The equation that describes the motion of an electron in the bubble is:

$$\frac{d^2r}{dz^2} + \frac{1}{\gamma} \frac{dr}{dz} \frac{d\gamma}{dz} + k_\beta^2 r = 0 \quad , \quad (2.47)$$

with  $k_\beta = \omega_p / c \sqrt{2\gamma}$  the betatron wavenumber and  $r$  is the amplitude of the oscillation (distance of electron position from axis of ion column). When the electron moves with constant speed then the term  $d\gamma/dz = 0$  and the divergence  $dr/dz$  depends only on the electron energy. Practically, this means that the higher the energy of the electron, the lower the divergence. If the electron experiences an acceleration, which is the case in the LWFA, then the term  $\frac{1}{\gamma} \frac{dr}{dz} \frac{d\gamma}{dz}$  from equation (2.47) controls the betatron oscillation amplitude by damping it. This result combined with an exit down-ramp plasma density (where the betatron wavenumber decreases) leads to a further decrease in divergence due to the betatron oscillation wavelength dependence on plasma density (Shaw, Vafaei-Najafabadi, Marsh, & Joshi, 2012).

The trajectory of the electron bunch inside the plasma channel due to betatron oscillation will be important in explaining some of the results of this thesis. For example, the interaction of the electron beam and laser pulse controls the divergence

and pointing of the electron beam in the direction of the polarisation of the laser, as shown very well by Mangles (Mangles, et al., 2006) (see Figure 2-6).

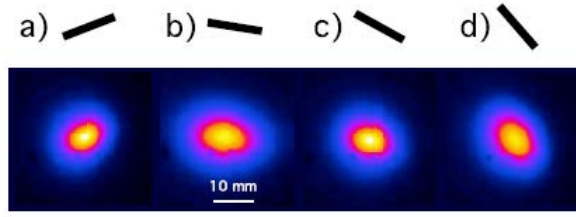


**Figure 2-6: Variation of the electron beam profile with the polarisation of the laser. The polarisation of the laser is a)  $-20^\circ$ , b)  $10^\circ$ , c)  $30^\circ$  and d)  $50^\circ$  (Mangles, et al., 2006)**

An analytical solution to the differential equation (2.47) obtained by Glinec (Glinec Y. , et al., 2008) has been used to obtain a general expression for the electron output angle  $\Theta$  which describes the direction or pointing of the electron beam(also connected to the well-known divergence of the electron beam) from a wakefield accelerator:

$$\Theta(\gamma) = -\frac{\Theta_0 (\gamma_0 \beta_0)^{1/4}}{\pi (\gamma \beta)^{3/4}} \sin \left[ \frac{E_0}{E_z} (\sqrt{2\gamma\beta} - \sqrt{2\gamma_0\beta_0}) \right], \quad (2.48)$$

where  $E_0 = m_e c \omega_p / e$  is the wave-breaking field,  $\Theta_0 = \pi \omega_p r_0 / 2c$  is the initial electron beam input angle,  $E_z$  is the accelerating field,  $\gamma_0 = \omega_0 / \sqrt{3} \omega_p$  is the electron injection energy,  $\beta_0 = \sqrt{1 - 1/\gamma_0^2}$  and  $\omega_0$  is the laser frequency. From equation (2.48) it can be observed that the electron oscillation amplitude, frequency and phase are controlled by  $\Theta_0$  (due to its direct dependence on the plasma frequency  $\omega_p$  and the injection position  $r_0$  relative to the centre of the wakefield bubble),  $E_z$  and  $\gamma_0$ , respectively. The electron beam transport system from the place where it is produced to the target location for applications ideally requires that the electron beam divergence at source is small. Using the above formula for the output of the electron beam it can be seen (Figure 2-7) that the divergence of the electron beam increases with the plasma frequency (red curve) and decreases (assuming electron injection energy constant) as the electron energy increases (black curve). In the Figure 2-7 the general variation of the divergence angle with both plasma frequency and electron energy are illustrated.

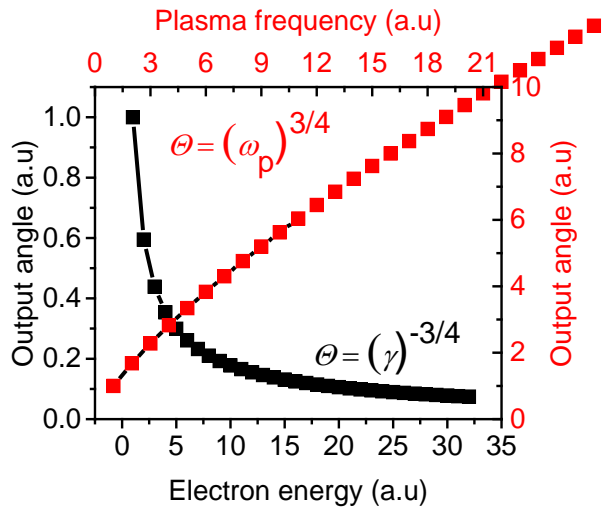


**Figure 2-7:** The evolution of the electron output angle as a function of the electron energy and plasma frequency

The electron beam output angle defined by the formula (2.48) could explain the shape of the electron angular distribution upon exiting the accelerator which, as reported in published literature such as Issac (Issac, et al., 2009), can be fitted with at least two Gaussian functions: one with small width corresponding to the main core of the electron beam and another with large width corresponding to the halo of electrons surrounding the main core (see Figure 2-8).

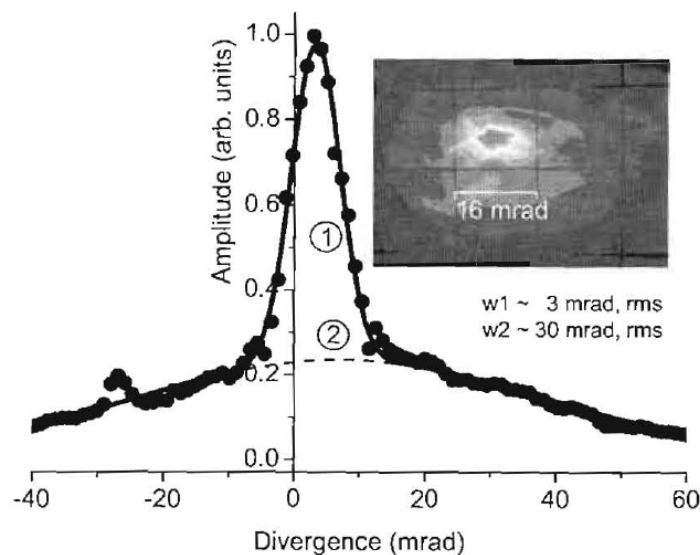


**Figure 2-8:** A false colour image of the electron distribution 64 cm from the accelerator exit (inset) The profile has a central spot surrounded by a halo. A line out of the profile fitted with double Gaussian is also shown. Caption taken from Issac et al. (Issac, et al., 2009)

From the recent work of Manahan (Manahan, 2013) it is known that the halo and the main electron beam are not only different in divergence (the Gaussian fits numbered with 1 and 2 in Figure 2-8) but also in energy: the electrons from the halo have much lower energy than the ones from the core. A part of this low energy halo can be seen as well in the electron spectrometer measurements where it forms the energy tail of the main electron bunch. This information could explain the origin of the halo of the electrons as follows:

- During the LWFA process the main electron bunch is injected in the bubble and accelerated. The effective accelerating field behind the main bunch is lowered due to beam loading.
- Some extra charge could be injected in the bubble after the main bunch but it will experience a lower accelerating field thus the final energy is small.
- The output angle of electrons depends inversely on the electron energy according to formula (2.48) thus the later injected electrons will exit the channel at high divergence angles and form the halo.

The above scenario although is very simplistic, ignoring for example the focussing forces inside the plasma channel or the plasma profile at the end of the plasma channel, it explains reasonably well the complex structure of the electron angular spread distribution.

## 2.3.2 General limitations of laser wakefield acceleration

The maximum accelerating field of a nonlinear plasma wave has been discussed in the previous chapter as if the electron bunch can be continuously accelerated with no limit to the acceleration length. Due to limitations imposed on the propagation of the laser pulse and electron bunches, there are three main limitations of the length of the LWFA: laser diffraction  $z_R$ , pump depletion length  $L_{pd}$  and dephasing length  $L_{dp}$ .

### 2.3.2.1 Laser diffraction

Laser pulses usually are approximated by a Gaussian beam profile with the electric field described by the equation:

$$E(x) = E_0 \frac{\exp(-ikz - \varphi(z))}{w(z)} \exp\left(-\frac{x^2 + y^2}{w(z)^2} - i \frac{\pi}{\lambda_0} \frac{x^2 + y^2}{R(z)}\right), \quad (2.49)$$

where  $\varphi(z)$  is the Guoy shift,  $w(z)$  is the transverse laser spot size along propagation direction  $z$  and  $R(z)$  is the beam radius of curvature.

The diffraction length or Rayleigh length (2.50) is the distance along the propagation direction,  $z$ , of a laser beam from the waist until the point where the area of cross-section is doubled (Siegman, 1986). The depth of focus of the beam, also called the ‘‘confocal parameter’’ is defined as twice the Rayleigh length.

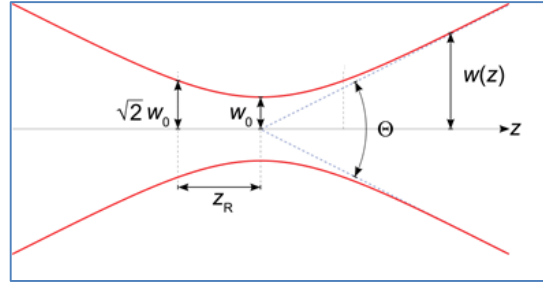


Figure 2-9: The diffraction and the Rayleigh length of a laser beam.

The laser diameter at position  $z$  from the waist is given by (2.51), and the total angular spread of the beam by (2.52):

$$z_R = \frac{\pi w_0^2}{\lambda}, \quad (2.50)$$

$$w(z) = w_0 \sqrt{1 + \left(\frac{z}{z_R}\right)^2}, \quad (2.51)$$

$$\Theta = 2 \frac{w_0}{z_R}. \quad (2.52)$$

$$\varphi(z) = \arctan \frac{z}{z_R} \quad (2.53)$$

Diffraction is an issue for LWFA when the laser beam is propagated over long distances. In this case guiding systems must be employed (Spence, Butler, & Hooker, 2003), (Leemans, et al., 2006), (Karsch, et al., 2007). For the LWFA with self-injection, diffraction is not important due to relativistic self-focussing of the laser beam. Also, before the laser beam starts to diffract, in the self-guided regime two more

phenomena can limit the acceleration length: dephasing and laser pump depletion. The laser spot size in the experiments presented in this thesis is  $\sim 21 \mu\text{m}$  which gives a confocal parameter of the order of  $\sim 3.46 \text{ mm}$  for a laser wavelength of  $800 \text{ nm}$ . This calculation does not take into account the laser relativistic self-focussing (see 2.2.2.1) which could reduce the spot size to less than  $10 \mu\text{m}$  thus reducing the confocal parameter from  $\sim 3.46 \text{ mm}$  to  $\sim 0.86 \text{ mm}$ .

### 2.3.2.2 Laser energy depletion

From the moment the laser starts interacting with the plasma it will continuously deplete its energy in order to create the wake. The length over which the laser energy is completely depleted is known as the depletion length and depends on the laser parameters and the plasma density through a relation given, for example, by Lu et al. (Lu, et al., 2007):

$$L_{pd} \cong \frac{\omega_0^2}{\omega_p^2} c \tau_{FWHM} . \quad (2.54)$$

Taking a plasma density of the order of  $1 \times 10^{19} \text{ cm}^{-3}$  and a laser pulse length of  $\sim 15 \text{ fs}$  (after relativistic self-focussing) the laser depletion length is of the order of  $L_{pd} \sim 0.86 \text{ mm}$  for a laser wavelength of  $800 \text{ nm}$ . Laser pulse head erosion has been ignored in this calculation .

### 2.3.2.3 Electron dephasing

Another important limitation of the LWFA is the dephasing length. The group velocity of the plasma wave is approximately equal to the group velocity of the laser, which is less than the speed of light  $c$ . Electrons injected in the bubble will have a velocity close to  $c$  so after some propagation distance they will outrun the wake and enter the decelerating part of the wake. The distance travelled by the electrons before entering the dephasing region of the wake is known as dephasing length, a relation for which is given by W. Lu (Lu, et al., 2007):

$$L_{dp} \cong \frac{4}{3} \frac{\omega_0^2}{\omega_p^2} \sqrt{a_0} k_p^{-1} . \quad (2.55)$$

Assuming a homogenous plasma density of the order of  $1 \times 10^{19} \text{ cm}^{-3}$  and a laser pulse length of  $\sim 15 \text{ fs}$  (after relativistic self-focussing) which gives a normalised vector potential of the order of  $a_0 \sim 4.5$ , the dephasing length is of the order of  $L_{dp} \sim 0.81 \text{ mm}$  for a laser wavelength of  $800 \text{ nm}$ .

A possible way to avoid electron dephasing is to shape the plasma profile so that the bubble length decreases continuously to ensure that the electron bunch maintains its position relative to the back of the bubble, which is known as phase locking. The electrons then experience a high accelerating field for their entire propagation length.

In this thesis the up-ramp density profiles have a special role in the experiments. When these kinds of density profiles are employed the previous formulae (calculated for constant plasma density) for plasma frequency, refractive index or phase/group velocity are not valid. To obtain new expressions for all these parameters the calculations of Wen (Wen, et al., 2010) has been followed. The size of the LWFA bubble is a function of the plasma density and has the form:

$$D_{bubble} = \sqrt{\gamma_a \lambda_p} = \sqrt{\frac{\gamma_a n_c}{n}} \lambda, \quad (2.56)$$

where  $D_{bubble}$  is the diameter of the bubble,  $\gamma_a = \sqrt{1 + a_0^2}$  is the relativistic gamma factor of the laser and  $n_c$  is the critical density. It is assumed that the laser wavelength changes insignificantly after the LWFA bubble has been generated. The bubble shrinks as it propagates as the density increases (in a positive plasma density taper) therefore the shrinkage speed of the bubble can be written as:

$$v_{sh} = -\frac{dD_{bubble}}{dt} = -\lambda \frac{d\sqrt{\gamma_a n_c / n}}{dx} v_{back}, \quad (2.57)$$

where the position of the bubble along the propagation direction  $x$  is given by

$$x = \int_0^t v_{back} dt.$$

The front velocity of the bubble is equal to the velocity of the front of the laser pulse. Due to laser pulse head erosion, velocity of the front of the laser pulse will be equal to the laser pulse group velocity minus the local pump depletion velocity (Esarey, Schroeder, & Leemans, 2009):

$$v_{front} = \left(1 - \frac{n}{2\gamma_a n_{cr}}\right) c - \frac{nc}{\gamma_a n_{cr}} = \left(1 - \frac{3n}{2\gamma_a n_c}\right) c. \quad (2.58)$$

The velocity of the back of the bubble (see Figure 2-10) can be written as the sum of the shrinking velocity and the front velocity:

$$v_{back} = v_{front} + v_{shrink} = v_{front} - \lambda \frac{d\sqrt{\gamma_a n_c/n}}{dx} v_{back}, \quad (2.59)$$

which leads to

$$v_{back} \approx \frac{1 - (3n/2\gamma_a n_{cr})}{1 + \lambda \left(\frac{d\sqrt{\gamma_a n_{cr}/n}}{dx}\right)} c. \quad (2.60)$$

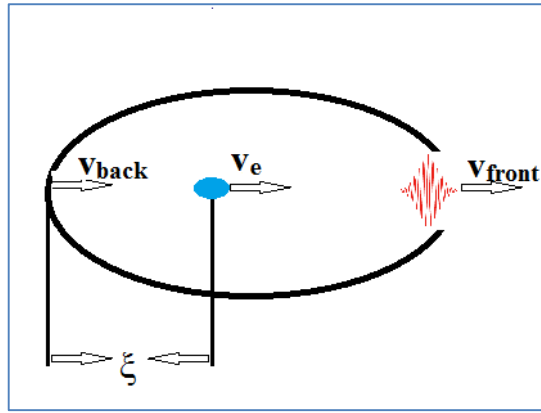


**Figure 2-10: The structure of the “bubble”.  $v_{back}$  is the velocity of the back of the bubble with respect to the front velocity  $v_{front}$  and  $v_e$  is the velocity of the electron bunch.**

Since the electron bunch moves at a speed close to  $c$ , it can be seen from relation (2.60) that  $v_{back}$  can be greater than the electron bunch velocity  $v_{bunch}$  when an up-ramp density profile is used.

The phase of the bunch in the bubble is  $\Omega = 2\pi\xi/D_{bubble}$ , where  $\xi = ct - x$  is the relative position of the electron bunch inside the bubble. Therefore, one can write:

$$\frac{d}{dx} \left( \frac{\Omega}{\omega} \sqrt{\frac{\gamma_a n_{cr}}{n}} \right) = \frac{1}{v_{back}} - \frac{1}{c}. \quad (2.61)$$

To keep the electron bunch inside the acceleration field and avoid dephasing, *i.e.* phase-locking, the plasma density must be adjusted continuously during acceleration. This condition can be written as:

$$n = \frac{n_0}{\left(1 - \frac{x}{L}\right)^{2/3}}, \quad (2.62)$$

$$L = \frac{2}{9} \left( \lambda - \frac{c\Omega_0}{\omega} \right) \left( \frac{\gamma_a n_{cr}}{n_0} \right)^{3/2}, \quad (2.63)$$

where  $n_0$  is the original plasma density (at  $x = 0$ ). When the phase locking condition is met then the electron bunch is accelerated over much longer distances and the effect of dephasing is avoided. The electric field of the electron bunch itself has an opposite direction to the electric field of the bubble. The accelerating field experienced by the electrons is the sum of the two fields. In an up-ward plasma density longitudinal profile, since the plasma density increases in the direction of laser propagation, the bubble shrinks as the laser propagates. In this case, the velocity of the bubble's back is continuously adjusted, and matches the velocity of accelerated electrons. Therefore, the electron bunch remains near the back of the bubble, experiencing a stable high accelerating field for the entire acceleration length (limited in this case only by the laser depletion length) and the tail electrons obtain nearly the same energy as that of the centre electrons. In this way the energy of the electron bunch is not only increased, but the energy spread is greatly reduced compared with the case of a homogenous plasma profile.

Another aspect of the dephasing is related to the focussing forces inside the plasma channel. The longitudinal accelerating field experienced by an electron in the plasma channel, for the linear case, has the form (Kalmykov, Gorbunov, Mora, & Shvets, 2006):

$$E_z \sim \exp\left(-\frac{2r^2}{w_0^2}\right) \cos(k_p \xi) \quad (2.64)$$

and the transverse focussing field is described by the formula:

$$E_r = \frac{4r}{k_p w_0^2} \exp\left(-\frac{2r^2}{w_0^2}\right) \sin(k_p \xi) \quad (2.65)$$

where  $r$  is the position of the accelerated charge relative to the channel axis. For  $r = 0$  the charge moving on-axis will feel no transverse force.

Plotting the normalised transverse and longitudinal forces it can be observed that for the first half of the plasma period the charge is accelerated, as already

mentioned previously in this chapter, and only for the first quadrant of the plasma period the charge is simultaneously accelerated and focused.

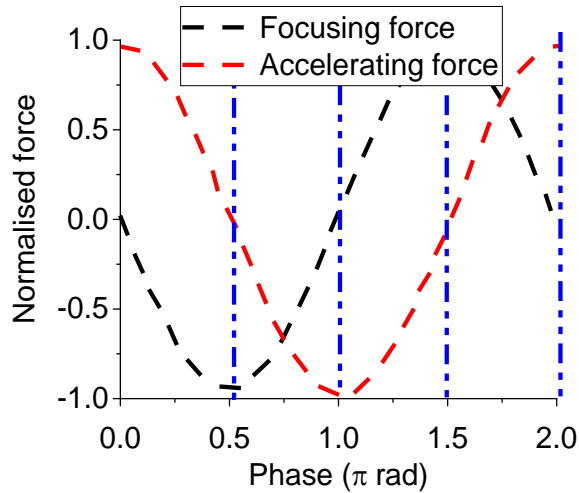


**Figure 2-11: Plasma wave phase representation. The charge will experience a focusing field and an accelerating field. Only the first quadrant is suitable for simultaneous focusing and acceleration.**

The optimised electron beam acceleration occurring only in the first quarter of plasma wake phase has direct influence on the divergence of the electron beam. Shaping the longitudinal plasma profile in order to rephase the electron beam relative to the accelerating field will place the electron beam in different regions of plasma wake phase thus the divergence of the electron beam, affected directly by the focussing field, will have a range of values depending on the parameters of the plasma density profile.

For the bubble regime the focussing force is linear thus when the up-ramp plasma densities are employed, the force acting on the electron beam from the transverse direction will depend, ignoring the influence of the betatron oscillation, on the position of the electron beam inside the bubble while accelerated as follows:

- An electron bunch accelerated mainly at the beginning of the density ramp will have an energy higher than the equivalent propagation in the equivalent homogenous plasma density, but the divergence will be the same
- An electron beam accelerated deeper in the up-ramp density will have a lower energy than the previous case, but with a lower divergence.

This consequence is experimentally explored in Chapter 6 when the measured divergence of the electron beam is compared in different experimental conditions as the plasma parameters are varied.

### 2.3.3 Scaling laws for the laser wakefield acceleration.

Due to the lack of an analytical theory of 3D nonlinear laser wakefield acceleration it is difficult to quantitatively describe the outcome of a LWFA experiment therefore one has to “rely” on numerical PIC simulations. In the past years different groups have tried to derive simple formulae to predict the optimum conditions for experiments and interpret their results. The derived formulae take into consideration the limitations discussed in the previous section and the accelerating field. Practically, the consensus shared by all groups is that the laser pulse should fit into half a plasma wavelength and the laser spot size should be less than one plasma wavelength. At the present time there are two main scaling laws developed by: Pukhov A. (Gordienko & Pukhov, 2005), (Pukhov & Gordienko, 2006), and Lu (Lu, et al., 2007).

“Pukhov” scaling is based on similarity theory (Pukhov & Gordienko, 2006) and uses the similarity parameter  $S = n_e/a_0 n_c$  with the assumption that  $S \leq 1$  and  $a_0 > 1$ . In these conditions the bubble takes on a spherical shape and the acceleration process is laser energy depletion limited. Also, the conversion efficiency is very high, greater than 20%. The main parameters of the LWFA, the peak energy of the mono-energetic bunch and the electric charge, depend strongly on the properties of the laser and are predicted by Pukhov to be:

$$E_{Pukhov} [MeV] \approx 0.3328 \sqrt{\frac{P[TW]}{0.0085}} \frac{\tau c}{\lambda}, \quad (2.66)$$

$$Q_{Pukhov} [nC] \approx 1.4 \frac{\lambda [\mu m]}{0.8} \sqrt{\frac{P[TW]}{100}}. \quad (2.67)$$

“Lu” scaling takes into account the complex phenomena involved in the LWFA: wake excitation, pump depletion, electron dephasing and beam loading. Also the “Lu” scaling assumes that the depletion length matches the dephasing length. The peak electron energy and electric charge predicted by Lu, are:

$$E_{Lu} [MeV] \approx 0.512 \left( \frac{P[TW]}{0.085} \right)^{1/3} \left( \frac{n_c}{n_e} \right)^{2/3}, \quad (2.68)$$

$$Q_{Lu} [nC] \approx 0.4 \frac{\lambda [\mu m]}{0.8} \sqrt{\frac{P[TW]}{100}}. \quad (2.69)$$

So far these scaling laws fail to fit the experimental results by overestimating or underestimating the peak energy and electric charge. Also, the predicted efficiency of 20% is far away from the  $10^{-5}$ - $10^{-6}$  % efficiency from the experimental results.

In this thesis, neither of the above mentioned scaling theories can be used to predict the experimental results since they use a homogenous plasma density profile and do not take into account the electron phase locking mechanism.

## 3 Gas target characterisation and optimisation

The supersonic nozzle (de Laval nozzle) creates a supersonic gas jet with a density profile within which the action of an intense, femtosecond, laser beam generates and accelerates electrons to relativistic velocities. The quality of the electron beam depends on the gas jet density profile. Understanding how supersonic gas jets are produced and controlled will help control different parameters of the electron beam.

A systematic analysis through numerical simulation of supersonic nozzles applied to laser wakefield acceleration is given in a published PhD thesis (Schmid K. , 2011) and also in a series of papers (Semushin & Malka, 2001), (Lemos , Lopes, Dias, & Viola, 2009), (Schmid & Veisz, 2012). Based on these results a series of nozzles have been modelled, numerically simulated and manufactured.

### 3.1 Theory of de Laval supersonic gas nozzles

The flow of gas between two vessels connected through a duct can be described as an adiabatic change of state. In Section 3.1.1, a general description of the thermodynamic system is given, defining some relevant parameters involved in the change of state. In Section 3.1.2, compressible flow is defined in relation to the Mach number, followed by a particular case of compressive flow through a convergent-divergent nozzle, for which the one-dimensional basic equations for flow are derived.

#### 3.1.1 A general description of thermodynamic systems

As shown further in this chapter, both the rate of change of mechanical energy in a compressible flow of gas and the rate of change of thermal energy must be taken into account. To track the changes of different parameters in a thermodynamic process a relationship between the state variables of a thermodynamic system is required. This kind of relationship is given by the thermal equation of state. The thermal equation of state (Krause, 2005) for an ideal gas is:

$$pv = rT , \tag{3.1}$$

where  $p$  is the pressure,  $v$  is a specific volume ( $\nu\rho = 1$ ),  $\rho$  is the density and  $T$  is the temperature. The physical constant  $r$  is the specific gas constant:

$$r = R / M , \quad (3.2)$$

where  $R = 8.3144621 \text{ mol}^{-1} \text{ K}^{-1}$  and  $M$  is the molar mass.

A gas is considered ideal if the dimensions of the particles are negligible compared with the specific dimensions of the thermodynamic system that contain the gas, and the collisions between particles are random. For an ideal gas, the internal energy  $e$  and enthalpy  $h$  per unit mass depend only on the temperature of the gas. Therefore, the ideal gas specific heat at constant volume and constant pressure (Krause, 2005) can be written as:

$$c_v = \left( \frac{\partial e}{\partial T} \right)_v = \frac{de}{dT} , \quad (3.3)$$

$$c_p = \left( \frac{\partial h}{\partial T} \right)_p = \frac{dh}{dT} . \quad (3.3)$$

The specific heat is defined as the quantity of heat necessary to raise the temperature of a unit mass of system by 1 degree.

The basic definition of enthalpy states that the enthalpy per unit mass of a system is equal to the sum of the internal energy of the system and the product of the pressure and volume of the system:

$$h = e + pv \quad (3.4)$$

and differentiating the equation of state (3.1) and equation (3.4) one obtains:

$$pdv + vdp = rdT , \quad (3.5)$$

and

$$dh = de + pdv + vdp . \quad (3.6)$$

The First Law of Thermodynamics, which states that when a quantity of heat  $dq$  is added to a thermodynamic system then the internal energy of the system increases and work  $pdv$  is done by the system, can be written as:

$$dq = de + pdv . \quad (3.7)$$

Using relations, (3.3), (3.5), (3.6), (3.7) with the approximation  $dp = 0$ , after some simple algebra, one obtains:

$$c_p - c_v = r . \quad (3.8)$$

Using the ratio of specific heats  $k$ ,  $k = c_p/c_v$ , one can rewrite the equations (3.8) and (3.3) as:

$$c_p = \frac{k}{k-1} r, \quad (3.9)$$

$$c_v = \frac{1}{k-1} r. \quad (3.10)$$

The ratio of specific heats  $k$  for a gas depends on the degrees of freedom  $f$  of the particles forming the gas:

$$k = (f + 2) / f. \quad (3.11)$$

The degrees of freedom define the number of independent directions in which a system (atom, molecule, etc.) can have motion. For monoatomic gases  $f=3$  and for a diatomic gases  $f=5$  (neglecting vibrational movement, which is a correct assumption for low temperatures) therefore for a monatomic gas  $k = 5/3$  and for a diatomic gas  $k = 7/5$ .

The entropy of a thermodynamic system, at temperature  $T$ , changes each time a quantity  $dq$  of heat is added or removed from the system:

$$ds = \frac{dq}{T}. \quad (3.12)$$

Using the formula for entropy after some calculations one obtains:

$$\frac{dq}{T} = c_v d(\ln pv^k). \quad (3.13)$$

After integrating (3.12) (Krause, 2005) for a system that changes its states from state  $(pv)_1$  to final state  $(pv)_2$  through a reversible process, then the specific entropy takes the form:

$$s_2 - s_1 = c_v \ln \left( \frac{p_2 v_2^k}{p_1 v_1^k} \right). \quad (3.14)$$

The following equations can also be obtained:

$$s_2 - s_1 = c_v \ln \left[ \frac{T_2}{T_1} \left( \frac{\rho_1}{\rho_2} \right)^{k-1} \right], \quad (3.15)$$

$$s_2 - s_1 = c_v \ln \left[ \left( \frac{T_2}{T_1} \right)^k \left( \frac{p_1}{p_2} \right)^{k-1} \right], \quad (3.16)$$

$$s_2 - s_1 = c_v \ln \left[ \frac{p_2}{p_1} \left( \frac{\rho_1}{\rho_2} \right)^k \right]. \quad (3.17)$$

If one assumes an isentropic change then  $s_2 - s_1 = \text{constant} = v$ , from (3.13), (3.14), (3.15) and (3.16) the following relations are obtained (Krause, 2005):

$$pv^k = v, \quad (3.18)$$

$$p = v\rho^k, \quad (3.19)$$

$$T = v\rho^{k-1} = vp^{\frac{k-1}{k}}. \quad (3.20)$$

As described in the next section, the last three equations of state for a reversible adiabatic process are very important in describing a compressible flow through a duct.

## 3.1.2 Compressible gas flows

### 3.1.2.1 Mach number and speed of sound

A compressible fluid behaves like an elastic solid. A disturbance can propagate in the fluid in a form of pressure wave, with a speed of propagation that depends on the rigidity of the medium. If the amplitude of the pressure wave is very small it is called a sound or acoustic wave.

To understand the notion of speed of sound, the 1D flow of an infinitesimally thin, weak pressure wave moving at the speed of sound through a steady continuous fluid is analysed (Figure 3-1). As the pressure wave propagates it creates two regions with different properties: ahead of the pressure pulse the medium is characterised by pressure  $p$ , density  $\rho$ , temperature  $T$  and speed  $u = 0$ , while behind the pulse the medium is characterised by pressure  $p + \delta p$ , density  $\rho + \delta\rho$ , temperature  $T + \delta T$  and speed  $\delta u$ .

Since the flow is steady the mass of fluid entering one section of the tube must pass through all the sections of the tube. This is practically a statement of law of conservation of mass:

$$A\rho c = \text{const}. \quad (3.21)$$

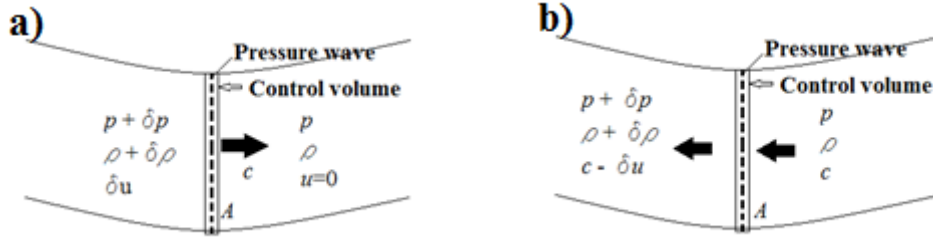


**Figure 3-1:** In a) a low amplitude pressure wave propagates through a fluid at rest while in b) the pressure wave is stationary and the fluid moves through the control volume.

The pressure wave can be analysed as a stationary wave if the fluid moves with the speed  $c$  in the counter direction of movement of the pressure wave. The pressure wave is now stationary, with a wavefront of surface  $A$ . The fluid enters the surface  $A$  with velocity  $c$  and leaves with a velocity  $c - \delta u$ .

Applying the equation of continuity for the surface  $A$  one obtains (Krause, 2005):

$$A\rho c = A(\rho + \delta\rho)(c - \delta u). \quad (3.22)$$

Taking into account the low amplitude of the pressure wave then:

$$\delta u = c \frac{\delta\rho}{\rho}. \quad (3.23)$$

From relation (3.23) it can be deduced that  $\delta u > 0$  when  $\delta\rho > 0$ , which is basically equivalent to a compressive wave.

Applying now the momentum equation for the flow through the surface  $A$ :

$$pA - (p + \delta p)A = (A\rho c)(c - \delta u) - (A\rho c)c. \quad (3.24)$$

After some simple algebra, formula (3.24) becomes:

$$\delta p = \rho c \delta u. \quad (3.25)$$

Using (3.23) and (3.25) one obtains:

$$c^2 = \frac{\delta p}{\delta\rho}. \quad (3.26)$$

In the limit  $\delta \rightarrow 0$  and assuming an isentropic flow (frictionless flow through the control volume and no heat transfer) the expression for the speed of sound can be written as:

$$c = \sqrt{\left(\frac{\partial p}{\partial\rho}\right)_s}, \quad (3.27)$$

where the subscript  $s$  indicates that the differentiation is carried out at constant entropy.

It should be stressed that formula (3.27) is valid only for the isentropic case where it represents the speed of sound in a compressible medium. In case of strong pressure waves the speed of propagation can be higher than the speed of sound. For an ideal gas, using (3.1) and (3.19), the expression (3.27) becomes (Kundu & Cohen, 2002):

$$c = \sqrt{krT} . \quad (3.28)$$

Taking the temperature of the gas as  $T = 298$  K, for example, the speed of sound in helium is 1016 m/s, in nitrogen 497 m/s and in hydrogen 1316 m/s.

Having determined the speed of sound one can now determine the Mach number, which will determine the compressibility effects in a gas flowing with speed  $u$ . The Mach number is defined as:

$$M \equiv \frac{u}{c} , \quad (3.29)$$

where  $c$  is given by relation (3.27).

The continuum approximation for a steady fluid is the foundation of all the models used in computational fluid dynamics (CFD). Continuity is ensured because the mean free path (the average distance a particle travels between two successive collisions) of particles of the fluid is much shorter than the characteristic dimensions of the system enclosing the fluid, e.g. duct. This condition is quantified via the Knudsen number (Kundu & Cohen, 2002):

$$Kn = \frac{\lambda}{L} , \quad (3.30)$$

where  $Kn$  is a dimensionless number,  $\lambda$  is the mean free path of the fluid particles and  $L$  is the characteristic dimension of the system, for example the outlet or throat of a nozzle. Written in terms of Mach and Reynolds numbers, relation (3.30) becomes:

$$Kn = \frac{M}{Re} \sqrt{\frac{k\pi}{2}} , \quad (3.31)$$

where  $k$  is the specific heat ratio and  $Re$  is the Reynolds number.

The Reynolds number (Krause, 2005) is defined through the relationship  $Re = \rho u L / \mu$ , where  $\rho$  is the density of the fluid,  $L$  is the characteristic linear dimension of a system and  $\mu$  is dynamic viscosity of the fluid. The Reynolds number defines different flow regimes with reference to the walls. It is considered laminar flow if  $Re \leq 2300$

and fully turbulent flow for  $Re \geq 4000$  (Holman, 2002). All the supersonic nozzles used in the present work had  $Re \geq 4000$ .

The continuum approximation is valid as long as  $Kn \leq 10^{-3}$  (Hsu, 2002). For all experiments presented in this thesis, the Knudsen number is below  $10^{-3}$  therefore the continuum hypothesis is always satisfied.

### 3.1.2.2 Navier-Stokes equations and the equations for one-dimensional isentropic flow

In this section the compressible flow in a one-dimensional approximation is described. A one-dimensional approximation is valid as long as the flow does not encounter any obstacles e.g. the flow through the throat does not meet an abrupt change in cross-section.

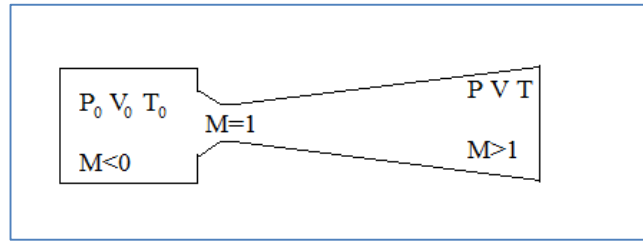


Figure 3-2: A typical convergent-divergent nozzle.

Let's assume that inside the nozzle considered in Figure 3-2 there is a fluid flow and a control volume with cross-section  $A$  is considered. The change of state between two points along the streamline can be completely described using three equations of state: the continuity equation, the equation of motion and the energy equation. These three equations can be written for a non-steady state Newtonian fluid in an external force volume-force  $\mathbf{f}$  (Kundu & Cohen, 2002):

$$\frac{D\rho}{Dt} = -\rho \operatorname{div}\mathbf{u}, \quad (3.32)$$

$$\rho \frac{D\mathbf{u}}{Dt} = \mathbf{f} - \operatorname{grad}p + \operatorname{div}\boldsymbol{\tau}, \quad (3.33)$$

$$\rho c_p \frac{DT}{Dt} = \operatorname{div}(\lambda \operatorname{grad}T) + \beta T \frac{D\rho}{Dt} + \Phi, \quad (3.34)$$

Here, the substantial derivative ( $D/Dt$ ) is defined as

$$\frac{Da}{Dt} = \left( \frac{\partial a}{\partial t} + \mathbf{u} \bullet \text{grad} a \right), \quad \frac{D\mathbf{b}}{Dt} = \left( \frac{\partial \mathbf{b}}{\partial t} + \text{grad} \left( \frac{1}{2} \mathbf{u}^2 \right) - \mathbf{u} \times \text{curl} \mathbf{b} \right), \quad \dot{\boldsymbol{\varepsilon}}$$

is the deformation rate tensor,  $\delta$  is the Kronecker tensor,  $\boldsymbol{\tau} = \left[ \mu \left( 2\dot{\boldsymbol{\varepsilon}} - \frac{2\delta \text{div} \mathbf{u}}{3} \right) \right]$  is tension tensor,  $\mu$  is

viscosity for Newtonian fluid,  $\Phi = \text{div}(\boldsymbol{\tau}\mathbf{u}) - \mathbf{u} \text{div} \boldsymbol{\tau}$  is the dissipation function,

$\beta = \frac{1}{\rho} \frac{\partial \rho}{\partial T}$  is the thermal expansion coefficient,  $\lambda$  is the heat conductivity coefficient.

These are known as Navier-Stokes equations and they are not be derived here for it is beyond the scope of this thesis. A derivation can be found in many textbooks on gas dynamics (Anderson, 1995). Navier-Stokes equations form a system of nonlinear partial differential equations that usually cannot be solved analytically and thus require numerical methods. They can be simplified assuming that there is no external force acting on the fluid considered with zero viscosity and no thermal conduction terms. In this case one obtains the Euler equations (Kundu & Cohen, 2002):

$$\frac{D\rho}{Dt} + \rho \text{div} \mathbf{u} = 0, \quad (3.35)$$

$$\frac{D\mathbf{u}}{Dt} + \frac{\text{grad} p}{\rho} = \mathbf{0}, \quad (3.36)$$

$$\frac{DE}{Dt} + \frac{p}{\rho} \text{div} \mathbf{u} = 0, \quad (3.37)$$

where  $E = \rho e + \frac{1}{2} \rho (u^2 + v^2 + w^2)$  is the total energy per unit volume,  $e$  is the internal energy per unit mass,  $\rho$  is the fluid density and  $p$  is the pressure. Assuming that the control volume is not under the action of external forces and the flow is one-dimensional and steady, then the Euler equations (3.35), (3.36) and (3.37) can be written (Kundu & Cohen, 2002) as:

$$\rho_1 u_{x1} = \rho_2 u_{x2}, \quad (3.38)$$

$$p_1 + \rho_1 u_{x1}^2 = p_2 + \rho_2 u_{x2}^2, \quad (3.39)$$

$$\frac{u_1^2}{2} + h_1 = \frac{u_2^2}{2} + h_2. \quad (3.40)$$

Since the distance between the two points is not defined where the equations of state can be applied, this region can be extended indefinitely and can be made infinitesimally thin. For an infinitesimally thin control region, the parameters of the fluid present sudden variations, such discontinuities are known as shock waves, which are described in the next section.

The equation of conservation of mass applied to the control volume must not depend on position  $x$  (steady condition):

$$\frac{\partial m}{\partial t} = \rho u_x A = \text{const} . \quad (3.41)$$

Differentiating (3.41) and using the Euler equation after some algebra it is obtained:

$$\frac{du_x}{u_x} = \frac{-dA/A}{1-M^2} . \quad (3.42)$$

Using the definition of the Mach number (3.29), the fluid flow (Kundu & Cohen, 2002) can be classified as:

- a) Incompressible flows for  $M < 0.3$  in the whole volume of flow, here the density is considered to be constant during the flow. A decrease in area results in a proportional increase in the speed.
- b) Subsonic flow for  $0.3 < M < 1$  without shocks anywhere in the volume of the flow. The flow is similar to the incompressible flow but in this case an increase or decrease of the area has a greater effect on speed.
- c) Transonic flow for  $0.8 < M < 1.2$  is a transitional regime, with or without shocks.
- d) Supersonic flow for  $1 < M < 3$ . Shock waves are usually present in the volume of the flow. Here the denominator becomes negative and an increase of the speed is obtained by increasing the area.
- e) Hypersonic flow for  $M > 3$ . In this case heat transfer must also be considered, especially in the boundary layers. Also, due to presence of the heat, for high  $M$ , dissociation of the molecules must be taken into account.

In this thesis only the subsonic-supersonic case is analysed and applied to the convergent-divergent nozzle (also known as the *de Laval* nozzle) and general properties of the flow inside the Laval nozzle are determined. The properties of the

fluid inside the nozzle at any point after the flow is initiated are found from the stagnation parameters.

The stagnation or reservoir state is defined now as a thermodynamic state where the velocity of the flow is zero. All the properties in an arbitrary point in the flow are denoted with subscript zero.

The stagnation enthalpy is defined as (Krause, 2005):

$$h_0 = h + \frac{u_x^2}{2} \text{ [kJ/kg]}. \quad (3.43)$$

Using (3.3) where the enthalpy is replaced by the product of static temperature and the specific heat at constant pressure one obtains for calorically perfect gases:

$$c_p T_0 = c_p T + \frac{u_x^2}{2}. \quad (3.44)$$

From (3.44), the equation of state (3.1) and the definition of speed of sound (3.28), gives

$$\frac{k}{k-1} \frac{p_0}{\rho_0} = \frac{k}{k-1} \frac{p}{\rho} + \frac{u_x^2}{2}, \quad (3.45)$$

and with the definition of the speed of sound

$$\frac{c_0^2}{k-1} = \frac{c^2}{k-1} + \frac{u_x^2}{2}. \quad (3.46)$$

From (3.45), Bernoulli's equation for compressible flow has the form:

$$\frac{k}{k-1} \frac{p_0}{\rho_0} = \frac{k}{k-1} \left( \frac{p_0}{\rho_0} \right) \left( \frac{p}{p_0} \right)^{\frac{k-1}{k}} + \frac{u_x^2}{2}, \quad (3.47)$$

Here the isentropic relation is combined with the expression for the speed of sound to

obtain  $c^2 = c_0^2 \left( \frac{p}{p_0} \right)^{\frac{k-1}{k}}$

Dividing (3.47) by the square of the speed of sound, pressure, temperature, density and speed of sound all the relevant expressions for stagnation parameters are expressed in terms of the Mach number (Krause, 2005):

$$\frac{T_0}{T} = \left( 1 + \frac{k-1}{2} M^2 \right), \quad (3.48)$$

$$\frac{p_0}{p} = \left(\frac{T_0}{T}\right)^{\frac{k}{k-1}} = \left[1 + \frac{k-1}{2}M^2\right]^{\frac{k}{k-1}}, \quad (3.49)$$

$$\frac{\rho_0}{\rho} = \left(\frac{T_0}{T}\right)^{\frac{1}{k-1}} = \left[1 + \frac{k-1}{2}M^2\right]^{\frac{1}{k-1}}, \quad (3.50)$$

$$\frac{c_0}{c} = \left(1 + \frac{k-1}{2}M^2\right)^{\frac{1}{2}}. \quad (3.51)$$

In addition, one also defines the sonic or critical conditions for which the control volume considered earlier changes its state through an isentropic transformation until it reaches sonic speed  $M = 1$ . All the critical parameters are denoted by an asterisk.

The above equations can be written in sonic conditions:

$$\frac{p^*}{p_0} = \left(\frac{2}{k+1}\right)^{\frac{k}{k-1}}, \quad (3.52)$$

$$\frac{T^*}{T_0} = \left(\frac{2}{k+1}\right), \quad (3.53)$$

$$\frac{\rho^*}{\rho_0} = \left(\frac{2}{k+1}\right)^{\frac{1}{k-1}}, \quad (3.54)$$

$$\frac{c^*}{c_0} = \left(\frac{2}{k+1}\right)^{\frac{1}{2}}. \quad (3.55)$$

For ideal monatomic and diatomic gases the numerical values of sonic conditions can be obtained and are shown in Table 1.

Ideal Gas	$p^*/p_0$	$T^*/T_0$	$\rho^*/\rho_0$	$c^*/c_0$
Monatomic	0.528	0.833	0.633	0.912
Diatomic	0.486	0.749	0.649	0.865

*Table 1: Sonic conditions for the monatomic ideal gas and diatomic ideal gas*

Using Bernoulli's equation (3.47) the maximum speed that a gas flow can reach after it exits a nozzle and expands in the surrounding medium is:

$$u_x = \sqrt{\frac{2krT_0}{k-1} \left(1 - \frac{p}{p_0}\right)^{\frac{k-1}{k}}}. \quad (3.56)$$

If the gas flow expands into a rarefied medium where the pressure tends to zero then the maximum speed that a gas flow can have in vacuum is obtained:

$$u_x = \sqrt{\frac{2krT_0}{k-1}}. \quad (3.57)$$

Using the equation for mass flow continuity (3.41) and the critical mass, a relationship between Mach number, critical pressure and cross-sectional area can be found (Krause, 2005):

$$\frac{A^*}{A} = M \left[ \frac{2}{k+1} \left( 1 + \frac{k-1}{2} M^2 \right) \right]^{\frac{k+1}{2(k-1)}}, \quad (3.58)$$

or depending on pressure:

$$\frac{A^*}{A} = \frac{\left( \frac{p}{p_0} \right)^{\frac{1}{k}} \sqrt{1 - \left( \frac{p}{p_0} \right)^{\frac{k-1}{k}}}}{\sqrt{\frac{k-1}{2} \left( \frac{2}{k+1} \right)^{\frac{k+1}{k-1}}}}. \quad (3.59)$$

The equations (3.42), (3.58) and (3.59) represent practically the basic equations that explain the flow through a supersonic nozzle.

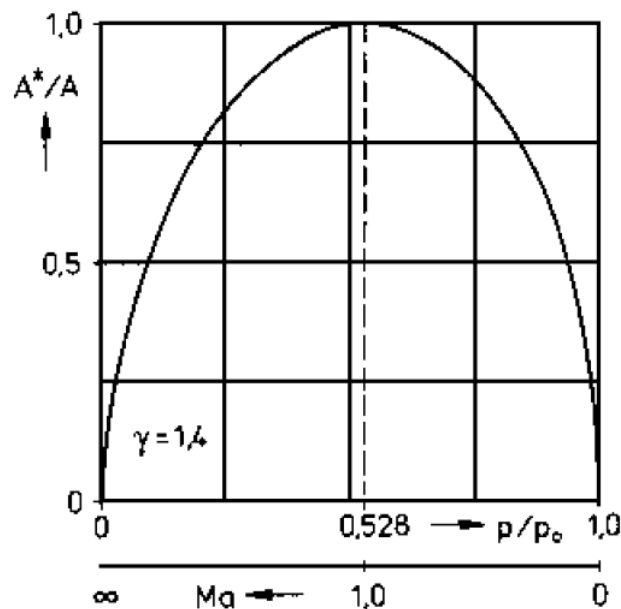


**Figure 3-3: Critical area ratio versus pressure ratio. For  $k = 1.4$  the maximum  $A^*/A = 1$  is obtained for  $p/p_0 = 0.528$ . The two branches of the graph represent two possible flow regimes: subsonic and supersonic regime (Krause, 2005).**

From (3.58) it can be seen that the critical area ratio  $A^*/A$  tends to zero from small Mach numbers and also for very high Mach numbers (see Figure 3-4). The critical area ratio is plotted in Figure 3-3 for  $k = 1.4$  as a function of the Mach number and the pressure ratio. The maximum critical area ratio  $A^*/A = 1$  is obtained when  $p/p_0 = 0.528$  and the two branches in the Figure 3-3 correspond to supersonic and subsonic flow.

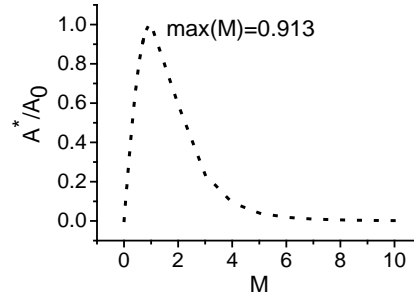


*Figure 3-4: Critical area versus Mach number. For  $k = 1.4$  the critical area  $A^*/A \approx 0$  for Mach numbers  $M \approx 0$  or  $M \rightarrow \infty$ .*

If the cross section is chosen to first converge and then diverge, and if the flow entering the downstream tube is subsonic, it is then accelerated and becomes sonic, and in the divergent part supersonic. This is the basic principle of supersonic nozzle or de Laval nozzle.

### 3.1.2.3 Normal shock waves

As discussed in the previous chapter, the Euler equations (3.35), (3.36) and (3.37) can be applied for two points inside a steady flow without imposing any limits on the distance between points. For an infinitesimal distance, the equations that describe the evolution of the fluid properties in a region where a shock wave is present can be obtained. A shock wave is defined as a discontinuous change of all flow quantities: pressure, density, temperature, etc.

Rearranging equation (3.39) and using the continuity equation (3.38) gives (Krause, 2005):

$$u_{x1} - u_{x2} = \frac{p_2}{\rho_2 u_2} - \frac{p_1}{\rho_1 u_1} = \frac{c_2^2}{k u_2} - \frac{c_1^2}{k u_1}. \quad (3.60)$$

Here the perfect gas relation  $c^2 = \frac{kp}{\rho}$  has been used.

The equation (3.40) can be written for sonic conditions as:

$$\frac{u_{x1}^2}{2} + \frac{c_1^2}{k-1} = \frac{u_{x2}^2}{2} + \frac{c_2^2}{k-1} = \frac{(k+1)a^{*2}}{2(k-1)}. \quad (3.61)$$

Using the last equation a relationship between the fluid velocity before and after the shock and the critical speed can be written as:

$$u_{x1}u_{x2} = a^{*2} \quad (3.62)$$

This relation is known as the Prandtl-Mayer relation. In terms of the speed ratio  $M^* = u/a^*$  the previous equation is  $M_2^* = \frac{1}{M_1^*}$  and shows that along the shock the speed can

change from supersonic to sonic. This equation permits also a change of speed from sonic to supersonic but, as will be seen shortly, this case is forbidden by the entropy requirements for an adiabatic system:

$$M_2^2 = \frac{1 + \frac{(k-1)M_1^2}{2}}{kM_1^2 - \frac{k-1}{2}}, \quad (3.63)$$

$$\frac{\rho_2}{\rho_1} = \frac{u_{x1}}{u_{x2}} = \frac{(k+1)M_1^2}{(k-1)M_1^2 + 2}, \quad (3.64)$$

$$\frac{p_2 - p_1}{p_1} = \frac{\rho_1 u_{x1}^2}{p_1} \left( 1 - \frac{u_{x2}}{u_{x1}} \right), \quad (3.65)$$

$$\frac{p_2 - p_1}{p_1} = \frac{2k(M_1^2 - 1)}{k+1}. \quad (3.66)$$

A relation for the specific entropy change can be written (Krause, 2005) using equations (3.9) (3.17) (3.64) and (3.65)

$$\frac{s_2 - s_1}{r} = \ln \left\{ \left[ 1 + \frac{2k(M_1^2 - 1)}{k+1} \right]^{\frac{1}{k-1}} \left[ \frac{(k+1)M_1^2}{(k-1)M_1^2 + 2} \right]^{\frac{k}{k-1}} \right\}. \quad (3.67)$$

For small values of  $M_1$  the relation (3.67) can be simplified to

$$\frac{s_2 - s_1}{r} = \frac{2k(M_1^2 - 1)^3}{3(k+1)^2}. \quad (3.68)$$

For an adiabatic process the entropy can only increase or stay constant. This condition applied to above relation is satisfied only if  $M_1 \geq 1$  therefore in a shock the speed can change only from supersonic to sonic and not vice versa.

## 3.2 Numerical simulation of supersonic gas jets

Here numerical simulations of the fluid dynamics through the nozzles used in LWFA experiments are discussed. In Section 3.2.1 a short description of the flow model and approximations used in simulations are given. In Section 3.2.2 numerical results of the supersonic flow through convergent-divergent nozzles are presented.

### 3.2.1 Flow model and approximations

As discussed in Section 3.1.2.2, equations (3.32) (3.33) and (3.34) are a system of coupled non-linear differential equations for  $p$ ,  $T$  and  $\mathbf{u}$ , which are closed when the equation of state is given. These equations are modified to include the effect of turbulences and this model is called the *SST k- $\omega$*  model.

The smallest-scale turbulences are assumed to be much larger than the molecular mean free path – the continuum hypothesis. In the simulations, the fluid is considered Newtonian, isotropic and tension-tensor symmetric. Tension tensor symmetric means that the fluid particles have negligible angular momentum or their angular momentum is not appreciably coupled to the external angular momentum and the torque will be zero.

Also, it is assumed that in the model there are no sources of heat, diffusion processes or heat radiation.

An important aspect that must be taken into account in fluid dynamic simulations is the existence of boundary layers. A boundary layer is a region close to the wall enclosing a fluid flow where the fluid will have different velocity gradients due to friction on the walls. Here velocity is used to define the boundary layer but actually any fluid parameter can be used, the most intuitive is the density. The

boundary layer is an issue in designing a nozzle with a very steep density profile. In this case great care must be taken in choosing proper nozzle geometry and proper fluid parameters.

In this thesis, the boundary layer is taken into consideration in simulations (see Figure 3-5) but is not considered important in the final nozzle design because the goal is to design a nozzle that has variable and not necessarily steep density ramps.

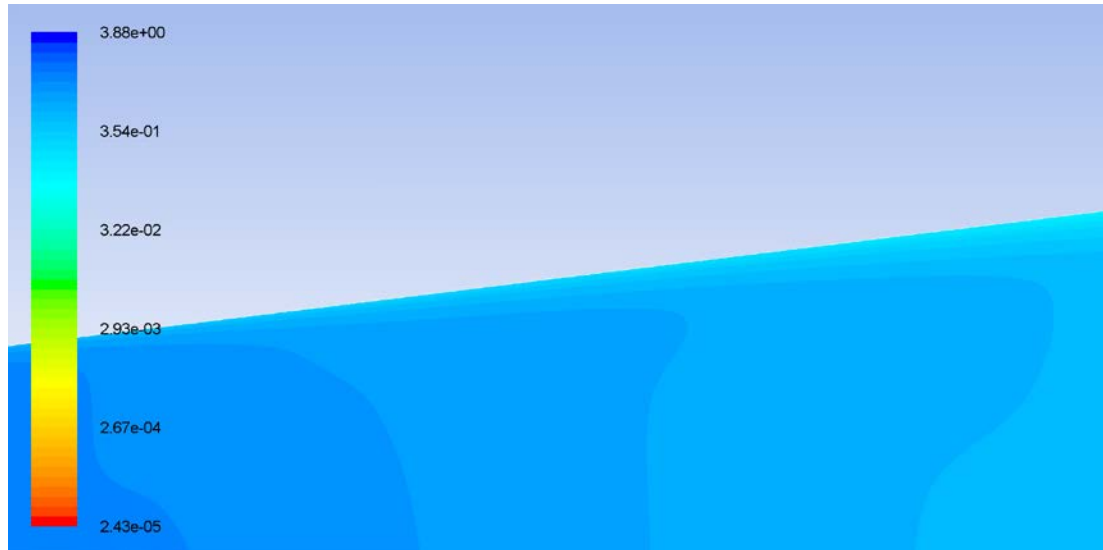


*Figure 3-5: Contours of density in a logarithmic scale of the zoomed interior of a supersonic flow close to the nozzle wall. Due to friction at the wall, boundary layers are produced which results in the generation of density gradients close to the nozzle wall.*

In order to resolve the smallest features of the flow, the turbulence, an appropriate mesh cell size is chosen, especially close to the nozzle walls where the existence of boundary layers required a mesh size smaller than that for the rest of the nozzle. To quantify how small the mesh should be close to the walls a quantity called  $Y^+$  was used:

$$Y^+ = \rho u_T y / \mu, \quad (3.69)$$

where  $\rho$  is the local density,  $u_T$  is tangential velocity and  $y$  is the distance between mesh cell centroid and the wall for wall adjacent cells. In order to resolve the boundary layer the mesh close to the wall should respect the condition:  $Y^+ \leq 1$  (as shown in Figure 3-6). This condition is verified each time a new CFD simulation is initiated.

All the simulations consider the steady-state condition *i.e.* the situation where the flow parameters are constant in time. This condition is chosen for two reasons:

- The reproducibility of the experiment from shot to shot. This means that each time the laser hits the gas jet it will meet the same flow condition therefore there is no need to consider variations in the flow.
- The computing time is greatly reduced as only the final state of the system is computed.

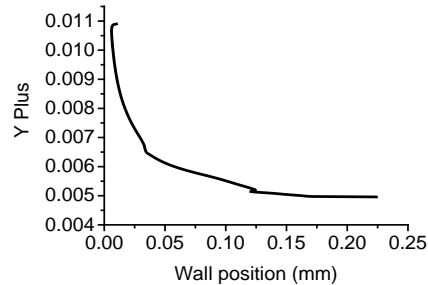


**Figure 3-6: The evolution of  $Y^+$  along the nozzle walls beginning with the throat position. The condition  $Y^+ < 1$  is satisfied for any wall nozzle position.**

To ensure that the simulations are mesh-independent the mesh size is reduced until the result of the simulation does not change. Theoretically, the mesh can be made arbitrarily small, but in reality one is bound by computing time, which increases with the number of cells from the mesh, and by the requirement that the molecular mean path should be less than the cell size (the continuum hypothesis).

The conical geometry of the nozzle allows simulations to be carried with a 2D axisymmetric geometry where practically only one side of the 2D nozzle is simulated (Figure 3-7). By mirroring the result the full flow profile can be visualised.

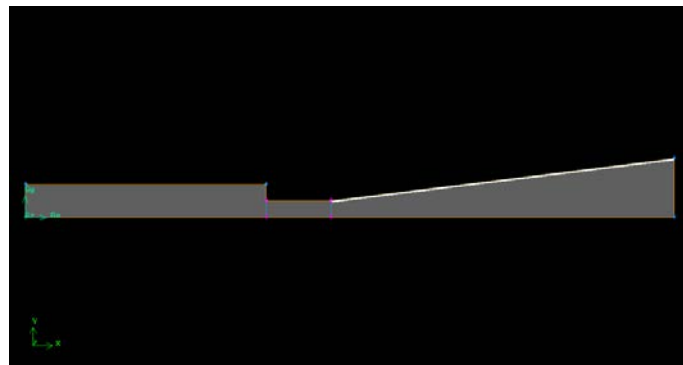


**Figure 3-7: The supersonic nozzle model used in simulations. Due to cylindrical symmetry only one side of the nozzle is simulated.**

### 3.2.2 Simulation results

In this thesis five different nozzles are used in experiments and characterised using CFD. Their parameters are given in Table 2. The commercial software ANSYS Fluent 6.3 is used for CFD simulations. Ansys Fluent solves the steady-state and transient Navier-Stokes equations on a grid using a finite volume method (Versteeg & Malalasekera, 1995). In this case the steady-state case has been chosen as the desired density profile for experiments is obtained when the flow is stabilised i.e. the steady-state regime is reached. The problem has been set up in 2D-axisymmetric with double precision accuracy. In a first step, the geometry and the grid is defined which forms a computational domain to solve the flow equations. Then the materials (helium or argon) and boundary conditions (Anderson, 1995) (*pressure inlet* at the nozzle inlet and *pressure outlet* confining volume around the nozzle exit) are set. According to the flow conditions (viscosity, laminar, transition, turbulent, etc.), an appropriate solver is chosen and the solution iterated. The convergence of the simulation is considered to be achieved when the flow parameters do not change with the iteration number. In the present case the monitored flow parameter was the flow rate. To ensure that the simulation results are mesh independent (see 3.2.1) a series of simulations have been done using different mesh sizes. It has been considered a solution mesh-independent when the simulation result do not change anymore as the mesh size is decreased. The result is then analysed by a post-processor and can be visualized. Depending on the parameters to be extracted, the simulation results are provided as contours plots. Two examples of density contours obtained for two different nozzles, 510 and 511, at the same backing pressure of 2.5 MPa are shown in Figure 3-8. From density contours lineouts of density can be extracted from different positions along the flow.

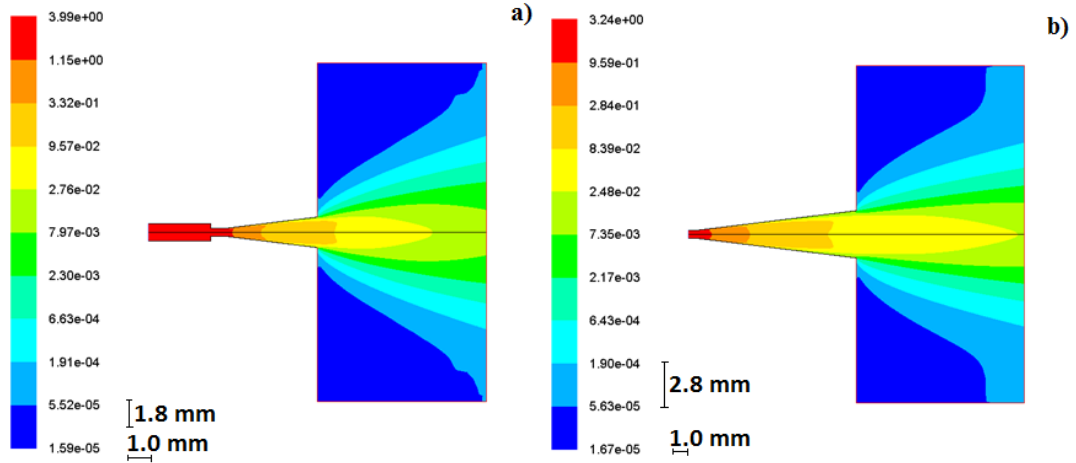


**Figure 3-8:** Example of simulation results showing logarithmic density contour plots for (a) Nozzle 510 and (b) Nozzle 511. The backing pressure is 2.5 MPa. The legend shows the gas density distribution from low density (blue) to high density (red)

Nozzle Code	$d$ throat diameter (mm)	$D$ outlet diameter (mm)	$\Phi$ semi-opening angle ( $^{\circ}$ )	$L$ conical section length (mm)
A	0.5	2	16.7	2.5
508	0.5	1	7	2.03
510	0.5	1.8	7	5.21
511	0.5	2.8	7	9.366
Gauss	0.5	0.5	0	-

**Table 2:** The geometrical parameters of the nozzles used in experiment and CFD simulations. For drawings see Section 8.3.

Nozzle behaviour is determined by the backing gas parameters (gas type, pressure and temperature) and the geometry of the nozzle (throat diameter  $d$ , outlet diameter  $D$  and semi-opening angle  $\Phi$ ), assuming that the flow exits the nozzle in vacuum. This conclusion is also drawn by Schmid (Schmid & Veisz, 2012), following extensive CFD simulations of Laval nozzles in different geometries and conditions. Using these results, on which the present nozzle geometries have been chosen it can be concluded that all Laval nozzles follow the same trend when the experimental conditions are varied. For example, the density along the centre line falls exponentially as one moves further and further away from the nozzle outlet, which is common for any Laval nozzle (Figure 3-9). Also, the local density in the gas jet increases linearly with increasing backing pressure.

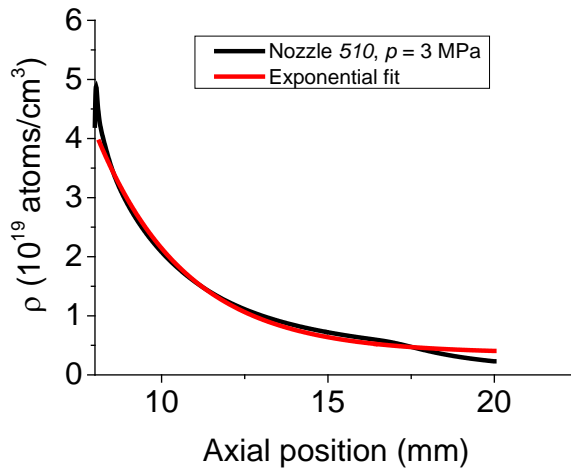


*Figure 3-9: The evolution of gas density along the centre line of the gas nozzle. The nozzle outlet is placed at 10 mm. Note the quasi-exponential decrease in density. The simulated nozzle is 510 with a backing pressure of 3 MPa and argon gas.*

### 3.2.2.1 Influence of the backing pressure and gas temperature over the gas density profile

One of the parameters monitored in CFD simulations is the backing pressure. The simulated gas is helium at a reservoir temperature of 293 K. Lineouts through the centre line of the nozzle are made and density profiles extracted. For a nozzle with  $d_{exit}/d_{throat} = 3$ , where  $d_{exit}$  is the outlet diameter and  $d_{throat}$  is the throat diameter, the density profiles through the centreline of the nozzle are shown in Figure 3-10.

As shown in Figure 3-11, the evolution of gas jet density as a function of the backing pressure is linear, except at 1.5 MPa, which presents a small deviation due to the presence of a shockwave. In general, a well-designed nozzle for LWFA experiments has no shockwaves therefore there is a linearity between backing pressure and local density. In this thesis, due to manufacturing technology constraints, the Laval nozzle is designed using a simple conical geometry without rounding the walls in the throat region as is required to avoid shock generation. The generated shocks due to the sharp edge in the throat region are damped out by choosing long divergent cones, as recommended by Schmid (Schmid & Veisz, 2012).

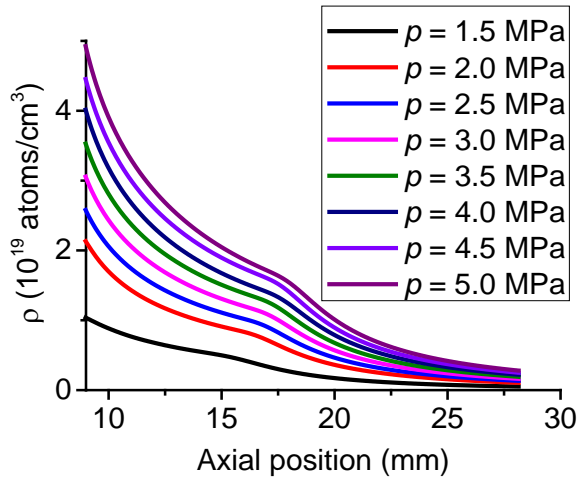


**Figure 3-10:** Lineouts of density at the axis of the nozzle taken at the nozzle outlet. The lineouts are shown for different backing pressures. The density profiles are obtained with Nozzle A.

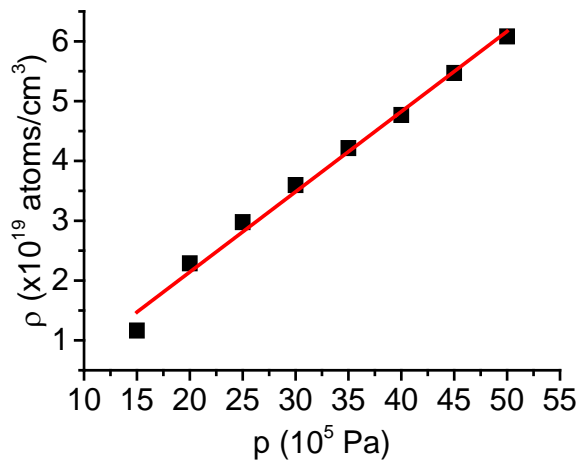


**Figure 3-11:** Density of the gas at a point situated at the middle of the gas nozzle outlet. The evolution of the density with backing pressure is linear.

For safety reasons, the bottles of gas used in the laser plasma wakefield acceleration experiments are placed in an isolated area. The temperature of this environment varies strongly during the day especially in the winter (around 15° C). Figure 3-12 shows that the density profiles depend on the temperature of the gas.

The simulated gas is helium with a constant reservoir pressure  $p_0 = 3.0$  MPa. From each simulation lineouts of density are taken at the nozzle outlet at different backing gas temperature (Figure 3-12), and for each case the results are averaged and represented on the same graph (Figure 3-13). As the temperature of the gas increases, the density of the supersonic gas jet decreases, as shown in Figure 3-12 and Figure 3-13, for each 10 ° C increase there is a 10% local mean density decrease. This result can be explained by taking into account the flux of gas through a given area (nozzle

outlet for example). As the temperature of the gas increases the velocity of the gas also increases, leading to lower local densities for higher temperatures.

This temperature variation can pose serious problems during the experiment because it can lead to a drift in plasma density profile and subsequently to a drift in the electron beam quality during a campaign of experiments. For example, a 15° C change in ambient temperature can lead to a 15% change in gas jet density. This density drift can be indeed compensated by a reduction in backing pressure but only after the temperature has been stabilised, which cannot be the case in a real situation where the thermal shielding is absent.

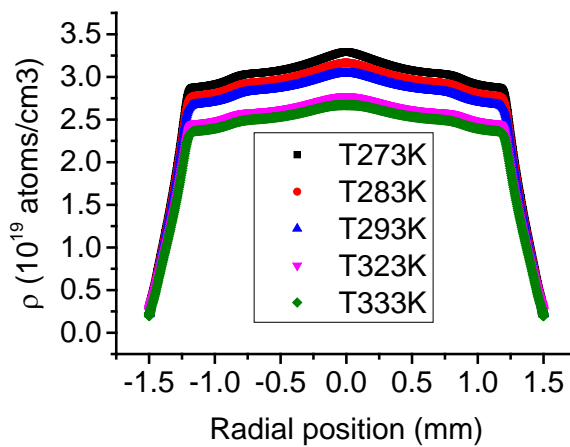


**Figure 3-12: Evolution of density profiles with gas temperature. The lineouts of density are determined at the outlet of the nozzle.**

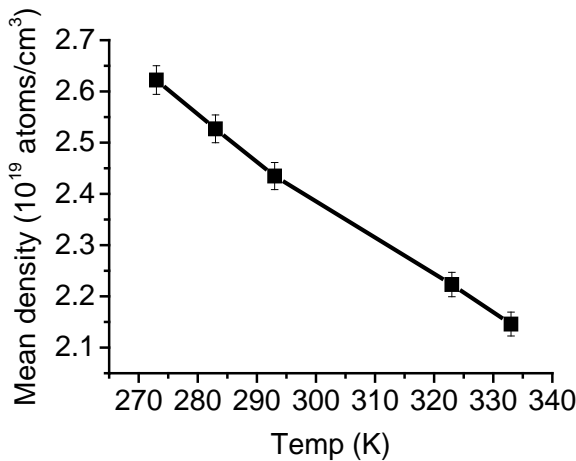


**Figure 3-13: The evolution of mean density with the gas temperature. Lineouts of density are made at the outlet of the nozzle and the density is averaged over whole radial direction. Vertical bars represent the standard error.**

An active control of the backing pressure depending on the ambient temperature or gas temperature can be a suitable solution although not yet implemented in the ALPHA-X laboratory.

### 3.2.2.2 Production of complex density profiles

To produce complex density profiles the gas jet is tilted at different angles relative to the direction of propagation of the laser. Practically, the tilting of the nozzle changes the slopes of the density profile ramps, as seen by the laser, giving a practical way of controlling the longitudinal density profile and therefore a way to manipulate the phase velocity of the LWFA bubble and electron beam.

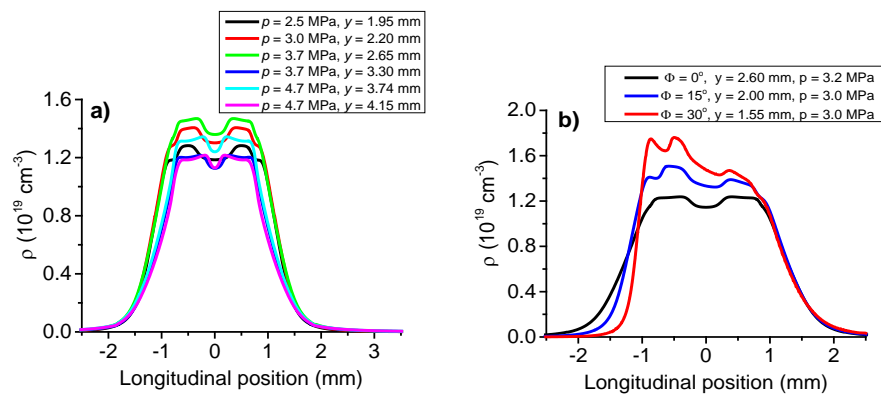


*Figure 3-14: Examples of plasma density profiles along the laser propagation direction crossing some distance  $y$  above the gas nozzle exit. a) Density profiles when the gas nozzle is in straight position and b) density profiles obtained when the gas nozzle is tilted.*

## 3.3 Experimental characterisation and optimisation of valve-Laval nozzles assembly

### 3.3.1 Characterisation of supersonic gas jets using interferometry

In this section the supersonic gas jets are characterised using a Mach-Zehnder interferometer. Not all Laval nozzles used in the experiments have been tested; the aim is to compare the results from interferometry with the CFD simulations for validation. In some experiments non-symmetric density profiles are used, which cannot be characterised using interferometry due to limitations in the commonly used inversion algorithms for density retrieval. Also, the experimental setup for tilting nozzles

blocked one of the laser beams used in the interferometer setup, therefore it could not be used to obtain the gas jet profiles. Therefore, the density profiles obtained from CFD simulations are used in the final analysis. For the purpose of this thesis only the trend of the density profiles in different experimental condition is relevant here, their absolute values having no meaning in this context.

The Mach-Zehnder interferometer set up and density measurements have been carried out by Anna Subiel, David Grant and Gregory Vieux. A basic schematic of the interferometer is shown in Figure 3-15.

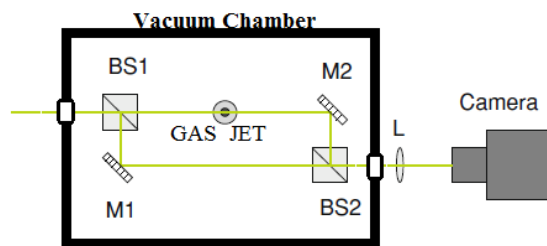


**Figure 3-15: Basic setup of Mach-Zehnder interferometer used in ALPHA-X experiments for density profile retrieval.**

The interferometer is set-up to measure the changes in refractive index due to laser-plasma interaction, therefore the densities obtained experimentally varied considerably depending on the laser power, as can be seen Figure 3-16. The electrons have complicated dynamics during the laser-plasma interaction therefore in the gas jet the electrons are depleted or accumulated along the laser propagation axis. All these factors modify the density profile measured by the interferometer and lead to a mismatch between the actual and measured profile.

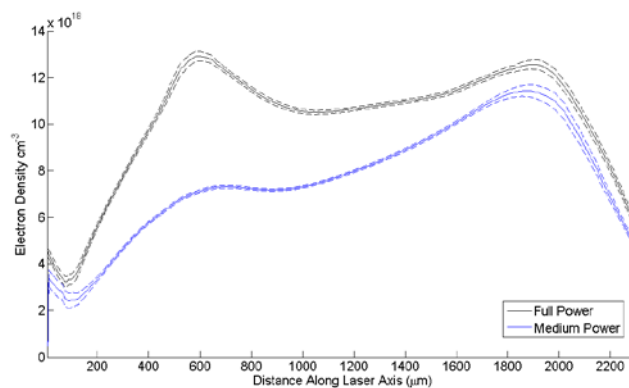


**Figure 3-16: Density profiles obtained from interferometry when different laser powers are employed. Courtesy of Anna Subiel (Subiel, 2012)**

After scanning a range of laser powers, experimental density profiles close to the results of CFD simulations have been found. The nozzle design tested here is identical to one of the nozzles tested by Schmid (Schmid & Veisz, 2012). Using an interferometer designed to diagnose the neutral atoms, Schmid et al. obtained a difference in density profile between experiment and simulation of less than 10%, a result that validates the use of CFD for supersonic nozzle characterisation.

What is really important is that a good match between density profile ramp shapes is obtained from CFD and interferometry as shown in Figure 3-17. As is further shown, in Chapter 4, only the density ramp parameters are used when the LWFA experimental data are compared.

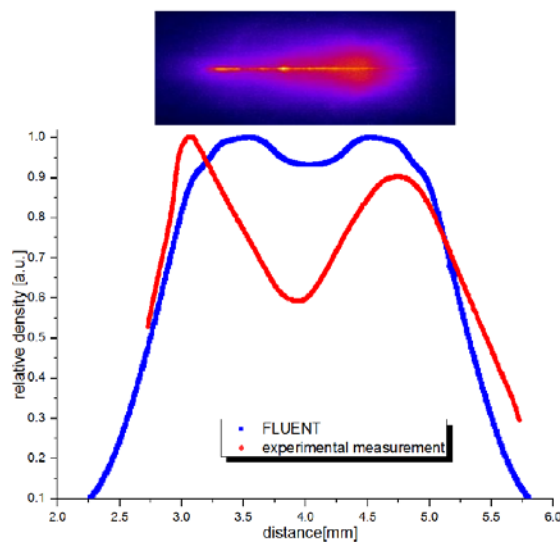


*Figure 3-17: The density profile obtained from interferometry (red curve) and the density profile obtained from CFD simulations (blue curve). The inset shows a false colour image of the plasma channel created by the laser. Courtesy of Anna Subiel (Subiel, 2012).*

### 3.3.1.1 On the use of high refractive index gases in interferometry measurements

It is mentioned in Section 3.1.2 that for the same nozzle geometry, backing pressure and environment pressure, the flow profiles depend on the type of gas used: monatomic or diatomic. This result is used in interferometry, where the fringe shift depends on the refractive index of the medium to be analysed. Due to the low refractive index of helium one can replace the gas with a high refractive index gas, such as argon. Since both helium and argon are monatomic gases then the flow parameters are the same as an ideal gas. It is assumed by many authors (Schmid K. , 2011), (Grittani, et

al., 2014) that the above conclusion is valid also for real gases, which is not true, as proved shortly.

For an ideal gas the gas parameter  $R$  is constant and the adiabatic constant  $k$  takes the value of 1.66 for monoatomic gases and 1.4 for diatomic gases thus the flow profile is the same for all monoatomic gases, for example, independent of their atomic mass. For real gases the values of  $k$ ,  $R$  and viscosity change for almost every gas (see Table 3), therefore the mass flow and consequently the gas jet profile, is unique for every gas.

Gas	Refractive index $n$ (at 587.6 nm)	Specific heat		Ratio of specific heats $k = c_p/c_v$	Individual gas constant $c_p - c_v = R$ (J/Kg K)	Viscosity ( $\times 10^{-5}$ kg/m-s)h
		$c_p$ (J/Kg K)	$c_v$ (J/Kg K)			
Argon	1.000281680	520.64	312	1.667	208	2.125
Helium	1.000034912	5193	3120	1.664	2073	1.990
Hydrogen	1.000139230	14283	10160	1.405	4120	0.8411
Neon	1.000066012	1030	618	1.667	412	2.938
Nitrogen	1.000298390	1040	743	1.400	297	1.663
Oxygen	1.000271800	919	659	1.395	260	1.919

*Table 3: Properties of different gases*

CFD simulations have been carried out using two gases, argon and helium, with their real specific heat, viscosity and gas constant values. The backing pressure is 3 MPa and the simulation is run using the geometry of Nozzle 510. Cross-sections through the density profiles taken at different heights above the nozzle outlet are shown in Figure 3-18, which shows a significant difference in profile flows although both gases are monoatomic.

Note that close to the nozzle outlet the density ramps are almost the same and only the peak density differs. As the flow moves further and further away from the nozzle the density ramps start to evolve differently for argon and helium due to significant difference in radial velocity of the gas jets. This difference in radial velocities leads to a faster divergence of helium gas jets compared with argon gas jets and therefore a difference in evolution of local gas jet density.

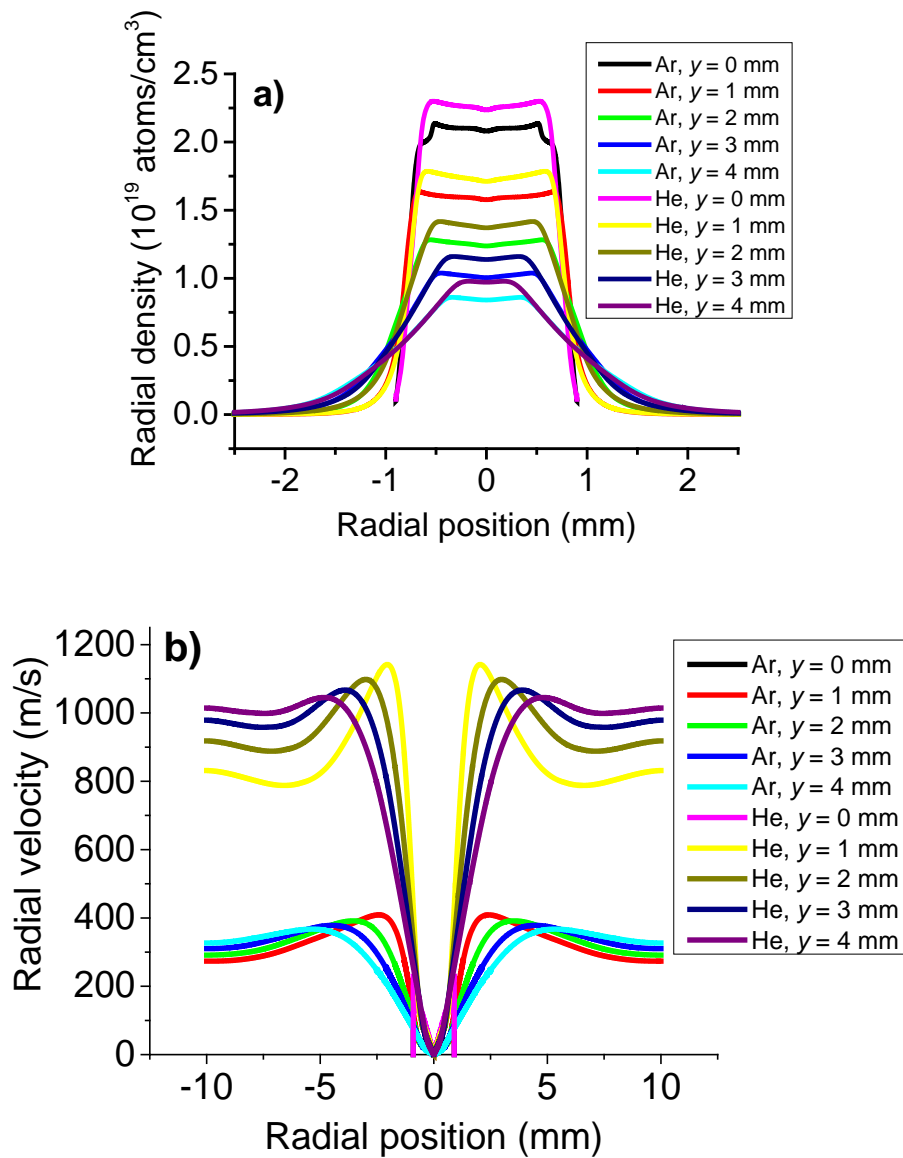


**Figure 3-18:** The lineouts of density (a) and radial velocity (b) at different heights from the nozzle outlet. CFD simulated gases: Ar and He with a backing pressure of 3 MPa for Nozzle 510. Note the difference in density profiles although both gases are monatomic.

The difference in flow of argon and helium has been observed experimentally by Quan-Zhi (Quan-Zhi, et al., 2004) (see Figure 3-19), although they incompletely explain their results by taking into account only the difference in atomic mass between argon and helium.

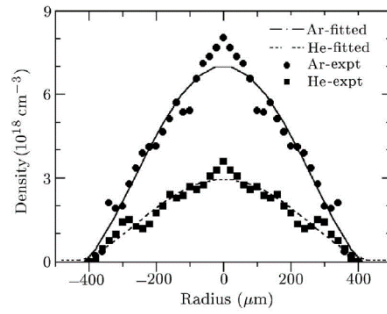


**Figure 3-19: Experimental observation of Ar and He flow under the same conditions. The lineouts of density are taken 170  $\mu\text{m}$  above the nozzle outlet. The data are taken from Quan-Zhi et al. (Quan-Zhi, et al., 2004).**

### 3.3.2 Optimisation of the solenoid valve – supersonic nozzle assembly for LWFA experiments

A pulsed gas jet compared with a continuous flow jet has obvious advantages: the size and cost of the vacuum systems can be greatly reduced and also, during the LWFA experiments, the pressure in the reaction chamber can be kept low so that the laser pulse duration is not affected by group velocity dispersion and the laser is not defocussed by ionisation of the gas.

The solenoid valve (Figure 3-20) is opened and closed by applying a pulse of current to the coil. The electric signal has two components: a high voltage pulse of approximately 275 V with a plateau duration of between 180  $\mu\text{s}$  and 320  $\mu\text{s}$  (see Figure 3-21), which opens the valve and a low voltage signal that keeps the valve open for the required opening time. The duration of the high voltage pulse can be changed using a series of switches on the circuit board driver. The value depends on the experimental conditions (mainly the backing pressure). If it is too low the valve becomes erratic or stops working.

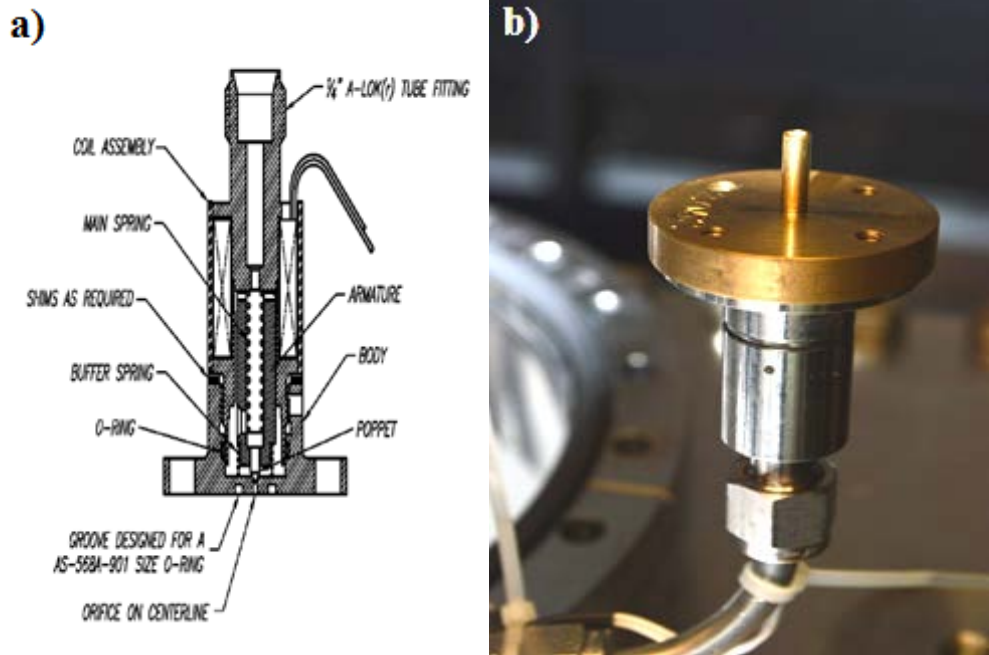


Figure 3-20: Mechanical design of the fast solenoid valve (a) and valve-nozzle assembly (b) (www.smijapan.com, 2015).

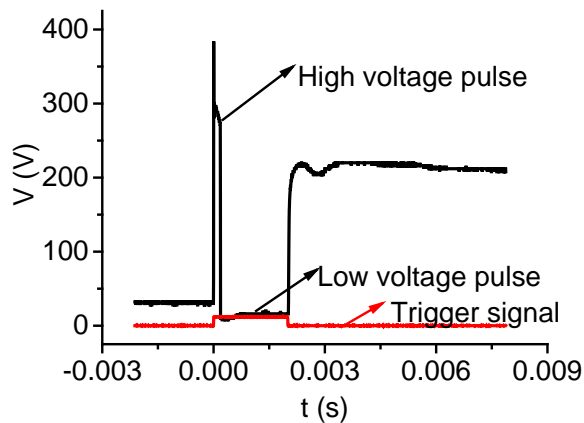


Figure 3-21: Typical valve driver pulse with the two components: high voltage pulse followed a low voltage plateau.

The solenoid valve is opened and closed by an armature inside a solenoid. A poppet attached to the armature forms the seal. The armature travel inside the valve between the open and the close position (the *stroke*) determines the total response time of the valve. The stroke can be adjusted by adding or removing a series of shims between the main body of the valve and the head containing the exit orifice. With factory settings a new valve will open and close in the shortest possible time. However, the number of shims can be adjusted to take into account working conditions (backing pressure or wear of the valve). For supersonic nozzles the mass flow rate should be

maximised (maximum flow possible through exit orifice) otherwise the gas jet profile densities will differ from those predicted using numerical simulation results. A solution to avoid the choked flow, described by R. Jung (Jung, 2007), involved reshaping the head of the poppet so that the effective exit valve orifice is as high as possible.

A different approach has been taken for experiments described in this thesis, which involved adjusting the high voltage pulse length (*HVPL*) part of the valve triggering signal and the stroke. Adjusting the *HVPL* to higher values allows operation of the valve at high pressures and a larger stroke distance. Adjusting the stroke allowed a larger effective exit orifice to be obtained. The high voltage pulse allows a fast open time of the valve while the low voltage pulse maintains the valve open as long as it is applied. The high voltage pulse length can be adjusted using an 8-position dual in-line package (DIP) switch on printed circuit board (PCB) (Figure 3-22). The timing selected for each switch is showed in Table 4.

Switch number	Timing value ( $\mu\text{s}$ )
1	100
2	100
3	100
4	80
5	40
6	20
7	10
8	5

*Table 4: Adjustable timings in the Iota One valve drive timing (www.smijapan.com, 2015)*

These timings are conveniently adjusted during testing to enable the valve to operate with the required parameters. The minimum high voltage pulse length is 50  $\mu\text{s}$  [limited by the Iota One driver (www.smijapan.com, 2015)] and the maximum is 320  $\mu\text{s}$  (the valve safety limit). During the tests the high voltage pulse length is adjusted between 180-300  $\mu\text{s}$  with a step of 40  $\mu\text{s}$ .

The initial length of the stroke is measured using a setup shown in Figure 3-23. It consists of a power supply used to activate the solenoid valve so that the armature/poppet can be moved inside the valve and a high precision micrometre gauge with a tip that rests on the poppet. As the poppet moves the tip of the micrometre moves with it so that the maximum and minimum position can be obtained. For a new

valve the stroke is found to be 180  $\mu\text{m}$ . The operation of the valve over the range 160  $\mu\text{m}$  to 260  $\mu\text{m}$  has been investigated in the present work.

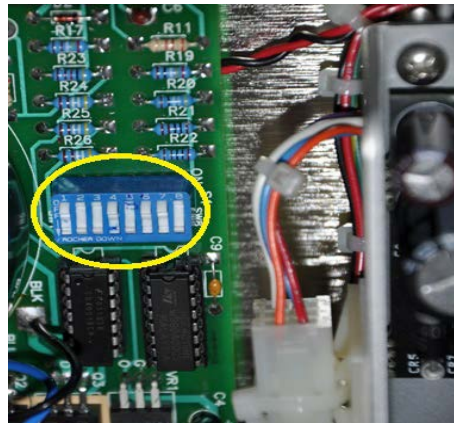


*Figure 3-22: DIP switches for controlling the high voltage pulse length.*

The stroke distance is one of the essential parameters of the valve. Its value determines the rise and fall time of the flow, and the flow rate. To optimise and monitor the valve operation, a pressure transducer (Omega PX01K1-1.5KG5T) is installed on the helium pipe-line immediately before the valve. The pressure transducer transforms a pressure reading into an electric signal that is recorded by an oscilloscope and acquisition system.

As mentioned above, the stroke can be changed by adjusting the number of shims between the main valve and the valve head. During the tests, the stroke distance changes from 160  $\mu\text{m}$  (the minimum stroke where the valve starts to operate) to 260  $\mu\text{m}$  (the maximum distance where the valve stops operating). The step for changing the stroke distance is 50  $\mu\text{m}$ .

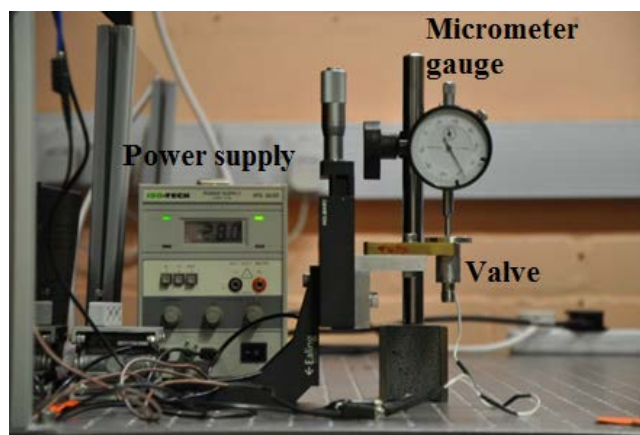


*Figure 3-23: Setup used for measuring the stroke distance of the solenoid valves. On the left side of the picture is the power supply used to move the poppet inside the valve. At the right side there is a micrometre gauge with the measuring tip resting inside the valve, on the poppet.*

From numerical simulations of the fluid flow one knows the pressure drop in the gas line during the operation of the valve. This value of the pressure drop can be obtained from the pressure transducer and is used to determine the valve setting (*HV* and stroke). In this case, for a pressure of 4 MPa, a pressure drop of at least 0.035 MPa is required to obtain the correct *HV* and stroke values. During the investigation and optimisation of the valve-nozzle assembly a series of parameters have been adjusted (Table 5) to determine their impact on the flow and also to determine the best settings.

The output of the fast pressure transducer is read 100 times for each parameter and a graph is produced from the averaged values. Calibrated values of the static pressure and pressure drop during the operation of the valve the pressure transducer have been obtained using the calibration curve of the pressure transducer (Figure 3-24). As shown in the Figure 3-24 the response of the transducer is linear.

<i>SD</i> Stroke length ( $\mu\text{m}$ )	<i>HVPL</i> High voltage pulse length ( $\mu\text{s}$ )	<i>T</i> Trigger pulse length (ms)	<i>p</i> Backing pressure (MPa)
160	180	1.0	2.1
210	220	1.2	4.0
260	260	1.4	5.0
260	300	1.6	5.0
260	300	1.8	5.0
260	300	2.0	5.0

**Table 5: The parameters changed during solenoid valve testing.**

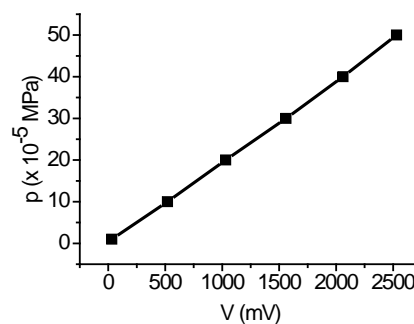


**Figure 3-24: Calibration of the pressure transducer.**

All the spare parts inside the solenoid valve (main spring, buffer spring, armature and poppet) are replaced with new ones before the experiment. This ensures that the results are not affected by previous wear of components. An assumption is made that during the experiment the component most susceptible to wear, the poppet, does not wear enough to affect the results of the experiment. During normal operation the poppet is

changed after around 200,000 strokes. In experiments here, the number of strokes is around 10,000, therefore this assumption is valid.

### 3.3.2.1 Trigger pulse length influence on the pressure drop during operation of the valve

The influence of the trigger pulse length  $T$  over the flow profile has been studied to establish the optimum value for the flow to reach a steady state condition. The stroke distance  $SD$  is set to  $160\ \mu\text{m}$  (factory setting), HVPL has been set to  $220\ \mu\text{s}$  and the backing pressure  $p$  to  $5\ \text{MPa}$ . The only modified parameter is the trigger duration which is varied between  $1\ \text{ms}$  to  $2\ \text{ms}$  in steps of  $0.2\ \text{ms}$ .

The evolution of the flow profile is the same when the trigger duration is scanned (Figure 3-25). By increasing the trigger duration the maximum pressure drop varies quickly from  $-53 \times 10^2\ \text{Pa}$  until it reaches a maximum  $-60 \times 10^2\ \text{Pa}$ . After this an increase of the trigger duration only increases the duration of the period where the maximum pressure drop is constant *i.e.* the steady state condition for the flow is fulfilled.

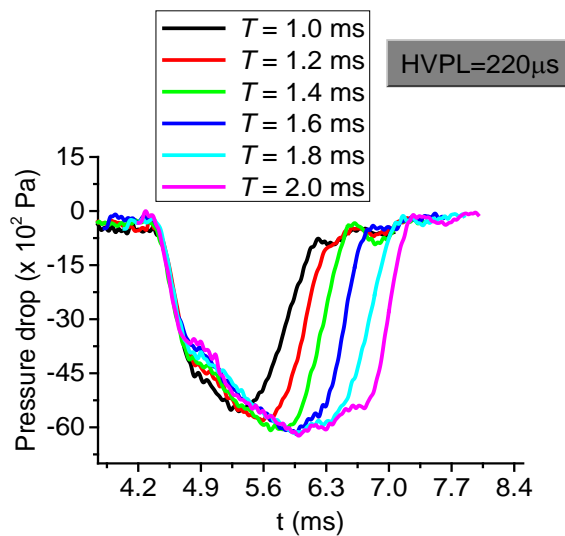


**Figure 3-25: Evolution of the pressure drop with the trigger duration  $T$  for stroke distance  $160\ \mu\text{m}$ , backing pressure  $2.1\ \text{MPa}$  and high voltage pulse duration of  $220\ \mu\text{s}$**

### 3.3.2.2 The influence of the high voltage pulse duration on the flow profile

For the same stroke distance of 160  $\mu\text{m}$ , pressure of 2.1 MPa and trigger pulse length of 2.0 ms, the high voltage pulse duration is changed from 180  $\mu\text{s}$  to 300  $\mu\text{s}$  with a step of 40  $\mu\text{s}$ . The influence of this on the flow profile is very small (Figure 3-27 and Figure 3-26), which is expected. The main effect of the high voltage pulse is to open the valve under particular conditions of pressure. When an optimum value is found, a further increase has small or negligible influence over the general performance of the valve. From testing it is seen that 220  $\mu\text{s}$  is the lowest value of the high voltage pulse duration where the valve performs optimally at a pressure of 5.0 MPa.

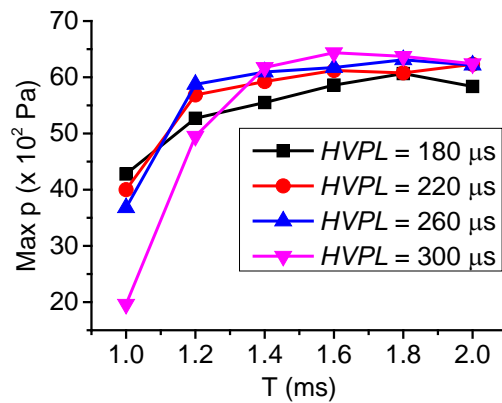


Figure 3-26: Maximum pressure drop with increase of the trigger pulse duration  $T$ . The high voltage pulse duration is changed from 180  $\mu\text{s}$  to 300  $\mu\text{s}$  with a step of 40  $\mu\text{s}$ .

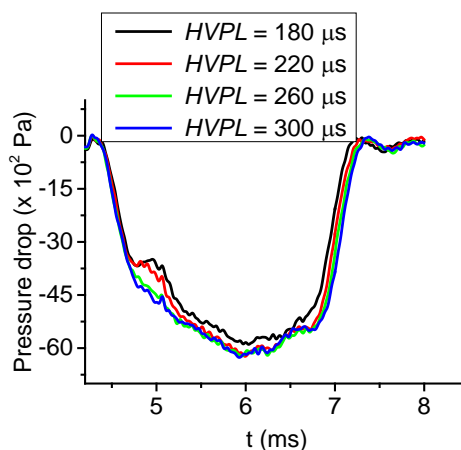
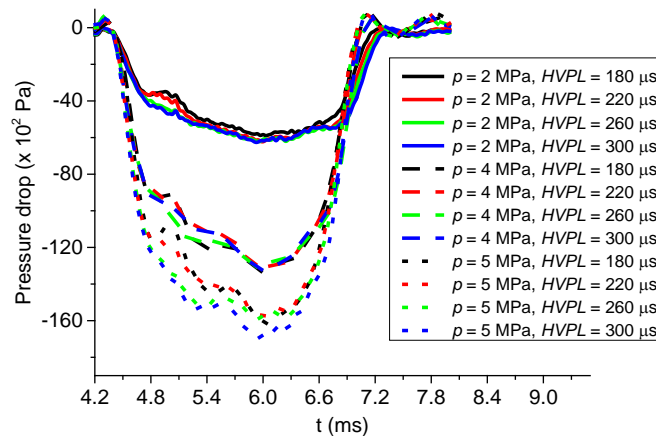


Figure 3-27: Evolution of the flow profile with the high voltage trigger window for stroke distance 160  $\mu\text{m}$ , backing pressure 2.1 MPa and trigger length 2 ms

### 3.3.2.3 Evolution of the flow profile with the backing pressure and stroke distance

As expected, the influence of the backing pressure over the flow profile is very pronounced. As shown in Figure 3-28, there is a strong relationship between backing pressure and maximum pressure drop. It is expected that the maximum pressure drop at a backing pressure of 5.0 MPa should be around 0.035 MPa thus it is straightforward to observe in Figure 3-28 that the valve underperforms by obstructing the flow.



*Figure 3-28: Evolution of pressure drop with backing pressure for 160  $\mu\text{m}$  stroke distance for four high voltage pulse durations: 180  $\mu\text{s}$ , 220  $\mu\text{s}$ , 260  $\mu\text{s}$  and 300  $\mu\text{s}$ . The trigger duration is 2.0 ms for all curves.*

Under the same conditions of backing pressure and trigger duration, the influence of the stroke distance is clear (Figure 3-29), the pressure drop increases as the stroke distance increases. For a stroke distance of 260  $\mu\text{m}$  it is observed that the measured pressure drop is very close to the predicted one thus it can be concluded that, for this value of stroke distance, the valve starts to perform as required by the requirements in terms of maximised flow rate.

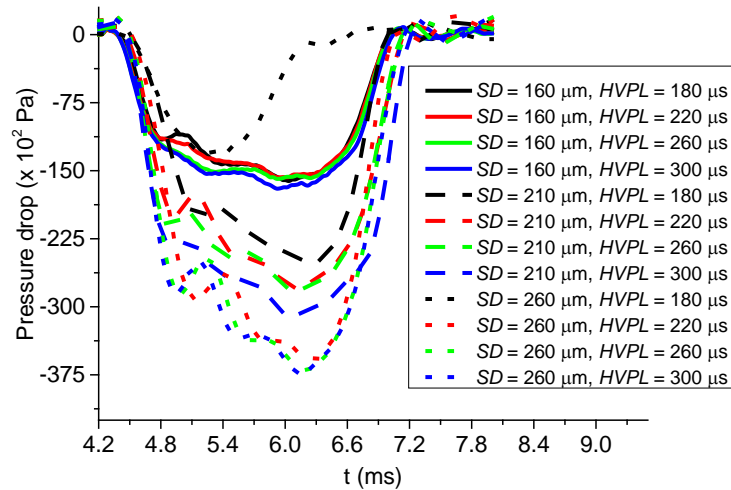


**Figure 3-29: Evolution of pressure drop with stroke distance (SD) under the same conditions of backing pressure  $p = 5$  MPa and trigger duration  $T = 2$  ms. For each stroke distance there are 4 curves for 4 different high voltage pulse durations: 180  $\mu$ s, 220  $\mu$ s, 260  $\mu$ s and 300  $\mu$ s.**

During the experiment an attempt to increase the stroke distance to more than 260  $\mu$ m was undertaken, but the valve started to underperform. This problem could only be solved by increasing the high voltage pulse duration to above 300  $\mu$ s. However, because the value is close to the safety limit given by the producer of the valve it was decided to use 260  $\mu$ m as the default value during laser-plasma wakefield acceleration experiments.

It should be stressed that the stroke distance is not constant in time; it increases as the internal parts, especially the poppet, wear out. Also, an optimised value of the stroke distance for a valve is not the same for all valves. Every valve is unique therefore great care must be taken to optimise each individually.

### **3.3.2.4 Comparison of an optimised valve with unchanged poppet, and a valve with an optimised poppet**

Following a recent article (Jung, 2007) the results from the optimised valve without changing the shape of the poppet have been compared with those from the valve with a modified poppet. The dimensions of the poppet (Figure 3-30a) have been measured and found to have tip length of 800  $\mu$ m. Approximately 350  $\mu$ m from the

poppet tip has been cut. Care has been taken so that the seal of the valve is not damaged. An image of the cut and original poppet is shown in Figure 3-30b.

From Figure 3-31 it can be seen that for short trigger durations (1 ms) the flow curve profile of the optimised valve lies between the curves for the valve with the cut poppet but without a large difference between them.

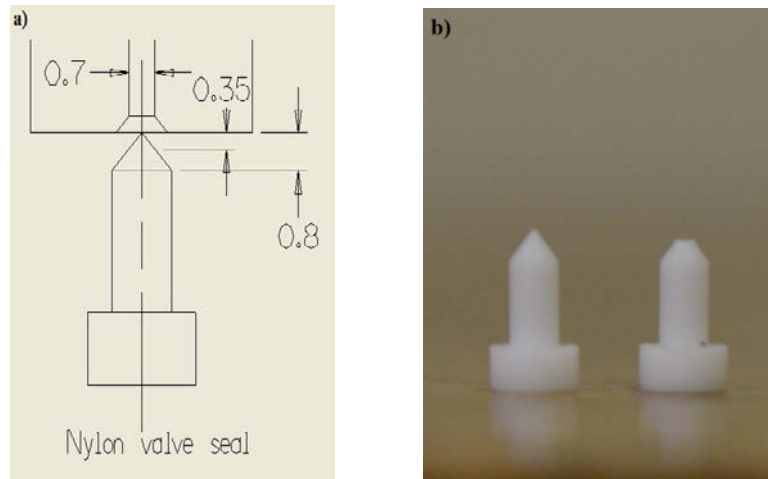


Figure 3-30: a) Sketch of the poppet and its dimensions, b) image of the cut and original poppets

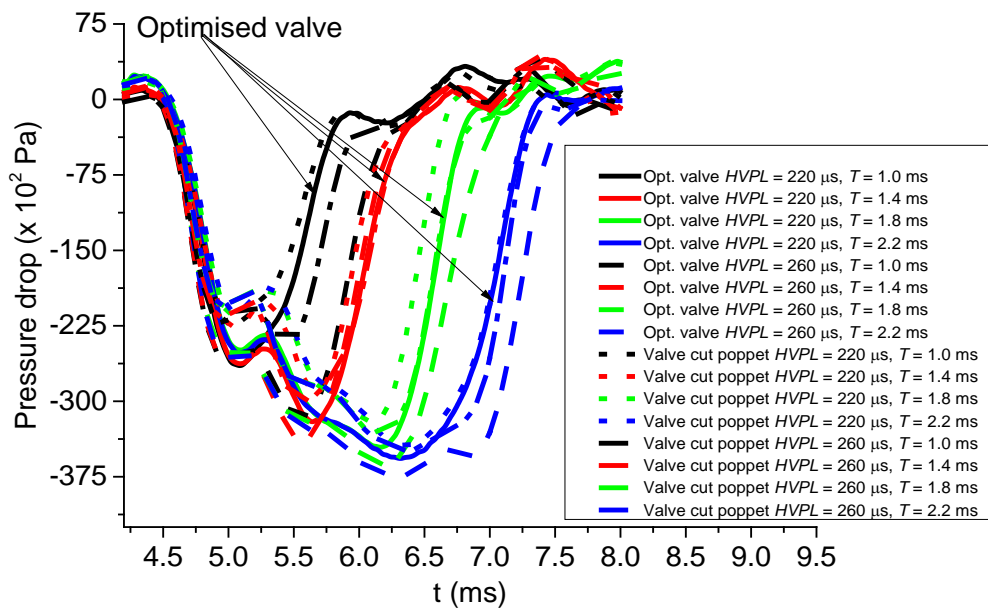


Figure 3-31: Comparison between the operation of the valve for the case where the poppet is cut by 350 µm (dotted and dash-dotted curves) and the poppet is unmodified (straight and dashed curves).

As the curves for optimised valve approaches the optimised parameters (HVPL = 220 µs and T = 1.8 ms) the flow profile curves for the valve with optimised poppet

( $HVPL = 260 \mu\text{s}$  and  $T = 1.8 \text{ ms}$ ) fits the curve corresponding to the valve with an unchanged poppet. This is proof that the same flow profile could be obtained by suitably shaping the poppet or adjusting the stroke distance of the valve and the high voltage pulse length.

### **3.4 Summary of the chapter and conclusions**

In this chapter a detailed description of the gas target used in the LWFA experiments is given. The gas target system consists of two main components: the Laval nozzle and the solenoid valve.

In Section 3.1 a theoretical description of the basic working principle of the Laval nozzles has been given. The gas reservoir and the Laval nozzle are assumed to be an adiabatic system therefore the flow of the gas through the system can be described using the laws of thermodynamics.

In Section 3.2 the Laval nozzle is modelled and simulated using the commercial software ANSYS Fluent 6.3. The main goal of the simulations is to obtain the gas jet density profile for different experimental conditions (different Laval nozzles, backing pressure, etc.). Also, the gas flow variation for different temperatures is simulated. It is found that as the temperature of the gas increases the gas jet density decreases due to increase in the gas velocity (which results in a decrease of gas flux).

Section 3.3 describes an interferometric method for measuring the gas jet density profile. It is observed that there is a systematic disagreement between simulations and interferometry results, although it is concluded that this will not affect the final conclusions since all the simulation results have the same trend. In this section, it is shown that different monatomic gases cannot be interchanged although the theory of ideal gases predicts that the flows are the same for monatomic gases. When the real properties of gases are taken into account the flows differ considerably even if the gases are all monatomic. If this is not taken into account the error in determining the gas density becomes significant.

Also, in this section a method of optimising the solenoid valve is given in detail. To monitor and optimise the flow through a solenoid valve a pressure transducer is attached upstream of the valve. Many LWFA experimentalists use the type of valve

described in this thesis, but not many of them are aware of the issues posed in experiments when it is not optimised. The results are compared with a different method of optimisation from another group, and it is concluded that the results coincide. Due to better control of the gas flow through the solenoid valve, the method here is recommended in combination with the “cut puppet” method. Thus, the maximum flow is obtained while the opening and closing time of the solenoid valve is reduced.

## 4 Experimental setup of LWFA for electron acceleration and diagnosis

The experimental setup used in LWFA experiments presented in this thesis is described in the following sections. First a basic description of the laser setup is given (Section 4.1), followed by gas target (4.2) and electron beam detection and characterisation setup (4.3).

### 4.1 Laser and laser beam transport system.

The 20 TW Ti:sapphire femtosecond laser system is based on the CPA technique and has central wavelength 800 nm, 10 Hz repetition rate and can deliver up to 0.8 J (after the compressor) in 36 fs. A schematic of the laser system is given in Figure 4-1.

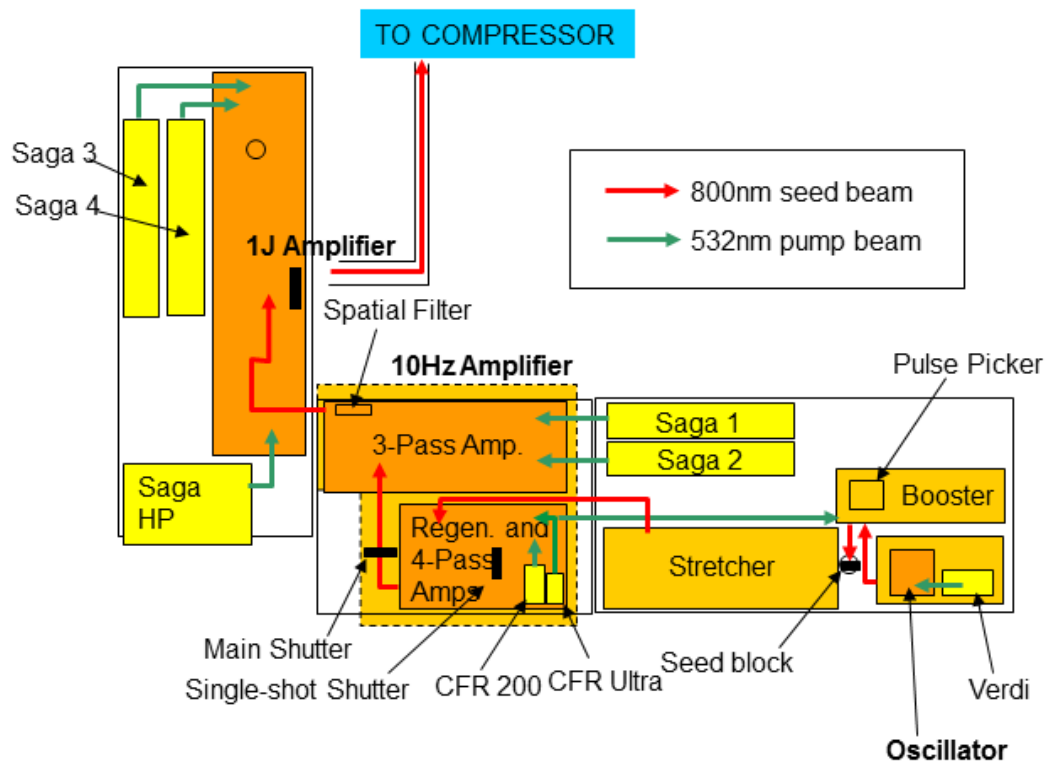


Figure 4-1: The Ti:sapphire laser system used in the LWFA experiments.

The front end of the laser system is a Ti:sapphire Kerr-lens mode locked oscillator (Verdi + Oscillator in Figure 4-1), which produces an 80 MHz train of short,

~ 16-20 fs, 9 nJ laser pulses with ~ 48 nm bandwidth centred around 800 nm. Immediately after the oscillator, a system consisting of a Pockels cell and a waveplate forms the Pulse Picker. Its role is to pick pulses from the 80 MHz train of laser pulses with a frequency of 10 Hz. The Pockels cells are voltage-controlled wave plates and are used to rotate the polarization of a beam that passes through them.

To amplify the laser pulses up to the Joule level a stretcher is employed. Due to the high peak power it is not possible to amplify the laser pulses directly, as the optics will be damaged. Therefore, to reduce the laser peak power the laser pulses are stretched using a single reflective grating and a pair of concave and convex mirrors. This method is the basis of the Chirped Pulse Amplification (CPA) technique. The laser pulses are negatively chirped from 20 fs to 250 ps in the stretcher.

After the stretcher an acousto-optic dispersive filter (Dazzler-Fastlite) ([www.fastlite.com](http://www.fastlite.com), 2015) (not shown in the figure) is used to modulate the laser beam. The Dazzler acts as a programmable, wavelength-dependent, diffractive element by launching an acoustic wave through an acousto-optic crystal, where the acoustic standing wave pattern creates a volume Bragg grating. The Dazzler is required mainly to compensate for gain narrowing. Each time the pulse passes through the Ti:sapphire crystal gain medium, the higher intensities of the spectrum are amplified more than the lower intensities of the spectrum “wings” resulting in a narrower spectrum. This effect is known as gain narrowing and leads to an increase in laser pulse length and subsequently to reduction in the achievable laser peak power.

After the Dazzler a system of three Pockels cells, two waveplates, a Ti:sapphire crystal, with 512 nm pump beams (CFR 200 and CFR Ultra in the Figure 4-1), forms the regenerative amplifier (Regen) and 4 Pass-preamplifier. In the Regen, laser pulses are amplified from nJ level to around 1 mJ and the ns pre-pulse (which represents practically the amplified spontaneous emission) are cleaned using the second Pockels cell (also called the pulse cleaner). The 1 mJ laser pulses are then passed to the preamplifier where, after a number of passes through the Ti:sapphire gain medium, are amplified to ~ 20 mJ.

The energy of the laser beam is further increased in a 3-pass amplifier (3-Pass Amp in the Figure 4-1) to ~ 300 mJ. The amplification is achieved by passing the laser beam three times through the gain medium and using two Saga Thales lasers (Saga 1

and Saga 2 in Figure 4-1) as pump beams with a combined energy of 1.1 J. To remove high order transverse modes a conical glass spatial filter is placed before the second stage amplifier.

The final amplification stage amplifies the laser beam up to  $\sim 1.5$  J using three 512 nm pump beams (Saga HP, Saga 3 and Saga 4 in Figure 4-1) with energy up to 4.5 J. Due to high thermal load (some of the pump laser energy heats the crystal), the crystal amplifier is cooled to 153 K using a cryogenic system. After amplification the laser beam diameter is expanded to  $\sim 4.4$  cm and transmitted to the compressor, where a pair of gold coated gratings compresses the laser pulses to  $\sim 36 \pm 2$  fs. An  $f/16$  spherical mirror is used in the experiments to focus the laser beam on the target down to a spot diameter of  $42 \pm 4$   $\mu\text{m}$  (measured at  $1/e^2$  of the intensity).

During the experiments great care is taken to maintain the quality of the laser beam as high as possible. Shot-to-shot stability of the laser pulse ensures a reproducible electron beam since parameters, such as laser energy, wavefront, intensity contrast, spot quality directly control the properties of the electron beam. For example Popp (Popp, et al., 2010) show that a tilt intensity wavefront (for wavefront tilting see Section 8.2) can change the pointing angle of the electron beam, while Bobbili (Bobbili, Juzer, Prasad, Mukund, & Parshotam, 2011) obtain an interesting experimental result which shows that the presence of a ns pedestal in the laser pulse is beneficial to the process of wakefield acceleration. Therefore, to quantify the experimental results, the laser stability is maintained not only over a day but also over the whole experimental campaign, that usually last 3-4 weeks. The presence of the ns pre-pulse is monitored using a fast detector placed after the 3 pass amplifier and the control of its level is achieved by changing the timing of the pulse cleaner Pockels cell.

During the alignment of the laser beam a correlation between pointing of the electron beam and the intensity wavefront tilting is observed. This correlation again affects the quality of the electron beam, a result which is experimentally shown by Popp (Popp, et al., 2010).

The laser spot size is periodically checked after the compressor (in vacuum or in air) using a 1 m focal length lens, a microscope objective and a CCD camera. An image of the laser spot can be seen in Figure 4-2. In general, a well aligned compressor is correlated with a symmetric laser spot.

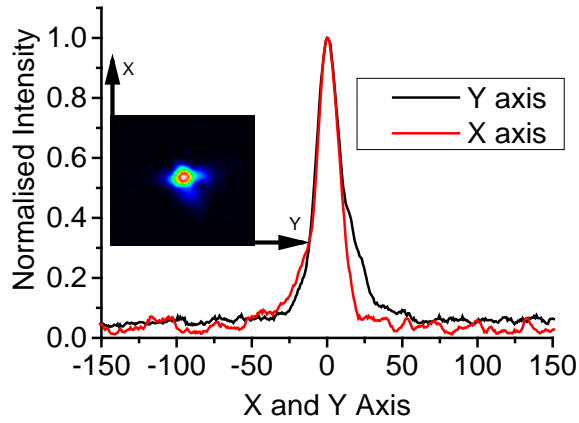


*Figure 4-2: An image of the laser spot (inset) after the compressor and the normalised intensity plots for X and Y axes. Correlation between spot shape/laser wavefront tilting and good quality electron beam requires symmetry in spot shape be as high as possible.*

During the alignment of the laser beam the gratings of the compressor are aligned until the most symmetric laser spot is obtained. The laser pulse length is simultaneously monitored, which is typically of the order of 35 - 36 fs.

Another laser parameter that must be carefully monitored is the laser intensity distribution in the spot profile. The presence of “hot” spots in the intensity profile can lead to laser filamentation (Hafz, et al., 2007), (Genoud, et al., 2013) and to an unstable electron beam due to limited laser energy in the FWHM of the spot (practically this is the energy that is directly involved in exciting the nonlinear plasma waves). The laser spot quality on target is checked in the interaction chamber, in vacuum, using a wedge to pick off the laser from the target chamber and a lens and a CCD camera. During the experimental campaign the laser spot waist diameter on the target is kept around  $42 \pm 4 \mu\text{m}$  with a slightly asymmetric shape.

## 4.2 Gas nozzle systems

All the experiments in this thesis have been carried out using a supersonic gas jet with helium gas. The supersonic gas jets are produced using Laval nozzles attached to a fast solenoid valve. The performance and initial optimisation of the solenoid valve have been carried out using a pressure transducer attached to the gas feed before the nozzle-valve assembly. A detailed description of the setup, valve optimisation steps and chosen nozzle geometries are given in Chapter 3. Other gas targets have been

explored by Salima Abu-Azoum and more details about her work can be found in the PhD thesis (Abu-Azoum, 2012) and also in the published article by Wiggins (Wiggins, et al., 2012) where discharge capillaries and tapered capillaries are presented in detail.

### 4.3 Electron beam diagnostic systems

A detailed schematics of the setup used for LWFA diagnosis is shown in the Figure 4-3.

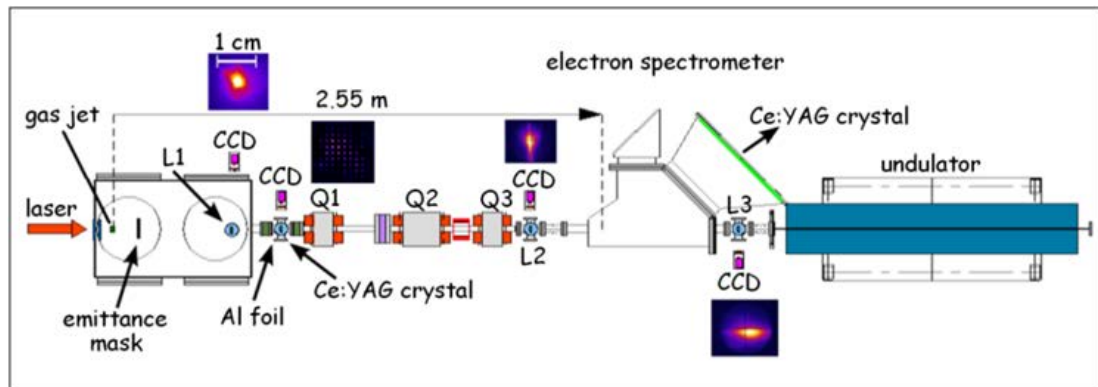


*Figure 4-3: Basic schematics of the LWFA setup after the compressor. It contains components for electron beam characterisation and different setups for applications (for instance an undulator).*

The gas target is placed in the main vacuum chamber at the focal plane of a spherical mirror with  $f = 0.71$  m. The gas target is imaged through a viewport in the target-chamber by a CCD camera with a macro lens and band-pass filter with centre wavelength at 400 nm. This has been used in the initial stage of the experiment to align the focal plane of the laser at the centre of the gas jet. The plasma channel formed in the gas jet is visible because of nonlinear Thomson scattering. This allows further correction of the alignment. A typical plasma channel from a LWFA is shown in Figure 4-4, where the total visible channel length is around 2 mm.

To visualise and diagnose the electron beam, a fluorescent screen (Kodak Lanex) is placed at 64 cm from the gas target and tilted at  $45^\circ$  relative to the horizontal beam line axis. The Lanex screen (L1) is covered by a  $50 \mu\text{m}$  aluminium foil to block the laser and electrons with energy below 300 keV. A CCD camera records shot-by-shot electron beam images from the Lanex screen with a calibrated pixel size of  $y = 30.7 \mu\text{m}$  (vertical) and  $x = 42.7 \mu\text{m}$  (horizontal). The difference in pixel size is due to

Lanex screen tilting relative to CCD vertical camera plane. The L1 screen is used to determine the divergence, pointing, pointing stability and relative charge of the electron beam.

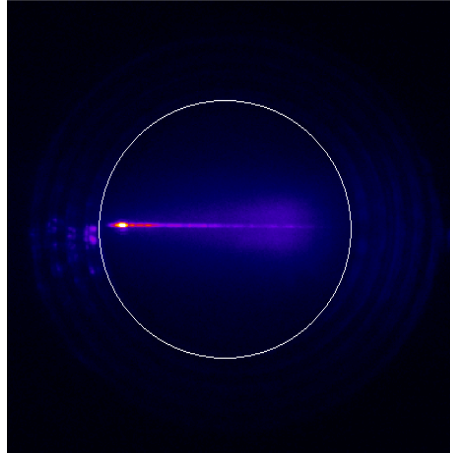


*Figure 4-4: A false colour image showing a typical plasma channel formed during the LWFA process. The laser travels from left to the right. The white circle marks the outlet of the nozzle and has 2.8 mm diameter.*

For each image recorded using L1, the centroid of the electron beam (defined here as the centre-of-mass of the intensity distribution), the root mean squared (r.m.s.) diameter of the electron beam and the total relative charge is calculated (by counting the number of photons recorded and knowing that is proportional to the number of incident electrons). Knowing the distance between the source of electrons and L1 ( $L = 64$  cm), the full divergence of the electron beam is determined using the formula:

$$\Theta = 2 \arctan \left( \frac{D_f - D_i}{2L} \right), \quad (4.1)$$

where  $\Theta$  is the full electron beam divergence,  $D_f$ ,  $D_i$  are the FWHM of the electron beam in initial position (source) and respectively in the final position (measurement location) and  $L$  is the distance between the electron source and measurement location. The source size is  $D_i \approx 5 \mu\text{m}$  and much smaller than the diameter of the electron beam on L1 (that is around 1 cm) therefore is neglected in calculations.

The electron beam generated from a LWFA in general does not have a simple Gaussian shaped structure but presents a distorted shape with a relatively large halo (see Figure 4-5a). The halo consists of low energy and high divergence electrons as shown by Manahan in her PhD thesis, (Manahan, 2013) and thus it is difficult to

collimate and transport for further characterisation and applications. This has an important consequence on the estimation of the size/divergence of the electron beam depending on the method/apparatus used in the setup for electron beam detection. A highly sensitive setup used for electron characterisation could give a relatively large beam size or divergence although the main beam core is much smaller.

Figure 4-5 shows two false images recorded on Lanex 1. Image a) is unprocessed and shows the main electron beam surrounded by a large halo of electrons with a r.m.s divergence of 42 mrad along the  $x$  axis and 23 mrad along the  $y$  axis. In picture b), the same image shown in a) is post-processed by subtracting the background so that the halo is minimised without affecting the main core of the electron beam. New measurements of the electron beam shows a divergence of 8.21 mrad along the  $x$  axis and 4.14 mrad along the  $y$  axis. Post-processing by subtracting the background also reduced the measured relative charge of electron beam by around 20 times compared with the charge extracted from the unprocessed Lanex1 images.

A more aggressive background subtraction can further reduce the influence of the electron beam halo but this is a subjective process therefore an absolute value of divergence cannot be obtained. In this thesis, unless otherwise specified, the halo corrected electron beam has been used in analysis. It has been assumed, without proof, that whatever error introduced by the presence of a small halo (as can be seen in Figure 4-5b) is negligible and thus will systematically overestimate or underestimate the final result in the same direction.

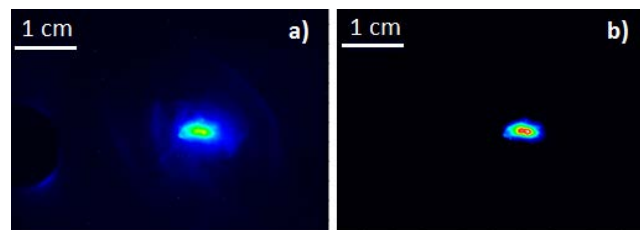


*Figure 4-5: False colour images recorded on Lanex 1 with a) halo + main electron beam and b) background subtracted in such a way that the halo visibility is decreased.*

The centroid of the electron beam image compared with the beam line centre gives the pointing (identified in this thesis as Ejection Angle  $EA$  and is measured in mrad) and its standard deviation, which determine the pointing stability (measured in mrad).

An electron beam is considered stable on L1 screen when the ejection angle is in the centre of the beam line (within  $\pm 5$  mrad), the full divergence is  $\leq 10$  mrad and the pointing stability permits a reasonable number of electron bunches to propagate close to the beam line axis so that they can be further analysed in the electron spectrometer. Figure 4-6 shows an accumulation of 300 images of the electron beam recorded on L1, where the centre is at  $x = 700$  px and  $y = 500$  px.

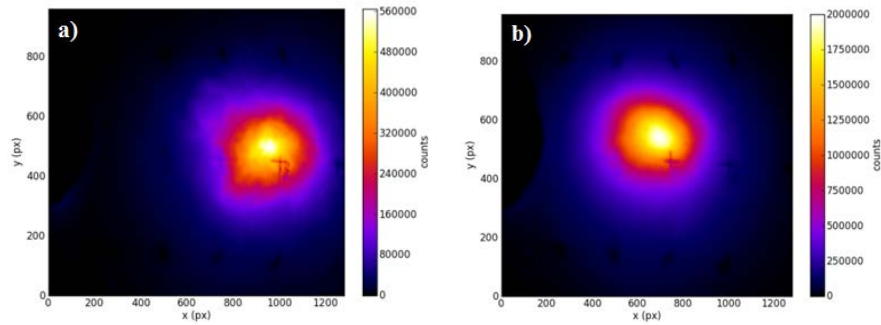


**Figure 4-6: Accumulated false colour images of the electron beam recorded on the L1 screen. The image a) shows the electron beam pointing to the right of the centre of the beam line. The image b) shows the electron beam pointing through the centre of the beam line. Further discussion on the electron beam pointing direction control is given in Chapter 6.**

The electron beam in the image on the left is not a “usable” beam due to the offset pointing direction. The image on the right shows an optimised electron beam that passes along the centre of the beam line.

Screen L1 could not be used to obtain a calibrated charge because it also detects a highly divergent electron beam (which forms a halo) and x-ray radiation. The charge calibration is carried out using a Fuji Film image plate (Sonoda, Takano, Miyahara, & Kato, 1983) that is placed in the electron beam path. The image plate consists of a photo-excitabile phosphor that stores incident electron energy in metastable colour centres (luminescence centres) that are proportional to the energy deposition per area. The energy loss in the image plates for electrons above 10 MeV is nearly constant (Glinec Y. , et al., 2006), therefore the deposited energy corresponds to the charge per unit area. The stored energy is read out by a Fuji scanner that employs a visible-wavelength laser (632.8 nm). The laser stimulates the emission of blue light; its intensity is proportional to the stored electron charge.

Through cross-correlation the fluorescent screens present in the LWFA setup are charge calibrated as explained further in this chapter. The halo of the electron beam

cannot propagate through the beam line (due to its high divergence and low energy) to the position where the image plate is installed therefore the measured charge is always smaller (by an unquantifiable amount) than the real one (the total charge generated by the LWFA process).

In addition to L1, a series of YAG:Ce screens (Ludziejewski, et al., 1997) with associated CCD cameras are mounted on pop-in stages to permit the alignment of the electron beam with the centre of the beam line. For example, a YAG:Ce screen placed before the electron spectrometer (espec) (Figure 4-7) is used to align the electron beam with its centre while a YAG:Ce screen placed after the spectrometer is used to align the electron beam with the undulator axis. The YAG:Ce crystal is a cerium doped yttrium-aluminium-garnet crystal that emits in the green when an electron beam or x-ray radiation is incident on it.

To diagnose the electron beam energy and energy spread, an electron spectrometer is installed after the gas jet at a distance  $\sim 2.56$  m. The layout of the “espec” is shown in Figure 4-7. The electro-magnets arranged at  $43^\circ$  relative to the beam line axis focus the electron beam vertically and three YAG:Ce screens ( $300 \text{ mm} \times 10 \text{ mm} \times 0.150 \text{ mm}$ ) are placed in the focal plane permitting energy measurements up to around 600 MeV.

Before the espec a series of dynamic electromagnetic quadrupoles (EMQs) are installed to transport the electron beams to the magnetic dipole electron spectrometer. The acceptance angle of the electron spectrometer is around 12.7 mrad, but for typical operation of the LWFA the pointing does not have a higher value than 2-3 mrad.

The energy and charge calibrated images of the YAG:Ce screens are recorded by a 14 bit CCD camera shot-by-shot. The energy calibration is carried out automatically during the recording taking into account the applied current to the espec. The charge calibration of the espec is carried out through cross-correlation using image plates: a number of electron beam shots (between 5 and 20) are recorded on a Fuji image plate and after that the same number of shots are recorded on espec; assuming that the total charge is equal then the espec can be calibrated as a function of the number of photons detected and the corresponding electric charge.

In addition to the peak energy and absolute charge, the espec also offers information on the electron beam energy spread. The data are deconvoluted by the

function representing the position-energy dependence for different current settings (known as the espec response function). It has been found, in a systematic analysis carried out by Manahan in her PhD thesis (Manahan, 2013), that the energy spread resolution of the espec is limited by the divergence and the absolute charge of the electron beam. For example, for an electron beam with an energy of 130 MeV, with an r.m.s. energy spread of 5%, r.m.s. divergence of 3 mrad, absolute 0.6 pC then the measured energy spread on the YAG:Ce screen is 6.8%, while increasing the r.m.s. divergence of the electron beam to 5 mrad and keeping the other parameters the same leads to a reading of energy spread on the YAG screen of up to 10.3%.

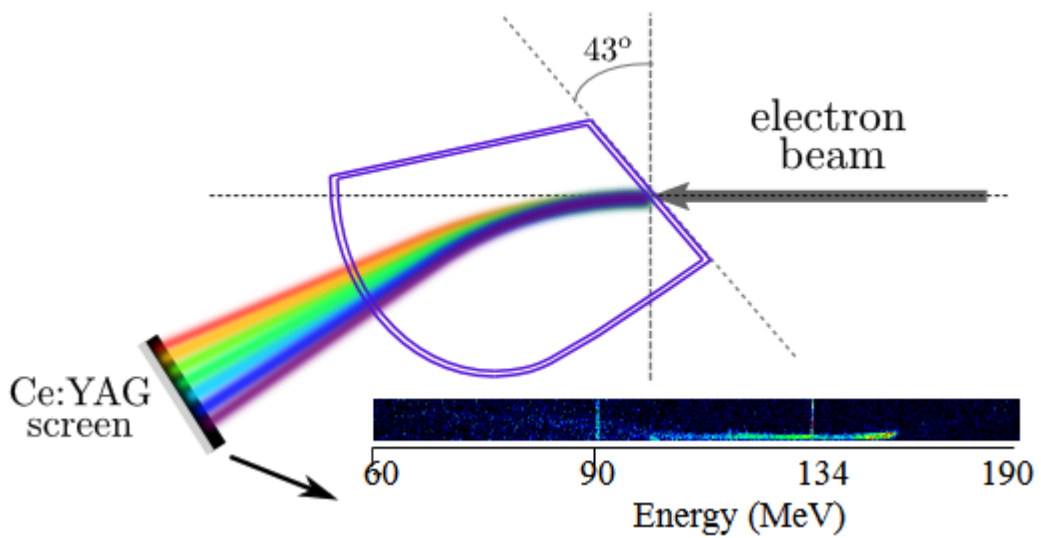


*Figure 4-7: Electron spectrometer layout with an example electron energy spectrum recorded (inset). Different colours correspond to different energies of the electrons forming the electron beam.*

For increased electron beam energy to 150 MeV (Figure 4-8), electron beams with 2 mrad divergence and with different charge and energy spread sent to the electron spectrometer, the resolution increases slightly but is still charge dependent.

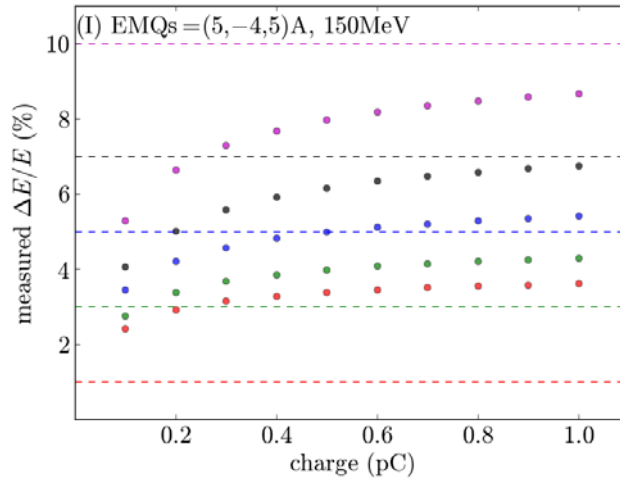


*Figure 4-8: Simulated energy spread vs charge. Predicted energy spread measurements for simulated electron spectra embedded with noise for a 2 mrad electron beam divergence and peak energy (at maximum fluence) of 150 MeV. EMQ currents are (5,-4, 5) respectively. The dotted lines indicate the theoretical/actual energy spread. Courtesy of Grace Manahan (Manahan, 2013)*

## 4.4 Experimental method

In all experiments the laser parameters have been kept the same: full energy on target  $E \approx 0.8$  J (0.5 J FWHM), spot waist on target  $w_0 \approx 21$   $\mu\text{m}$ , FWHM pulse length  $\tau = 36$  fs and horizontal polarisation. The only parameters varied are the gas jet ramp length, density profile and peak density and the laser focal plane position relative to the initial position established at the beginning of the experiment (zero position). It is worthwhile noticing that the laser focal plane position has been chosen to optimise the electron beam quality. The electron beam has been considered optimised when the charge is maximised (typical values in the main bunch around 0.7 pC), the pointing instability has the smallest values (typical less than 5 mrad variation) and shot-to-shot stability is as high as possible.

The direction of the propagation of the laser is considered in the negative  $z$  axis direction therefore, in this thesis, when the gas jet is moved in positive  $z$  direction this refers to the laser focal plane moving in the negative  $z$  direction. The vertical distance between the laser axis and the outlet of the gas nozzle is the *height* and it is increased by moving the gas nozzle in the negative  $y$  axis direction. The lateral movement of the gas nozzle along the  $x$  axis permits centring horizontally the laser and the centre of the gas jet (see Figure 4-9).

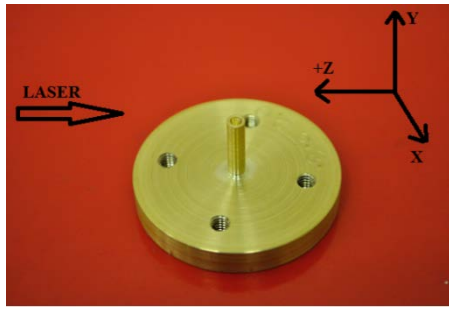


*Figure 4-9: An upper view of the nozzle axis configuration. The laser moves in the negative z axis direction and the distance between laser and the position of the outlet of the nozzle relative to the laser focal plane is varied by moving the nozzle in the negative y axis direction.*

For each experimental condition at least 200 electron density profiles are recorded using the fluorescent screen L1. The post-processing is carried out automatically using a program written by Enrico Brunetti (Brunetti, Private communication, 2012) and taking into account different calibrations (pixel size, photons per pixel, etc.). An equal number of images are recorded using the electron spectrometer. However, in this case, the images are analysed individually because of the complexity of the spectra recorded.

From the electron beam images recorded in the espec, the following information is extracted: the electron beam peak energy, r.m.s energy spread and absolute electron beam charge. From the energy spectrum only the single peak energy is chosen (Figure 4-10) to be quantified and used in data analysis. It is considered that the rest of the electron energy spectrum is the halo contribution. A detailed study of the halo contribution is not included in the present work since it requires dedicated research and experiments. Multi-energy peaks and continuous spectra are also discarded from the analysis.

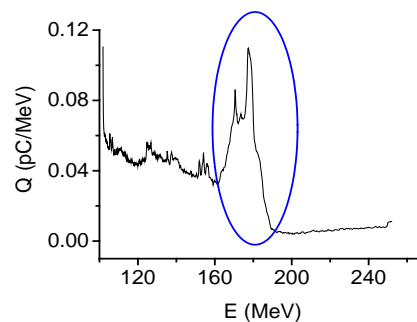


*Figure 4-10: An example electron energy spectrum obtained in the electron spectrometer. Only the marked part of the spectrum is used in data analysis.*

To prove the possibility of controlling the electron bunch velocity inside the bubble by shaping the longitudinal plasma profile experimentally, another degree of freedom has been added to the gas nozzle used in the experiments. This is achieved by mounting the gas nozzle on a tilting setup so that the angle between the laser and gas jet, at the interaction point, can be continuously varied (Figure 4-11). By changing the nozzle tilting angle the slope of the gas jet ramp can be varied, which changes the longitudinal shape of the plasma profile. During the LWFA experiments in longitudinally tailored plasma profile three different nozzles have been tested and their geometric parameters are given in Table 2.

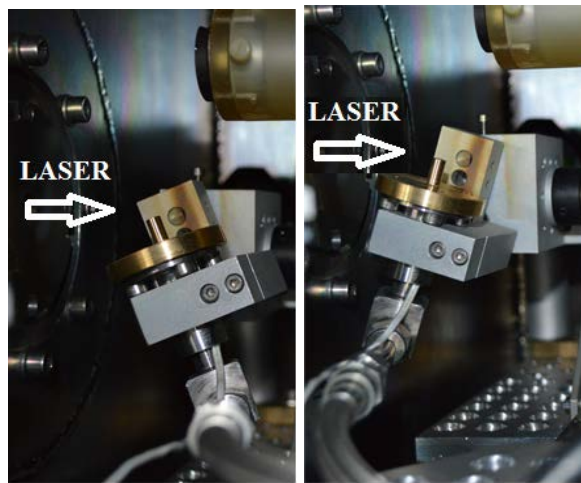


*Figure 4-11: Pictures of the gas nozzle on the tilt configuration setup. The angle between the direction of propagation of the laser and the normal to the nozzle outlet defines the tilting angle.*

In vertical configuration the laser axis is parallel with the surface of the nozzle outlet therefore the tilting angle is considered to be  $0^\circ$ . During the experiments the tilting angle is changed between  $0^\circ$  and a maximum of  $30^\circ$  in both directions (towards and away from the direction of laser propagation). The maximum tilting angle is dictated by available space constraints inside the vacuum chamber. In this thesis, when considering positive tilting, the nozzle is tilted in the direction of the propagation of the laser, and negative tilting when the nozzle is tilted opposite to the direction of propagation of the laser. Due to tilting of the nozzle, the centre of the nozzle moves in the direction of nozzle tilting in  $z$  direction, therefore the laser focal plane has been adjusted accordingly. Also, due to nozzle tilting the effective distance between the outlet of nozzle and laser focus is higher than the measured one and it has been taken into account when the density profiles are extracted from the CFD simulations.

## **5 LWFA experimental results with different plasma density profiles**

In this chapter the most important results of LWFA experiments mainly with vertical nozzles are presented. In Section 5.1 the influence of plasma density ramp on different parameters of the electron beam is investigated, followed in Section 5.2 by a discussion of the results involving the electron beam energy variation.

### **5.1 Influence of density ramp on electron beam properties**

In this section, the main LWFA results with a top-hat shape plasma density profile are presented. In Section 5.1.1 the quality of electrons from LWFA is analysed and quantified by taking into account the plasma density ramps in the leading edge of the top-hat shape. In Section 5.1.2 results from other research groups, available in the published literature, are analysed taking into account the influence of plasma density ramps. In Section 5.1.3 the angular distribution of the electron beam is analysed using different gas jet targets and taking into account the influence of the laser focal plane position inside the gas. The angular spread distribution and its centroid are analysed in Section 5.1.3.1, taking into account the asymmetry of the plasma channel and in Section 5.1.3.2 assuming a strong interaction between electron beam and plasma that can be present at the exit of the LWFA channel.

#### **5.1.1 Quality of the electron beam for plasma medium with density ramps**

The typical quasi-flat top plasma density profile with ramps (Figure 5-1) is widely used in LWFA experiments and is generated using de Laval nozzles.

During the LWFA experiments it is possible to increase the interaction length by varying the *height*  $y$  and/or using gas nozzles with different outlet diameters. However, when varying the interaction length by using any of the above mentioned methods, the density profile also varies, especially at the edge of the gas jet where the density ramps are located.

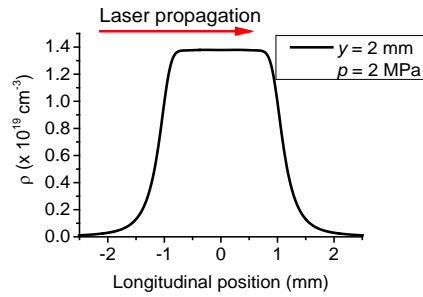


**Figure 5-1: Typical density profile used in LWFA experiments with supersonic gas jets as generated by Nozzle 511.**

Ignoring the changes in the plasma density profile by taking into account only the total interaction length or the flat top density profile part may lead to an incomplete interpretation of the results. For example, McGuffey (McGuffey, et al., Experimental laser wakefield acceleration scalings exceeding 100 TW, 2012) experimentally explored the influence of the interaction length on the quality of the electron beam using nozzles with different outlet diameters (Figure 5-2) but without accounting for the corresponding different density ramps.

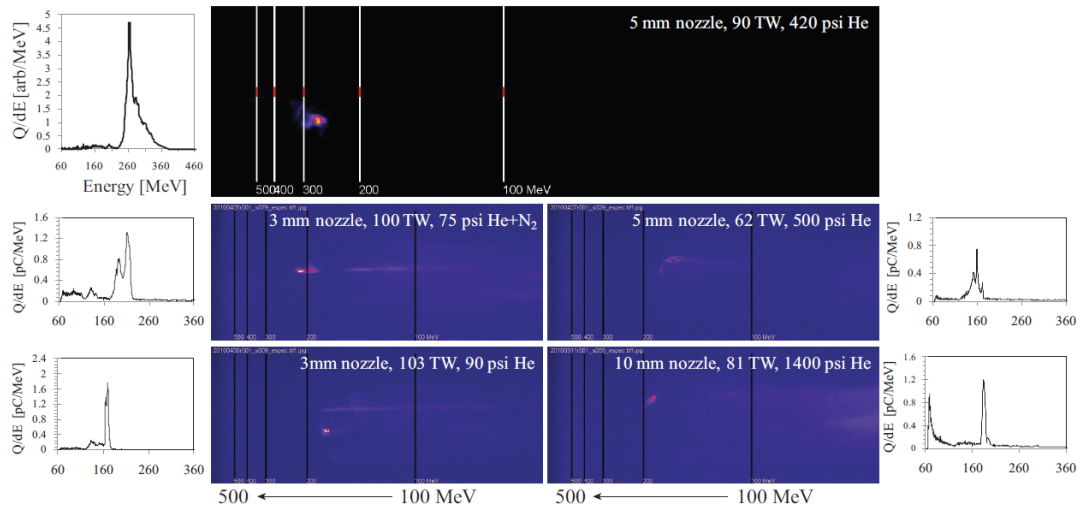


**Figure 5-2: Five example spectra of quasi-mono-energetic electron beams produced at various experimental conditions by McGuffey. (McGuffey, et al., Experimental laser wakefield acceleration scalings exceeding 100 TW, 2012)**

While there is a clear link between the interaction length and the quality of the electron beam (if the interaction length is shorter or longer than dephasing or depletion length), the two density ramps (at the beginning and at the end of the plasma channel) can also influence the quality of the electron beam. In the work presented here, several experiments to investigate the impact of density ramps on the performance of the

LWFA have been carried out. Here, the results obtained using Nozzles A, 510 and 511, which are described in Section 3.2.2, are reported. On average, a total of about 200 shots per run (a “run” is equivalent with a fixed experimental condition such as the laser parameters and the same plasma parameters) have been analysed for different plasma density profiles obtained by changing the height and adjusting the gas backing pressure until the most stable electron beam is obtained. As discussed in Section 4.3, in this thesis, electron beams are considered spatially stable when the propagation direction coincides with the beam line axis to within  $\pm 5$  mrad and the full divergence is less than 10 mrad.

The density profiles tested are shown in Figure 5-3 and have been obtained from CFD simulations.

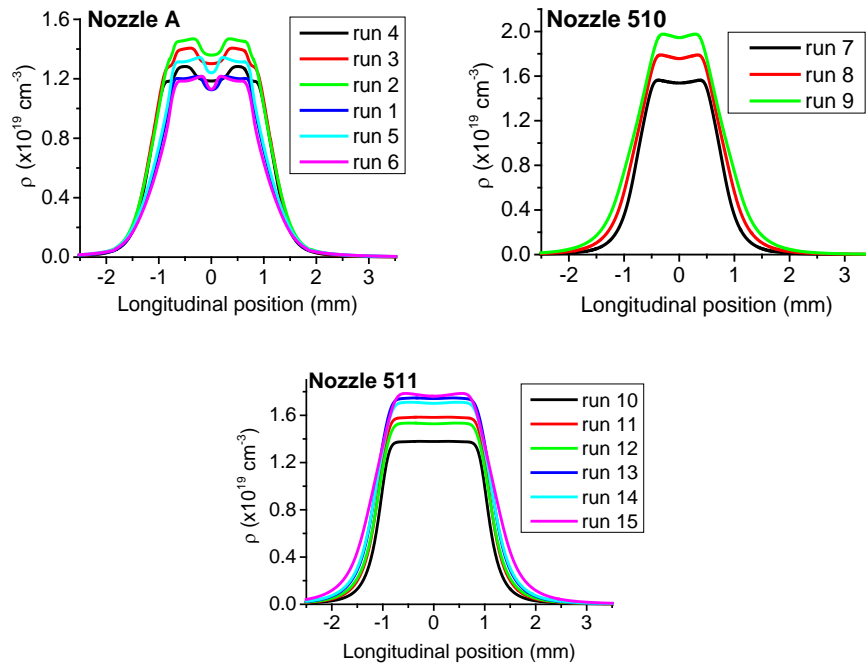


**Figure 5-3: Different density profiles used in experiments to test the influence of the density ramp on the quality of the electron beam. These density profiles correspond to conditions for stable electron beam formation by adjusting the backing pressure  $p$ , the height  $y$  and the laser focal point  $z$ .**

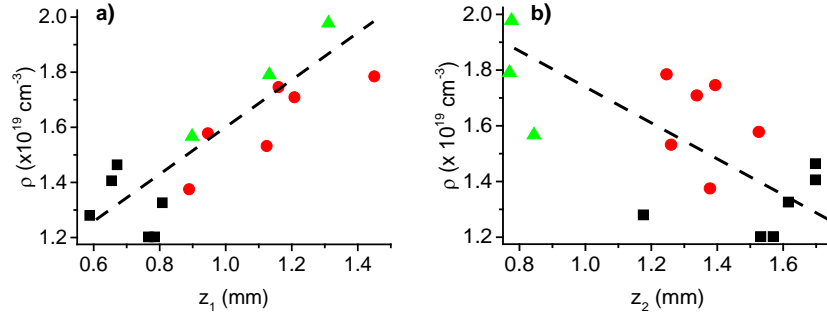
The relative position of the laser focal plane inside the gas jet, along the  $z$  axis, is changed slightly for each experimental run (see Table 6) to stabilise the electron beam (see Section 5.1.3 for further discussions on the influence of the laser focal plane inside the gas jet).

The first ramp  $z_1$  is arbitrarily chosen to start at a point where the condition for relativistic self-focusing is not met, in this case where the plasma density is  $1 \times 10^{18} \text{ cm}^{-3}$ , and extends to the point where the plasma density reaches 95% of its maximum. This location is considered as the beginning of the plateau  $z_2$ . The plateau  $z_2$  ends at a point where the maximum plasma density drops by 5%. The third ramp  $z_3$  is the reverse of  $z_1$  on the exit side. The sum of ramp lengths and the plateau length is defined as the total interaction length or gas length  $L$ . Parameter  $\rho$  is the peak plasma density in the plateau region.

Nozzle	run	$y$ (mm)	$z$ (mm)	$p$ (MPa)	$z_1$ (mm)	$z_2$ (mm)	$z_3$ (mm)	$L$ (mm)	$\rho$ ( $\times 10^{19} \text{ cm}^{-3}$ )
A	1	3.30	-0.25	3.7	0.766	1.532	0.766	3.064	1.202
A	2	2.65	0.25	3.7	0.671	1.698	0.671	3.040	1.464
A	3	2.20	0.50	3.0	0.654	1.698	0.654	3.006	1.406
A	4	1.95	1.20	2.5	0.588	1.176	0.588	2.352	1.280
A	5	3.74	0.16	4.7	0.808	1.616	0.808	3.232	1.326
A	6	4.15	-0.14	4.7	0.785	1.570	0.785	3.140	1.202
510	7	1.95	0.40	1.5	0.898	0.844	0.898	2.640	1.567
510	8	2.50	0.05	2.0	1.132	0.770	1.132	3.034	1.791
510	9	3.00	0.55	2.5	1.311	0.776	1.311	3.398	1.978
511	10	2.00	-0.15	2.0	0.889	1.378	0.889	3.156	1.375
511	11	2.40	0.65	2.5	0.946	1.526	0.946	3.414	1.578
511	12	2.70	0.75	2.5	1.124	1.260	1.124	3.508	1.532
511	13	2.90	0.45	3.0	1.160	1.394	1.160	3.714	1.746
511	14	3.10	0.65	3.0	1.208	1.338	1.208	3.754	1.709
511	15	3.90	0.85	3.5	1.450	1.246	1.450	4.146	1.785

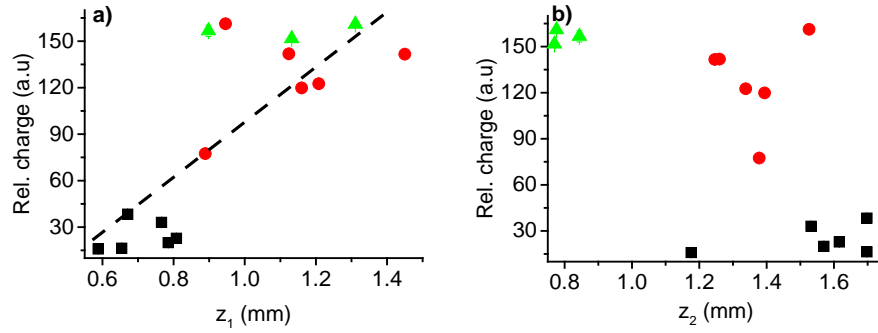
**Table 6: The experimental conditions when the influence of the plasma density ramp is experimentally investigated. The position of the laser focal plane  $z$  inside the gas jet is tuned by optimising the quality of the electron beam in terms of stability. In this experiment Nozzles A, 510, and 511 are used.**

Figure 5-4 shows the changes in the peak plasma density as a function of the ramp and plateau lengths for each density profile used in the experiments. The density is seen to increase linearly with ramp lengths. No trend is found with the plateau length for any of the nozzles (Figure 5-4b).



**Figure 5-4:** The evolution of plasma density, assuming full ionisation vs a) entrance ramp length, and b) vs. plateau length for the Nozzle A (black squares), Nozzle 510 (green triangles) and Nozzle 511 (red dots). The dashed line is drawn just to guide the eye.

The variation of the electron beam charge for each density profile of Nozzles A, 510, and 511 (Figure 5-3 and Table 6) are presented in Figure 5-5.



**Figure 5-5:** The relative charge recorded on Lanex1 vs entrance ramp length (a) and density plateau length (b). The vertical bars represent the standard error. The data is recorded with the Nozzle A (black squares), Nozzle 510 (green triangles) and Nozzle 511 (red dots). The dashed line is drawn just to guide the eye.

It can be seen that, for Nozzle A, when the ramp length is increased, the charge appears to increase suddenly around 0.675 mm and then decrease again for ramp lengths longer than 0.775 mm (Figure 5-5a). The same trend is observed for Nozzle 511, but in this case the maximum charge is obtained for an entrance ramp length of 0.946 mm. No conclusion is reached for Nozzle 510 because only 3 experimental points are present in the analysis. For different plateau lengths (Figure 5-5b), no direct dependence could be found between charge and plateau length.

This result can be explained by taking into account that the laser pulse evolves in an up-ramp density region due to non-linear effects such as relativistic self-focussing, laser pulse steepening and compression (see Section 2.2.2.1). Therefore, different plasma ramp parameters can lead to different laser pulse evolution (see

discussion in Section 5.2). As a consequence of the different evolution, the laser pulse can have different spot size, intensity, temporal length, etc. when it excites the nonlinear wakes. The bubble can therefore have different properties, which in turn can affect the amount of charge injected into the accelerating field.

When the relative charge is plotted as a function of the peak plasma density (Figure 5-6) one obtains a quasi-linear dependence, which is much more obvious if the data for all the nozzles is taken into account. This trend is expected since there is a linear dependence between plasma density and entrance ramp length (Figure 5-4a), thus these two plasma density profile parameters cannot be separated when the LWFA experimental data is analysed. Furthermore, as marked by the blue circle in the Figure 5-6, the same peak density can produce two different values of relative charge, an observation that can be attributed to the difference in ramp lengths (these two data points correspond to run1 and run6 in Table 6).

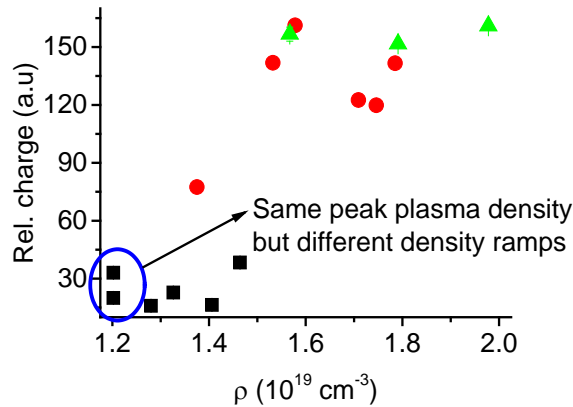


**Figure 5-6: The relative charge vs. peak density. It can be seen that for the same peak density, the relative charge is different; this difference is determined by the density ramp. The vertical bars represent the standard error. The data is recorded with the Nozzle A (black squares), Nozzle 510 (green triangles) and Nozzle 511 (red dots).**

Although from CFD simulations the two plasma profiles (magenta and navy curves corresponding to nozzle A in Figure 5-3) have the same peak plasma density, in experimental conditions it is possible that they differ but is not expected that the difference is significant. The only source of error is the backing pressure that must be set manually and has a reading error of  $\pm 0.25 \times 10^5$  Pa and the *height* that has an error of  $\pm 0.1 \mu\text{m}$ . From CFD simulations it has been observed that these errors, in pressure and in *height*, corresponds to a standard error in density around  $\pm 0.6\%$  for a backing pressure of 3.7 MPa and around  $\pm 0.53\%$  for a backing pressure of 4.7 MPa thus this

error cannot support the variation in the electron beam quality. Furthermore, LWFA simulations (not shown here) using the small variations in the plasma profile mentioned above have not shown any detectable effect on the electron beam (Tooley, 2014).

Therefore, it is reasonable to assume that plasma ramps play an important role in determining the electron beam quality, as argued further in this section.

Extending the data analysis to the electron beam peak energy, a controversial trend is observed: the energy of the electron beam increases as the plasma density is increased, and in some cases reaches a plateau and starts to decrease (Figure 5-7). Moreover, for similar values of plasma density the electron beam energy differs greatly depending on the type of nozzle used (see data circled in green in Figure 5-7).

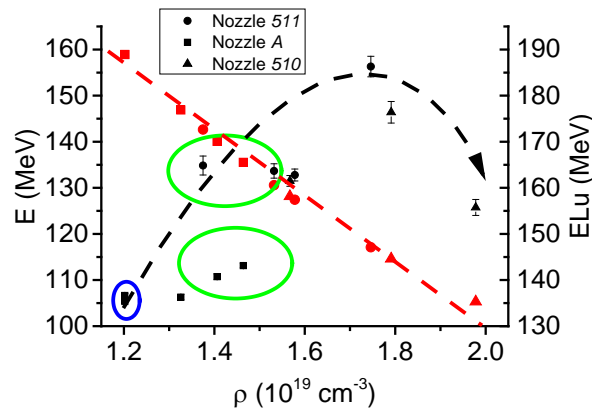


**Figure 5-7: Mean peak electron beam energy measured as a function of the maximum plasma density. This result seems to contradict the predicted trend (red points) if the density ramps are ignored in the data analysis. The vertical bars represent the standard error.**

It is known from LWFA theory that the electron energy decreases as the plasma density increases (Lu, et al., 2007), see for example Eq. (2.68) that is plotted in Figure 5-7 in red points, this result is confirmed by many experimental observations (McGuffey, et al., 2012), (Banarjee, et al., 2013). To explain the dependence observed here the influence of the plasma density ramp length must be taken into account, thus revealing why for the same peak plasma density two different electron beam energies (marked by a blue circle in Figure 5-7) can be obtained. The difference in energies is very small because the difference in plasma profiles is very small. This result confirms the reproducibility of the results and indicates that parameters other than the density, including the density ramp, are an important element in a LWFA.

To quantify the influence of the ramp on the electron beam energy, the plasma density ramp slope  $m$  is defined as the ratio between peak plasma density  $\rho$  and plasma ramp length  $z_1$ :

$$m = \frac{\rho \text{ [cm}^{-3}\text{]}}{z_1 \text{ [mm]}}. \quad (5.1)$$

The electron beam energy is represented as a function of the newly defined parameter  $m$  (Figure 5-8) and it is observed that the data points corresponding to different peak electron energy obtained at similar plasma density now correspond to different experimental conditions *i.e.* different density ramps (the data points circled with green ellipses in Figure 5-8). This confirms again that the parameters of an electron beam generated through LWFA in a gas jet depend on the parameters of the flat top region and on the ramp density region. In the majority of the experimental studies published in the literature, so far, only the homogenous part of the gas jet has been taken into analysis.

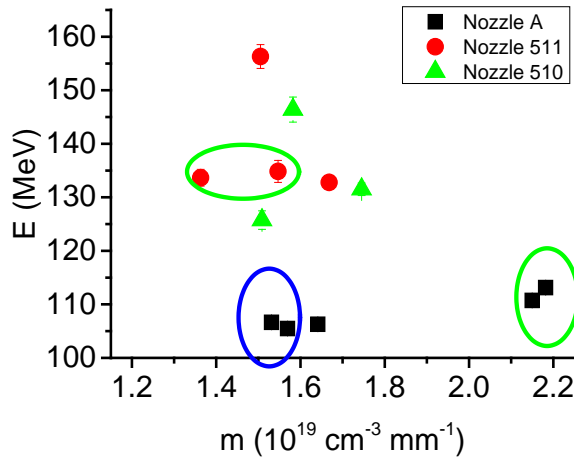


**Figure 5-8: Electron beam energy as a function of the plasma density ramp slope. The two results corresponding to two different electron beam energies at the same plasma density make sense when taking into account the ramp slope (the 2 points marked by a blue circle). The vertical bars represent the standard error.**

The influence of the plasma density ramps on the energy and energy spread of laser driven electron beams is discussed in 6 in the context of the phase-locking mechanism (Katsouleas, 1986), (Rittershofer, Schroeder, Esaray, Gruner, & Leemans, 2010), (Wen, et al., 2010). This is a mechanism that can operate in the presence of an upward density profile and consists of locking the phase of the electron bunch inside

the bubble so that it cannot advance, as it propagates, towards the second half of the bubble, where it would experience deceleration and therefore a decrease in the maximum attainable energy and an increase in energy spread as explained in Chapter 6. The phase locking mechanism can explain the results for Nozzles A (black squares) and 511 (black dots) marked with green ellipses in Figure 5-7 where, for the same range of plasma densities the electron energy ( $\approx 112$  MeV for Nozzle A and  $\approx 135$  MeV for Nozzle 511) greatly differs due to difference in ramp lengths (and subsequently different plasma density slopes).

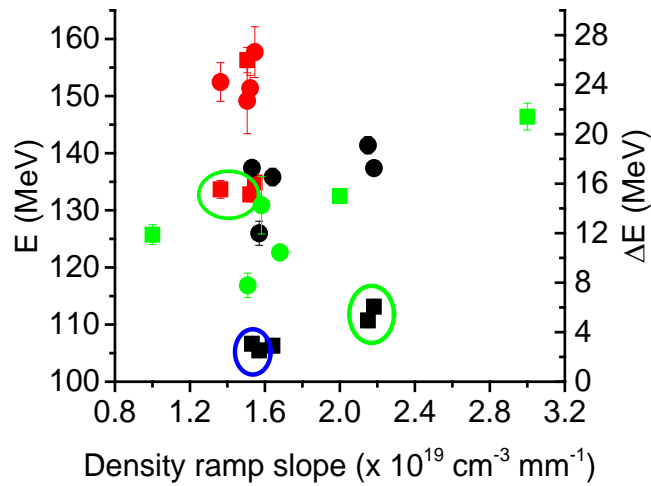


*Figure 5-9: Electron beam energy (square data points) and absolute energy spread (round data points) as a function of the plasma density ramp slope. Black, green and red data points are obtained with the Nozzle A, B, and C, respectively.*

The plasma profile is considered positively tapered because the leading plasma up-ramp interacts first with the laser. Although there is a positively tapered plasma density, no significant increase in energy is observed for Nozzle A and the energy spread is not enhanced compared with the results shown for Nozzle 510 and 511 (Figure 5-8 and Figure 5-9). This is because the length of the density ramp for Nozzle A may be too short (see in Table 6 the change in mean  $z_1$  from  $0.71 \pm 0.08$  mm for nozzle A to  $1.11 \pm 0.2$  mm for nozzle 510 and  $1.13 \pm 0.2$  mm 511) for the electron to experience the benefit of phase-locking before entering the homogenous plasma profile. Therefore, an alternative explanation for the results is proposed in Section 5.2.

## 5.1.2 Electron beam charge control

It has been shown in the previous section that the leading ramp of the laser interacting with the plasma density profile can control some of the properties of the generated electron beam. During LWFA experiments, changes in plasma density ramp are often not monitored when other parameters are changed. Figure 5-10 reports results of a LWFA experiment published by McGuffey (McGuffey, et al., Experimental laser wakefield acceleration scalings exceeding 100 TW, 2012) showing the dependency of electron beam charge with plasma density and the presence of an optimum plasma density which maximises the charge. The average laser power on target in these experiments is 84 TW and the pulse length is 35 fs and with a central wavelength at 810 nm. The laser is focused to a FWHM size of 12  $\mu\text{m}$  giving an initial normalised vector potential of  $a_0 = 2.93$ . A gas jet is used as a target and its density is varied from  $7.25 \times 10^{18} \text{ cm}^{-3}$  to  $1.40 \times 10^{19} \text{ cm}^{-3}$  at 1 mm above the nozzle outlet by changing the backing pressure up to 10 MPa. The shape of the gas density profile is considered top-hat, sharp vacuum-gas jet interface and an unspecified ramp length. The position of the laser focal plane inside the gas jet is fixed 1 mm above the gas nozzle outlet for the entire experiment. The accuracy and trend of the results shown in Figure 5-10 cannot be denied, but there is a possible explanation that take into account parameters other than the plasma density and interaction length, in contrast to McGuffey's interpretation.

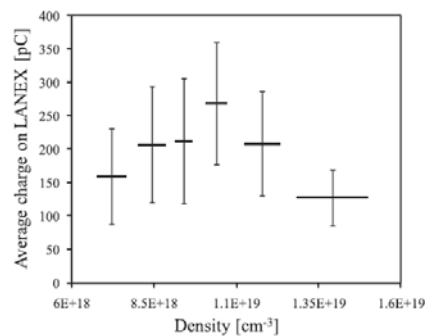


*Figure 5-10: The charge vs. plasma density according to McGuffey et al. (McGuffey, et al., Experimental laser wakefield acceleration scalings exceeding 100 TW, 2012)*

McGuffey (McGuffey, et al., 2012) does not take into account the increase of the density ramp parameters (such as ramp length and ramp slope) with the plasma

density. To fully understand Figure 5-10, the ramp parameters also need to be taken into account.

To investigate the effect of the density ramp length, a LWFA experiment has been designed to keep the laser focal plane at the same height  $y$  (1.5 mm above the nozzle in this case) and  $z$  position, relative to the gas nozzle outlet, while the plasma density is continuously increased from  $4.27 \times 10^{19} \text{ cm}^{-3}$  to  $5.64 \times 10^{19} \text{ cm}^{-3}$  by increasing the backing pressure from 2.6 MPa to 3.4 MPa. It must be stressed that the range of plasma densities used in this experiment is not the same as that of McGuffey's due to differences in laser parameters. Here, the laser power on target is around 20 TW with a spot diameter of  $42 \mu\text{m}$  at  $1/e^2$ , these values giving a normalised vector potential  $a_0 = 1$  for the vacuum focus.

The goal here is to show that the same trend shown by McGuffey can be obtained using very different experimental conditions and the conclusions must, for completeness, take into account not only the plasma density but also the ramp parameters. The gas jets for this experiment have been produced using nozzle 508 (see Table 2) and the experimental conditions are summarised in Table 7.

run	$y$ (mm)	$p$ (MPa)	$z_1$ (mm)	$z_2$ (mm)	$z_3$ (mm)	$L$ (mm)	$\rho$ ( $\times 10^{19} \text{ cm}^{-3}$ )
1	1.5	2.8	2.711	1.090	2.711	3.801	4.597
2	1.5	3.0	2.784	1.101	2.784	3.885	4.984
3	1.5	3.2	2.879	1.109	2.879	3.988	5.264
4	1.5	3.4	2.907	1.117	2.907	4.024	5.639
5	1.5	2.6	2.653	1.079	2.653	3.732	4.270

**Table 7: The parameters used in the experiment designed to replicate McGuffey's experiment. Nozzle 508 is used and the laser focal plane is fixed for the entire experiment at relative position  $z = -5.25 \text{ mm}$ .**

Under these experimental conditions each time the plasma density is increased, as with McGuffey's experiment, the density profile ramp length is also increased from 2.65 mm to 2.9 mm (Figure 5-11a). The evolution of the charge of the electron beam as a function of the plasma density is shown in Figure 5-11b where the relative charge increases from  $\sim 16.75$  [a.u.] (plasma density  $\sim 4.26 \times 10^{19} \text{ cm}^{-3}$ ) to a maximum of  $\sim 27$  [a.u.] (for a plasma density of  $\sim 4.98 \times 10^{19} \text{ cm}^{-3}$ ) and then decreases to  $\sim 21$  [a.u.] (for a plasma density of  $\sim 5.64 \times 10^{19} \text{ cm}^{-3}$ ). This shows that the trend obtained by McGuffey et al (Figure 5-10) is also obtained in our experiment.

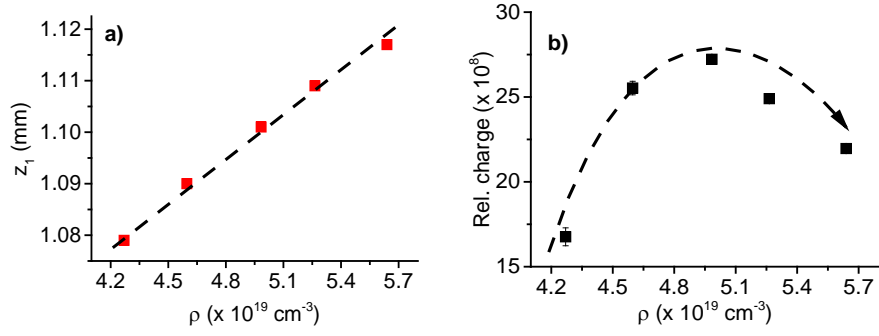


**Figure 5-11: The entrance ramp length (a) and relative charge (b) versus plasma density in the experiment designed to replicate the trend observed in McGuffey’s experiment. The vertical bars represent the standard error. The gas jet is generated by Nozzle 508. The dashed line is drawn just to guide the eye.**

As shown in the previous sections and also presented in an article by Ciocarlan, Aniculaesei *et al.* (Ciocarlan, et al., 2013), the presence of a plasma density ramp before the homogenous part of the density profile has a significant impact on the evolution of self-focussing of the laser pulse (Figure 5-12). The laser pulse that excites the nonlinear wakes can have therefore different parameters depending on the density ramp parameters (such as length and slope).

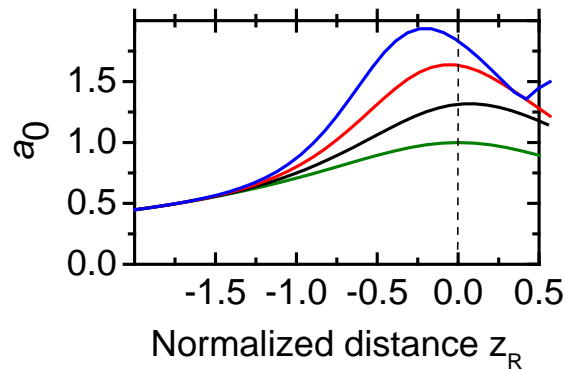


**Figure 5-12: Numerical simulation results showing the laser pulse  $a_0$  evolution in the plasma ramp region as a function of the longitudinal distance normalized to the Rayleigh length (negative axis up to zero position). Maximum plasma density values are  $\rho_1 = 1.54 \times 10^{18} \text{ cm}^{-3}$  (black curve),  $\rho_2 = 2.75 \times 10^{18} \text{ cm}^{-3}$  (red curve) and  $\rho_3 = 3.49 \times 10^{18} \text{ cm}^{-3}$  (blue curve) and  $\rho_0 = 0$  (green curve) (Ciocarlan, et al., 2013).**

It can be concluded that in the LWFA process, one cannot ignore the importance of the region of plasma (density ramp in the case of gas jets or plasma plume in the case of capillaries or gas cells) that can exist before the homogeneous plasma region. The existence of such a region changes the evolution of the laser pulse

due to relativistic self-focussing in addition to the impact on the electron acceleration dynamic. In these conditions, when the laser pulse enters the constant plasma density region it consequently determines important changes in the electron beam generated by the LWFA. For further discussion see Section 5.2.1.

### **5.1.3 Angular distribution of the electrons and influence of the laser focal plane position inside the gas jet**

As mentioned in the previous sections, for normal operation of the LWFA, the focal plane of the laser inside the gas jet is optimised during the experiments for the best pointing and the most stable electron beams. It is assumed by many authors that, in general, the laser focal plane is situated at the beginning of the density ramp of a gas jet. For a supersonic gas jet in vacuum it is difficult to establish exactly where “the beginning” is because there is no step-like function to describe the density boundary. Ideally, the atoms/molecules from the gas jet should have only axial velocity thus forming a collimated gas jet. In reality, no matter how well the gas nozzle is designed there will always be a fraction of atoms with a radial velocity distribution that forms a background of low pressure gas. Thus, in general, the gas jet ramps are described by a density function with an initial density different than zero therefore the “beginning” and the “end” of the density profile is a matter of choice. Also, in general, there is no justification why the laser focal plane should be at the “beginning” of the density profile.

For the majority of the data analysed for this thesis the variation of the electron beam charge as a function of the laser focal plane  $z$  inside the gas jet shows the same trend, exemplified in Figure 5-14a, which shows data recorded using Nozzle A (parameters given in Table 8 and plasma density profile in Figure 5-13).

For instance, in Figure 5-14 when  $z$  is close to the edge of the gas jet,  $z = 1.4$  mm, the charge is low and increases as  $z$  moves toward the centre of the gas jet reaching a maximum (at  $z = 1.7$  mm) and starts to decrease as  $z$  moves farther away from the edge. The maximum charge is not reached when  $z$  is in the centre of the gas jet but when it is situated inside the ramp of the gas jet. In this example the ramp length is around 0.9 mm. Assuming that the ramp starts at  $z = 1.4$  mm then a variation of 0.3

mm is required to reach the maximum charge, which places the laser focal plane deep inside the ramp, approximately 1/3 of its total length.

run	y (mm)	z (mm)	p (MPa)	z <sub>1</sub> (mm)	z <sub>2</sub> (mm)	z <sub>3</sub> (mm)	L (mm)	ρ (× 10 <sup>19</sup> cm <sup>-3</sup> )
1	2.95	1.40	3.5	0.843	1.226	0.843	2.912	1.274
2	2.95	1.50	3.5	0.843	1.226	0.843	2.912	1.274
3	2.95	1.60	3.5	0.843	1.226	0.843	2.912	1.274
4	2.95	1.70	3.5	0.843	1.226	0.843	2.912	1.274
5	2.95	1.80	3.5	0.843	1.226	0.843	2.912	1.274
6	2.95	1.90	3.5	0.843	1.226	0.843	2.912	1.274
7	2.95	2.00	3.5	0.843	1.226	0.843	2.912	1.274

**Table 8: Nozzle A's gas jet parameters in LWFA experiment where z been varied inside the gas jet from 1.2 mm to 1.5 mm.**

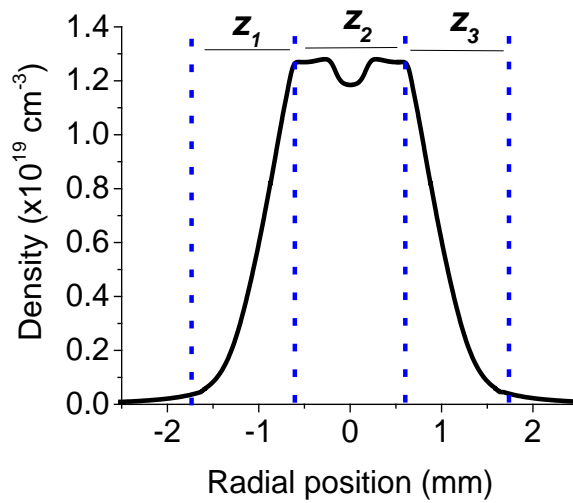


**Figure 5-13: Plasma density profile at y = 2.95 mm above the Nozzle A. The backing pressure is 3.5 MPa.**

The same trend as the charge is seen in electron beam pointing: Figure 5-14b shows how the vertical Ejection Angle  $EA_y$  moves from -5.6 mrad to a position closer to the beam line axis as the laser focal plane moves from  $z = 1.4$  mm (which corresponds to a relative position inside the gas jet) toward  $z = 2$  mm (which is placed in the vicinity of the gas jet). The same trend is apparent in the horizontal Ejection Angle  $EA_x$  but usually the variation in pointing is not as significant as  $EA_y$ .

Taking into account the pointing stability in terms of standard deviation (Figure 5-14c) it can be concluded that there are no absolute values of the laser and plasma parameters for which all the electron beam parameters are optimum. Here, for the highest charge the pointing is reasonably close to the centre, within  $\pm 5$  mrad as

required by the electron beam transport system, and the pointing stability is considered acceptable.

The trend in electron beam pointing observed is difficult to explain if it is assumed that the electron beam motion is controlled only in the laser polarisation direction by betatron resonance (Mangles, et al., 2006), (Cipiccia, et al., 2011). Many results prepared for this thesis showed a pointing offset, mainly along the y axis (perpendicular on the laser polarisation direction) which is present independent of the parameters of the plasma density profile.

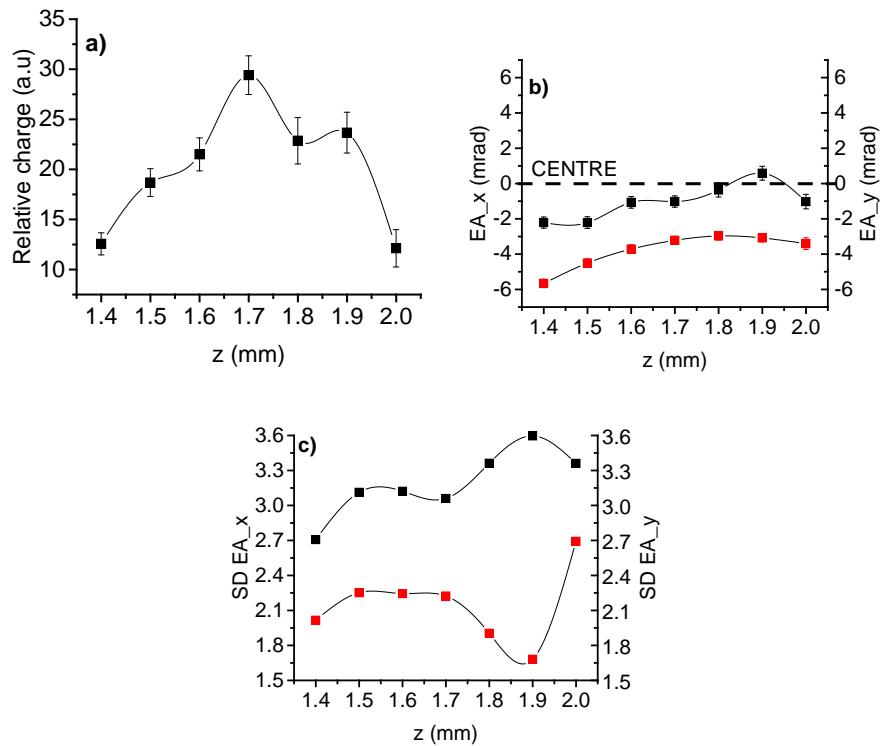


**Figure 5-14:** a) The relative charge evolution, b) the electron beam pointing and c) the pointing stability as a function of the laser focal plane inside the gas jet. The vertical bars represent the standard error.

One could argue that a “plasma lens effect” deflects the laser slightly as it propagates (Jaroszynski, 2013), and therefore affects the direction of the LWFA channel. In this case there should be a relationship between the plasma density and electron pointing a result that systematically cannot be confirmed here, as shown in Figure 5-15 for a random chosen data set. Thus no obvious evidence for laser deflection is, within experimental error, observable.

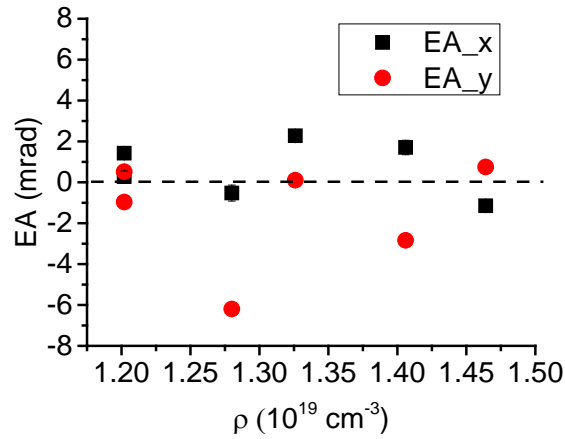


*Figure 5-15: The Ejection Angle EA on both x and y axes as a function of the peak plasma density. The vertical bars represent the standard error. The gas jet is generated by nozzle A.*

Also, images of the plasma channel show no obvious deviation (Figure 5-16) supporting the hypothesis that the electron beam deviation is not due to laser beam deviation. In Figure 5-16 the total plasma channel length visible is around 3 mm and the images have been extracted from a set of data obtained in the same experimental conditions. Assuming that the laser beam is deviated at the beginning of the channel then, when it exits the gas jet, it should have a deviation of  $28.8 \mu\text{m}$ . Taking into account the magnification of optical system, this deviation corresponds to 3 pixels deviation on the image. A cross-section taken close to the end of the visible plasma channel showed no deviation of the plasma channel (see the graph in Figure 5-16).

Chen (Chen , et al., 2007) reported an observation on laser beam deviation and seen in simulations, where the most energetic electrons accelerated by the wakefield can overtake the laser pulse and modify locally the refractive index of the plasma. The change in plasma properties is anisotropic (Naumova, Bulanov, Nishihara, Esirkepov, & Pegoraro, 2002) therefore the laser beam deviates from the normal direction (Figure 5-17). When the electron beam overtakes the back of the laser pulse, it is expected that the dephasing length is reached and passed therefore the energy and energy spread are affected. Also, the interaction with the laser pulse leads to further change in the electron beam parameters. None of these effects have been seen in experiments here (Figure 5-16) therefore the conclusions drawn by Chen cannot be applied to the present results.

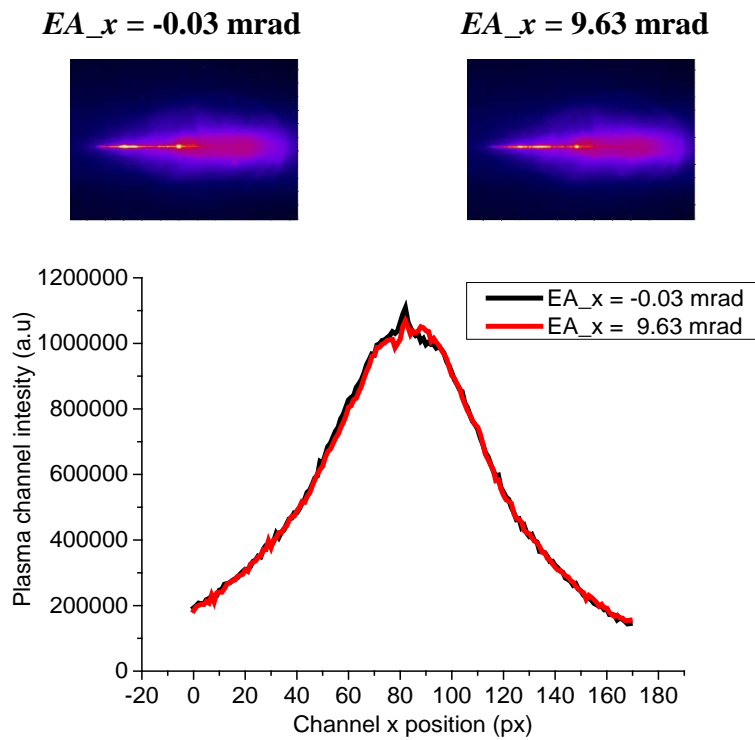


*Figure 5-16: Two false colour pictures of the plasma channel taken during experiments. The left plasma channel produced an electron beam with  $EA_x = -0.03$  mrad (almost no deviation) and the right channel produced an electron beam with  $EA_x = 9.63$  mrad (strong deviation). In both cases no deviation of the plasma channel can be observed (bottom). The laser is propagating from left to right in the figures.*

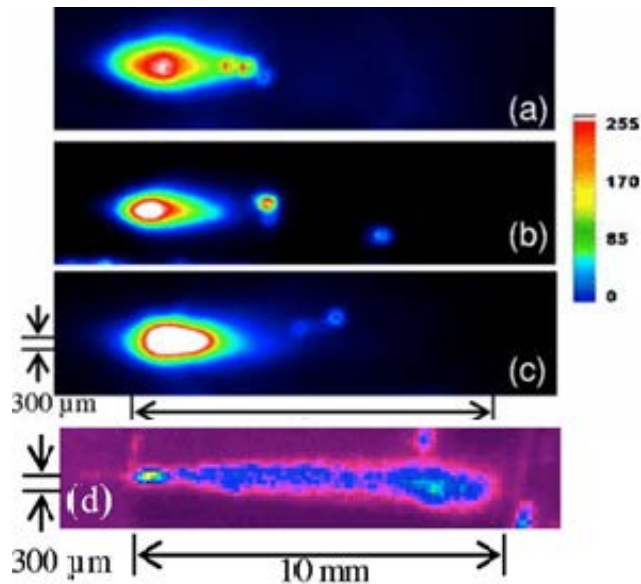


*Figure 5-17: The side-view plasma imaging in the experiment described by Chen et al. (Chen, et al., 2007) when the laser energy is 2.5 J and plasma density  $5 \times 10^{18} \text{ cm}^{-3}$  for different shots (a,b,c). d) represents the Thomson scattering measurement corresponding to image b). The laser deviation is clearly seen, a result that cannot be confirmed in experiments here.*

It can be concluded that the assumption made by many experimentalists that the laser focal plane is at the beginning of the ramp is not supported by the data presented in this thesis. The laser is focused inside the gas jet ramp at a position where most of the electron beam parameters are optimised.

The data already presented in this chapter can be organised into three categories. The first category includes some of the data already presented in this chapter, which shows on-axis electron beams with normal angular distribution that changes as the laser focal plane changes its position inside the gas jet. Also the electron beam has a higher divergence, ~60%, along the  $x$  axis compared with  $y$  axis. This result has been observed by other authors (Mangles, et al., 2004) and can be correlated with the laser polarisation plane and the shape of the laser spot.

The remaining data to be presented in this chapter demonstrated two effects:

- Data that shows a preferential distribution of the electron beam, mainly along the axis that makes  $45^\circ$  with the positive  $x$  and  $y$  axis. A consistent pointing offset is present although its average value can be reduced, but not made zero, by moving the laser focal plane towards the edge of the gas jet where the plasma density is lower than the plasma density in the centre. This situation is discussed in detail in Section 5.1.3.1.
- Data that shows a strong correlation between the charge and the pointing and this happens when the laser focal plane is in the regions relatively close to edge of the gas jet where the plasma density is lower than the plasma density in the centre. Usually, the higher charge bunches are distributed at lower angles than the lower charge bunches and the pointing offset increases as  $z$  is scanned toward the beginning of the density ramp. This case is discussed in Section 5.1.3.2.

### **5.1.3.1 Angular distribution of electrons due to an asymmetric plasma channel**

The second category of data mentioned at the end of previous section is exemplified in an experiment where the Nozzle A is tilted at positive  $30^\circ$  (plasma density profile shown in Figure 5-18 and parameters given in Table 9).

run	y (mm)	z (mm)	p (MPa)	z <sub>1</sub> (mm)	z <sub>2</sub> (mm)	z <sub>3</sub> (mm)	L (mm)	ρ (× 10 <sup>19</sup> cm <sup>-3</sup> )
13	1.55	0.0	3	1.555	1.281	0.477	3.313	1.761
14	1.55	-0.2	3	1.555	1.281	0.477	3.313	1.761
15	1.55	-0.4	3	1.555	1.281	0.477	3.313	1.761
16	1.55	-0.6	3	1.555	1.281	0.477	3.313	1.761
17	1.55	-0.8	3	1.555	1.281	0.477	3.313	1.761
18	1.55	-1.0	3	1.555	1.281	0.477	3.313	1.761
19	1.55	-1.2	3	1.555	1.281	0.477	3.313	1.761

**Table 9: Gas jet parameters in LWFA experiment where z varies inside the gas jet from 1.2 mm to 1.5 mm. The gas jet has been generated by Nozzle A.**

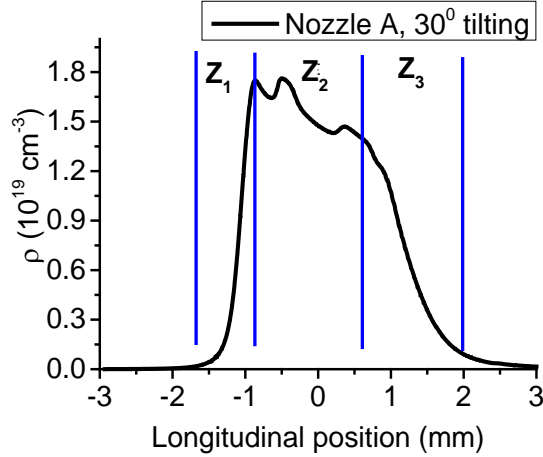


**Figure 5-18: The plasma density profile for the Nozzle A tilted at positive 30°**

It is observed that the electron distribution shows the normal symmetric distribution when the laser focal plane is at the edge of the gas jet and an elliptic distribution as the laser focal plane shifts towards the centre of the gas jet (Figure 5-19). The asymmetric plasma lens effect cannot explain the observation because there is no correlation between the charge and the electron bunch ejection angle (see further in Section 5.1.3.2. Furthermore, the individual and accumulated electron bunches in general display the same shape: elliptical for the laser focal plane close to the centre of the gas nozzle and circular for a laser position close to the edge of the gas jet.

Usually the electron beam is slightly elongated in the direction of the polarisation of the laser (Geddes, et al., 2004), (Cipiccia, et al., 2011) but here no clear mechanism can be identified to rotate the polarisation of the laser and affect at the same time the parameters of the electron beam. Other experimental results recorded for this thesis showed no elliptical electron angular spread, in general, although the laser focus has been scanned in a plethora of experimental conditions. This particular shape of the angular spread of the electron beam has been observed in other experimental data

recorded but its presence is not predictable and it could have the same cause as explained further in this section.

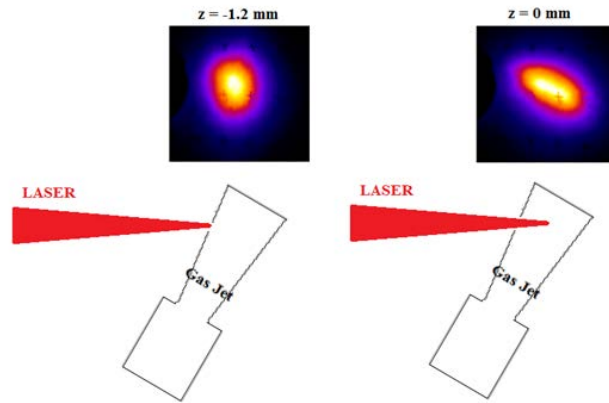


**Figure 5-19:** Change in the cumulative (400 shots) electron beam distribution on L1 (top right and left false colour images) as the laser focal plane is moves from the edge of the gas jet (left) towards a position inside the gas jet (right). This effect cannot be explained using a plasma lens effect.

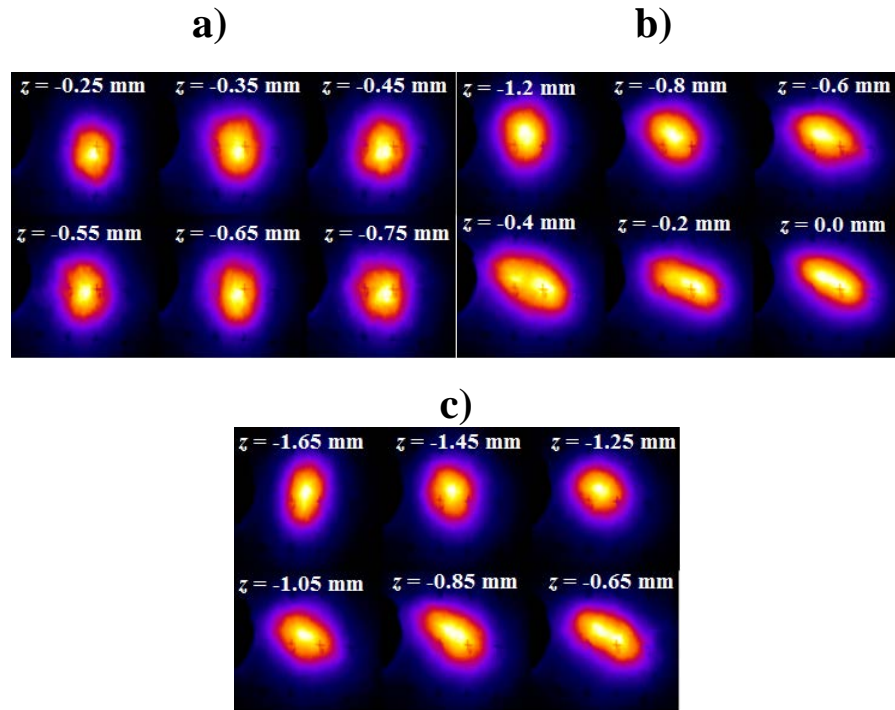


**Figure 5-20:** An accumulation of 400 shots showing the distribution of the electron beam on Lanex screen L1 as the laser focal plane moves from a position deep inside the gas jet towards the edge of the gas jet. The electron distribution changes from “polarised” to normal but only in the experiments run after the laser alignment (b and c group of images). Pictures recorded before laser realignment (image a) show normal angular distribution. The gas jets are produced by Nozzle A tilted at 30°.

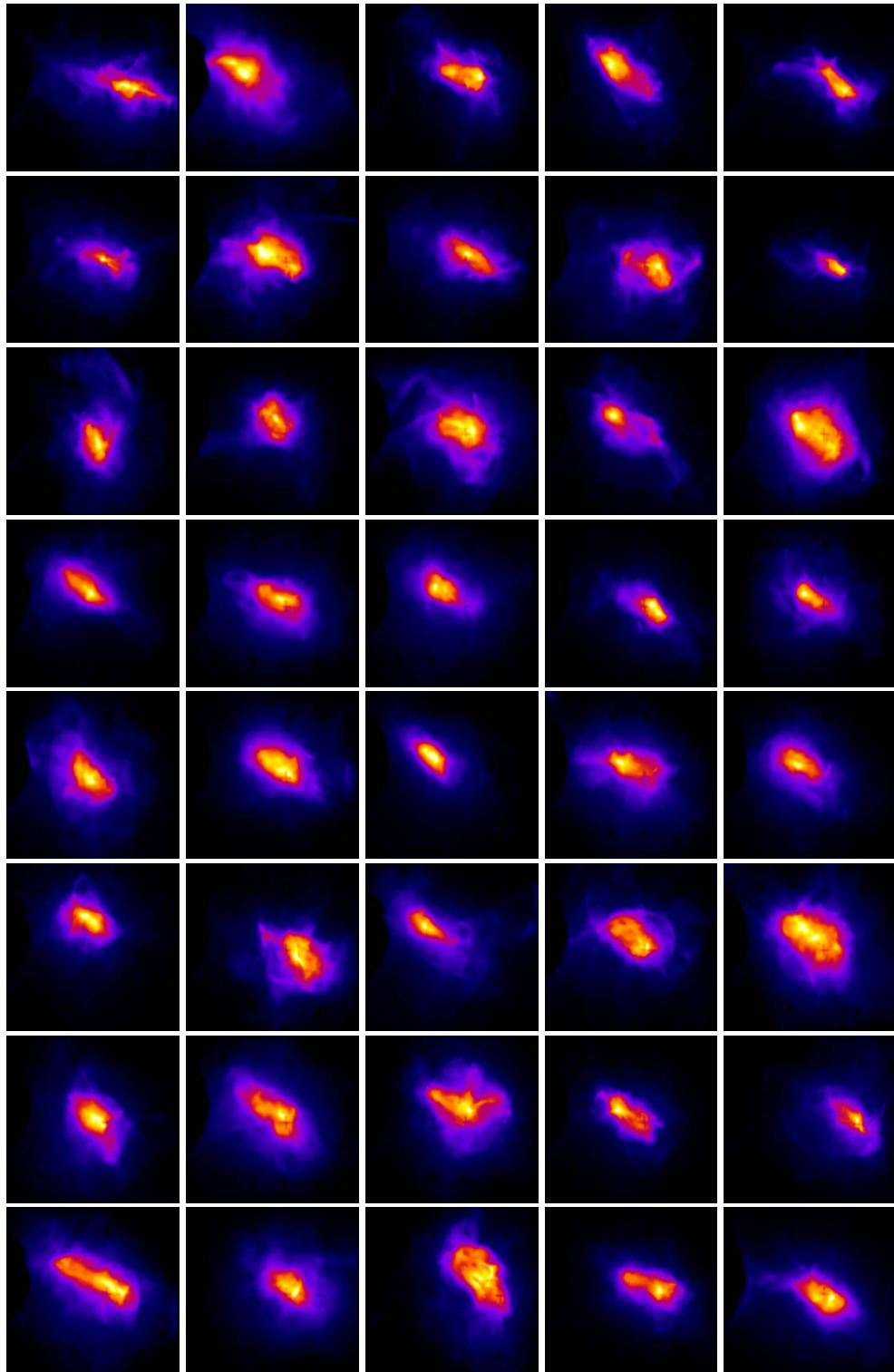


*Figure 5-21: False colour images of individual electron bunches recorded on the fluorescent screen L1 when the laser focal plane is  $z = 0$ .*

The elliptical distribution of the electrons on L1 and its shape dependence on the acceleration length can be explained only if it is assumed that the electron beam pointing and transverse shape depend on the symmetry of the LWFA bubble. The

asymmetric bubble can be due to, for example, an asymmetric laser focal spot (Thaury, et al., 2013) or laser wavefront aberration (Popp, et al., 2010), which leads to off-axis bubble propagation. The electron beam follows the bubble direction of propagation and will also be deflected.

Due to some technical problems, the laser was completely realigned before the present experiment. An experiment carried out just before the laser realignment showed no electron beam distortion (see Figure 5-20a). The tilting angle was  $30^\circ$  and the laser focal point varied inside the gas jet.

Following realignment, it is possible that a laser wavefront aberration or laser focus distortion has been present in this experiment (no wavefront sensor is installed in the system) creating the conditions for asymmetric wake bubble formation, as described above. As the laser focal plane is varied inside the gas jet, the laser focal spot can have different elliptical intensity distribution (see Figure 5-22) thus, after relativistic self-focussing, the distorted laser pulse wavefront can excite nonlinear plasma waves that also exhibit the distortion.

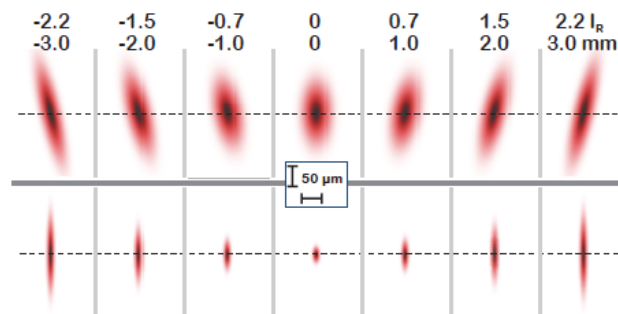


**Figure 5-22: Evolution of the pulse intensity envelope with the focus parameters in the presence of wavefront aberration (upper row) and without aberration (lower row). Caption from Popp et al. (Popp, et al., 2010)**

The electron beam deflection due to distorted plasma channel has been proved through numerical simulations by Popp et al. (Popp, et al., 2010). Their simulations, shown in Figure 5-23, highlight important differences between the propagation of a distorted LWFA compared with an undistorted one such that a laser wavefront aberration can lead to a deflection of the electron beam. This result has an important impact on the performance of the plasma accelerators especially when the electron beam has to be transported for further applications.

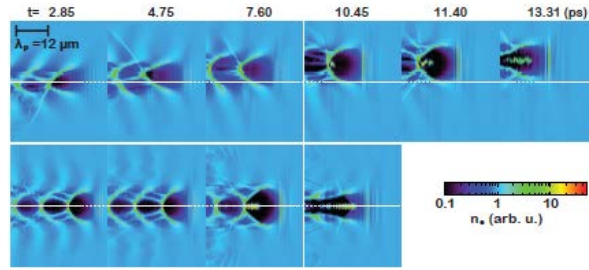


**Figure 5-23: Cross-section through the central  $x$ - $z$  plane (laser polarisation plane) of a 3D LWFA-simulation volume with (top) and without (bottom) a pulse-front-tilted driver laser. Caption from Popp et al. (Popp, et al., 2010)**

The presence of a pointing offset in the electron beam, stronger along the  $y$  axis, which cannot be corrected no matter the parameters of the plasma, is an indication that an asymmetric plasma channel is present. When this is the case (including the experiments described in the above section) the electron beam charge distribution changes each time the laser focal plane is scanned inside the gas jet. More exactly, when  $z$  is placed deep in the plasma ramp, the charge has a random distribution. Moving the  $z$  towards the beginning of the plasma density ramp not only moves the centre of the electron angular distribution more off axis but also determines an electron beam splitting depending on the charge in the bunch. In this situation the higher charge beam tends towards the centre of the distribution while the low charge is found distributed farther away. This case is exemplified by plotting the pointing as a function of the charge (see Figure 5-24) for run 13 and run 19 the Table 9.

To explain the results presented in Figure 5-24 it must be assumed that the electron beam interacts with a transient structure inside the gas jet. The existence of this structure depends on the position of the laser focal point inside the gas jet and on the longitudinal length of the plasma profile. As the laser focal plane moves inside the gas jet, the plasma channel moves as well (see Figure 5-25) therefore a scenario is possible where the wakefield acceleration region does not cease at the end of the density profile but inside the density profile, being followed by a region of plasma.

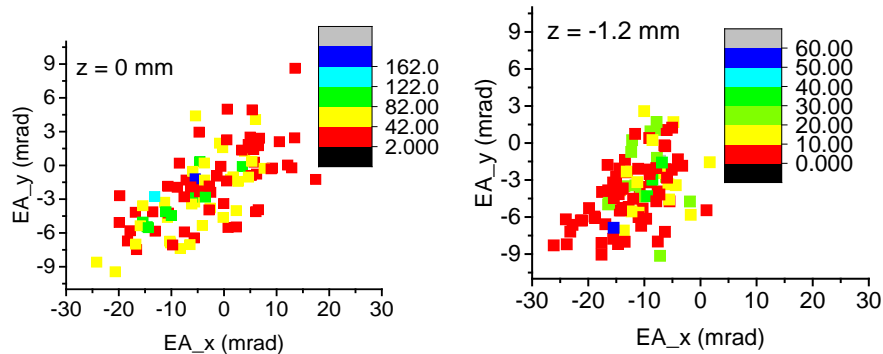


*Figure 5-24: The pointing of the electron beam as a function of the charge for two different values of  $z$ .  $z = 0$  corresponds to a position deep in the density ramp,  $\sim 1.2$  mm from the edge, and  $-1.2$  mm corresponds to a position close to edge of the gas jet. The legend shows the distribution of charge from lower values (black) to higher values (blue).*

The presence of a plasma region may be favourable to the generation of an asymmetric plasma lens (a transient electrically charged plasma structure) that deflects the incident electron beam depending on the charge, energy, length and incidence angle. This hypothesis is discussed further in the next section.

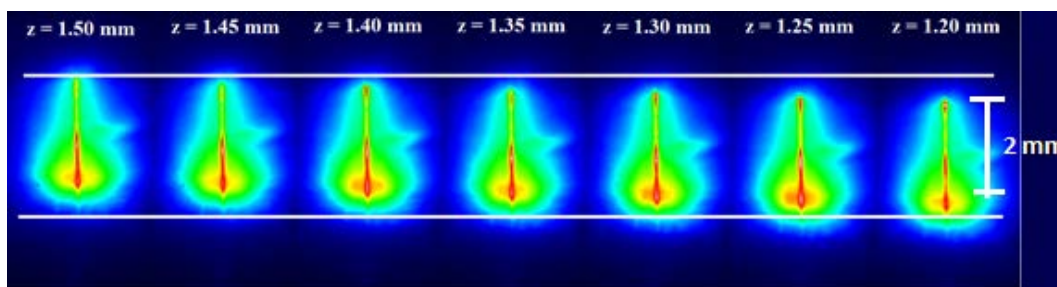


*Figure 5-25: False colour images showing the plasma channel movement as the laser focal position is changed inside the gas jet. The laser is propagating from up to down in the images and the white lines mark the initial position of the beginning of the channel and the final position of the end of the channel as the laser focal plane is scanned inside the gas jet.*

### 5.1.3.2 Angular distribution of the electrons due to asymmetric plasma lens

Now, to explain the results from the last part of the Section 5.1.3.1 some assumptions must be made. It is known from numerical simulations that the entire process of LWFA happens for distances of 100's of micrometres (Pukhov & Gordienko, 2006), depending on the laser parameters and plasma parameters. After the LWFA process, the laser can have sufficient energy to create an ion channel in what is called the linear regime (the electrons are oscillating behind the laser pulse with the plasma frequency). This ion channel can extend until the end of the gas region (in this

case gas jet) or until the laser energy is so low that it cannot create the ion channel anymore. In the latter case, the laser can still be strong enough to ionise the gas therefore it is reasonable to assume that the ion channel can continue with a region of plasma. Due to highly non-linear regime of interaction it is impossible to say, without numerical simulations, if the ion channel region can exist or not and will be subject of further studies.

The existence of the ion channel can influence the divergence of the electron beam, as discussed in 2.3.1, although no such evidence could be found in the experimental data prepared for this thesis. The existence of an ion channel is mentioned here only for completeness.

A schematic of the separation of regions in the LWFA plasma channel is shown in Figure 5-26. Using the above separation in regions of the plasma channel one can have the following scenarios:

1. Scenario 1: The plasma channel consists of three regions: LWFA region, ion channel region and plasma region.
2. Scenario 2: The plasma channel length is equal to or shorter than the acceleration length (the effective distance over which the process of LWFA happens). By choosing shorter interaction lengths than the effective acceleration length, the electron beam is extracted from the plasma channel before it fully develops *i.e.* before it acquires full energy or reaches the dephasing length. This case has been extensively discussed in the literature, for example by Shaw et al. (Shaw, Vafaei-Najafabadi, Marsh, & Joshi, 2012) and McGuffey *et al.* (McGuffey, et al., Experimental laser wakefield acceleration scalings exceeding 100 TW, 2012), therefore this is not discussed in this thesis.

To avoid any confusion in this thesis, the plasma channel is defined as the region in the gas jet that is directly (Thomson scattering, plasma recombination or any other emissive processes) or indirectly (monitoring the changes in refractive index for example) visible. The plasma channel can consist of the LWFA region, ion channel region and plasma region. LWFA region starts from the point where the laser hits the gas region and ends at a point where the process of electron acceleration stops (it can be limited by dephasing or depletion). The ion channel can follow the LWFA region if the ponderomotive force of the laser is high enough

to push the electrons out of its way and create a linear wake. The plasma region follows the LWFA region or ion region and consists of ionised gas.

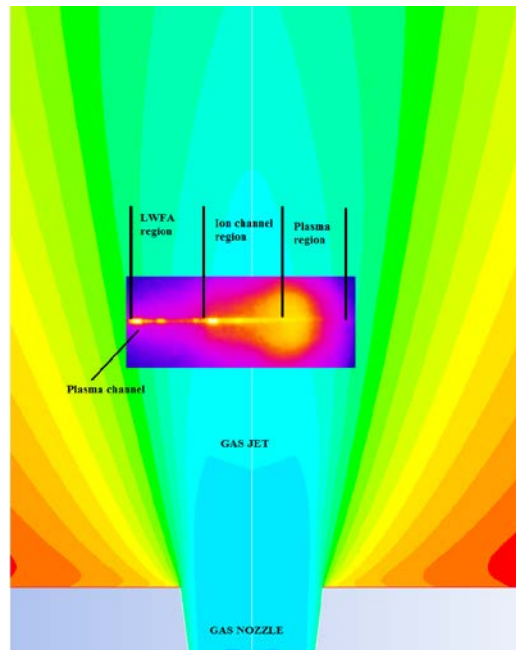


*Figure 5-26: A schematic view of a LWFA plasma channel created by the laser. It starts with the LWFA region, followed by an ion channel region and ends with a region where only plasma is found*

#### **5.1.3.2.1 Scenario 1: the plasma channel consists of LWFA region, ion channel region and plasma region**

The existence of a plasma region immediately after the wakefield interaction region or after the ion channel creates conditions, after interaction with an electron beam, for the formation of a plasma lens (Muggli P. , et al., 2001), which is produced by the front of the electron bunch that pushes radially and axially the plasma electrons. A recent paper (Masson-Laborde, et al., 2014) showed experimentally and through simulations that an electron beam generated by a LWFA can drive a nonlinear plasma wave which can lead to electron injection and further acceleration in the PWFA regime. The requirements for the nonlinear regime of wake excitation are much higher than those required by a linear plasma wave excitation, so these processes could also (at moderate parameters) give rise to a plasma lens.

The geometry of the plasma lens is different depending on the incidence angle of the electron beam on the plasma interface: a symmetric plasma lens is generated for

normal incidence, or an asymmetric plasma lens for electron beams hitting the plasma interface at an angle.

When a symmetric plasma lens is formed, the electrons in the bunch experience a focussing force that leads to a radial compression of the electron beam. This effect has been proposed by Chen (Chen P. , 1987) as a method to control the divergence of the electron beam, instead of using conventional magnetic quadrupoles. Proof-of-principle experiments proving the generation of a symmetric plasma lens have been successfully performed, for example by Thompson. (Thompson, et al., 2010).

The creation of an asymmetric plasma lens has been investigated theoretically by Chen in 1987 (Chen P. , 1987) and experimentally by Muggli in 2001 (Muggli P. , et al., 2001) where they show that an asymmetric plasma lens created in plasma with a density around  $10^{14} \text{ cm}^{-3}$  can refract and even reflect an electron beam with energy of 28.5 GeV. Chen deduced a formula (see 8.1) for the deflection angle  $\Theta$  of the electron beam due to an asymmetric plasma lens as:

$$\Theta = \frac{8\alpha Q r_e}{\pi e \sqrt{2\pi} \gamma \sigma_z \sin \phi}, \quad (5.2)$$

where  $\alpha$  is a weak function of plasma density and bunch length given by

$$\alpha = \begin{cases} 1 & \text{if } \sigma_z > \lambda_p \\ 2 & \text{if } \sigma_z = \lambda_p \\ \frac{8\sigma_z}{\lambda_p} & \text{if } \sigma_z < \lambda_p \end{cases}, \quad (5.3)$$

$Q$  is the total charge in the bunch,  $\lambda_p$  is plasma wavelength,  $\sigma_z$  is electron bunch length,  $r_e$  is the classical electron radius,  $\gamma$  is the electron beam gamma factor,  $\phi$  is the incidence angle of the electron beam on the plasma boundary. This formula shows a dependence of the electron beam ejection angle on the incidence angle, electron beam energy and also on electron bunch charge per unit length of the beam. The variation of electron beam incidence angle on the plasma interface is due to dynamics of the electron beam inside the plasma channel, mainly the betatron oscillation. The betatron oscillation occurs in the plane of the polarisation of the laser (in this case along the  $x$  plane) and is quickly damped by the transverse focussing force of the ion channel.

Thus, the pointing of the electron beam has a variation around a stable position, in the centre if there is no interaction with a plasma lens and off-centre if the electron beam interacts with a plasma lens. A very basic estimation gives  $\sim 4.71$  mrad deviation angle for 0.5 pC electron beam with incidence angle of 1 mrad, energy 120 MeV and plasma wavelength 8.1  $\mu\text{m}$ . This value is within the range of deviation angles observed in this experiment.

Although the plasma lens effect can affect the pointing of the electron beam, its direct dependence on the parameters of the electron beam makes it unsuitable as a tool to control the pointing of an electron beam generated from a LWFA. In this stage of development, the parameters of the electron beam from LWFA have a relative large, unpredictable variation around a mean value, in general, this is a problem shared by all LWFA setups. For example, on average, for an experimental run of 100 shots prepared for this thesis, the data show around 64% variation in charge, 13% variation in energy, 53% variation in energy spread. Using some of these values in (5.2) and assuming constant electron bunch length and incidence angle, one obtains a maximum 64% variation in electron beam pointing due to the asymmetric plasma lens effect, a result quite close to experimental value of 75% (assuming that the difference is the initial electron incidence angle). It can be concluded that the existence of a plasma region after the LWFA channel should be suppressed as it can lead to an uncontrollable electron beam pointing thus the plasma channel length should not be longer than the effective LWFA acceleration length. Furthermore, a variable gas length would experimentally permit extraction of the electron beam at different stages of its evolution (for example immediately after the acceleration length or before interactions with the gas/plasma).

The asymmetric plasma lens effect cannot explain by itself the results when the electron beam betatron oscillation in one plane ( $xz$  plane or the laser polarisation plane) is taken into account. As can be seen in Section 5.1.3.1, the electron beam can be affected not only in the  $x$  direction but also in  $y$ . This result can be explained only if one assumes that the electron beam pointing is controlled by the laser wavefront properties as explained in section 5.1.3.1 where it is shown that an asymmetric spot size or a tilted laser wavefront can lead to the creation of an asymmetric LWFA bubble.

The distorted bubble propagates off-axis accelerating the electron beam in the same direction and distorting the shape of the plasma channel.

A small asymmetry of the laser spot in focal plane has been experimentally observed (see Figure 4-2) and the laser wavefront tilting has not been monitored during this experimental campaign. Therefore, it is possible that laser wavefront tilting is present in different experimental runs on different days. The asymmetry of the plasma channel affects the electron beam pointing in both  $x$  and  $y$  planes depending on the propagation length, while the asymmetric plasma lens changes the electron beam pointing depending on its parameters. This hypothesis has been confirmed when the above experiment has been run on a different day. The dependence of the electron beam charge on the ejection angle is shown Figure 5-27 where the laser focal plane has been moved from  $z = 0.95$  mm inside the gas jet to  $z = 0.45$  mm towards the edge of the gas jet. As the laser focal plane moves towards the edge of the gas jet the electron beam distribution as a function of the charge becomes ellipsoidal, its ejection angle depending on its electric charge.

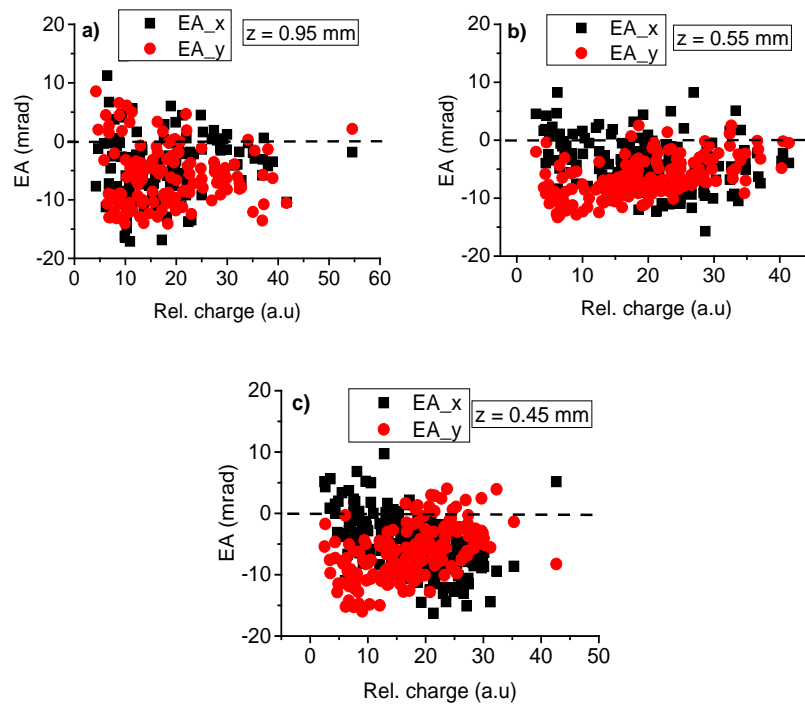


**Figure 5-27: The relative electron charge as a function of the Ejection Angle for different laser focal positions inside the gas jet. As the laser focal plane moves from  $z = 0.95$  mm (a) to  $z = 0.45$  mm (c), towards the edge of the gas jet, the electron beam ejection angle depends on the charge of the electron beam.**

The above assumption on laser wavefront tilt is supported by the daily LWFA operation procedure on the ALPHA-X beamline. When a deviation of the electron beam is observed, after checking all the possible sources (such as the laser pointing, laser alignment relative to the centre of the gas jet on  $x$  axis, etc.) the next step is to adjust the alignment of gratings in the compressor. The alignment is done by monitoring the changes of the laser spot size until the best symmetry is obtained. Usually after this alignment the electron beam shows a normal statistical distribution that is centred on-axis. The accumulated distribution of 200 shots of electron beam on the fluorescent screen L1 for the laser focal plane  $z = 0.45$  mm (Figure 5-28 top) shows an asymmetry of the beam profile. This distortion changes in shape as the laser focal plane is varied and can be linked to the existence of a distorted plasma channel therefore explaining the electron beam angular distribution along the axis that makes an angle with the main axes  $x$  and  $y$ .

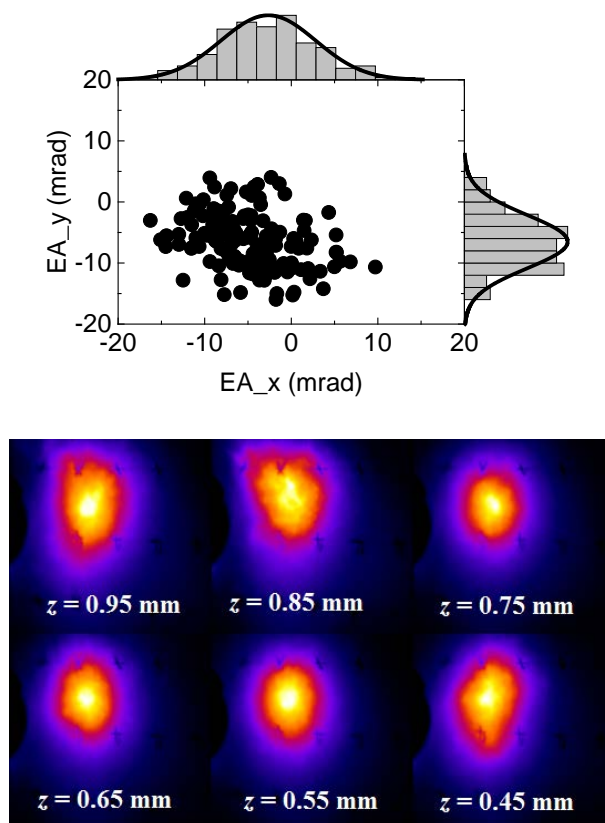


**Figure 5-28: Angular distribution of electron bunches on the Lanex screen corresponding to laser focal plane placed at  $z = 0.45$  mm (top) and false colour images of accumulated electron shots on L1 when the laser focal plane is changed from 0.95 mm to 0.45 mm (bottom).**

### **5.1.3.2.2 Scenario 2: The plasma channel length is equal to or shorter than the acceleration length**

The plasma channel length is equal or shorter than the acceleration length (the effective distance over which the process of LWFA occurs). As mentioned previously, by choosing shorter interaction lengths than the effective acceleration length, the electron beam is extracted from the plasma channel before it fully develops i.e. before it acquires full energy or reaches the dephasing length. This case has been extensively discussed in the literature, for example by Shaw (Shaw, Vafaei-Najafabadi, Marsh, & Joshi, 2012) and McGuffey (McGuffey, et al., 2012), therefore this is not discussed in this thesis.

The hypothesis of existence of a plasma lens to explain the coupling of the beam pointing with the accelerate charge noticed when the laser focus is near the edge of the gas jet Figure 5-24 used in this thesis is based on Occam's razor principle applied in science that says that "*when you have two competing theories that make exactly the same predictions, the simpler one is the better*". It must be stressed that, although the plasma lens effect explains the results reasonably well, it does not exclude other possibilities such as the creation of magnetic fields during the laser wakefield interaction (Walton, et al., 2013) or laser/electron beam head erosion (Esarey, Schroeder, & Leemans, 2009) (Chen , et al., 2007). In this stage of development of nonlinear laser-plasma interaction there is no reasonable scenario that involves magnetic fields or other phenomena that can explain the above mentioned results. All these scenarios are currently under investigation, theoretically and experimentally.

## **5.2 Discussion**

### **5.2.1 Possible mechanism that controls, for a limited range, the energy of the electron beam**

Experimental results presented in Section 5.1 show that increasing the plasma density does not necessarily lead to a decrease in electron beam energy (see Figure 5-7), a result that contradicts other published results (McGuffey, et al., Experimental laser wakefield acceleration scalings exceeding 100 TW, 2012), (Lu, et al., 2007),

(Mangles, et al., 2006). Since the plasma density ramp is much shorter than the plateau length and the energy spread enhancement is not present, this result cannot be explained using the electron phase-locking mechanism.

For short up-ramps, the up-ramp plasma density induced reduction of the laser spot size could be the dominant mechanism which determines the energy of the electrons. Sadighi-Bonabi (Sadighi-Bonabi, Habibi, & Yazdani, 2009) show in their simulations that it is possible to decrease by 20% the laser spot size due to relativistic self-focussing when density up-ramps are used (Figure 5-29). A decrease in the laser spot size results in an increase in the laser intensity and subsequently an increase in the maximum accelerating field. Using for example the formula for energy gain derived for the case when the acceleration process is pump depletion limited (Esarey, Schroeder, & Leemans, 2009):

$$E [\text{MeV}] \approx 400 \frac{I [\text{W cm}^{-2}]}{n_e [\text{cm}^{-3}]}, \quad a_0^2 \geq 1, \quad (5.4)$$

where  $E$  is the electron energy gain,  $I$  is the laser intensity and  $n_e$  is the plasma density, the energy gain can be 1.56 times higher when up-ramp density profiles are used compared with an homogeneous plasma density (taking into account the 20% decrease in spot size).

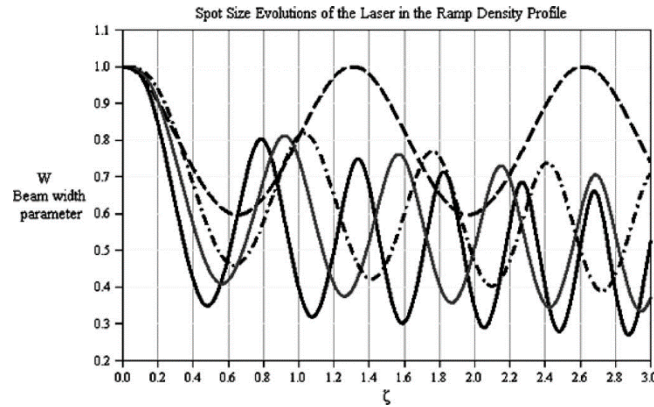


**Figure 5-29: Dependence of the beam width parameter  $W$  on the distance of propagation  $\zeta$  in the under-dense plasma with the ramp density profile with the function of  $n(\zeta) = \tan(\zeta/d)$  with various conditions such as a laser intensity of  $I = 1.21 \times 10^{18} \text{ W cm}^{-2}$  and the laser wavelength is  $\lambda_0 = 1.06 \mu\text{m}$  and  $n_0 = 1.7 \times 10^{21} \text{ cm}^{-3}$ ,  $d = 5.8$  (black curve),  $n_0 = 1.2 \times 10^{21} \text{ cm}^{-3}$ ,  $d = 7.3$  (grey curve),  $n_0 = 0.6 \times 10^{21} \text{ cm}^{-3}$ ,  $d = 5.8$  (dash-dotted curve), and the uniform density profile (dashed curve). (Sadighi-Bonabi, Habibi, & Yazdani, 2009)**

Although Sadighi-Bonabi *et al.* use a maximum plasma density two orders of magnitude higher than the plasma density in experiments here, their article shows that

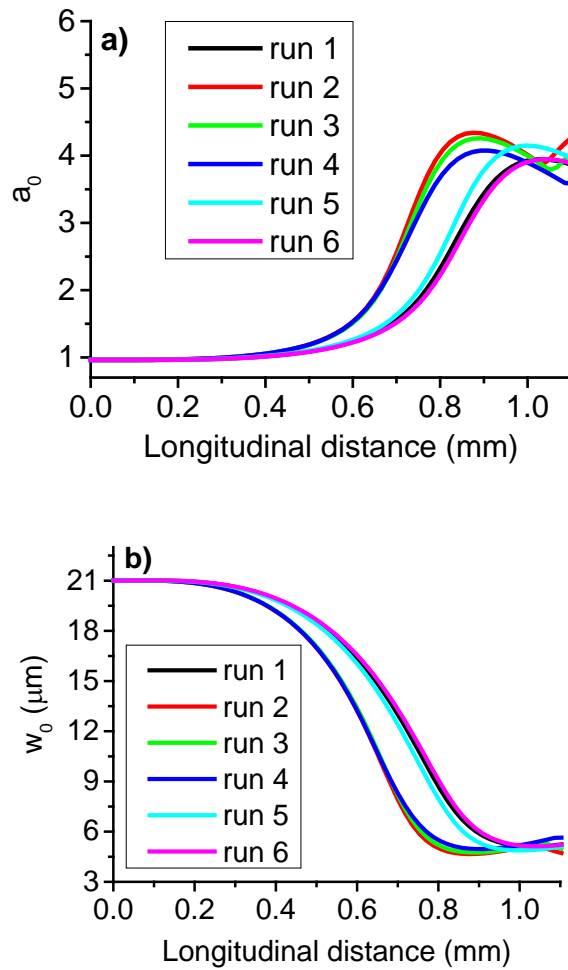
laser self-focussing mechanism in up-ramp plasma densities is still possible for lower densities than the ones they used and the spot size reduction is very small but still present.

This result may explain why the peak electron energy in experiments with the Nozzle A (see Section 5.1.1) shows only a small variation, around 8%, a conclusion confirmed experimentally as well by other groups, such as Kim (Kim, Ju, & Yoo, 2011). Moreover, the above analysis does not take into account the laser pulse compression due to nonlinear effects (Esarey, Schroeder, & Leemans, 2009), which can lead to an increase in laser power and subsequently an increase in intensity.

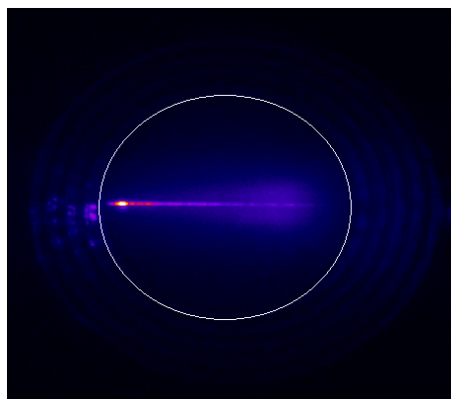
A series of numerical simulations using the 2D axisymmetric code WAKE (Mora & Antonsen, 1997) with the plasma density profiles shown in Figure 5-3 confirm the above results obtained by Sadighi-Bonabi for the evolution of laser spot radius. In

Figure 5-30a and Figure 5-30b the normalised laser intensity  $a_0$  and laser spot waist  $w_0$ , respectively, show a visible variation with a maximum in the longitudinal direction (laser propagation direction) depending on the up-ramp plasma density, although the changes in the parameters of the plasma density entrance ramp are very small. For example, for plasma density of  $1.20 \times 10^{19} \text{ cm}^{-3}$ , a maximum  $a_0 = 3.94$  is reached after the laser pulse propagated 1.03 mm in the longitudinal direction, while for a plasma density of  $1.46 \times 10^{19} \text{ cm}^{-3}$  a maximum  $a_0 = 4.36$  is reached after the laser pulse has propagated 0.87 mm in the longitudinal direction.

The laser parameters used in the simulations match those used in the experiment: laser energy in focus  $E_{FWHM} = 0.5 \text{ J}$ , spot size radius at waist  $r = 21 \text{ }\mu\text{m}$  and laser pulse length  $\tau_{FWHM} = 36 \text{ fs}$ . The longitudinal distance of the plasma density profile is taken as 0 to 1.1 mm to model the changes of the laser pulse parameters in the plasma density ramp region.



*Figure 5-30: Numerical simulations using the 2D axisymmetric code WAKE showing the evolution of the laser pulse normalised intensity  $a_0$  and spot waist  $w_0$  as it propagates in a different plasma density ramps.*



*Figure 5-31: A false colour camera image of the Thomson scattering from a LWFA plasma channel. A band-pass filter centred at 400 nm has been used. The plasma channel diameter is about  $10 \mu\text{m}$  and occupies around 5 pixels in the image therefore could not be used to monitor the small changes due to relativistic self-focussing in different plasma density ramps. The white circle marks the outlet of the nozzle.*

As explained in Chapter 4 on experimental setup and diagnostics, the plasma channel created by the LWFA process is monitored by recording the Thomson scattering signal (Figure 5-31). This diagnostic can be used to monitor changes in the plasma channel diameter under different experimental conditions. Due to the low resolution of the Thomson scattering diagnostic the experimental evidence of laser spot size shrinking in up-ramp plasma densities could not be proved in this thesis.

### **5.3 Conclusions of the chapter**

In Chapter 5 it is shown that different parts of the plasma density profile involved in LWFA experiments can control the electron generation and propagation in different ways. In Section 5.1.1 and Section 5.1.2 it is shown that the density ramp that interacts first with the laser pulse has a critical influence on the parameters of the electron beam, controlling the charge and, for a small range, the energy of the electron beam. In Section 5.1.3 it is shown that the position of laser focal plane in the plasma density ramp controls the parameters of the electron beam, mainly the charge, pointing and pointing stability.

The shape of the plasma channel is controlled by the parameters of the laser such as spot shape and wavefront aberrations. A distorted channel will subsequently affect directly the parameters of electron beam such as the pointing and angular distribution as shown in Section 5.1.3.1. After the process of LWFA stops, the electron beam propagates further in the plasma medium and, as shown in Section 5.1.3.2, the creation of asymmetric plasma lens can deflect the electron beam depending on its incidence angle, charge and energy.

The electron beam energy spread has a large range of values, depending on the nozzle used in experiments. It is suspected that the electron beam suffers a significant dephasing relative to the accelerating phase of the bubble leading to an increase in energy spread and limited energy gain. The injected electrons at first have nearly the same energy but as the electron bunch moves forward from the back of the bubble, the longitudinal bubble electric field in the bunch becomes weaker and its gradient smaller. When the gradient of the electron bunch Coulomb potential becomes comparable to the bubble electric field the tail electrons gain relatively less energy

from the field. The continuous change of the acceleration gradient until it becomes zero leads to the above mentioned increase in energy spread and decrease in the maximum electron energy.

Using the formulae for dephasing and depletion length from the Section 2.3.2.3, a dephasing length of the order of  $\approx 0.81$  mm and a laser depletion length of 0.86 mm are obtained when  $a_0 = 4.5$ , laser pulse length  $\tau_{\text{FWHM}} = 15$  fs and plasma density  $\rho = 1.202 \times 10^{19} \text{ cm}^{-3}$ . The values of  $a_0$  and  $\tau_{\text{FWHM}}$  have been calculated taking into account the relativistic self-focussing. In this case the gas length is much larger than the calculated dephasing and depletion lengths thus no obvious dependence of the electron beam parameters on the plateau length (see Figure 5-32) is observed.

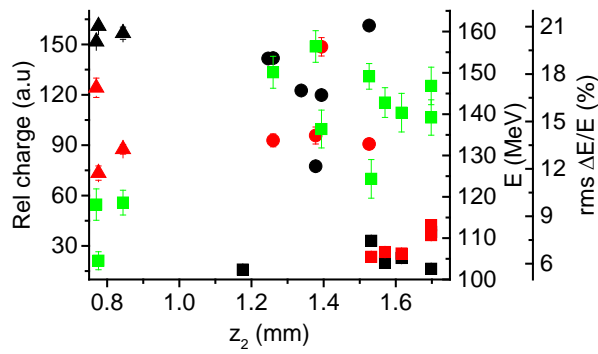


*Figure 5-32: The relative charge (black), the peak energy (red) and the energy spread (green) as a function of the plasma plateau length. The data has been recorded with the Nozzle A (squares), Nozzle 510 (triangles) and Nozzle 511 (dots).*

Any change in density profile changes the laser pulse quite significantly due to its nonlinear longitudinal and transverse evolution in plasma medium as shown in Section 5.2.1 thus leading to a laser pulse longitudinal and transversal compression. Due to these changes, the dephasing length can be systematically higher than the depletion length (that depends on laser pulse length) therefore one could conclude that the electron dephasing, as defined in Section 2.3.2.3, might not be an issue in these experiments. This conclusion is supported by the results presented in Section 5.1.1 where the main electron beam parameters obtained in the experiment do not show dependence only on plasma density but on the parameters of the plasma density profile ramp. As the plasma density increases the electron energy also increases, for a limited range, (see Section 5.2.1) while the energy spread doesn't change significantly. A

dephasing-limited acceleration process should affect the parameters of the electron beam, which cannot be confirmed here.

Due to this significant dependence of the electron beam parameters on the plasma density ramp it has been concluded that a more detailed experimental investigation is required. The parameters of a plasma density profile, generated by a gas nozzle for example, can be varied by changing the backing pressure or the interaction point between laser focus and gas jet. To give much more flexibility in shaping the gas jet profile, especially the gas jet edge that forms the ramp part of the density profile, a new degree of freedom has been added to the gas jet by tilting it relative to the direction of the propagation of the laser. The tilting capability has already been exploited to investigate the impact the density profile may have on the pointing of the electron beam in Section 5.1.3. The tilt of the gas jet allows a continuous and fine variation of the gas profile ramp and hence its influence on the quality of the electron beam generated from a LWFA is the main subject of the next chapter.

## **6 LWFA experiments with tilted supersonic gas nozzles.**

In this chapter results are presented of LWFA experiments with tilted nozzles. In Section 6.1 the density profiles are generated by tilting the nozzle relative to the direction of propagation of the laser and using three different nozzles *A*, *510* and *511* (see Table 2). The parameters of the electron beam (mainly charge, energy, energy spread and divergence) are quantified and correlated with the parameters of the plasma density profile such as ramp slope, peak density and ramp length.

In Section 6.2 LWFA experimental results with downward plasma densities are discussed.

### **6.1 Electron beam energy and energy spread control from a wakefield accelerator using tilted nozzles**

The control of electron beam properties such as pointing, energy or charge is an essential requirement for LWFA applications. In Section 5.1.1 the effects of the ramp density profile on the electron beam pointing and pointing stability has been discussed. As far as energy is concerned, few research groups have managed to improve the controllability of the LWFA for acceleration process based on self-injection. Faure (Faure, et al., 2006) has proposed to tune the energy of the electron beam using a counter-propagating laser beam to inject the electron bunch inside the bubble. However, while they have managed to control the energy of the electron beam, the control over the charge and energy spread has been lost (Figure 6-1) because the beam loading could not be compensated for.

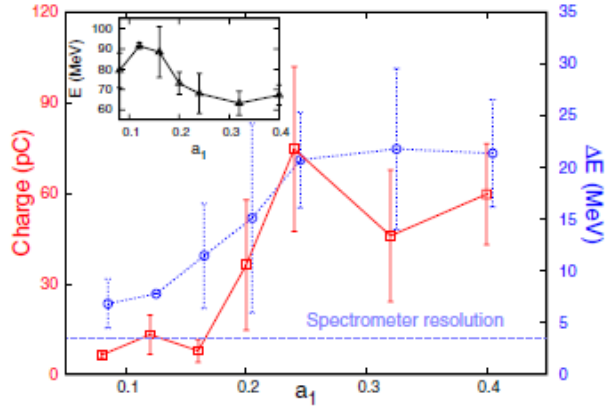


**Figure 6-1: Evolution of charge (red solid line with squares), electron energy spread  $\Delta E$  at FWHM (blue dotted line with circles) as a function of the counter propagating laser normalised vector potential  $a_1$ . The error bars represent the r.m.s. fluctuation. Inset: variation of peak electron energy. Caption from Faure (Faure, et al., 2006).**

In this thesis a different approach has been used to tune the electron energy, which is based on electron bunch phase locking (see Section 2.3). The phase locking mechanism has been proposed for the first time by Katsouleas for 1D geometry (Katsouleas, 1986). It consists of adjusting the longitudinal plasma density so that the velocity of the electron bunch is maintained constant, during acceleration, relative to the velocity of the back of the bubble wall. As a consequence the influence of the dephasing is delayed, beam loading is partially compensated and the acceleration length is extended.

A comparison between a flat top density profile (SII) and an up-ramp density (SI) has been numerically investigated by Wen (Wen, et al., 2010). In their simulations a circularly polarised laser has been considered with centre wavelength at  $\lambda_0 = 800$  nm, normalised laser amplitude  $a_0 = 1.41$ , transverse Gaussian distribution with size  $FWHM = 15.24$   $\mu\text{m}$  and duration 30 fs. The laser propagates in the positive  $z$  direction. The wave-breaking and subsequently the electron injection in the bubble has been triggered using a small disturbance generated at  $z = 200$   $\mu\text{m}$ , for example, by a nanowire (Shen, et al., 2007).

It is not entirely clear why Wen chose to initialise the wave-breaking using a nanowire instead of relying on transverse wave-breaking. Previous theoretical and experimental studies published by Shen (Shen, et al., 2007) shows that the use of localised disturbances to initialise the wave-breaking reduces the requirements

imposed on minimum laser energy for electron beam injection through wave-breaking while the stability of the LWFA is increased.

For the case SI where the plasma density is continuously varied, the plasma density is set to  $n = n_0 / [1 - (z - z_0) / L]^{2/3}$  where  $n_0 = 6 \times 10^{18} \text{ cm}^{-3}$ ,  $z_0 = 300 \text{ } \mu\text{m}$ ,  $z - z_0 < L$ ,  $z > z_0$  and  $L$  has been defined in section 2.3.2.3. For the case SII the plasma density is homogenous and constant at  $n_0 = 6 \times 10^{18} \text{ cm}^{-3}$ .

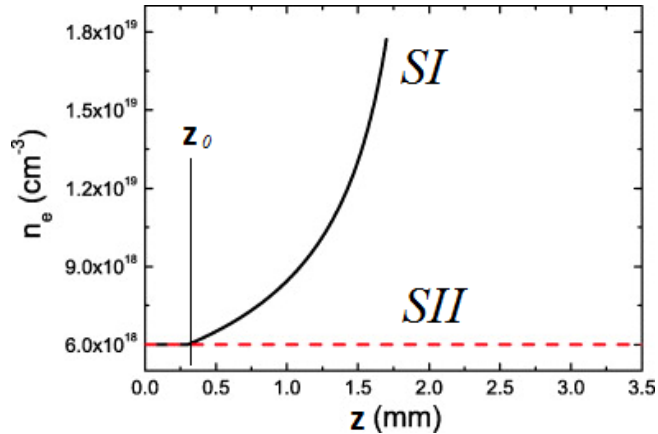


**Figure 6-2:** The plasma density profiles used in simulations for the cases when the plasma density has been continuously adjusted (continuous line) and for the case when the plasma density has been kept constant (dashed line).  $z_0$  marks the beginning of the plasma density ramp of the SI profile. (Wen, et al., 2010)

The simulation results predict (Figure 6-3) 40% improvement of the energy spread (from 21% to 12%) and 20% peak energy increase (from 227 MeV to 273 MeV) in the up-ramp case SI when compared with the flat top profile case SII although both profiles start at the same point with an initial electron energy of 20 MeV.

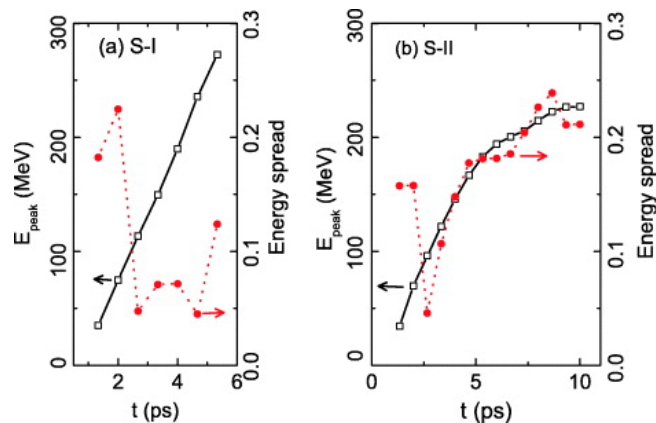


**Figure 6-3:** The evolution of the peak energy (squares) and energy spread (full dots) when an up-ramp density (SI) or a flat top profile (SII) is used. (Wen, et al., 2010)

When constant plasma density is used, the effect of the electron dephasing is pronounced, after approximately 5 ps of propagation the electron beam energy reaches a plateau and the energy spread increases continuously. In the case of *SI* density profile the electron energy increases linearly with the propagation distance while the energy spread shows a sudden decrease to 5% after 3 ps of propagation, followed by a sudden increase after 4.7 ps.

The electric field of the electron bunch itself is opposed to the electric field of the bubble. The accelerating field experienced by the electrons is the sum of the two fields. In an up-ward plasma density longitudinal profile, since the plasma density increases in the direction of laser propagation, the bubble shrinks as the laser propagates. In this case, the velocity of the bubble's back is continuously adjusted, and matches the velocity of accelerated electrons. Therefore, the electron bunch remains near the back of the bubble, experiencing a stable high accelerating field for the entire acceleration length (limited in this case only by the laser depletion length) and the tail electrons obtain nearly the same energy as that of the centre electrons.

Although the electron energy has been increased using the positive tapered plasma density, the presence of the sudden increase in energy spread shows the limitations of the phase locking mechanism in simulations which is *electron self-injection*. The electron self-injection happens, according to LWFA theory (Kostyukov, Nerush, Pukhov, & Seredov, 2009), when the plasma density increases up to the wave-breaking threshold which triggers a continuous injection of electrons, inhibiting further acceleration of the electron bunch (Figure 6-4). It is possible that this limitation exists only in this particular case because in the simulations the electron injection is triggered by a nanowire and not self-induced. In a LWFA experiment the electron injection happens when the electron bunch velocity matches the phase velocity of the bubble, therefore, in an upward plasma density electron re-injection could be inhibited by the increase in bubble phase velocity (which consequently increases the minimum electron energy required to self-inject in the bubble).

To prove experimentally the possibility of controlling the electron bunch velocity inside the bubble by shaping the longitudinal plasma profile an additional degree of freedom has been added to the gas nozzle used in the experiments. This has

been achieved by mounting the gas nozzle and solenoid valve assembly on a tilting setup as explained in Section 4.4.

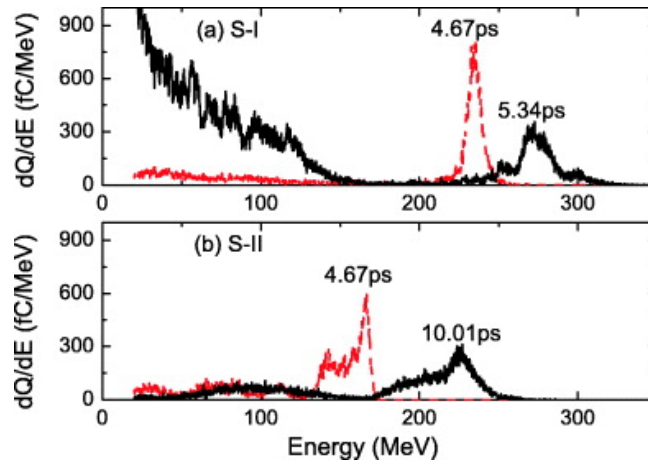


*Figure 6-4: Energy spectra at different times for cases S-I and S-II. Solid lines show the energy spectra of electron bunches before exiting the plasma, and dashed lines show the energy spectra at  $t = 4.67$  ps. (Wen, et al., 2010)*

The following work focuses on the study of the density ramp role in LWFA process assuming, for simplicity, that all the ramps are linear. The emphasis is put on the entrance ramp, where the laser focus plane usually is located and where electron injection and acceleration is expected to take place.

### 6.1.1 Influence of tilted gas jet with relatively short density ramps and in presence of gas density shocks

The first nozzle tested has been Nozzle A (parameters given in Table 2). The plasma density profiles are shown in Figure 6-5 and correspond to different tilting angles from  $0^\circ$  to  $30^\circ$  in the positive direction of the laser propagation axis (see Table 10). During the experiment, as the tilting angle is increased, the peak plasma density increases from  $1.1 \times 10^{19} \text{ cm}^{-3}$  to  $1.8 \times 10^{19} \text{ cm}^{-3}$  by changing the interaction point  $y$  and adjusting the backing pressure  $p$ .

run	$\Phi$	$y$	$z$	$p$	$z_1$	$z_2$	$z_3$	$\rho$
	( $^\circ$ )	(mm)	(mm)	(MPa)	(mm)	(mm)	(mm)	( $\times 10^{19} \text{ cm}^{-3}$ )
1	0	2.60	0.65	3.2	1.069	1.65	1.069	1.294
2	15	2.00	-1.8	3.0	0.981	1.381	1.173	1.507
3	30	1.55	-0.8	3.0	0.477	1.281	1.555	1.761

*Table 10: Experimental conditions for tilted Nozzle A*

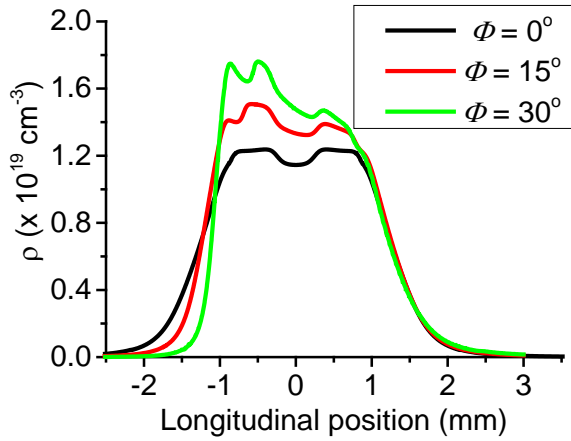


*Figure 6-5: The plasma density profiles corresponding to different gas nozzle tilting angles  $\Phi$ . The laser is incident on the gas jet from the left side.*

One of the predicted theoretical results (Wen, et al., 2010) is the electron energy tuning, a result observed here (Figure 6-7a), with the electron beam energy normal distribution shifted from an average  $118.7 \pm 1.7$  MeV (for  $0^\circ$  tilting) to  $129.9 \pm 1.5$  MeV (for  $15^\circ$  tilting) and  $135.6 \pm 3.0$  MeV (for  $30^\circ$  tilting).

The predicted energy spread reduction could not be seen in this part of the experiment (Figure 6-6 and Figure 6-7b), the mean energy spread varying from  $14.8 \pm 1.1$  % to  $13.2 \pm 1.0$  % and  $15.3 \pm 1.6$  %. There can be multiple reasons for this:

1. The longitudinal shape of the up-ramp density ramps (in this case it is almost linear but this is just an approximation).
2. The length of the entrance density ramp (where the electron injection and acceleration occurs) is too short for the electron beam to be phased locked long enough to lead to a significant energy increase and energy spread control.
3. The electron injection and/or acceleration occurs in the down-ramp part of the profile where the bubble size increases (since it depends inversely on the plasma wavelength), accelerating field decreases and consequently the electron energy decreases while the energy spread increases.
4. The longitudinal shape of the density profile that shows multiple density bumps due to presence of shocks and also two linear down-ramp densities are present.
5. The beam loading effect has not been compensated for.

The effect of the longitudinal density modulations and profile shape is not quantified yet, experimentally or theoretically, therefore the first and fourth hypotheses are not discussed here.

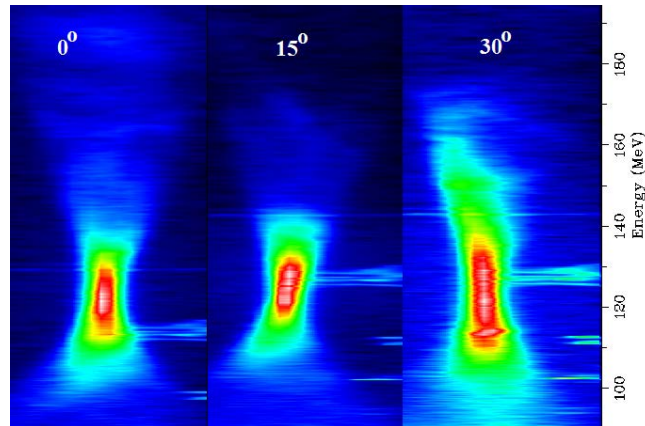


**Figure 6-6: False colour images of accumulated spectra corresponding to the three tilting angles:  $0^\circ$ ,  $15^\circ$  and  $30^\circ$ .**

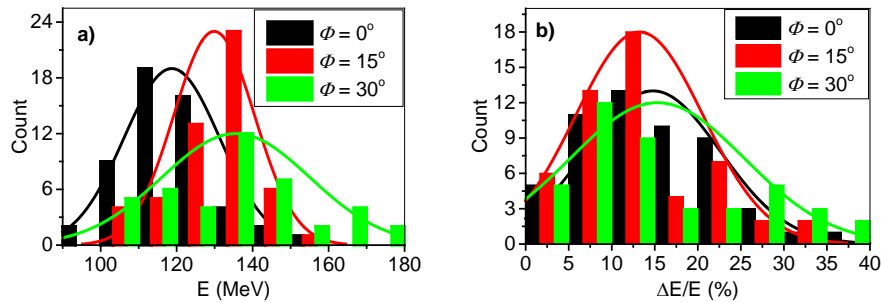


**Figure 6-7: Histograms of the electron peak energy (a) and energy spread (b) corresponding to different tilting angles. The energy tune is achieved but the energy spread is not controlled and remains quasi-constant.**

The most probable scenario that applies here is a combination between the second and the third hypotheses: the electron self-injection and acceleration start close to the end of the entrance ramp and the influence of the downward plasma density gradient is predominant. The LWFA in downward plasma density is discussed in greater detail in Section 6.2.

In a down-ramp density region, as the plasma wavenumber decreases, the phase velocity of the bubble decreases, which increases the number of self-injected electrons, as Kalmykov has shown for example in his theoretical study (Kalmykov, Yi, Khudik, & Shvets, 2009). This leads to an increase in the dark-current (the electrons forming the halo or the long tail observed in electron energy spectra). This conclusion is

confirmed by the experimental results presented in Figure 6-8 that show the histograms for total relative charge measured by Lanex1 (Figure 6-8b) and for charge in the main electron bunch measured by the espec (Figure 6-8a). When compared, the trend for relative charge shows a fast increase from 11 a.u for  $0^\circ$  tilting angle (which corresponds to a density profile with 1.069 mm ramp length and  $1.294 \times 10^{19} \text{ cm}^{-3}$  peak plasma density) to 20 a.u for the tilting angle  $15^\circ$  (corresponding to a density profile with 0.981 mm ramp length and  $1.507 \times 10^{19} \text{ cm}^{-3}$  plasma density) and a fast decrease to 11 a.u for  $30^\circ$  tilting angle (corresponding to a density profile with 0.477 mm ramp length and  $1.76 \times 10^{19} \text{ cm}^{-3}$  peak plasma density), while the charge in the main bunch shows almost no variation, thus the difference in the histograms distribution. A possible explanation for this trend is given further in this section.

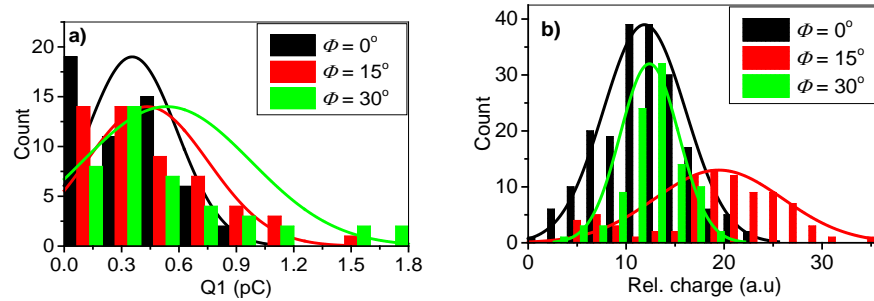


**Figure 6-8: Histograms of the charge of the electron bunch in the electron spectrometer a) and on LI b).**

Also the influence of the downward plasma density has a direct effect on the electron energy and energy spread. An increasing bubble size, due to increase in plasma wavelength, reduces the maximum acceleration field and leads to a decrease in electron energy and increase in energy spread. This assumption has been tested experimentally by changing the laser focal plane position inside the gas jet and quantifying the changes in electron beam parameters as shown in Figure 6-9.

It is observed that the electron beam quality changes rapidly as soon as the laser focal point moves towards the exit ramp of the density profile. For example, for  $30^\circ$  tilting angle (Figure 6-9b), when the laser focal plane is moved from -1.2 mm to 0 mm the electron beam energy decreases from  $\sim 134 \pm 2.7 \text{ MeV}$  to  $\sim 118 \pm 2.1 \text{ MeV}$ , the energy spread decreases from  $\sim 15 \pm 1.1 \%$  to  $\sim 11 \pm 0.9 \%$  and the charge in the main bunch decreases from  $\sim 0.65 \pm 0.04 \text{ pC}$  to  $\sim 0.39 \pm 0.04 \text{ pC}$ . The changes in energy are consistent with LWFA in a downward plasma density, as depicted above, including

the increase in dark current (see Figure 6-10) when the laser focal point is placed on the downward plasma density profile. The energy spread shows a decreasing trend because of the decrease in the charge in the main bunch which lowers the influence of the beamloading.

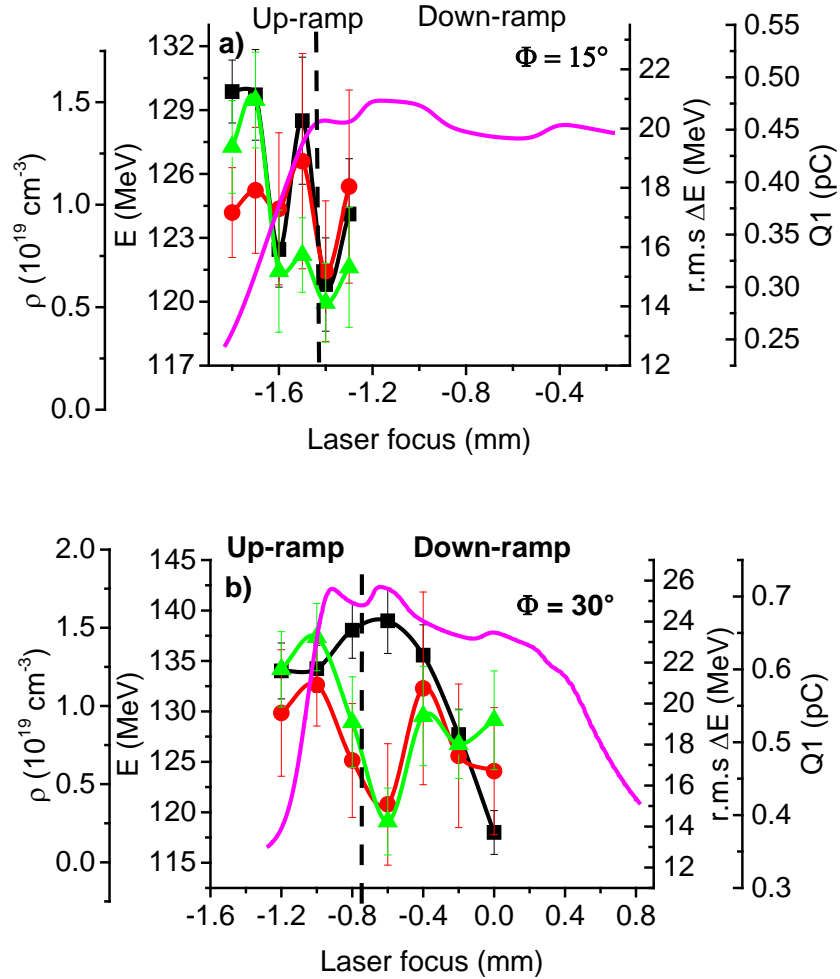


**Figure 6-9:** Evolution of the electron beam energy (black squares), r.m.s energy spread (red dots) and charge in the main bunch (green triangles) as the laser focal point is scanned inside the tilted gas nozzle A. Tilting angles are a)  $15^\circ$  and b)  $30^\circ$ . The density profiles (magenta solid line) are given at  $15^\circ$  and  $30^\circ$  tilt, respectively. The vertical dotted line approximate the beginning of the down-ramp plasma density

Using the data from Table 10 for the first ramp length corresponding to  $30^\circ$  tilting ( $z_1 = 0.475$  mm) and assuming that the laser focal plane is close to the edge of the plasma density profile when  $z = -1.2$  mm it can be seen that the density down-ramp starts when  $z$  is  $\approx -0.8$  mm. This position is consistent with the changes in the electron beam properties, the electron energy decrease and the dark current increase.

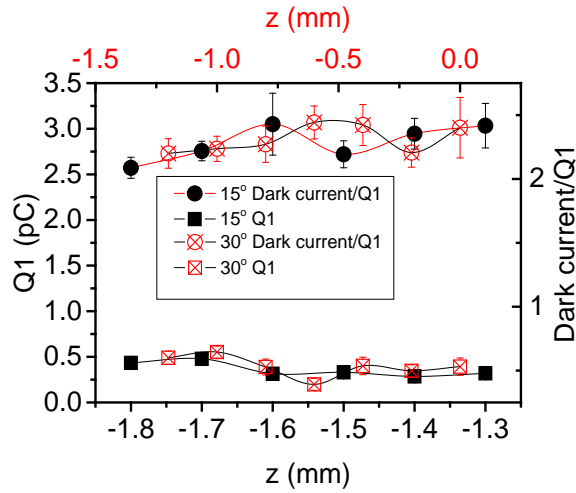


*Figure 6-10: The evolution of the dark current/Q1 ratio (circles) and of charge in the main bunch (full squares) as a function of the laser focal plane  $z$  inside the gas jet. Red data points correspond to 30° nozzle tilting and black data points correspond to 15° nozzle tilting.*

The assumption that the entrance ramp of the density profile is too short to reliably explore the phase locking mechanism is therefore supported by the experimental data and consequently no important electron energy increase and energy spread decrease could be observed in this part of the experiment. Based on these results the supersonic nozzle has been redesigned to generate longer plasma density ramps.

### 6.1.2 Influence of tilted gas jet with relatively long density ramps and smooth profile

For further investigation of the influence of the upward plasma densities two new nozzles have been designed: Nozzle 510 and Nozzle 511 (parameters are given in Table 2). For Nozzle 511 and Nozzle 510 the simulated plasma density profiles for different experimental conditions (backing pressure, tilting angle, height, etc.) are shown in Figure 6-11 and Table 11 respectively in Figure 6-18 and Table 12. The density profiles are shock-free in the interaction region with quasi flat-top and ramps (for nozzle in the vertical position).

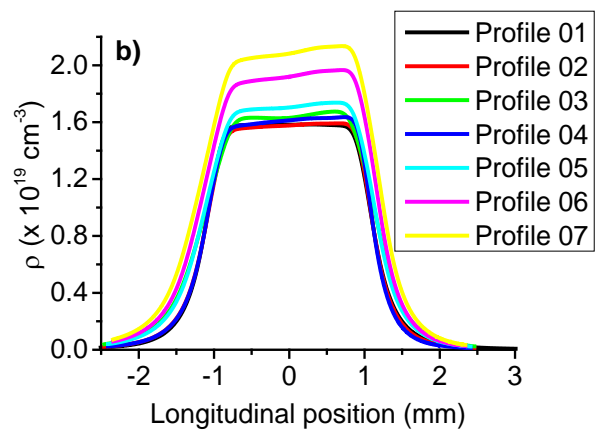
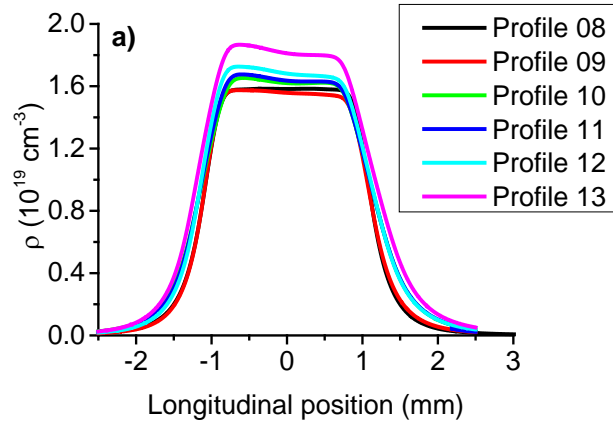


**Figure 6-11: The plasma density profiles generated by the Nozzle 511 tilted in different experimental conditions. Note the density profiles which are “smoother” compared with the density profile generated by the Nozzle A. Please see Table 11 for full conditions.**

Profile	$\Phi$ (°)	y (mm)	p (MPa)	z <sub>1</sub> (mm)	z <sub>2</sub> (mm)	z <sub>3</sub> (mm)	$\rho$ ( $\times 10^{19} \text{ cm}^{-3}$ )	m ( $\times 10^{19} \text{ cm}^{-3} \text{ mm}^{-1}$ )
1	0	2.40	2.5	0.946	1.526	0.946	1.578	1.668
2	10	2.00	2.5	1.027	1.445	0.947	1.547	1.506
3	10	2.75	3.0	1.399	1.242	1.207	1.630	1.165
4	15	1.60	2.5	1.065	1.453	0.846	1.573	1.477
5	15	2.45	3.0	1.311	1.327	1.122	1.679	1.280
6	20	2.30	3.5	1.477	1.333	1.104	1.881	1.273
7	20	2.55	4.0	1.511	1.421	1.181	2.032	1.344
8	0	2.40	2.5	0.946	1.526	0.946	1.578	1.668
9	-10	2.10	2.5	0.920	1.522	1.021	1.578	1.715
10	-10	3.10	3.0	1.226	1.344	1.355	1.655	1.349
11	-15	2.80	3.0	1.146	1.388	1.355	1.675	1.461
12	-20	2.35	3.0	1.082	1.393	1.355	1.724	1.593
13	-20	2.80	3.5	1.221	1.366	1.491	1.869	1.530

**Table 11: Experimental conditions for Nozzle 511**

The results with Nozzle 511 and Nozzle 510 confirm the electron bunch phase-locking mechanism as a method to control the parameters of the electron beam. The electron energy is tuned from  $135 \pm 2$  MeV up to  $171 \pm 2$  MeV (Figure 6-12a and Figure 6-13a), while the r.m.s energy spread is greatly improved (Figure 6-12b and Figure 6-13b): the normal distribution of the energy spread is shifted from an average of  $20.7 \pm 1.2\%$  down to  $8.9 \pm 0.9\%$ .

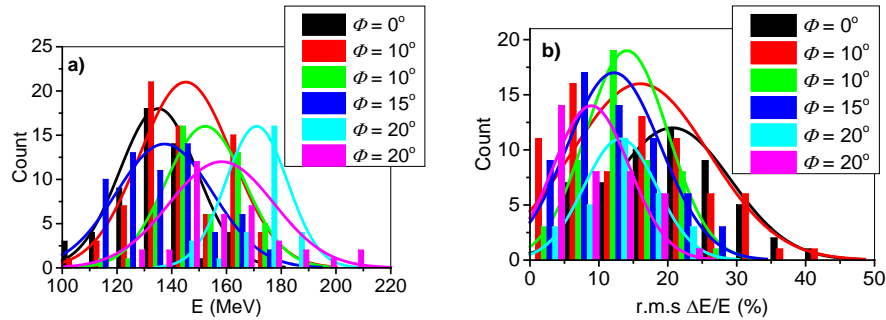


**Figure 6-12: Histograms of the a) electron peak energy and b) r.m.s. energy spread corresponding to density profiles of Nozzle 511 with positive tilting.**

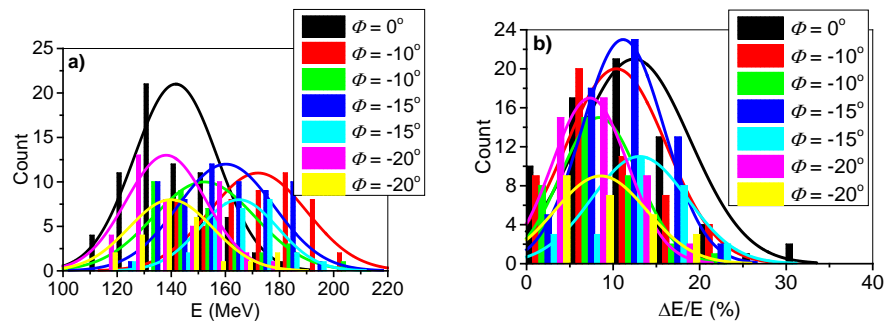


**Figure 6-13: Histograms of the a) electron peak energy and b) r.m.s. energy spread corresponding to density profiles of Nozzle 511 with negative tilting.**

Because the changes in peak plasma density and ramp length determine the evolution of the electron beam parameters, the entrance density ramp slope is chosen as a parameter to describe the experimental data. As described in Section 5.1, the slope represents the rate of density increase, which determines the evolution of the laser/bubble phase velocity. In this chapter, due to the complex density profiles caused by tilting the nozzle, care has been taken to determine the correct, local, density gradient. This aspect is important for negative nozzle tilting where the entrance ramp peak density cannot be taken at 95% from the maximum plasma density. It has been chosen here as local peak plasma density a position where the slope of the density ramp visibly changes.

The variation of the electron beam parameters as a function of the plasma density slope are shown in Figure 6-14a. The energy shows a strong increase from  $135.1 \pm 1.9$  MeV to  $172.1 \pm 2.5$  MeV when the plasma density slope is changed from  $1.66 \times 10^{19} \text{ cm}^{-3} \text{ mm}^{-1}$  to  $1.50 \times 10^{19} \text{ cm}^{-3} \text{ mm}^{-1}$ . In the same time, the relative and absolute energy spread show a significant decrease from  $20.6 \pm 1.2$  % ( $27.8 \pm 2.3$  MeV) to  $10.3 \pm 0.8$  % ( $17.7 \pm 2.0$  MeV). The only parameters that change in an undesirable way are the charge and divergence (shown further in this section), which follows closely the evolution of the energy spread but there is not necessarily a relationship between them.

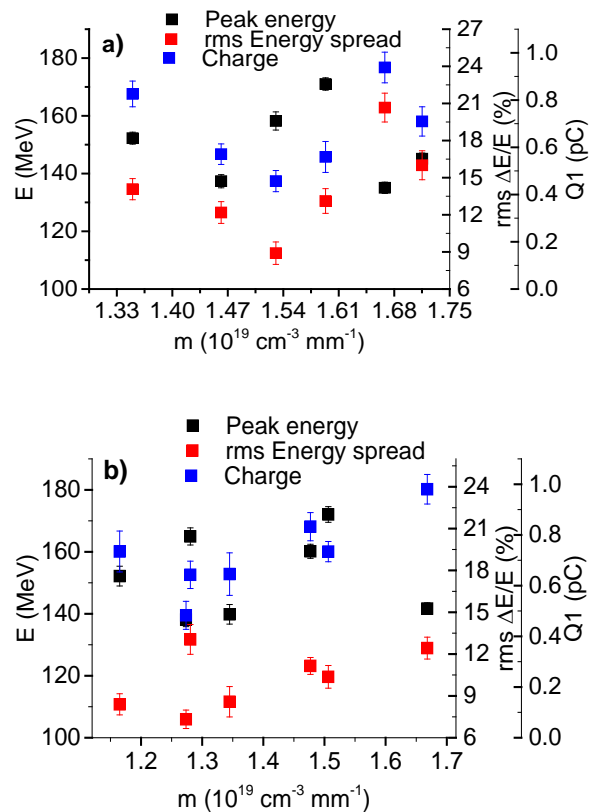


**Figure 6-14:** The mean values of electron beam parameters as a function of the entrance ramp slope. The electron beam shows a periodic strong enhancement as the slope varies. The vertical bars represent the standard error. The figure a) corresponds to data recorded with positive nozzle tilting and the figure b) corresponds to data recorded with negative nozzle tilting.

According to the theory presented in Section 2.3.2.3, for each different value of the slope the phase of the accelerating field advances or retards relative to the electron bunch. This phase adjustment during the period before the electron beam reaches dephasing allows the maximum attainable energy and energy spread to be

tuned but it also controls the divergence of the electron beam. The divergence of the electron beam depends on its betatron oscillation but also on the focussing force inside the LWFA channel which depends directly on the plasma density: a higher the plasma density means a smaller channel radius and consequently higher the radial focussing field. The above trend could form a characteristic signature of phase locking mechanism and can be used in experiments to identify the position of the electron bunch relative to the wake phase.

To complete the above scenario the relation between electron bunch size and its charge is taken into account. An increase in charge could determine an increase in transverse, longitudinal or both sizes. The transverse size increase can lead to a quadratic (Shanks, 2012) or cubic dependence (Rosenzweig & Colby, 1994) between charge and divergence but this dependence is not present in the data, for example from experimental run4 (Figure 6-15a). The increase in the r.m.s energy spread when the charge increases could be a proof that the longitudinal size of the bunch increases but it is difficult to separate from beam loading.

The trend of the divergence in Figure 6-15a and of electron energy in Figure 6-15b suggests that the bubble is formed in different locations in the density ramp, possibly due to fluctuations in either or both of the laser and plasma parameters, giving rise to the variation in the charge. This is similar to the experiment where the laser focal plane in the gas jet was systematically changed (see Section 5.1.3).

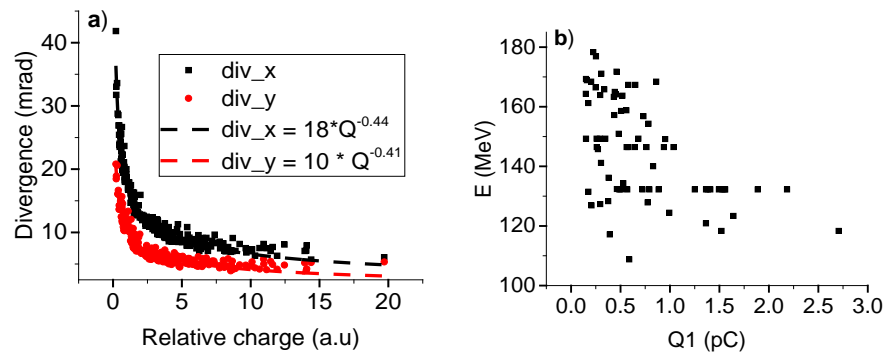


**Figure 6-15: a) The divergence and b) electron beam energy as a function of the charge.**

The variation of the bubble position generation is due to the variation of the laser beam parameters such as energy or spot size. A bubble formed at the beginning of the ramp will generate a low charge beam while a bubble formed farther away in

the ramp generate higher charge beam. In any case, the divergence and electron energy have the same trend which suggests that these two parameters are correlated. In order to evaluate this the electron energy, energy spread, charge and divergence are plotted as a function of the nozzle tilting angle (Figure 6-16).

Let's assume that the electron beam is phase-locked in the first half of the plasma period, although not in the most suitable position (close to the back of the wakefield bubble, where the accelerating field has maximum value). The increase in electron energy is accomplished by continuously adjusting the electron bunch longitudinal position closer to the back of the wake bubble. Experimentally this is accomplished for example by increasing the plasma density and/or gradient. This, theoretically, also increases the value of focussing field but also changes the parameters of the electron betatron oscillation inside the channel which controls the electron divergence as shown in Section 2.3.1. Thus the electron divergence consequently should decrease as the electron energy increases. It is obvious that this does not happen in Figure 6-15 where a ~ 61% increase in energy (from 110 MeV to 180 MeV) is expected to lead to ~ 68% reduction in divergence (or output angle). Using solely the formula (see Section 2.3.1) for the output angle the only parameters that could compensate for the reduction in divergence due to increase in energy is the injection radius  $r_0$  or the plasma density. It is unknown at this moment why these parameters would change so drastically when the other parameters related to plasma and the laser are kept constant.

Based on this available information it can be concluded that although the parameters of the laser and the plasma are kept constant during an experimental run there can be observed a significant variation in the parameters that determine the generated electron beam. It is possible that although the impact of variation in laser or plasma parameters is thought to be weak, that these results indicate a significant impact on the electron injection in the wake bubble and also may set the time of injection while the wake bubble is placed in different positions inside up-ramp plasma density.

Figure 6-16, shows variation of the tilt angle from  $0^\circ$  to  $\sim 20^\circ$ , which results in a variation in energy and divergence, with a sudden drop at  $\sim 15^\circ$ , while for positive tilting the variation happens from  $0^\circ$  to  $20^\circ$  with a sudden decrease at  $\sim 15^\circ$ . At the same tilting angles there are two values of energy and divergence because they have

been recorded in different experimental conditions i.e. using different plasma density slopes.

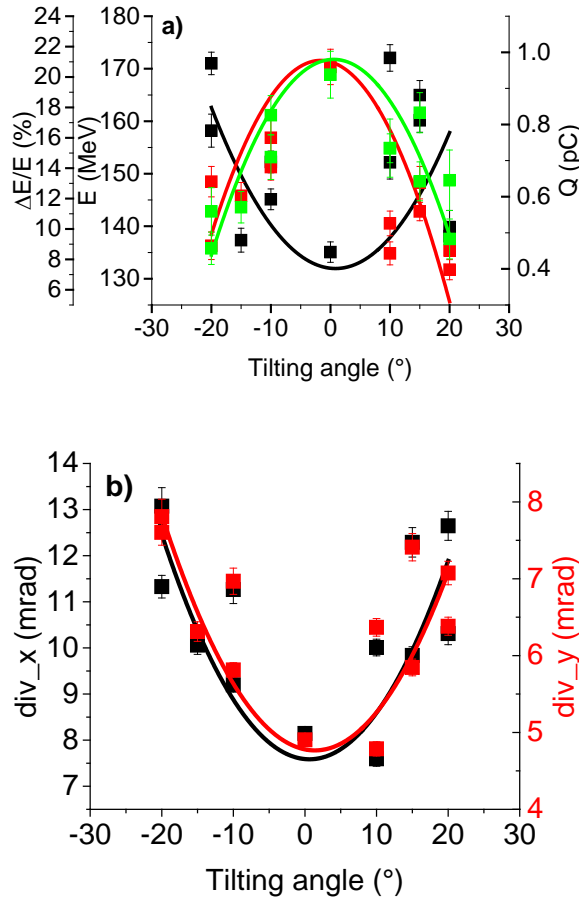


**Figure 6-16: a) The electron peak energy (black), energy spread (red) and charge (green) and b) the r.m.s divergence of the electron beam as a function of the nozzle tilting angle. Data points with the same tilting angle correspond to different plasma density slopes. The curves are drawn just to guide the eye and do not necessarily have a physical meaning.**

The relative energy spread decreases from  $20.7 \pm 1.1\%$  to  $7.3 \pm 0.7\%$  as the charge decreases from  $0.94 \pm 0.06$  pC to  $0.48 \pm 0.05$  pC. It is not very clear why the charge decreases so fast when the other parameters vary. There are two possible explanations:

- 1) When the nozzle is tilted between  $-20^\circ$  to  $20^\circ$ , in general, the peak plasma density is adjusted more than 78%, from  $1.57 \times 10^{19} \text{ cm}^{-3}$  to  $2.03 \times 10^{19} \text{ cm}^{-3}$  to obtain a stable electron beam. It is known from the theory of wakefield acceleration that the wakefield bubble size decreases as it propagates in an upward plasma density thus the amount of charge injected in the bubble is greatly reduced.

2) The second explanation takes into account the efficiency of the electron transport system, mainly the magnetic quadrupoles system. For the same dataset recorded in the same experimental conditions (Figure 6-17a) it can be seen that there is proportionality between the charge recorded on the Lanex1 (situated before the transport system) and the charge transported through the magnetic quadrupoles and recorded on espec. When the corresponding divergences are compared it is found that they are very low and almost the same, around  $8.5 \pm 0.5$  mrad for  $x$  axis and around  $4.5 \pm 0.5$  mrad for  $y$  axis thus the linear trend. This charge proportionality between Lanex1 and espec is not statistically valid when different datasets (which show different divergences) (Figure 6-17b) are compared because the divergence varies wildly between datasets (from  $7.5 \pm 0.1$  mrad to  $13.1 \pm 0.4$  mrad for the  $x$  axis and from  $4.8 \pm 0.1$  mrad to  $7.8 \pm 0.2$  mrad for the  $y$  axis).

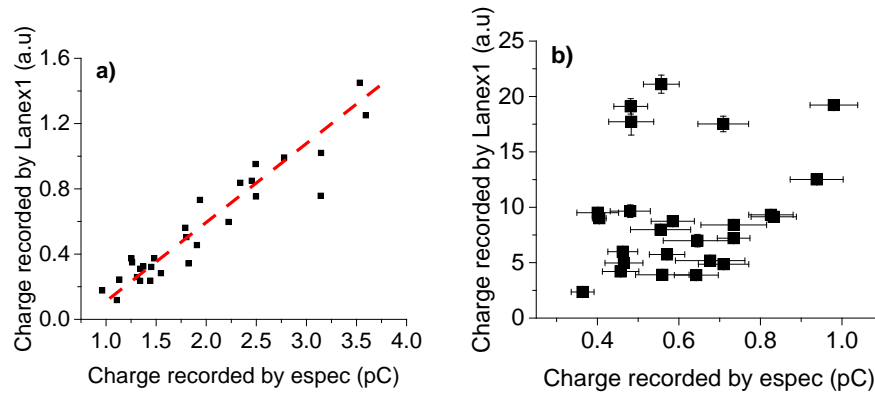


**Figure 6-17: The charge recorded by the espec versus the charge recorded by the Lanex1 for a) the same dataset and b) for different datasets**

Similar to Nozzle 511, the density profiles for Nozzle 510 are changed by changing the interaction point, backing pressure and tilting angle. The plasma density profiles are shown in Figure 6-18. Since no theoretical approach can predict yet what kind of density profile provides the best electron beam from a LWFA, here the nozzles have been designed such that the density profiles generated are slightly different but in a quantifiable way (see Section 3.2).

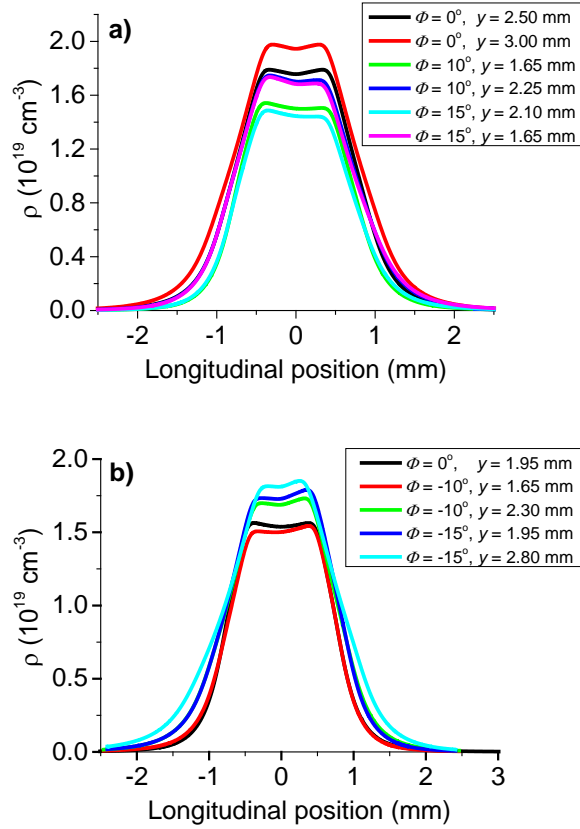


**Figure 6-18: Density profiles generated with the Nozzle 510. The nozzle is in straight or tilted geometry so that the density ramp slope can be varied.**

run	$\Phi$ ( $^\circ$ )	$y$ (mm)	$p$ (MPa)	$z_1$ (mm)	$z_2$ (mm)	$z_3$ (mm)	$\rho$ ( $\times 10^{19} \text{ cm}^{-3}$ )	$m$ ( $\times 10^{19} \text{ cm}^{-3} \text{ mm}^{-1}$ )
1	0.0	2.50	2.0	1.132	0.770	1.132	1.791	1.582
2	0.0	3.00	2.5	1.311	0.776	1.311	1.978	1.508
3	10	1.65	1.5	0.877	0.816	0.988	1.540	1.755
4	10	2.25	2.0	1.139	0.719	1.241	1.747	1.533
5	15	2.10	2.0	1.120	0.709	1.305	1.737	1.550
6	15	1.65	1.5	0.924	0.750	1.093	1.483	1.604
7	0.0	1.95	1.5	0.930	0.760	0.930	1.563	1.680
8	-10	1.65	1.5	1.032	0.737	0.908	1.505	1.458
9	-10	2.30	2.0	1.309	0.634	1.179	1.699	1.297
10	-15	1.95	2.0	1.303	0.670	1.101	1.733	1.330
11	-15	2.80	2.5	1.659	0.481	1.424	1.814	1.093

**Table 12: Experimental conditions for the Nozzle 510 tilted**

The Nozzle 510 provides, in general, density profiles with the same slope range as in the case of Nozzle 511 but the length of the plateau region is significantly shorter. The main effect of a shorter plateau length is to reduce the amount of time spent by electron bunches in a region where the effect of dephasing is increased.

The effect on electron beam quality is quite significant when Nozzle 510 is used. While the energy of electrons is controlled by tilting the nozzle as before (and subsequently changing the slope) the energy spread and electric charge stay quasi-constant around average values (8% for energy spread and 0.5 pC for charge).

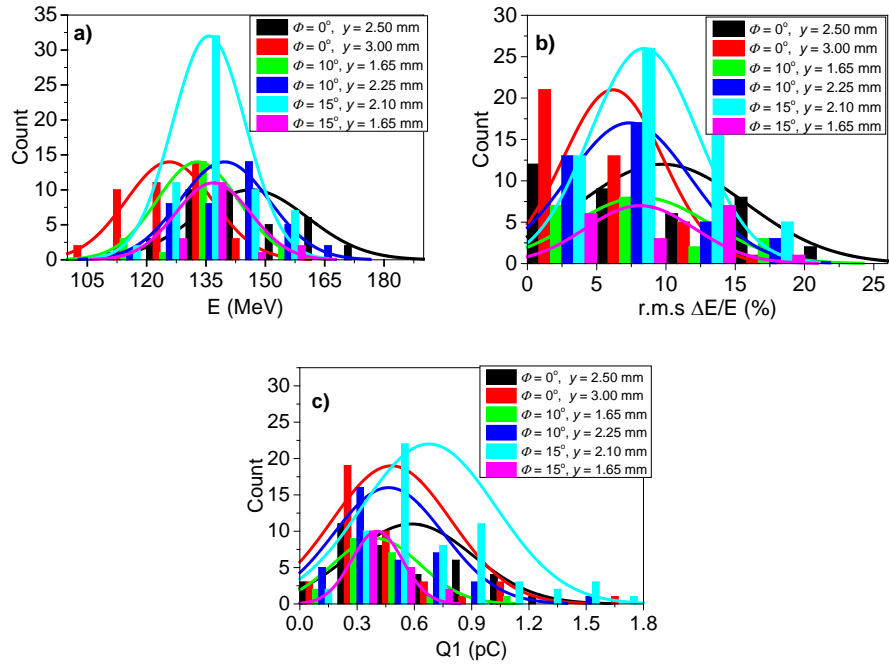


Figure 6-19: Histograms of a) electron energy, b) energy spread and c) charge when Nozzle 510 is used in experiments with positive nozzle tilting.

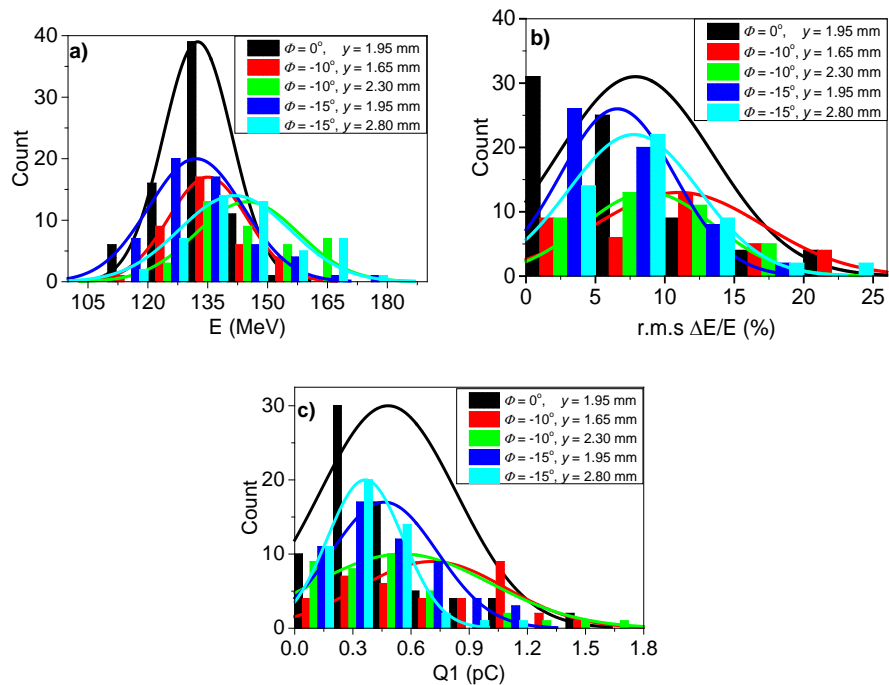


Figure 6-20: Histograms of a) electron energy, b) energy spread and c) charge when Nozzle 510 is used in experiments with negative tilting

The LWFA process is a highly nonlinear process thus the electron beam parameters do not necessarily scale linearly with plasma parameters. For the same tilting angle of the gas jet one might expect to generate electron beams with the same parameters, but from the figures shown above this is not the case since the plasma density profile is not the same. Even for 0° tilting angle the LWFA generates electron beams with a wide range of energies as can be seen for the results recorded with Nozzle 510 and Nozzle 511, shown in Table 13.

Although Nozzles 510 and 511 have very different geometries (510 has a 1.8 mm outlet and 511 has a 2.8 mm outlet) there are situations when they generate electron beams with almost the same parameters, as seen in the first and the last row of data in Table 13.

This result is obtained because the plasma density profiles are almost the same (ramp length, top profile and peak density). For LWFA experiments with different nozzles reported in the literature, the electron beam parameters are scaled with the outlet aperture of the nozzles (McGuffey, et al., 2012). Such experiments analysed using the plasma density profiles at the laser interaction point might lead to different interpretation of the results.

Tilt (°)	Nozzle	$z_1$ (mm)	$z_2$ (mm)	$\rho$	$y$ (mm)	E (MeV)	$\Delta E/E$ (%)	Q (pC)
0	511	0.89	0.84	1.56	1.95	131.5 $\pm 1.16$	9.86 $\pm 0.78$	0.55 $\pm 0.04$
0	510	1.13	0.77	1.79	2.5	146.5 $\pm 2.34$	9.74 $\pm 0.99$	0.58 $\pm 0.05$
0	510	1.31	0.77	1.97	3	125.7 $\pm 1.73$	6.18 $\pm 0.56$	0.48 $\pm 0.04$
0	510	0.93	0.76	1.56	1.95	132.4 $\pm 1.01$	7.88 $\pm 0.65$	0.48 $\pm 0.04$

*Table 13: The main parameters of the electron beam for Nozzles 510 and 511 at 0° tilting angle*

## 6.2 Very large gas nozzle tilting angle. LWFA experiments with down-ramp plasma density

Here, the experiments are designed to investigate laser wakefield acceleration with plasma media with a down-ramp density. To accomplish this, Nozzle A is tilted at 30° in the direction of laser propagation (Figure 6-21), which minimises the length

of up-ramp, to a length of  $z_1 = 0.477$  mm, and introducing a plateau  $z_2$  with a 15% down-ramp profile.

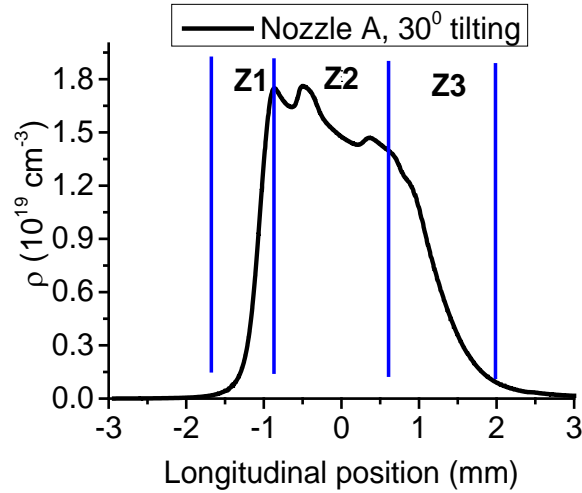


**Figure 6-21:** The plasma density profile for the experiments with a down-ramp density profile. This is split into three ramps, an up-ramp  $z_1$  and two down-ramps  $z_2$  and  $z_3$ . By focusing the laser inside the gas jet, the LWFA is constrained to the down-ramp density segment.

By changing the laser focal plane inside the gas jet, injection in the LWFA is initiated in the density down-ramp region. In this experiment the laser focal position is varied from an optimum position (where the most stable electron beams are obtained) to 1.2 mm towards the centre of the gas jet. The plasma wavelength increases with propagation in the down-ramp region. This causes the relative position of the wake to drift back as the laser propagates, decreasing the wake phase velocity even though the laser group velocity increases due to the lower density. This reduces the threshold for trapping by reducing the velocity electrons must achieve, and allows control over the trapping process by controlling the gradient.

The theory of electron injection developed by Kalmykov (Kalmykov, Yi, Khudik, & Shvets, 2009) is supported by experiments by Geddes (Geddes, et al., 2007), (Geddes, et al., 2008) where a 10 TW laser is focused at different positions inside a gas jet. The laser pulse duration is 47 fs FWHM length and spot size on target is  $7.5 \mu\text{m}$  FWHM. The charge of the accelerated electron beam is measured using an Integrating Current Transformer (ICT) placed immediately after the gas jet. The plasma density profile is Gaussian with a peak density of  $(2.2 \pm 0.3) \times 10^{19} \text{ cm}^{-3}$ .

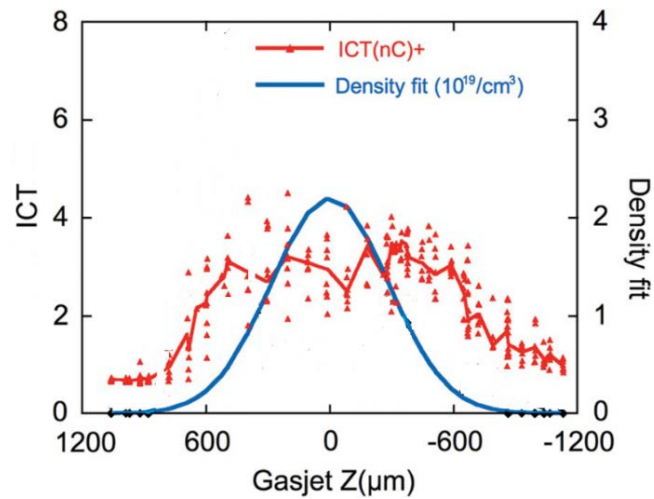


*Figure 6-22: Charge measured by the ICT as a function of gas jet position with respect to the laser focus. The Gaussian fit to the plasma density indicates the relative laser focus position in the profile. (Geddes, et al., 2008)*

In his experiments, Geddes observed an increase in charge as the laser focal point moves into the downward part of the density profile, while the energy spread is significantly improved (10 times smaller than the values obtained in their previous experiments). The average electron energy obtained is  $0.76 \pm 0.12$  MeV and an energy spread of 0.17 MeV FWHM. It can be observed that, although the intensity of the laser on target is quite high,  $I = 1.7 \times 10^{19}$  W cm<sup>-2</sup> and  $a_0 = 2.8$ , the energy of the electrons is relatively low. This observation is explained by considering that these results are obtained when the laser focal plane is situated around 400 μm before the end of the plasma profile, therefore the acceleration length is very short so that the electron beam is extracted long before beam loading or electron dephasing changes significantly the parameters of the electron beam. This conclusion explains why the energy spread is relatively low (compared with their previous results) despite the large charge injected into the bubble.

One of Geddes' results has been confirmed in the work presented in this thesis: the charge increase (Figure 6-23). Indeed, the relative charge (the charge recorded on L1) shows a continuous increase as the laser focal plane moves from the edge of the gas jet towards the centre of the gas jet, where the two down-ramps are located (see Figure 6-21). An interesting trend observed is that the charge in the main bunch (the mono-energetic peak) does not following the total charge (relative charge) trend. Also

the energy spread follows closely the trend of charge in the main bunch, as expected due to beam loading (Figure 6-24).

The electron peak energy increases as the laser focal plane moves towards the centre of the gas nozzle until it reaches a maximum and then starts to decrease. The electron energy decrease cannot be due to increased charge in the bunch but to a decrease in plasma density, which limits the accelerating field (for example, using linear theory it is known that the accelerating field is proportional to the square root of the plasma density). It can be argued that the decrease in electron energy is due to the reduction in acceleration length. This cannot be the case here because it is not followed by a reduction in energy spread (absolute and normalised).

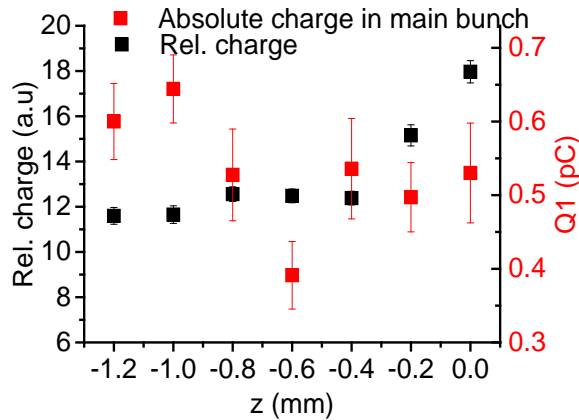


**Figure 6-23: Evolution of the relative charge and absolute charge as the laser focal plane varies from -1.2 mm (edge of the gas nozzle) towards 0 mm (centre of the gas nozzle)**

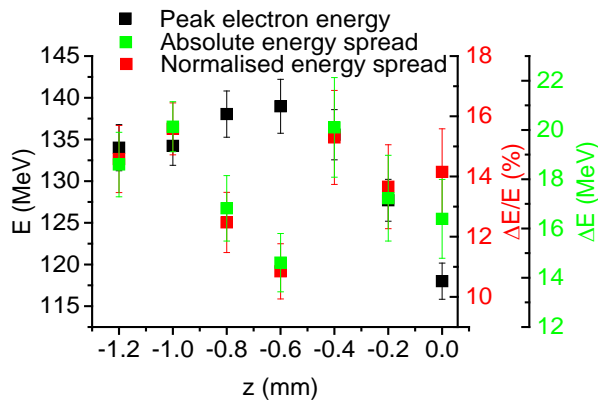


**Figure 6-24: Evolution of the energy, absolute energy spread and relative energy spread as the laser focal position varies from -1.2 mm (edge of nozzle) to 0 mm (centre of nozzle). The vertical bars represent the standard error.**

The variation of the electron beam charge (total and in the main bunch) shows that there is no advantage in using the downward plasma density ramp. Since the increase in the total electron beam charge is not observed in the main electron bunch, it can be concluded that the extra-injected charge forms a large diverging electron beam (or “halo”) that cannot be transported downstream and used in experiments that require a low energy spread and low divergence electron beam.

This conclusion does not necessarily exclude the use of downward plasma densities in LWFA acceleration experiments. There is the possibility of using this method in a multi-stage accelerator (Trines, et al., 2010) to generate a low energy, low energy spread and high charge injection electron beam. This electron beam can be injected into a second stage, for example in an up-ramp plasma density and accelerated to higher energies.

## **7 Conclusions**

### **7.1 Summary of results**

#### **7.1.1 Supersonic gas jet simulations and optimisation**

This thesis explores experimentally the influence of different plasma density profiles on the parameters and quality of an electron beam generated by a laser wakefield accelerator. The emphasis of the study is on the possibility of controlling the electron beam properties by tailoring the longitudinal plasma profile.

The density profiles are produced using different types of supersonic nozzles and different experimental conditions. The theory of supersonic fluid flow through a nozzle and numerical simulations has been presented in Chapter 3. Supersonic nozzles are attached to a fast solenoid valve that is optimised for LWFA experiments, using methods presented at the end of Chapter 3. The optimisation of solenoid valves aims to maximise the fluid flow rate, while maintaining the other valve parameters in an optimum operation range. Without this optimisation, a fit between numerical simulation of fluid flow and experimental characterisation results cannot be carried out.

#### **7.1.2 LWFA experiments with vertical nozzles**

A range of plasma density profiles are produced for different experimental conditions (backing pressure, nozzle geometry, laser gas-jet interaction point, etc.), for the production of electron beams. Top-hat shaped plasma density profiles are studied in Section 5.1.1. It is observed that the parameters of the density ramp at the beginning of top-hat profile have a large influence on the quality of the electron beam. Plasma density profiles with the same peak density show large differences in experimental results: a factor of 1.4 difference in charge, 1.1 difference in electron energy, 2 difference in pointing and 1.45 difference in energy spread. These differences in electron beam properties are linked to the density ramps both at the beginning and end of the density profile. It is argued that the first ramp controls the laser pulse nonlinear

evolution due to relativistic self-focussing and pulse compression. Thus, the plasma ramp density properties affect both the laser evolution in the LWFA and therefore the quality of the accelerated electron beam.

It is observed in Section 5.1.3.1 that the angular distribution of the centroid of the electron beam depends on the position of the laser focal plane inside the gas jet. This result can be explained if one takes into account that the electron beam properties depend on the properties of the accelerating structure, *i.e.* the LWFA bubble. A laser wavefront that presents aberrations can modify the conditions in which the bubble regime is excited.

Depending on the propagation length, *i.e.* the position of the laser focal plane inside the gas jet, the angular electron distribution can have a range of shapes, from round to elliptical. This result can be used to diagnose indirectly the properties of the laser taking into account that an asymmetric laser spot or a laser wavefront with aberration leads to creation of an asymmetric wakefield bubble.

It is shown in Section 5.1.3.2 that when the laser focal position is placed at the beginning of the gas jet, and the gas jet is relatively long, a plasma region can exist immediately after the LWFA ion channel. Due to the interaction between plasma and the electron beam, which depends on the incidence angle of the electron beam on the plasma interface between plasma and LWFA channel, the electron beam is deflected at various angles depending on the parameters of the electron beam such as: pointing, charge, bunch length, and energy. The electron deflection due to asymmetric plasma lens effect can be quantified using a formula that takes into account the properties of the electron beam and the plasma properties (see Section 8.1).

This effect is found in many experimental results in the present work, where the above conditions are fulfilled. The plasma lens effect (Muggli P. , et al., 2001) is identified in this work through a dependence of the electron beam pointing on charge: high charge beams are agglomerated towards the centre of the screen while the low charge beams are distributed more towards the edge of the detecting screen (see Section 5.1.3.2).

The difference between theoretical and experimental electron pointing variation due to asymmetric plasma lens is found to be relatively small, around 10%.

### 7.1.3 LWFA experiments with tilted nozzles

Chapter 6 investigates the effect of complex plasma profiles on the laser wakefield acceleration. A complex plasma profile refers to any kind of density profile except top-hat. To generate complex density profiles the gas jet is tilted relative to the direction of the propagation of the laser. The slope of the density ramp that first interacts with the laser is varied by tilting the gas jet, thereby controlling the phase velocity of the back of wakefield bubble in such a way that the electron beam maintains the same phase relative to the accelerating field. Manipulation of the plasma density ramp is accomplished by varying the backing pressure, interaction point or tilt angle and employing different geometries for the nozzle.

Important electron beam improvements in energy spread and energy control, predicted by simulations, are demonstrated experimentally in Section 6.1. The electron energy is tuned from 120 MeV to 172 MeV and the r.m.s energy spread is reduced from 22% to 8.6% by tilting the nozzle at various angles relative to the direction of propagation of the laser. A fully characterised electron beam for a range of plasma profile parameters can be used in experiments where, for example, electron energy tuning is required.

Downward ramp plasma density influence on LWFA is investigated in Section 6.2 by tilting the gas jet in the direction of the propagation of the laser and placing the laser focal position in the downward part of the density profile. It is demonstrated that the amount of charge injected into the bubble can be increased using a downward plasma density gradient but this does not necessarily lead to an increase in charge in the mono-energetic part of the electron spectra. Despite this limitation, it is concluded that a downward plasma density ramp can be used in a multi-stage LWFA, for example before an upward plasma density ramp: while the downward plasma density maximises the amount of charge injected, the upward plasma density produces the increase in electron energy.

## **7.2 Future developments of the present work and suggestions for improvement**

### **7.2.1 Supersonic gas jet generation and characterisation**

It has been shown in Chapter 3 that the gas jet parameters generated by a Laval nozzle depend not only on the geometrical dimensions of the nozzle but also on the parameters of the gas used. In this context a further study could clarify for example if the temperature of the gas, which changes during the day, affects quantifiably the parameters of the gas jet. In that case it might be recommended an active control of the gas bottle pressure so that the plasma density profile is kept constant during the experiments thus increasing the reproducibility of the results. In this context an interferometer which is designed to characterise the neutral gas would be recommended. A Mach-Zehnder interferometer is installed in the ALPHA-X beamline but it has been set up to diagnose the LWFA plasma channel and not the gas jet before interaction with the laser. As shown in Section 3.3 the density profile obtained with the present interferometer depends on the intensity of the laser on the gas jet thus giving no information about the gas jet density profile before the interaction.

### **7.2.2 Electron beam transport and characterisation**

While this thesis has been written a detailed study on the influence of the electron transport system on the electron beam measured parameters has been published by Manahan (Manahan, 2013) in her PhD thesis. Based on those results and the results presented in Section 6.1.2 which show that the charge transported through the ALPHA-X beamline depends on the divergence of the electron beam it is recommended that all the diagnostic systems are placed as close as possible to the source of electrons. This not only will reduce the electron beam travel time, thus minimising the charge lost but also will permit the exploration of new phenomena such as those related to the electron beam betatron oscillation. This could be relatively easily achieved by placing an electron spectrometer immediately after the LWFA with appropriate orientation of the magnetic field relative to the betatron oscillation plane for its observation on a fluorescent screen.

### **7.2.3 Energy and energy spread control by tilted nozzle**

The most important result in this work is the energy spread improvement and energy tuning when upward plasma density ramps are used in experiments. In this work the laser parameters are at the limits of what is required to access the bubble regime directly, therefore the LWFA process relies on the nonlinear evolution of the laser pulse in plasma. Fluctuations in the parameters of the laser or plasma can therefore lead to fluctuations in the electron beam quality.

Energy spread reduction and energy tuning must be validated for higher laser parameters, such as laser energy above 1 J and  $a_0 \geq 1$  on target. If the results from this thesis regarding the phase-locking mechanism can be extrapolated then a 50% electron energy increase is expected while the energy spread is halved for any laser intensities greater than the ones used in experiments here.

### **7.2.4 LWFA experiments with upward and downward plasma density ramps**

The experimental results obtained with upward and downward plasma density ramps further opens the road towards staged plasma accelerators where different plasma profiles can be employed to control different parameters of the electron beam. For example, a downward plasma density profile can maximise the amount of charge trapped in the wakefield bubble and an up-ramp density profile can increase the electron energy and reduce the energy spread. Therefore, upward, downward and homogeneous plasma density profiles can be used together to control the parameters of the electron beam over long acceleration distances. Such an experiment can use, for example, a plasma profile proposed by Pukhov et al. (Pukhov & Kostyukov, 2008), where the electron beam injection and acceleration is controlled for the entire acceleration length. Compared with a homogenous plasma profile (dashed curve in Figure 7-1), the advantage of using this kind of longitudinally shaped profile is obvious: the energy gain is significant while the laser parameters are kept constant.

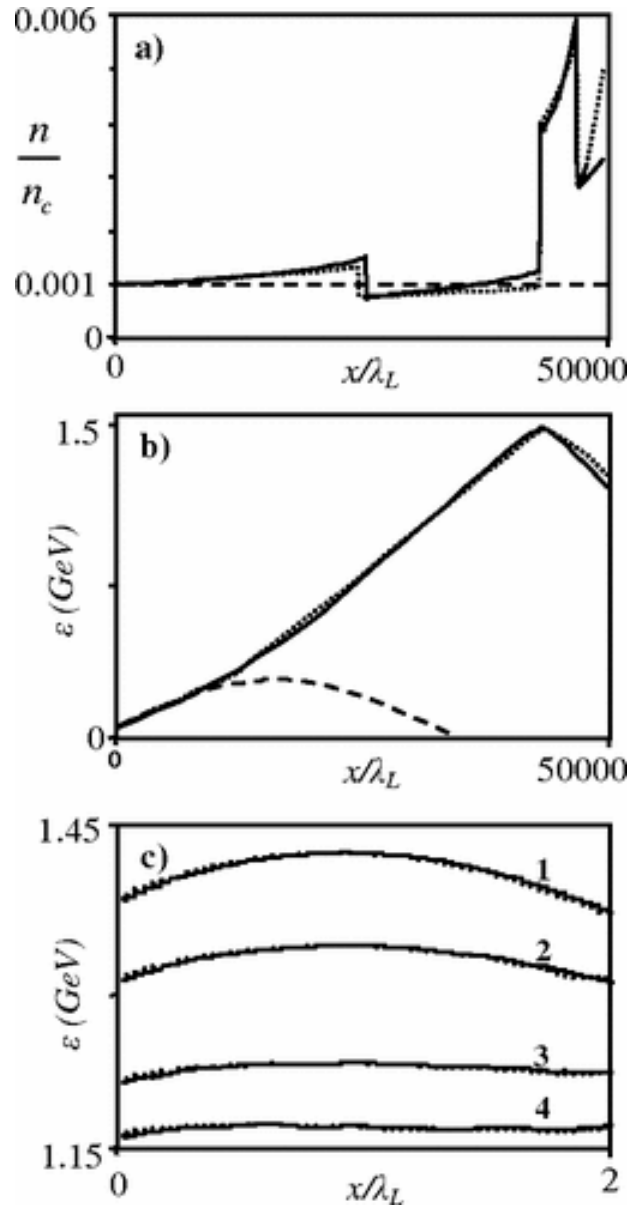


**Figure 7-1: Electron bunch acceleration and energy spread reduction in plasma layers: (a) the plasma-density profile, (b) the mean energy of the electron bunch, (c) electron energy vs electron position in the bunch. Electrons are accelerated by the first laser pulse in the first two layers ( $0 < x < 43370\lambda_L$ ), whereas they are decelerated in the third and fourth layers ( $43370\lambda_L < x < 49820\lambda_L$ ). The solid and dotted lines correspond to the particle-in-cell (PIC) simulation results and theoretical estimates, respectively. To compare, the dashed line shows acceleration in homogeneous plasma with the constant density  $n_0 = 0.001n_c$ . The energy distributions in frame (c) are shown at the beginning of the deceleration at  $x = 43370\lambda_L$  (line 1), at  $x = 45370\lambda_L$  (line 2), at  $x = 47370\lambda_L$  (line 3), and the end of deceleration at  $x = 49820\lambda_L$  (line 4), respectively. The laser pulses are circularly polarised with Gaussian profile and wavelength  $1 \mu\text{m}$ . The laser pulse parameters are  $T = 10.6\lambda_L/c$ ,  $a_0 = 0.6$  for the pulse on the acceleration stage and  $T = 5.3\lambda_L/c$ ,  $a_0 = 0.5$  for the pulse on the deceleration stage. The image and caption is taken from Pukhov (Pukhov & Kostyukov, 2008).**

The effect of the shape of the plasma density ramp on the quality of the electron beam has not been studied in this thesis. The ramps have been assumed linear for simplicity but a more detailed study, experimental and theoretical, would be required

to clarify if the electron beam parameters are affected by the shape of the upward or downward plasma density.

### **7.2.5 Plasma lens effect investigation. Symmetric and asymmetric case**

To investigate the existence of the plasma lens effect for both symmetric and asymmetric cases, it is required that the experiments presented in 5.1.3 are replicated and the gas jet monitored in terms of magnetic field and refractive index. The obtained data, in conjunction with simulations, can be used to create a model to confirm (or not) the existence of the plasma lens effect in wakefield accelerators. While this thesis was written some studies, theoretical and experimental, have been published confirming that indeed the plasma lens effect can be encountered in a wakefield accelerator and even excite a nonlinear wakefield in the PWFA regime. For example Lehe (Lehe, Thaury, Guillaume, Lifschitz, & Malka, 2014) show that, theoretically, a gas jet placed after a wakefield accelerator can reduce the divergence of the incident electron beam, due to the plasma effect, by at least a factor of three while Masson-Laborde (Masson-Laborde, et al., 2014) shows experimentally that an electron beam from a LWFA can excite a wakefield in a second gas jet and accelerate an electron beam in PWFA regime.

It is obvious that the presence of a plasma lens cannot be ignored in the LWFA especially when the gas jets are millimetres long and the theoretical acceleration length is much less than the gas jet length thus creating conditions for the electron beam to interact with the plasma as it propagates.

## 8 Appendices

### 8.1 Plasma lens effect: asymmetric case

The formulae derived here follow closely those derived by P. Muggli (Muggli P. , et al., 2001). A dense electron beam with density  $n_b$  is incident on a planar boundary forming a plasma medium with plasma density  $n_0$ . For simplicity, Coulomb scattering is neglected in this analysis. It is considered that  $n_b > n_0$ . As it enters the plasma, the head of the electron beam repels the plasma electrons out to a radius  $r_c$  (Whittum & Sessler, 1990) and the remaining ions form a positive charge channel through which the electrons following the head travel. An estimation of the ion channel radius is given by (Whittum & Sessler, 1990):

$$r_c = \alpha \sqrt{\frac{n_b}{n_0}} r_b \quad (8.1)$$

where  $r_b$  is the electron beam radius and  $\alpha$  is a small factor that depends on electron beam length and plasma wavelength through relationship  $\alpha \propto \frac{8\sigma_z}{\lambda_p}$ .  $\alpha$  takes the value 1 for an electron bunch longer than the plasma wavelength, 2 when the plasma wavelength equals the electron bunch length (due to resonance) and less than one when the electron beam length is very short compared with the plasma wavelength.

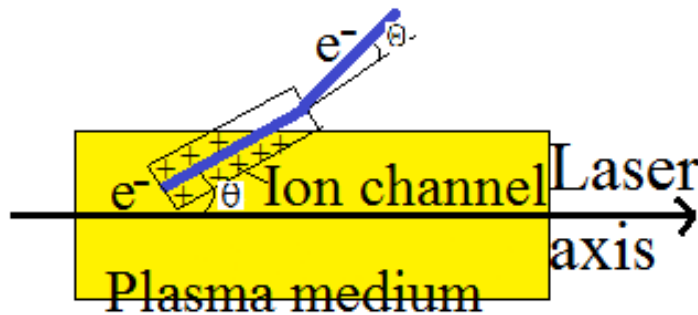


*Figure 8-1: Deviation of the electron beam due to refraction at a plasma boundary medium. The incidence and deviation angles are exaggerated for demonstration purposes.*

The existence of the ion channel provides a focussing force on the electron beam (Chen P. , 1987). When the electron beam incidence angle on the plasma

boundary is not zero, the plasma channel becomes asymmetric and a deflecting force is produced in addition to focussing forces. Thus, the creation of an asymmetric plasma lens can lead to a deflection of an electron beam, this effect being similar with refraction of photons on a dielectric boundary.

The force that acts upon the electron beam can be estimated using Coulomb's law (Whittum & Sessler, 1990):

$$F = -eE = 2n_0 e^2 r_c \quad (8.2)$$

The impulse on the beam is the force (8.2) multiplied by the time spent by the electron beam near the edges of plasma boundary  $2r_c \sin(\theta/c)$ . The scaling law for the deflection angle  $\Theta$  is obtained by dividing the impulse on the beam by the electron beam parallel momentum  $\gamma m_0 c$ :

$$\Theta = \frac{8\alpha Q r_c}{\pi e \sqrt{2\pi} \gamma \sigma_z \sin \theta} \quad (8.3)$$

From the formula (8.3) it can be observed that the deflection of an electron beam in an asymmetric plasma lens is directly proportional to the electron beam charge and inversely proportional to the electron beam energy, bunch length and incidence angle.

## 8.2 Laser wavefront aberrations

It has been shown in this thesis that a distorted laser wavefront (which is equivalent to a laser pulse intensity tilting relative to the direction of propagation) can generate a distorted wakefield bubble which consequently affects the parameters of the accelerated electron beam, especially the pointing. In this section a very short account of the laser wavefront aberration is given. More detailed information can be found in the published literature such as Martinez (Martinez, 1986), Hebling (Hebling, 1996) Pretzler (Pretzler, Kasper, & Witte, 2000) or Akturk (Akturk, Gu, Zeek, & Trebino, 2004).

A “perfect” Gaussian beam has the temporal amplitude  $E_t(t)$  completely separable from the spatial amplitude  $E_x(x)$ . The same relationship is preserved for its corresponding functions in Fourier space:  $E_\omega = F(E_t)$  and  $E_{k_x} = F(E_x)$ . In the presence of spatio-temporal distortions the spatial and temporal amplitudes are coupled and, depending on the relationship between them, three kinds of connected laser pulse wavefront aberrations can be defined. For simplicity it is assumed that only one spatial direction is affected ( $x$ ) and the influences in the longitudinal direction are ignored:

$$E(x, t) = E_x(x) E_t\left(t + \frac{dt_0}{dx}(x - x_0)\right) \text{ Pulse front tilt} \quad (8.4)$$

$$E(k_x, \omega) = E_{k_x}\left(k_x + \frac{dk_{x_0}}{d\omega}(\omega - \omega_0), k_y, k_z\right) E_\omega(\omega) \text{ Angular chirp} \quad (8.5)$$

$$E(x, \omega) = E_x\left(x + \frac{dx_0}{d\omega}(\omega - \omega_0), y, z\right) E_\omega(\omega) \text{ Spatial chirp} \quad (8.6)$$

The pulse front tilt (PFT) defines the tilt of the intensity envelope relative to the direction of propagation but with the preservation of the angle ( $90^\circ$ ) between wavefront and propagation direction.

The spatial chirp (SC) is defined by a separation of different frequencies in the transverse direction relative to the direction of propagation and is characterised by a spatial dispersion  $\zeta = dx_0/d\omega$ , which depends on the characteristics of the optical

system, or a frequency gradient  $\nu = \frac{d\omega_0}{dx} = \frac{\zeta}{\zeta^2 + \left(\frac{w_0}{\sigma_\omega}\right)^2}$  that depends on the optical

system and also on the parameters of the initial laser pulse (through the spatial width  $w_0$ , where  $\sigma_\omega$  is the bandwidth in Fourier space). In the presence of a spatial chirp, the initial laser pulse duration increases (due to a decrease in the bandwidth  $\sigma_\omega$ ) and the laser spot size grows (due to the spatial separation of different frequencies).

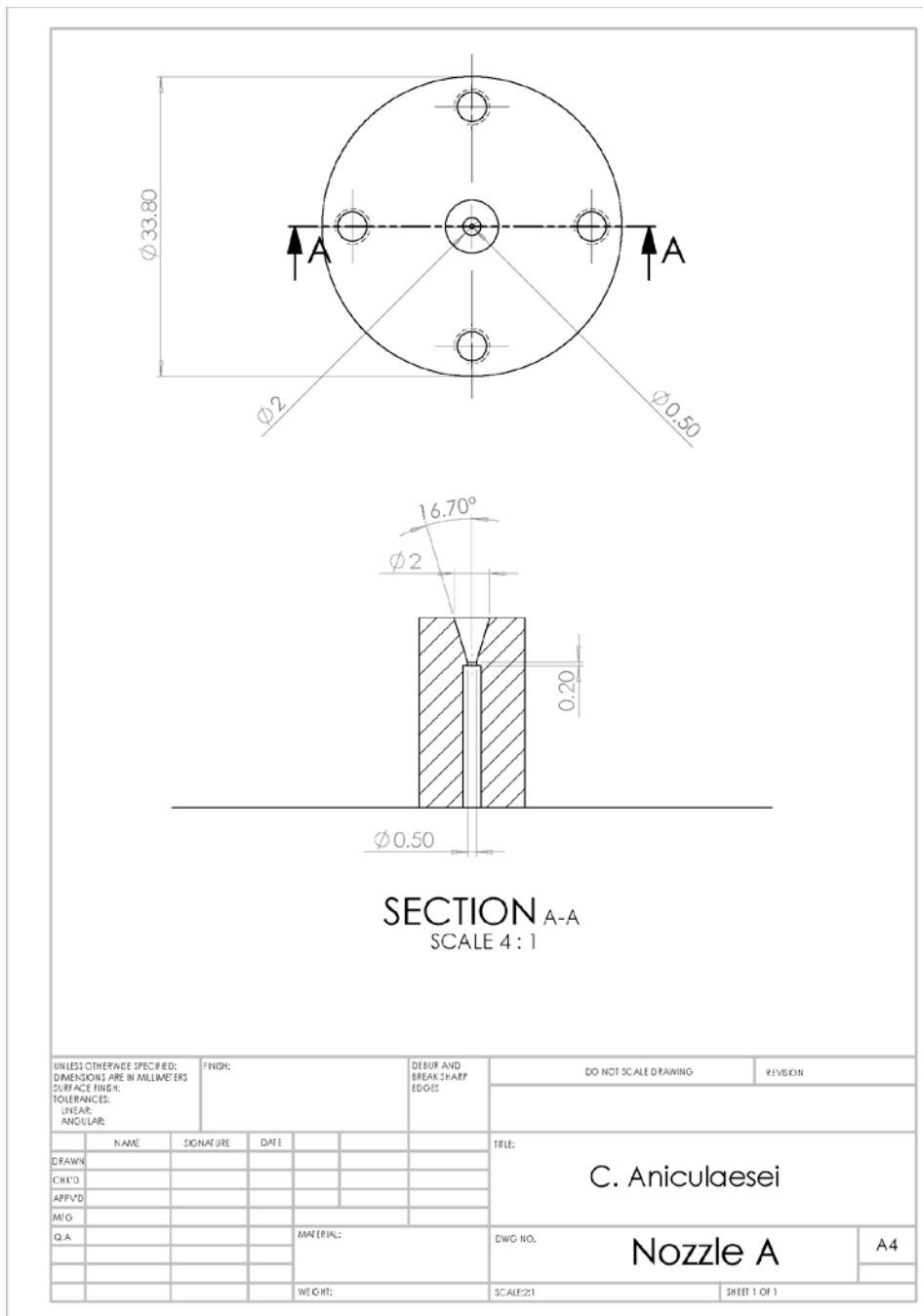
The angular chirp (AC) describes the situation where the virtual phase fronts of different frequencies propagate at different angles relative to the direction of propagation. This usually happens after the laser pulse passes through an optical element such as a prism or a diffraction grating which are the usual components of a CPA system. The angular chirp introduced by a diffraction grating can be expressed by a simple formula (Akturk, Gu, Zeek, & Trebino, 2004), which takes into account the diffraction grating spacing  $s$ , the diffraction angle  $\beta$  and the diffraction order  $m$ :

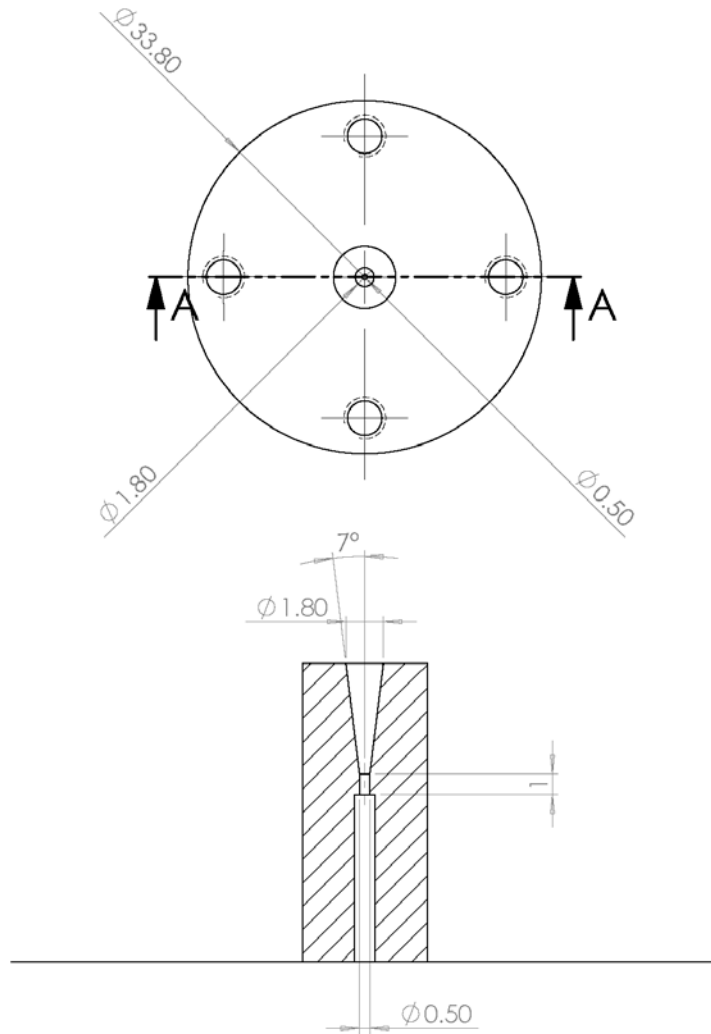
$$\frac{d\alpha}{d\lambda} = \frac{c}{\lambda_0} \frac{dk_x}{d\omega} = \frac{m\lambda_0}{s \cos \beta} \quad (8.7)$$

where  $d\alpha/d\lambda$  is the angle between the propagation direction of the whole pulse and the direction of the virtual phase front of a certain wavelength component.

As shown by Popp (Popp, et al., 2010) the above formulae represent aspects of the same effect: an angular chirp determines a pulse front tilt but the same front tilt can be caused by a combination of spatial and temporal chirp. It must be stressed here that the angular chirp and spatial chirp are created only by the optical system and are independent of the input pulse.

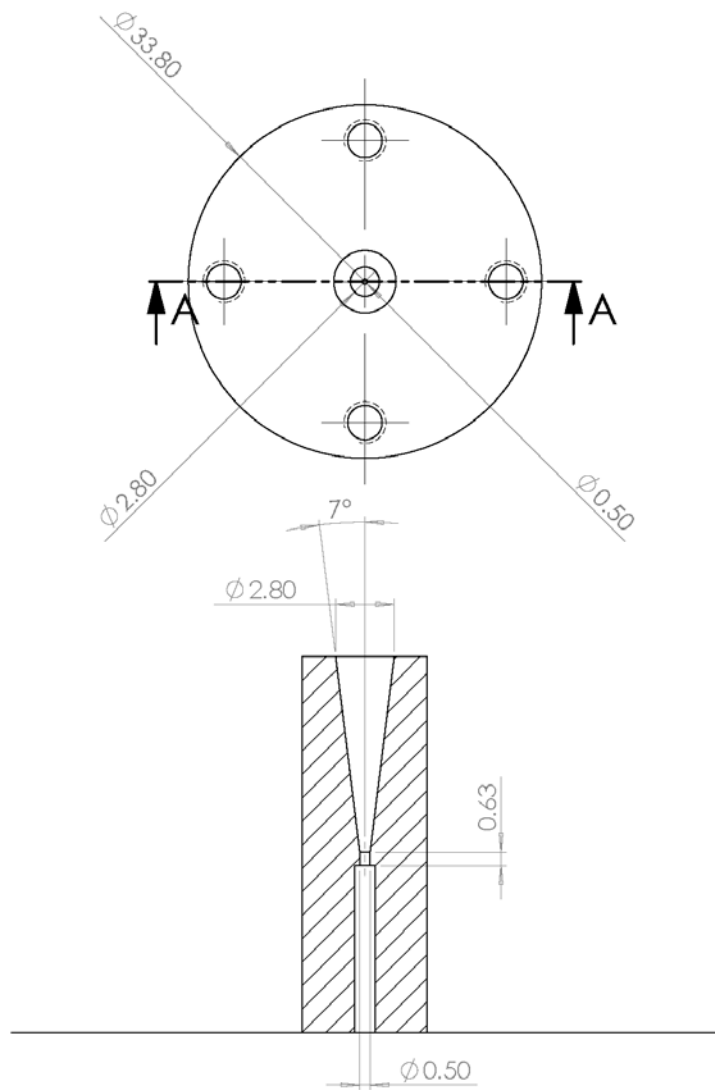
### 8.3 Supersonic nozzles drawings





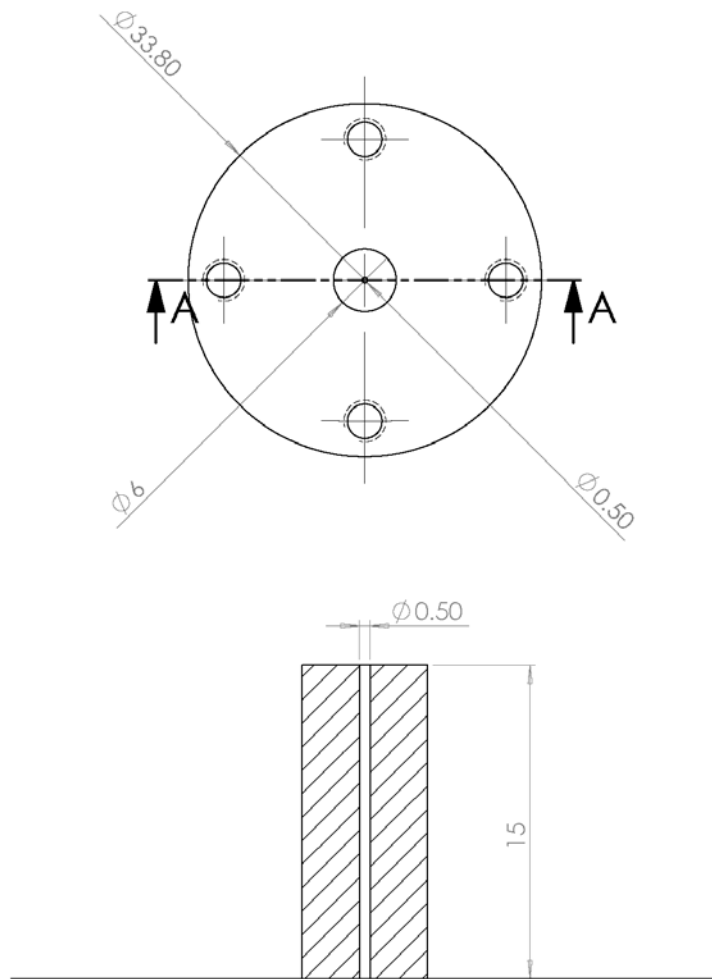
SECTION A-A  
SCALE 4 : 1

UNLESS OTHERWISE SPECIFIED: DIMENSIONS ARE IN MILLIMETERS				FINISH:		DEBUR AND BREAK SHARP EDGES		DO NOT SCALE DRAWING		REVISION	
TOLERANCES: LINEAR: ANGULAR:											
DRAWN		NAME	SIGNATURE	DATE			TITLE:		C. Aniculaesei		
CHK'D											
APP'VD											
MFG											
Q.A					MATERIAL:		DWG. NO.		Nozzle 510		A4
					WEIGHT:		SCALE:2:1		SHEET 1 OF 1		



SECTION A-A  
SCALE 4 : 1

UNLESS OTHERWISE SPECIFIED: DIMENSIONS ARE IN MILLIMETERS				FINISH:		DEBUR AND BREAK SHARP EDGES		DO NOT SCALE DRAWING		REVISION	
TOLERANCES: LINEAR: ANGULAR:											
DRAWN		NAME	SIGNATURE	DATE			TITLE:		C. Aniculaesei		
CHK'D											
APP'VD											
MFG											
Q.A					MATERIAL:		DWG. NO.		Nozzle 511		A4
					WEIGHT:		SCALE:2:1		SHEET 1 OF 1		



SECTION A-A  
SCALE 4 : 1

UNLESS OTHERWISE SPECIFIED: DIMENSIONS ARE IN MILLIMETERS				FINISH:		DEBUR AND BREAK SHARP EDGES		DO NOT SCALE DRAWING		REVISION	
TOLERANCES: LINEAR: ANGULAR:											
DRAWN		NAME		SIGNATURE		DATE		TITLE:		C. Aniculaesei	
CHK'D											
APPV'D											
MFG											
Q.A						MATERIAL:		DWG. NO.		Nozzle Gauss	
										A4	
						WEIGHT:		SCALE:2:1		SHEET 1 OF 1	

## 9 Bibliography

- Abu-Azoum, S. (2012). Experimental study of laser-driven electron and proton acceleration, PhD Thesis. University of Strathclyde.
- Akhiezer, A. I., & Polovin, R. V. (1956). Theory of wave motion of an electron plasma. *Soviet Physics JETP-USSR*, 3(5), 696-705.
- Akturk, S., Gu, X., Zeek, E., & Trebino, R. (2004). Pulse front tilt caused by spatial and temporal chirp. *Optics Express*, 12(19), 4399-4410.
- Amiraniff, F., Ardonneau, J., Bercher, M., Bernard, D., Cros, B., Debraine, A., . . . Specka, A. (1994). Electron acceleration in the plasma beat-wave experiment at Ecole Polytechnique. *Proceedings of the AIP Conference on Advanced Accelerator Concepts* (pp. 612-634). Fontana, Wisconsin: AIP.
- Anderson, J. D. (1995). *Computational fluid dynamics: The basics with applications*. Singapore: McGraw-Hill.
- Banarjee, S., Kalmykov, S. Y., Powers, N. D., Golovin, G., Ramanathan, V., Cunningham, N. J., . . . Umstadter, D. P. (2013). Stable, tunable, quasimonoenergetic electron beams produced in a laser wakefield near the threshold for self-injection. *Phys. Rev. ST Accel. Beams*, 16(3), 1302-1314.
- Berezin, A. K., Fainberg, Y. B., Kiselev, V. A., Linnik, A. F., Uskov, V. V., Balakirev, V. A., . . . Sotnikov, G. V. (1994). Wake field excitation in plasma by a relativistic electron pulse with a controlled number of short bunches. *Plasma Phys. Rep.*, 20(7), 596-602.
- Blumenfeld, I., Clayton, C. E., Decker, F. J., Hogan, M. J., Huang, C., Ischebeck, R., . . . Zhou, M. (2007). Energy doubling of 42 GeV electrons in a metre-scale plasma wakefield accelerator. *Nature*, 445(7129), 741-747.
- Bobilli, S. R., Juzer, A. C., Prasad, A. N., Mukund, K., & Parshotam, D. (2011). Laser wake-field acceleration in pre-formed plasma channel created by pre-pulse pedestal of terawatt laser pulse. *Phys. Plasmas*, 18(9), 31041-31049.
- Bosch, R. A., & Gilgenbach, R. M. (1988). Radial oscillations and the ion hose instability of an electron beam propagating in a periodic ion channel. *Phys. Fluids*, 31(3), 634-640.
- Boyd, T. M., & Sanderson, J. J. (2003). *The physics of plasmas*. Cambridge: Cambridge University Press.

- Brunetti, E. (2012). Private communication.
- Brunetti, E., Shanks, R. P., Manahan, G. G., Islam, M. R., Ersfeld, B., Anania, M. P., . . . Jaroszynski, D. A. (2010). Low Emittance, High Brilliance Relativistic Electron Beams from a Laser-Plasma Accelerator. *Phys. Rev. Lett.*, *105*(21), 50071-50074.
- Buck, A., Wenz, J., Xu, J., Khrennikov, K., Schmid, K., Heigoldt, M., . . . Veisz, L. (2013). Shock-Front Injector for High-Quality Laser-Plasma Acceleration. *Phys. Rev. Lett.*, *110*(18), 50061-50065.
- Bulanov, S. V., Kirsanov, V. I., & Sakharov, A. S. (1989). Excitation of ultrarelativistic plasma waves by pulse of electromagnetic radiation. *JETP Lett.*, *50*, 198-201.
- Bulanov, S. V., Pegoraro, F., Pukhov, A. M., & Sakharov, A. S. (1997). Transverse-Wake Wave Breaking. *Phys. Rev. Lett.*, *78*(22), 4205-4208.
- Burza, M., Gonoskov, A., Svensson, K., Wojda, F., Persson, A., Hansson, M., . . . Lundth, O. (2013). Laser Wakefield Acceleration Using Wire Produced Double Density Ramps. *Phys. Rev. ST Accel. Beams*, *16*(1), 130-134.
- Catravas, P., Esarey, E., & Leemans, W. P. (2002). Radiation sources and diagnostics with ultrashort electron bunches. *Phys. Plasmas*, *9*(5), 2428-2436.
- CERN. (2000). [http://est-div-lea-at.web.cern.ch/est-div-lea-at/atlas\\_lhcpicturesAERIAL.htm](http://est-div-lea-at.web.cern.ch/est-div-lea-at/atlas_lhcpicturesAERIAL.htm).
- CERN. (2013). <http://home.web.cern.ch/about/updates/2013/03/new-results-indicate-new-particle-higgs-boson>.
- Chen, L. M., Kotaki, H., Nakajima, K., Koga, J., Bulanov, S. V., Tajima, T., . . . Lin, Y. Z. (2007). Self-guiding of 100 TW femtosecond laser pulses in centimeter-scale underdense plasma. *Phys. Plasmas*, *14*(04), 07031-07034.
- Chen, F. F. (1984). *Plasma Physics and Controlled Fusion* (Vol. 1). New York: Plenum Press.
- Chen, M., Sheng, Z. M., Ma, Y. Y., & Zhang, J. (2006). Electron injection and trapping in a laser wakefield by field ionization to high-charge states of gases. *Journal of Applied Phys.*, *99*(5), 61091-61093.
- Chen, P. (1987). A possible final focusing mechanism for linear colliders. *Particle Accelerators*, *20*, 171-182.

- Cheshkov, S., Tajima, T., Chiu, C., & Breitling, F. (2000). Emittance control in Laser Wakefield Accelerator. In *AIP Conference Proceedings* (pp. 163-176). AIP.
- Chien, T. Y., Chang, C. L., Jin, J. Y., Wang, J., & Chen, S. Y. (2005). Spatially Localized Self-Injection of Electrons in a Self-Modulated Laser-Wakefield Accelerator by Using a Laser-Induced Transient Density Ramp. *Phys. Rev. Lett.*, *94*(11), 500-503.
- Ciocarlan, C., Wiggins, S. M., Islam, M. R., Ersfeld, B., Abuazoum, S., Wilson, R., . . . Jaroszynski, D. A. (2013). The role of the gas plasma plume and self-focusing in a gas-filled capillary discharge waveguide for high-power laser-plasma applications. *Phys. Plasmas*, *20*(9), 31081-31087.
- Cipiccia, S., Islam, M. R., Ersfeld, B., Shanks, R. P., Brunetti, E., Vieux, G., . . . Jaroszynski, D. A. (2011). Gamma-rays from harmonically resonant betatron oscillations in a plasma wake. *Nat. Phys.*, *7*(11), 867-871.
- Clayton, C. E., Everett, M. J., Lal, A., Gordon, D., Marsh, K. A., & Joshi, C. (1994). Acceleration and scattering of injected electrons in plasma beat wave accelerator experiments. *Phys. Plasmas*, *1*(5), 1753-1760.
- Cook, C. (1960). Pulse compression - Key to more efficient radar transmission. *Proc. IRE*, (pp. 310-316).
- Coverdale, C. A., Darrow, C. B., Decker, C. D., Mori, W. B., Tzeng, K. C., Marsh, K. A., . . . Joshi, C. (1995). Propagation of intense subpicosecond laser pulses through underdense plasmas. *Phys. Rev. Lett.*, *74*(23), 4659-4662.
- Decker, C. D., Mori, W. B., Tzeng, K. C., & Katsouleas, T. (1996). The evolution of ultra-intense, short-pulse lasers in underdense plasmas. *Phys. Plasmas*, *3*(5), 2047-2056.
- DeMartini, F., Townes, C. H., Gustafson, T. K., & Kelley, P. L. (1967). Self-Steepening of Light Pulses. *Phys. Rev.*, *164*, 312-323.
- Downer, M. C., Siders, C. W., Fisher, D. F., LeBlanc, S. P., Rau, B., Gaul, E., . . . Sergeev, A. (1995). Laser wakefield photon accelerator: optical diagnostics for the laser wakefield accelerator based on longitudinal interferometry. *Bulletin of American Physical Society*, *40*, 1862.

- Ebrahim, N. A. (1994). Optical mixing of laser light in a plasma and electron acceleration by relativistic electron plasma waves. *Journal of App. Phys.*, 76(11), 7645-7647.
- Esarey, E., Schroeder, C. B., & Leemans, W. P. (2009). Physics of laser-driven plasma-based electron accelerators. *Rev. Modern Phys.*, 81(3), 1229-1285.
- Everett, M. J., Lal, A., Gordon, D., Clayton, C. E., Marsh, K. A., & Joshi, C. (1994). Trapped electron acceleration by a laser-driven relativistic plasma wave. *Nature*, 368(6471), 527-529.
- Faure, J., Glinec, Y., Pukhov, A., Kiselev, S., Gordienco, S., Levebvre, E., . . . Malka, V. (2004). A laser-plasma accelerator producing monoenergetic electron beams. *Nature*, 431, 541-544.
- Faure, J., Rechatin, C., Norlin, A., Lifschitz, A., Glinec, Y., & Malka, V. (2006). Controlled injection and acceleration of electrons in plasma wakefields by colliding laser pulses. *Nature*, 444, 737-739.
- Geddes, C. G., Cormier-Michel, E., Leemans, W. P., Esarey, E., Nakamura, K., Panasenko, D., . . . Cary, J. R. (2007). Stable electron beams with low absolute energy spread from a laser wakefield accelerator with plasma density ramp controlled injection. *Particle Accelerator Conference* (pp. 1916-1918). Albuquerque, New Mexico: IEEE.
- Geddes, C. R., Toth, C., Tilborg, J., Esarey, E., Schroeder, C. B., Bruhwiler, D., . . . Leemans, W. P. (2004). High-quality electron beams from a laser wakefield accelerator using plasma-channel guiding. *Nature*, 431, 538-541.
- Geddes, G. R., Nakamura, K., Plateau, G. R., Toth, C., Cormier-Michel, E., Esarey, E., . . . Leemans, W. P. (2008). Plasma-Density-Gradient Injection of Low Absolute-Momentum-Spread Electron Bunches. *Phys. Rev. Lett.*, 100(21), 50041-50044.
- Genoud, G., Bloom, M. S., Vieira, J., Burza, M., Najmudin, Z., Persson, A., . . . Mangles, S. P. (2013). Increasing energy coupling into plasma waves by tailoring the laser radial focal spot distribution in a laser wakefield accelerator. *Phys. Plasmas*, 20(6), 45011-45014.
- Gibbon, P. (2005). *Short Pulse Laser Interactions with Matter: An Introduction*. London: Imperial College Press.

- Ginzburg, V. L. (1964). *The propagation of electromagnetic waves in plasmas*. Oxford: Pergammon Press.
- Glinec, Y., Faure, J., Guemnie-Tafo, A., Malka, V., Monard, H., & Larbre, J. P. (2006). Absolute calibration for a broad range single shot electron spectrometer. *Rev. Sci. Ins.*, 77(10), 33011-33016.
- Glinec, Y., Faure, J., Lifschitz, A., Vieira, J. M., Fonseca, R. A., Silva, L. O., & Malka, V. (2008). Direct observation of betatron oscillations in a laser-plasma electron accelerator. *EPL Journal*, 81, 64001p1-64001p5.
- Gorbunov, L. M., & Kirsanov, V. I. (1987). Excitation of plasma waves by an electromagnetic wave packet. *SOV Phys. JETP*, 66, 290-294.
- Gordienko, S., & Pukhov, A. (2005). Scalings for ultrarelativistic laser plasmas and quasi-monoenergetic electrons. *Phys. Plasmas*, 12(4), 3109-3111.
- Grittani, G., Anania, M. P., Gatti, G., Giulietti, D., Kando, M., Krus, M., . . . Gizzi, L. A. (2014). High energy electrons from interaction with a structured gas jet at FLAME. *Nuclear Ins. and Met. in Phys. Research Sec. A*, 740, 257-265.
- Hafz, N. A., Jeong, T. M., Choi, I. W., Lee, S. K., Pae, K. H., Kulagin, V. K., . . . Lee, J. (2008). Stable generation of GeV class electron beams from self-guided laser-plasma channels. *Nat. Phot.*, 2, 571-577.
- Hafz, N. M., Choi, I. W., Sung, J. H., Kim, H. T., Hong, K. H., Jeong, T. M., . . . Lee, J. (2007). Dependence of the electron beam parameters on the stability of laser propagation in a laser wakefield accelerator. *App. Phys. Lett.*, 90(15), 15011-15012.
- Halliday, R., & Resnick, R. (1970). *Fundamentals of physics*. New York: John Wiley and Sons.
- Hamster, H., Sullivan, A., Gordon, S., White, W., & Falcone, R. W. (1993). Subpicosecond, electromagnetic pulses from intense laser-plasma interaction. *Phys. Rev. Lett.*, 71(17), 2725-2728.
- Hebling, J. (1996). Derivation of the pulse front tilt caused by angular dispersion. *Optical and Quntum Electronics*, 28, 1759-1763.
- Hemker, R. G., Hafz, N. M., & Uesaka, M. (2002). Computer simulations of a single-laser double-gas-jet wakefield accelerator concept. *Phys. Rev. ST Accel. Beams*, 5(4), 1301-1309.

- Hidding, B., Pretzler, G., Rosenweig, J. B., Konigstein, T., Schiller, D., & Bruhwiler, D. L. (2012). Ultracold Electron Bunch Generation via Plasma Photocathode Emission and Acceleration in a Beam-Driven Plasma Blowout. *Phys. Rev. Lett.*, *108*(3), 500-504.
- Hogan, M. J., Barnes, C. D., Clayton, F. J., Decker, C. E., Deng, S., Emma, P., . . . Walz, D. (2005). Multi-GeV energy gain in a plasma-wakefield accelerator. *Phys. Rev. Lett.*, *95*(5), 48021-48024.
- Holman, J. P. (2002). *Heat Transfer*. New York: McGraw Hill.
- Hsu, T. (2002). *MEMS and Microsystems: Design and manufacture*. Boston: McGraw Hill.
- Issac, R. C., Vieux, G., Welsh, G. H., Shanks, R., Brunetti, E., Cipiccia, S., . . . Jaroszynski, D. A. (2009). Electron pointing stability of a laser wakefield accelerator. *SPIE - Invited paper*, *7359*, 151-157.
- Jaroszynski, D. A. (2013). Private communication.
- Jaroszynski, D. A., Bingham, R., Brunetti, E., Ersfeld, B., Gallacher, J., Geer, v., . . . Wiggins, S. M. (2006). Radiation sources based on laser-plasma interactions. *Phil. Trans. R. Soc. A*, 689-710.
- Jung, R. (2007). PhD Thesis. Heinrich-Heine University. Retrieved from STFC - Central Laser Facility.
- Kainz, K. K., Hogstrom, K. R., Antolak, J. A., Almond, P. R., & Bloch, C. D. (2005). Dose properties of x-ray beams produced by laser-wakefield-accelerated electrons. *Physics in Medicine and Biology*, *50*(1), N1-N10.
- Kainz, K. K., Hogstrom, K. R., Antolak, J. A., Almond, P. R., & Bloch, C. D. (2005). Dose properties of x-ray beams produced by laser-wakefield-accelerated electrons. *Physics in Medicine and Biology*, *50*(1), N1-N10.
- Kalmykov, S. Y., Gorbunov, L. M., Mora, P., & Shvets, G. (2006). Injection, trapping, and acceleration of electrons in a three-dimensional nonlinear laser wakefield. *Phys. Plasmas*, *13*(02), 1131021-11310211.
- Kalmykov, S., Yi, S. A., Khudik, V., & Shvets, G. (2009). Electron Self-Injection and Trapping into an Evolving Plasma Bubble. *Phys. Rev. Lett.*, *103*(13), 50041-50044.

- Karsch, S., Osterhoff, J., Popp, A., Rowlands-Rees, T. P., Major, Z., Fuchs, M., . . . Hooker, S. M. (2007). GeV-scale electron acceleration in a gas-filled capillary discharge waveguide. *New Journal of Phys.*, 9(11), 1-11.
- Katsouleas, T. (1986). Physical mechanisms in the plasma wake-field accelerator. *Phys. Rev. A*, 33(3), 2056-2064.
- Katsouleas, T. (1987). Beam loading in plasma accelerators. *Particle Accelerators*, 22, 81-99.
- Kim, J., Jang, H., Yoo, S., Hur, M., Hwang, I., Lim, J., . . . Lee, J. (2007). Quasi-Monoenergetic Electron-Beam Generation Using a Laser Accelerator for Ultra-Short X-ray Sources. *Journal of Korean Physical Society*, 51, 397-401.
- Kim, J., Ju, G., & Yoo, H. S. (2011). Energy Enhancement Using an Upward Density Ramp in Laser Wakefield. *Journal of the Korean Physical Society*, 59(51), 3166-3170.
- Kitagawa, Y., Matsumoto, T., Minamihata, T., Sawai, K., Matsuo, K., Mima, K., . . . Nakai, S. (1992). Beat-wave excitation of plasma wave and observation of accelerated electrons. *Phys. Rev. Lett.*, 68(1), 48-51.
- Kostyukov, I., Nerush, E., Pukhov, A., & Seredov, V. (2009). Electron Self-Injection in Multidimensional Relativistic-Plasma Wake Fields. *Phys. Rev. Lett.*, 103(17), 50031-50034.
- Kostyukov, I., Nerush, E., Pukhov, A., & Seredov, V. (2010). A multidimensional theory for electron trapping by a plasma wake generated in the bubble regime. *New Journal of Phys.*, 12(04), 50091-500923.
- Krause, E. (2005). *Fluid Dynamics*. Berlin: Springer.
- Kundu, P. K., & Cohen, I. R. (2002). *Fluid Mechanics*. New York: Academic Press.
- Leemans, W. P., Geddes, C. R., Faure, J., Toth, C., van Tilborg, J., Schroeder, C. B., . . . Martin, M. C. (2003). Observation of Terahertz Emission from a Laser-Plasma Accelerated Electron Bunch Crossing a Plasma-Vacuum Boundary. *Phys. Rev. Lett.*, 31(7), 48021-48024.
- Leemans, W. P., Nagler, B., Gonsalves, A. J., Toth, C., Nakamura, K., Geddes, C. R., . . . Hooker, S. M. (2006). GeV electron beams from a centimetre-scale accelerator. *Nat. Phys.*, 2, 696-699.

- Leemans, W. P., van Tilborg, J., Faure, J., Geddes, C. R., Toth, C., Schroeder, C. B., . . . Dugan, G. (2004). Terahertz radiation from laser accelerated electron bunches. *Phys. Plasmas*, *11*(5), 2899-2906.
- Lehe, R., Thaur, C., Guillaume, E., Lifschitz, A., & Malka, V. (2014). Laser-plasma lens for laser-wakefield accelerators. *Phys. Rev. ST Accel. Beams*, *17*(12), 13011-13019.
- Lemos, N., Lopes, N., Dias, J. M., & Viola, F. (2009). Design and characterization of supersonic nozzles for wide focus laser-plasma interactions. *Rev. Sci. Ins.*, *80*(10), 33011-33015.
- Lindl, J. D., & Kaw, P. K. (1971). Pondermotive force on laser-produced plasmas. *Phys. Fluids*, *14*(2), 371-377.
- Lu, W., Huang, C., Mori, W. B., & Katsouleas, T. (2006). Nonlinear theory for relativistic plasma wakefields in the blowout regime. *Phys. Rev. Lett.*, *96*(16), 50021-50024.
- Lu, W., Tzoufras, M., Joshi, C., Tsung, F. S., Mori, W. B., Vieira, J., . . . Silva, L. O. (2007). Generating multi-GeV electron bunches using single stage laser wakefield acceleration in a 3D nonlinear regime. *Phys. Rev. ST Accel. Beams*, *10*(6), 13011-130112.
- Lu, W., Tzoufras, M., Tsung, F. S., Joshi, C., Mori, W. B., Vieira, J., . . . Silva, L. O. (2007). Designing LWFA in the blowout regime. *IEEE Particle Accelerator Conference* (pp. 3050-3051). Albuquerque, NM : IEEE.
- Ludziejewski, T., Moszynski, M., Kapusta, M., Wolski, D., Klamra, W., & Moszynska, K. (1997). Investigation of some scintillation properties of YAG:Ce crystals. *Nuclear Ins. and Met. in Phys. Research*, *398*(2-3), 287-294.
- Maine, P., Strickland, D., Bado, P., Pessot, M., & Mourou, G. (1988). Generation of ultrahigh peak power pulses by chirped pulse amplification. *IEEE J. Quantum Electron*, *24*, 398-403.
- Malka, V., Fritzler, S., Lefebvre, E., Aleonard, M. M., Burgy, F., Chambaret, J. P., . . . Dangor, A. E. (2002). Electron acceleration by a wake field forced by an intense ultrashort laser pulse. *Science*, *298*(5598), 1596-1600.

- Manahan, G. G. (2013). Studies of transverse properties of relativistic electrons from laser wakefield accelerator, PhD Thesis. University of Strathclyde.
- Mangles, S. P., Murphy, C. D., Najmudin, Z., Thomas, A. R., Collier, A. J., Dangor, A. E., . . . Krushelnick, K. (2004). Monoenergetic beams of relativistic electrons from intense laser-plasma interactions. *Nature*, *431*, 535-538.
- Mangles, S. P., Thomas, A. G., Kaluza, M. C., Lundth, O., Lindau, F., Persson, A., . . . Krushelnick, K. (2006). Laser-Wakefield Acceleration of Monoenergetic Electron Beams in the First Plasma-Wave Period. *Phys. Rev. Lett.*, *96*(21), 50011-50014.
- Marquès, J. R., Geindre, J. P., Amiranoff, F., Audebert, P., Gauthier, J. C., Antonetti, A., & Grillon, G. (1996). Temporal and spatial measurements of the electron density perturbation produced in the wake of an ultrashort laser pulse. *Phys. Rev. Lett.*, *76*(19), 3566-3569.
- Martinez, O. E. (1986). Pulse distortions in tilted pulse schemes for ultrashort pulses. *Optics Communications*, *59*(3), 229-232.
- Masson-Laborde, P. E., Zo, M. Z., Ali, A., Fourmaux, S., Lassonde, P., Kiefer, J. C., . . . Fedosejevs, R. (2014). Giga-electronvolt electrons due to a transition from laser wakefield acceleration to plasma wakefield acceleration. *Phys. Plasmas*, *21*(13), 31131-311312.
- Max, C. E., Arons, J., & Langdon, A. B. (1974). Self-modulation and self-focusing of electromagnetic waves in plasmas. *Phys. Rev. Lett.*, *33*(4), 209-212.
- Maxwell, J. C. (1873). *A treatise on electricity and magnetism*. Oxford: Clarendon Press.
- McGuffey, C., Matsuoka, T., Kneip, S., Schumaker, W., Dollar, F., Zulick, C., . . . Najmudin, Z. (2012). *Phys. Plasmas*, *19*(6).
- McGuffey, C., Matsuoka, T., Kneip, S., Schumaker, W., Dollar, F., Zulick, C., . . . Najmudin, Z. (2012). Experimental laser wakefield acceleration scalings exceeding 100 TW. *Phys. Plasmas*, *19*(6), 31131-31136.
- Miura, E., Koyama, K., Kato, S., Saito, N., Adachi, M., Kawada, Y., . . . Tanimoto, M. (2005). Demonstration of quasi-monoenergetic electron-beam generation in laser-driven plasma acceleration. *Applied Phys. Lett.*, *86*(25), 15011-15013.

- Modena, A., Najmudin, Z., Dangor, A. E., Clayton, C. E., Marsh, K. A., Joshi, C., . . . Walsh, F. N. (1995). Electron acceleration from the breaking of relativistic plasma waves. *Nature*, *377*(6550), 606-608.
- Moore, C. I., Ting, A., Krushelnick, K., Esarey, E., Hubbard, R. F., Hafizi, B., . . . Sprangle, P. (1997). Electron trapping in self-modulated laser wakefields by raman backscatter. *Phys. Rev. Lett.*, *79*(20), 3909-3912.
- Mora, P., & Antonsen, M. (1997). Kinetic modeling of intense, short laser pulses propagating in tenuous plasmas. *Phys. Plasmas*, *4*(217), 217-229.
- Mori, W. B. (1997). The physics of the nonlinear optics of plasmas at relativistic intensities for short-pulse lasers. *IEEE Journal of Quantum Optics*, *33*(11), 1942-1953.
- Mourou, G., & Umstadter, D. (1992). Development and applications of compact high-intensity lasers. *Phys. Fluids*, *4*(7), 2315-2326.
- Muggli, P., Lee, S., Katsouleas, T., Assmann, R., Decker, F. J., Hogan, M. J., . . . Wang, S. (2001). Boundary effects: Refraction of a particle beam. *Nature Brief Communications*, *411*(43), 43.
- Muggli, P., Lee, S., Katsouleas, T., Assmann, R., Decker, F. J., Hogan, M. J., . . . Wang, S. (2001). Collective refraction of a beam of electrons at a plasma-gas interface. *Phys. Rev. ST Accel. Beams*, *4*(9), 13011-13013.
- Nakajima, K., Fisher, D., Kawakubo, T., Nakanishi, H., Ogata, A., Kato, Y., . . . Tajima, T. (1995). Observation of ultrahigh gradient electron acceleration by a self-modulated intense short laser pulse. *Phys. Rev. Lett.*, *74*(22), 4428-4431.
- Nakajima, K., Kawakubo, T., Nakanishi, H., Ogata, A., Kitagawa, Y., Kodama, R., . . . Nishida, N. (1995). Proof of principle experiments of laser wakefield acceleration using a 1 ps 10 TW Nd:glass laser. *AIP Conference Proceedings*, 144-155.
- Nakanishi, H., Enomoto, A., Ogata, A., Nakajima, K., Whittum, D., Yoshida, Y., . . . Nishida, Y. (1993). Wakefield accelerator using twin linacs. *Nuclear Instruments Methods*, *328*(3), 596-598.

- Naumova, N. M., Bulanov, S. V., Nishihara, K., Esirkepov, T. Z., & Pegoraro, F. (2002). Polarisation effects and anisotropy in three-dimensional relativistic self-focussing. *Phys. Rev. E*, *65*(04), 54021-54024.
- Nemeth, K., Shen, B., Li, Y., Shang, H., Crowell, R., Harkay, K. C., & Cary, J. R. (2008). Laser-Driven Coherent Betatron Oscillation in a Laser-Wakefield Cavity. *Phys. Rev. Lett.*, *100*(9), 50021-50024.
- newscenter.lbl.gov. (2015, April 25). <http://newscenter.lbl.gov/feature-stories/2009/12/21/accelerators-tomorrow-part1/>.
- Osterhoff, J., Popp, A., Major, Z., Marx, B., Rowlands-Rees, T. P., Fuchs, M., . . . Karsch, S. (2008). Generation of Stable, Low-Divergence Electron Beams by Laser-Wakefield Acceleration in a Steady-State-Flow Gas Cell. *Phys. Rev. Lett.*, *101*(8), 50021-50024.
- Perry, M. D., & Mourou, G. (1994). Terawatt to Petawatt Subpicosecond Lasers. *Science*, *264*(5161), 917-924.
- Phuoc, K. T., Corde, S., Fitour, R., Shah, R., Albert, F., Rousseau, J.-P., . . . Mercier, B. (2006). Imaging Electron Trajectories in a Laser-Wakefield Cavity Using Betatron X-Ray Radiation. *Phys. Rev. Lett.*, *97*(22), 50021-50024.
- Phuoc, K. T., Corde, S., Fitour, R., Shah, R., Albert, F., Rousseau, J.-P., . . . Pukhov, A. (2008). Analysis of wakefield electrons orbits in plasma wiggler. *Phys. Plasmas*, *15*(7), 31061-31068.
- Popp, A., Vieira, J., Osterhoff, J., Major, Z., Horlein, R., Fuchs, M., . . . Karsch, S. (2010). All-Optical Steering of Laser-Wakefield-Accelerated Electron Beams. *Phys. Rev. Lett.*, *105*(21), 50011-50014.
- Pretzler, G., Kasper, A., & Witte, K. J. (2000). Angular chirp and tilted light pulses in CPA lasers. *Applied Phys. B*, *70*, 1-9.
- Pukhov, A., & Gordienko, S. (2006). Bubble regime of wakefield acceleration: similarity theory and optimal scalings. *Phil. Trans. R. Soc. A: Mathematical, Physical and Engineering Sciences*, *364*(1840), 623-633.
- Pukhov, A., & Kostyukov, I. (2008). Control of laser-wakefield acceleration by the plasma-density profile. *Phys. Rev. E*, *77*(2), 54011-54014.
- Pukhov, A., & Meyer-ter-Vehn, J. (2002). Laser wake field acceleration: the highly non-linear broken-wave regime. *Applied Phys. B*, *74*(4-5), 355-361.

- Quan-Zhi, Y., Yu-Tong, L., Jie, Z., Jun, Z., Han-Ming, L., Xiao-Yu, P., & Kun, L. (2004). Characterisation of density profile of cylindrical pulsed gas jets. *Chin. Phys. Lett.*, *21*(5), 874-876.
- Rechatin, C., Davoine, X., Lifschitz, A., Ben Ismail, A., Lim, J., Lefebvre, E., . . . Malka, V. (2009). Observation of beam loading in a laser-plasma accelerator. *Phys. Rev. Lett.*, *103*(19), 48041-48044.
- Reitsma, A. J., Cairns, R. A., Bingham, R., & Jaroszynski, D. A. (2005). Efficiency and Energy Spread in Laser-Wakefield Acceleration. *Phys. Rev. Lett.*, *94*(8), 50041-50044.
- Rittershofer, W., Schroeder, C. B., Esaray, E., Gruner, F. J., & Leemans, W. P. (2010). Tapered plasma channels to phase-lock accelerating and focusing forces in laser-plasma accelerators. *Phys. Plasmas*, *17*(6), 31041-310411.
- Rosenzweig, J. B., Cline, D. B., Cole, B., Figueroua, H., Gai, W., Konecny, R., . . . Simpson, J. (1988). Experimental observation of plasma wake-field acceleration. *Phys. Rev. Lett.*, *61*(1), 98-101.
- Rosenzweig, J. B., Schoessow, P., Cole, B., Gai, W., Konecny, R., Norem, J., & Simpson, J. (1989). Experimental measurement of nonlinear plasma wake fields. *Phys. Rev. A*, *39*(3), 1586-1589.
- Rosenzweig, J., & Colby, E. (1994). Charge and wavelength scaling of rf photoinjector design. *6th advanced accelerator concepts workshop*, 335, 724-737.
- Sadighi-Bonabi, R., Habibi, M., & Yazdani, E. (2009). Improving the relativistic self-focusing of intense laser beam in plasma using density transition. *Phys. Plasmas*, *16*(8), 31051-31054.
- Santala, M. I., Najmudin, Z., Clark, E. L., Tatarakis, M., Krushelnick, K., Dangor, A. E., . . . Clarke, R. J. (2001). Observation of a hot high current electron beam from a self-modulated laser wakefield accelerator. *Phys. Rev. Lett.*, *86*(7), 1227-1230.
- Schluter, A. (1968). Pondermotive action of light. *Plasma Phys.*, *10*(4), 471.
- Schmid, K. (2011). *Laser Wakefield Electron Acceleration: A Novel Approach Employing Supersonic Microjets and Few-Cycle Laser Pulses*. Berlin: Springer.

- Schmid, K., & Veisz, L. (2012). Supersonic gas jets for laser-plasma experiments. *Rev. Sci. Ins.*, 83(05), 33041-330410.
- Schmid, K., Buck, A., Sears, C. M., Mikhailova, J. M., Tautz, R., Herrmann, D., . . . Veisz, L. (2010). Density-transition based electron injector for laser driven wakefield accelerators. *Phys. Rev. ST Accel. Beams*, 13(9), 130-134.
- Schmid, K., Veisz, L., Tavella, F., Benavides, S., Tautz, R., Herrmann, D., . . . Krausz, F. (2009). Few-cycle laser-driven electron acceleration. *Phys. Rev. Lett.*, 102(12), 124-128.
- Semushin, S., & Malka, M. (2001). High density gas jet nozzle design for laser target production. *Rev. Sci. Ins.*, 72, 2961-2965.
- Shanks, R. (2012). Comprehensive Characterisation of Laser Plasma Wakefield Accelerated Electrons, PhD Thesis. University of Strathclyde.
- Shaw, J. L., Vafaei-Najafabadi, N., Marsh, K. A., & Joshi, C. (2012). Retrieved from UCLA:  
[http://www.ee.ucla.edu/~plasma/files/conference%20proceedings/2012\\_Shaw\\_AAC.pdf](http://www.ee.ucla.edu/~plasma/files/conference%20proceedings/2012_Shaw_AAC.pdf)
- Shen, B., Li, Y., Nemeth, K., Shang, H., Chae, Y. C., Soliday, R., . . . Cary, J. (2007). Electron injection by a nanowire in the bubble regime. *Phys. Plasmas*, 14(5), 31151-31155.
- Siegman, A. E. (1986). *Lasers*. Mill Valley, California: University Science Books.
- Sonoda, M., Takano, M., Miyahara, J., & Kato, H. (1983). Computed radiography utilising scanning laser stimulated luminiscence. *Radiology*, 148(3), 833-838.
- Spence, D. J., Butler, A., & Hooker, S. M. (2003). Gas-filled capillary discharge waveguides. *Journal of Optical Society of America B*, 20, 138-151.
- Sprangle, P., Esarey, E., & Ting, A. (1990). Nonlinear interaction of intense laser pulses in plasmas. *Phys. Rev. A*, 41(8), 4463-4469.
- Sprangle, P., Esarey, E., & Ting, A. (1990). Nonlinear theory of intense laser-plasma interactions. *Phys. Rev. Lett.*, 64(17), 2011-2014.
- Sprangle, P., Hafizi, B., Penano, J. R., Hubbard, R. F., Ting, A., Moore, C. I., . . . Antonsen Jr., T. M. (2001). Wakefield generation and GeV acceleration in tapered plasma channels. *Phys. Rev. E*, 63(5), 64051-640511.

- Sprangle, P., Penano, J. R., Hafizi, B., Hubbard, R. F., Ting, A., Gordon, D. F., . . .  
 Antonsen, T. M. (2002). GeV acceleration in tapered plasma channels. *Phys. Plasmas*, *9*(5), 2364-2370.
- Strickland, D., & Mourou, G. (1985). Compression of amplified chirped optical pulses. *Optical communications*, *56*, 219-221.
- Subiel, A. (2012). Private communication.
- Swanson, D. G. (2003). *Plasma waves*. Philadelphia: Institute of Physics Publishing.
- Tajima, T., & Dawson, J. M. (1979). Laser Electron Accelerator. *Phys. Rev. Lett.*, *43*(4), 267-270.
- Thaury, C., Gauillaume, E., Corde, S., Lehe, R., Bouteiller, M. L., Phuoc, K. T., . . .  
 Malka, V. (2013). Angular momentum evolution in laser-plasma accelerators. *Phys. Rev. Lett.*, *111*(13), 50021-50025.
- Thompson, M. C., Badakov, H., Rosenzweig, J. B., Travish, G., Barov, N., Piot, P., . . .  
 . . Tikhoplav, R. (2010). Observations of low-aberration plasma lens focusing of relativistic electron beams at the underdense threshold. *Phys. Plasmas*, *17*(07), 31051-310510.
- Ting, A., Moore, C. I., Krushelnick, K., Manka, C., Esarey, E., Sprangle, P., . . .  
 Baine, M. (1997). Plasma wakefield generation and electron acceleration in a self-modulated laser wakefield accelerator experiment. *Phys. Plasmas*, *4*(5), 1889-1899.
- Tomassini, P., Galimberti, M., Giulietti, A., Giulietti, D., Gizzi, L. A., Labate, L., &  
 Pegoraro, F. (2003). Production of high-quality electron beams in numerical experiments of laser wakefield acceleration with longitudinal wave breaking. *Phys. Rev. ST Accel. Beams*, *6*(12), 13011-13017.
- Tooley, M. (2014). Private communication.
- Trines, R. M., Bingham, R., Najmudin, Z., Mangles, S., Silva, L. O., Fonseca, R., &  
 Norreys, P. A. (2010). Electron trapping and acceleration on a downward density ramp: a two-stage approach. *New Journal of Phys.*, *12*(04), 50271-502710.
- Tzoufras, M., Lu, W., Tsung, F. S., Huang, C., Mori, W. B., Katsouleas, T., . . .  
 Silva, L. O. (2008a). Beam loading in the nonlinear regime of plasma-based acceleration. *Phys. Rev. Lett.*, *101*(14), 50021-50024.

- Van der Wiel, M. J., Luiten, O. J., Brussaard, G. H., van der Geer, S. B., Urbanus, W. H., van Dijk, W., & van Oudheusden, T. (2006). Laser wakefield acceleration: the injection issue. Overview and latest results. *Phil. Trans. R. Soc. A*, 364(1840), 679-687.
- Versteeg, H. K., & Malalasekera, W. (1995). *An introduction to computational fluid dynamics. The finite volume method*. New York: Longman Scientific & Technical.
- Wagner, R., Chen, S. Y., Maksimchuk, A., & Umstadter, D. (1997). Electron acceleration by a laser wakefield in a relativistically self-guided channel. *Phys. Rev. Lett.*, 78(16), 3125-3128.
- Walton, B., Dangor, A. E., Mangles, S. P., Najmudin, Z., Krushelnick, K., Thomas, A. G., . . . Malka, V. (2013). Measurements of magnetic field generation at ionisation fronts from laser wakefield acceleration experiments. *New Journal of Phys.*, 15(02), 50341-503411.
- Wen, M., Shen, B., Zhang, X., Wang, F., Jin, Z., Ji, L., . . . Nakajima, K. (2010). Controlled electron acceleration in the bubble regime by optimizing plasma density. *New Journal of Phys.*, 12(4), 50101-50109.
- Whittum, D. H., & Sessler, A. M. (1990). Ion-Channel Laser. *Phys. Rev. Lett.*, 64(21), 2511-2515.
- Wiggins, M., Reijnders, M. P., Abu-Azoum, S., Hart, K., Vieux, G., Welsh, G., . . . Jaroszynski, D. A. (2012). Straight and linearly tapered capillaries produced by femtosecond laser micromachining. *Journal of Plasma Phys.*, 78(04), 355-361.
- Wiggins, S. M., Gallacher, J. G., Schlenvoigt, H. P., Schwoerer, H., Welsh, G. H., Issac, R. C., . . . Jaroszynski, D. A. (20-21 April 2011). Laser-driven radiation sources in the ALPHA-X project. In *Harnessing relativistic plasma waves as novel radiation sources from terahertz to x-rays and beyond II*. Prague, Czech Republic.
- Wiggins, S. M., Issac, R. C., Welsh, G. W., Brunetti, E., Shanks, R. P., Anania, M. P., . . . Jaroszynski, D. A. (2010). High quality electron beams from a laser wakefield accelerator. *Plasma Phys. and Controlled Fusion*, 52(12), 538-541.

Woods, L. C. (2008). *Physics of plasmas*. Weinheim: WILEY-VCH Verlag GmbH & Co. KGaA.

www.fastlite.com. (2015). <http://www.fastlite.com/en/cat465015--Dazzler.html?Cookie=set>.

www.linearcollider.com. (2015). <http://www.linearcollider.org/>.

www.nature.com. (2004, September 30).

<http://www.nature.com/nature/links/040930/040930-1.html>.

www.scapa.co.uk. (2015). <http://www.scapa.ac.uk/>.

www.smijapan.com. (2015).

[http://www.smijapan.com/download/IotaOne\\_UserManual.pdf](http://www.smijapan.com/download/IotaOne_UserManual.pdf).

Yamazaki, A., Kotaki, H., Daito, I., Kando, M., Bulanov, S. V., Esirkepov, T. Z., . . .

Nemoto, K. (2005). Quasi-monoenergetic electron beam generation during laser pulse interaction with very low density plasmas. *Phys. Plasmas*, *12*(9), 31011-31015.